

Effective-Medium-Clad Dielectric Components Towards Terahertz Integrated Platform

by

Weijie Gao

B Eng (Mechanical Design, Manufacturing and Automation),
Hubei University of Technology, China, 2011

M Eng Sci (Telecommunications),
University of New South Wales, Sydney, Australia, 2016

Thesis submitted for the degree of

Doctor of Philosophy

in

School of Electrical & Electronic Engineering
Faculty of Engineering, Computer & Mathematical Sciences
The University of Adelaide

December, 2021

Supervisors:

Assoc. Prof. Withawat Withayachumnankul,

School of Electrical & Electronic Engineering, The University of Adelaide

Prof. Christophe Fumeaux,

School of Electrical & Electronic Engineering, The University of Adelaide



© 2021
Weijie Gao
All Rights Reserved



Contents

Contents	iii
Abstract	vii
Originality Declaration	ix
Acknowledgments	xi
Publications	xv
List of Figures	xvii
List of Tables	xxi
Chapter 1. Introduction	1
1.1 Terahertz technology	3
1.2 Existing terahertz integrated systems	7
1.3 Existing terahertz waveguides	10
1.3.1 Non-planar waveguides	11
1.3.2 Planar waveguides	15
1.3.3 Performance comparison of various waveguide designs	22
1.4 Thesis outline and original contributions	22
Chapter 2. Effective-medium-clad dielectric waveguides: A proof of concept	27
2.1 Introduction	28
2.2 Waveguide design and analysis	29
2.2.1 Overview	29
2.2.2 Effective medium	31
2.2.3 Modal analysis	32
2.3 Experiments	35

2.3.1	Transmission measurements	36
2.3.2	Communications measurements	39
2.4	Conclusion	42
Chapter 3. Analysis of effective-medium-clad waveguides and peripherals		43
3.1	Introduction	44
3.2	Design principle	44
3.2.1	Overview	44
3.2.2	Modal analysis	46
3.2.3	Parametric study	48
3.3	Characteristics of waveguide	51
3.3.1	Transmission	52
3.3.2	Dispersion	54
3.3.3	Cross polarisation	55
3.3.4	Crosstalk between parallel waveguides	56
3.3.5	Bend	61
3.3.6	Crossing	64
3.4	Conclusion	67
Chapter 4. Effective-medium-clad Bragg grating filters		69
4.1	Introduction	70
4.2	Design principles	72
4.2.1	Overview	72
4.2.2	Design considerations	72
4.2.3	Impact of different waveguide width Δw	75
4.3	Characteristics of filters	76
4.3.1	Transmission performance	77
4.3.2	Bandwidth	86
4.3.3	Central frequency	88
4.3.4	Dispersion	90
4.3.5	Fabrication tolerance and resultant effects	91
4.4	Applicability at high terahertz frequencies	94
4.5	Conclusion	96

Chapter 5. Effective-medium-clad polarisation splitters	99
5.1 Introduction	101
5.2 Existing techniques for polarisation splitting	102
5.2.1 Microwave-based orthomode transducers	102
5.2.2 Optics-based polarisation splitters	104
5.3 Proposed design	109
5.3.1 Design principles	109
5.3.2 Effective-medium-clad tapered directional couplers	112
5.4 Characteristics of the polarization splitter	118
5.4.1 Transmission and path crosstalk	118
5.4.2 Port isolation and higher-order modes	126
5.4.3 Dispersion	128
5.5 Conclusion	129
Chapter 6. Summary and outlook	131
6.1 Thesis conclusion	133
6.2 Outlook	134
Appendix A. Transmission sensitivity to waveguide misalignment	137
Appendix B. Packaging for practical applications	139
Appendix C. Coupling loss between effective-medium-clad waveguide and WR-3.4 hollow waveguide	141
Bibliography	143
Biography	167

Abstract

Over the past few decades, optics-based time-domain spectroscopic systems have significantly promoted the developments of terahertz science and technology. Despite their success in physics, the bulky and costly optical systems are not readily amendable to various applications such as communications, imaging, sensing, and radar. These applications require devices with structural compactness, integrability, and portability. Leveraging both electronic and photonic technologies, terahertz integrated circuits have emerged and gradually bridged the gap between 'concept' and 'application'. To realise multifunctional terahertz integrated circuits, efficient and broadband platforms able to accommodate various passive and active components are in great demand, while interconnects with low loss, low dispersion, and broad bandwidth are vital.

To this end, this thesis focuses on an efficient and broadband terahertz integrated platform based on silicon. Firstly, a class of self-supported substrateless dielectric waveguides are proposed based on the effective medium theory. The effective-medium-clad dielectric waveguides are purely built into a high-resistivity intrinsic float-zone silicon wafer to achieve extremely low loss and low dispersion. The effective medium is realised by periodically perforating the silicon slab with a deep subwavelength spacing, leading to a tailorable effective relative permittivity tensor. Consequently, an additional degree of freedom is granted in this design to manipulate the waveguides' modal indices and adapt to different guiding scenarios. Through in-depth investigations of various propagation characteristics, the proposed waveguides show a potential to establish a terahertz integrated platform with a high level of design flexibility.

Benefiting from the concept of effective medium to create this new waveguide platform, various fundamental building blocks and functional components are proposed including bends, crossings, directional couplers, filters, and polarisation splitters. All these components inherit high efficiency and broad bandwidth, which are much needed for terahertz applications that typically leverage a vast available bandwidth with limited source power. The proposed concepts can benefit terahertz integrated circuits at large, in analogy to the silicon-on-insulator platform for integrated photonics.

Originality Declaration

I certify that this work contains no material which has been accepted for the award of any other degree or diploma in my name, in any university or other tertiary institution and, to the best of my knowledge and belief, contains no material previously published or written by another person, except where due reference has been made in the text. In addition, I certify that no part of this work will, in the future, be used in a submission in my name, for any other degree or diploma in any university or other tertiary institution without the prior approval of the University of Adelaide and where applicable, any partner institution responsible for the joint award of this degree.

The author acknowledges that copyright of published works contained within the thesis resides with the copyright holder(s) of those works.

I give permission for the digital version of my thesis to be made available on the web, via the University's digital research repository, the Library Search and also through web search engines, unless permission has been granted by the University to restrict access for a period of time.

16/12/2021

Signed

Date

Acknowledgments

This doctoral dissertation is dedicated to my Ph.D. supervisors Assoc. Prof. Withawat Withayachumnankul and Prof. Christophe Fumeaux, and my dearest families.

First and foremost, I would like to express my deepest gratitude to my principal supervisor Assoc. Prof. Withawat Withayachumnankul and co-supervisor Prof. Christophe Fumeaux, who have imparted me knowledge, built my confidence, and trained my research capabilities to get through this doctoral journey.

I first met Dr. Withayachumnankul back to 2016, when I first joined the Adelaide Applied Electromagnetics Group as a junior volunteer researcher under his joint supervision. With his extensive knowledge in terahertz and microwave, since then he has been generously and patiently teaching me everything in electromagnetics related from fundamental knowledge, simulation techniques, article writing to advanced academic concepts. Due to a lack of sufficient background knowledge at the beginning, I suffered with a little progress on my first microwave antenna project for long. It was his excellent guidance, encouragement, patience, kindness, and famous "strictness" that took me out of the blue and on the right research track. His words that 'do it step-by-step' completely opened the door for my research journey. In 2018, he provided me a full scholarship and recruited me as a Ph.D. student working on terahertz waveguides, while the solid fundamental knowledge accumulated in the past two years enabled me to quickly move into the role. During this period, he drew a blueprint at the very beginning of my candidature by discussing a lot of novel ideas and sending me abundant papers in the frontier. This significantly broadened my horizon and inspired my enthusiasm, leading to the following achievements. He has been intentionally cultivating me to be an independent researcher with critical thinking abilities. Without his countless constructive comments and inspirations, I would not have been making progresses all the way. Always, he has been greatly supporting me throughout my candidature by offering every opportunity that can benefit my growth as a researcher. For example, he fully funded me to visit Osaka University to conduct the terahertz communications experiments in 2018. It is my fortune to be his student, and nothing than hard working and keeping moving forward can express my gratitude to him. His kindness, rigorous

Acknowledgments

spirits, dedication to students and work, and outstanding academic successes have set a goal for me, which worths my whole life to pursue.

Prof. Fumeaux is my Ph.D. co-supervisor, an outstanding scholar in electromagnetics, and the person who changed my life. In 2016, when I was a freshly graduated Master student from the University of New South Wales, as a principal supervisor, he recruited me as a volunteer researcher working with his group, while I had been rejected by more than ten research groups due to a lack of notable research experiences and transcripts. Since then he had been generously and patiently teaching me in-depth knowledge in electromagnetics and microwave antennas by treating me in no difference with other formal Ph.D. students. Importantly, his always kindness and encouragements built my confidence in both research and life, which was the core that has mentally supported me to overcome various challenges through my Ph.D. journey. He has kept helping me explore my research potentials and providing me numerous valuable novel ideas to improve the designs. His every detailed, constructive, and insightful comment led me to understand the principles deeper and progressed step by step. Under his superb joint guidance, I proposed a multifunctional microwave reconfigurable antenna, which has been published on the top journal in the field. This was also my very first research achievement. After then, he had been actively seeking various scholarship opportunities for me to support my potential Ph.D study. Since 2018, he has been my co-supervisor with an unchanged dedicated supervision. His kindness, rigorous spirits, selfless dedication to students and work together with his outstanding research achievements will always inspire me. Likewise, only my constant efforts in the future work and life can reward him.

I would also like to take this opportunity to express my gratitude to the researchers in Ngatsuma's Laboratory, Osaka University, Japan, including Prof. Tadao Nagatsuma, Assoc. Prof. Masayuki Fujia, and Dr. Xiongbin Yu for their guidance and assistance on the waveguide samples fabrication and terahertz communications experiments together with their constructive and insightful comments on my research papers. Assoc. Prof. Fujita and Prof. Nagatsuma warmly hosted me as a visiting student in their laboratory and unconditionally provided me any assistance to complete the experiments. Dr. Yu as a senior student then introduced me a lot of research experience and had many in-depth discussions with me, which was very helpful throughout my Ph.D. study.

During the study at the University of Adelaide since 2016, I have received extensive support from scientists and experts in all kinds of areas, and without their help, I would

not have completed my degree smoothly. Here, I would like to specially thank Dr. Frank Demming-Jassen from SIMUSERV for his technical support in CST simulations, and Mr. Danny Di Giacomo, Mr. Alban O'Brien, Mr. Aubrey Benjamin Slater, and Mr. Bradon Pullen from the school workshop for their technical support in fabrications and measurements. In addition, I would also like to acknowledge the staff of the school and the faculty, IT officers for their assistance throughout my candidature, namely Prof. Cheng-Chew Lim, Assoc. Prof. Wen Soong, Prof. Nelson Tansu, Mr. Pavel Simcik, Ms. Jodie Schluter, Ms. Laura McNamara, Ms. Tayla Allison, Ms. Julie Mayo, Ms. Stella Ho, Ms. Allison Dinan, and Mr. David Bowler.

The positive academic atmosphere and support from my colleagues are indispensable to the success in this Ph.D. degree. Here, I would like to sincerely thank the past and present members of both Applied Electromagnetics Group and Terahertz Engineering Laboratory at the University of Adelaide, Dr. Cheng Zhao, Dr. Shengjian Jammy Chen, Dr. Nghia Nguyen Trong, Dr. Chengjun Zou, Dr. Nicholas Lawrence, Dr. Daniel Headland, Dr. Wendy. S. L. Lee, Dr. Sree Pinapati, Dr. Seyedali Malakooti, Dr. Siti Nailah Mastura Zainarry, Mr. Ken Paramayudha, Dr. Xiaolong You, Dr. Xiaojing (Alex) Lv, Dr. Morteza Shahpari, Mr. Andrew Udina, Ms. Yuan (Grace) Yuan, Mr. Baoqi Zhu, Mr. Xiaoyang Yin, Mr. Quoc Hung Dang, Mr. Mohamed Shehata, Ms. Panisa Dechwechprasit, Mr. Mingxiang (Stephen) Li, and Mr. Harrison Lees. Special thanks go to Dr. Shengjian Jammy Chen for his tremendous encouragement and help in CST simulation, paper writing, and antenna measurement at the early stage of my study. In addition, I am grateful to Dr. Wendy. S. L. Lee and Mr. Harrison Lees for their responsible, in-time, and excellent sample measurements for my work, especially when I was offshore and not able to access the laboratory during the COVID-19 period. Furthermore, warm thanks go to my good friend and brother Mr. Chongming Wang, who did not only take good care of me during the days when I was sick and the workload was heavy, but also photographed many samples with excellent qualities for my work.

I sincerely thank the University of Adelaide, Faculty of Engineering, Computer and Mathematical Sciences, and School of Electrical and Electronic Engineering for providing me Full-fee Scholarship, Research Travel Scholarship, ECMS Divisional Scholarship, ECMS Travelling Scholarship, and other subsidies, respectively. These financial assistances have allowed me to complete this Ph.D. degree and attend international conferences to communicate and connect with researchers worldwide. I would also like

Acknowledgments

to appreciate the university, the faculty, and the school for offering excellent studying environments, resources, and facilities, which all benefited my research at large. Additionally, I am thankful for Adelaide Graduate Centre providing me every convenience to complete the Ph.D. program smoothly.

Last but not least, my endless appreciation goes towards my dearest families, my mother and father, grandmothers, aunts, uncles, and cousins, who are the power source of my heart by giving me infinite love, support, and trust forever.

Publications

Journal publications

- GAO-W., LEE-W. S. L., FUMEAUX-C., AND WITHAYACHUMNANKUL-W. (2021). Effective-medium-clad Bragg grating filters, *APL Photonics*, **6**(7), p. 076105
- Liang-J., GAO-W., LEES-H., AND WITHAYACHUMNANKUL-W. (2021). All-silicon planar horn antenna, *IEEE Antennas Wireless Propagation Letters*, **20**(11), pp. 2181–2185.*
- Lees-H., GAO-W., AND WITHAYACHUMNANKUL-W. (2021). All-silicon, low-crosstalk terahertz waveguide crossing based on effective medium *Optics Letters*, **46**(21), pp. 5469–5472.*
- GAO-W., LEE-W. S. L., YU-X., FUJITA-M., NAGATSUMA-T., FUMEAUX-C., AND WITHAYACHUMNANKUL-W. (2020). Characteristics of effective-medium-clad dielectric waveguides, *IEEE Transactions on Terahertz Science and Technology*, **11**(1), pp. 28–41.
- GAO-W., YU-X., FUJITA-M., NAGATSUMA-T., FUMEAUX-C., AND WITHAYACHUMNANKUL-W. (2019). Effective-medium-cladded dielectric waveguides for terahertz waves, *Optics Express*, **27**(26), pp. 38 721–38 734.
- GAO-W., CHEN-S. J., WITHAYACHUMNANKUL-W., AND FUMEAUX-C. (2019). Horizontally polarized 360° beam-steerable frequency-reconfigurable antenna, *IEEE Transactions on Antennas and Propagation*, **67**(8), pp. 5231–5242.*

Conference publications

- GAO-W., CHEN-S. J., WITHAYACHUMNANKUL-W., AND FUMEAUX-C. (2021). 360° beam-steerable pattern- and frequency-reconfigurable antenna with 3D printed dielectric lens, *2021 Asia Pacific Microwave Conference*, Brisbane, Australia, (**Student Prize**).*
- GAO-W., FUMEAUX-C., AND WITHAYACHUMNANKUL-W. (2021). Terahertz integrated polarization beam splitter based on effective-medium waveguide, *2021 Asia Pacific Microwave Conference*, Brisbane, Australia, (**Invited for special session**).

- GAO-W.**, LEE-W. S., FUMEAUX-C., AND WITHAYACHUMNANKUL-W. (2021). Integrated terahertz band-stop filter based on effective medium, *46th International Conference on Infrared, Millimeter, and Terahertz Waves*, Chengdu, China. **(Keynote)**.
- Lees-H., **GAO-W.**, AND WITHAYACHUMNANKUL-W. (2021). Waveguide crossing based on air-silicon effective medium, *46th International Conference on Infrared, Millimeter, and Terahertz Waves*, Chengdu, China.*
- GAO-W.**, FUMEAUX-C., AND WITHAYACHUMNANKUL-W. (2020). All-silicon terahertz components towards efficient integrated systems, *45th International Conference on Infrared, Millimeter, and Terahertz Waves*, Buffalo, United States. **(Keynote)**.
- GAO-W.**, LEE-W. S. L., YU-X., FUJITA-M., NAGATSUMA-T., FUMEAUX-C., AND WITHAYACHUMNANKUL-W. (2020). Effective-medium-cladded dielectric waveguides towards terahertz integrated platform, *14th Pacific Rim Conference on Lasers and Electro-Optics (CLEO)*, Sydney, Australia.
- GAO-W.**, YU-X., FUJITA-M., NAGATSUMA-T., FUMEAUX-C., AND WITHAYACHUMNANKUL-W. (2019). Effective-medium-cladded dielectric waveguides towards terahertz integrated platform, *44th International Conference on Infrared, Millimeter, and Terahertz Waves*, Paris, France. **(Keynote)**.

Note: Articles with an asterisk are not directly relevant to this thesis.

List of Figures

1.1	Conventional table-top terahertz systems	4
1.2	Impact of atmospheric attenuation and free-space path loss on terahertz waves	6
1.3	Terahertz intergated circuits for various applications	9
1.4	Terahertz waveguide packaging	12
1.5	Fibres	14
1.6	Millimetre-wave substrate integrated waveguide and image guides . . .	16
1.7	Rectangular dielectric waveguides	18
1.8	Terahertz silicon-on-insulator waveguides	19
1.9	Terahertz photonic crystal waveguides and associated passive components	20
1.10	Terahertz photonic crystal waveguide connected with active components	21
1.11	Loss comparison between microwave-inspired and photonics-inspired planar waveguides	24
<hr/>		
2.1	Effective-medium-clad dielectric waveguide	30
2.2	Characteristics of the waveguide	33
2.3	Simulated dispersion characteristics	35
2.4	Fabricated effective-medium-clad dielectric waveguide	36
2.5	Transmission measurement setup	37
2.6	Transmission and attenuation coefficients of the waveguides	38
2.7	Communications measurement diagram	40
2.8	Communications measurement results	41
<hr/>		
3.1	Schematic of the effective-medium-clad dielectric waveguide operating over 220 to 330 GHz	45
3.2	Analysis of the straight waveguide	47

List of Figures

3.3	Dispersion characteristics based on Marcatilli's theory	49
3.4	Fabricated straight waveguide at WR-3.4 band	52
3.5	Measurement setup	53
3.6	Transmission and attenuation coefficients of the straight waveguides . .	55
3.7	Dispersion characteristics of the straight waveguides	56
3.8	Group velocity and group velocity dispersion (GVD)	57
3.9	Simulated GVD for the E_{11}^y mode with increasing waveguide thickness .	57
3.10	Cross polarisation measurement setup	58
3.11	Simulated and measured transmission coefficients for the cross polarisa- tion of straight waveguide samples	58
3.12	Two parallel waveguides	59
3.13	Simulated and measured S -parameters of the parallel waveguides	60
3.14	Bent waveguides	62
3.15	Simulated bending loss with various bending radius r_b	64
3.16	Transmission coefficients and bending loss of cascaded waveguide bends with two different total lengths of 62 mm and 87 mm	65
3.17	Waveguide crossing	66
3.18	Simulated and measured S -parameters of the crossing	67
<hr/>		
4.1	Effective-medium-clad Bragg grating filter	73
4.2	Characteristics of a uniform Bragg grating as a function of waveguide segment width difference	76
4.3	Uniform effective-medium-clad waveguide Bragg grating filter	78
4.4	Fabricated uniform effective-medium-clad Bragg grating filter	79
4.5	Measurement setup	79
4.6	Simulated and measured S -parameters and simulated E -field amplitude distributions of the uniform waveguide Bragg grating filter	80
4.7	Schematics of Bragg grating filters with various claddings	81
4.8	Fabricated waveguide Bragg gratings with various claddings	82
4.9	Simulated and measured S -parameters of the filters with different claddings	83

4.10	Bragg grating filter with apodisation	85
4.11	Simulated and measured S -parameters of the filter with apodisation and two-layer mixed cladding	86
4.12	Simulated and measured S -parameters of the filters clad by mixed effective medium claddings with various bandwidths achieved by different strategies	87
4.13	Simulated and measured S -parameters of the filters clad by mixed claddings with various Bragg frequencies	89
4.14	Simulated and measured group delay of the uniform filter shown in Fig. 4.3 and the apodised filter with mixed claddings shown in Fig. 4.10	90
4.15	Simulated impact of fabrication tolerances on the performance of a uniform filter	92
4.16	Simulated and measured S -parameters for the uniform waveguide Bragg grating filter shown in Fig. 4.4	92
4.17	Operation frequency range and hole diameter for different wafer thicknesses	95
4.18	Simulated S -parameters of a uniform effective-medium-clad Bragg grating filter operating at WR-0.65 band	96
—————		
5.1	Microwave-based orthomode transducers (OMTs)	103
5.2	Optics-based polarisation beam splitters	105
5.3	Optical polarisation beam splitters (PBSs) based on directional couplers	107
5.4	Schematic of the proposed integrated polarisation splitter	110
5.5	Performance comparison between a single tapered directional coupler clad by effective medium (EM) and air, respectively	117
5.6	3D model of the effective-medium-clad polarisation splitter fed by the WR-3.4 hollow waveguides	118
5.7	Evolution of polarisation splitter design based on the homogeneous artificial materials	119
5.8	Simulated S -parameters of the polarisation splitter with various accessories as shown in Fig. 5.7	120
5.9	Simulated S -parameters of the polarisation splitters with artificial and effective medium claddings as shown in Figs. 5.4(a) and Fig. 5.7(d)	122

List of Figures

5.10	Simulated insertion losses of the effective-medium-clad polarisation splitter for the E_{11}^x and E_{11}^y modes	123
5.11	Simulated maximum E -field amplitude distributions of the effective-medium-clad polarisation splitter for the E_{11}^x and E_{11}^y modes at various frequencies	124
5.12	S-parameters for the port isolation for the effective-medium-based polarisation splitter model	127
5.13	Simulated electromagnetic field distributions of higher-order modes . . .	127
5.14	S-parameters for the higher-order modes conversion	128
5.15	Simulated group velocity dispersions (GVDs) of the effective-medium-clad polarisation splitter	129
<hr/>		
A.1	Simulated transmission coefficients for waveguide misalignment investigation	138
<hr/>		
B.1	Hollow waveguide package accommodating a 1-cm effective-medium-clad dielectric waveguide	140
B.2	Simulated transmission coefficients of 1-cm waveguide sample with and without package	140
<hr/>		
C.1	Coupling loss between the effective-medium-clad waveguide and the WR-3.4 hollow waveguide for the E_{11}^x and the E_{11}^y modes	142
C.2	Simulated E -field distributions at 275 GHz	142

List of Tables

1.1	Comparison of guiding structures at terahertz and millimetre-wave frequencies	23
2.1	Comparison of interconnects inspired by microwave and photonic technologies	40
4.1	Compensated dimensions for various effective-medium-clad filters	93
4.2	Compensated dimensions for air-clad filter	93
5.1	Dimensions for the effective-medium-clad polarisation splitter	111
5.2	Comparison of polarisation splitting devices at optical and terahertz frequencies	125

THE terahertz spectrum bridges the microwave and optical frequency regimes and promises a wide range of applications such as imaging, sensing, communications, and radar. Terahertz integrated systems with low dissipation, broad bandwidth, low cost, and portability are in significant demand to promote those applications. Leveraging the technologies across electronics and optics, significant progress in terahertz integrated circuits has been achieved in the past decade. One key enabling element is an efficient planar platform able to host various passive and active components to achieve comprehensive functionalities. This introductory chapter offers a background in terahertz technology, integrated circuit, and waveguide, along with an outline of the thesis.

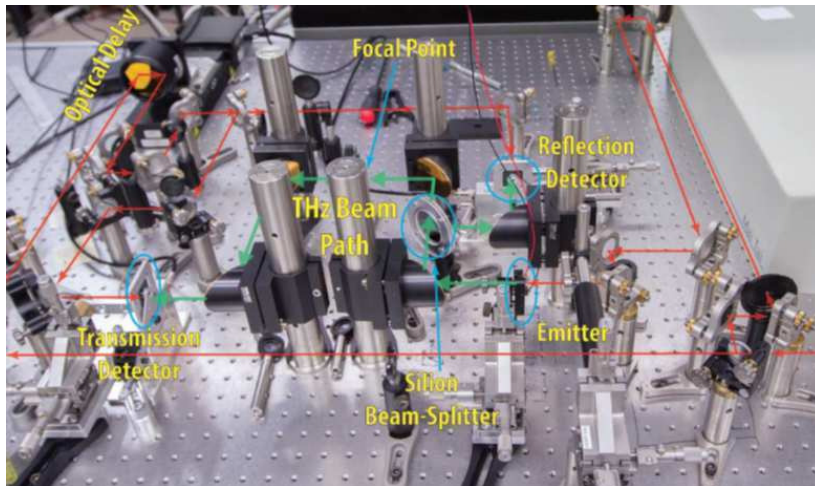
1.1 Terahertz technology

The terahertz spectrum is loosely defined as an electromagnetic frequency range from 0.1 to 10 THz, which is situated between millimetre-wave (MMW) and infrared frequencies. Owing to its unique characteristics including vast absolute bandwidth, strong penetration in non-metallic materials, and non-ionising radiation, the terahertz spectrum promises a wide range of applications such as high-speed communications, noninvasive imaging, sensing, radar, astronomy, and biomedicine (Withayachumnankul, 2010; Lee, 2018). However, due to a lack of efficient signal generators and detectors, the terahertz spectrum has been underutilised for long. In the past few decades, the “THz gap” has been gradually filled up by virtue of the development of laser-based technologies particularly of femtosecond lasers and light-to-terahertz converters such as photoconductive antennas and nonlinear optical crystals, which can be used either to emit or to detect terahertz signals (Sengupta *et al.*, 2018; Song and Nagatsuma, 2011).

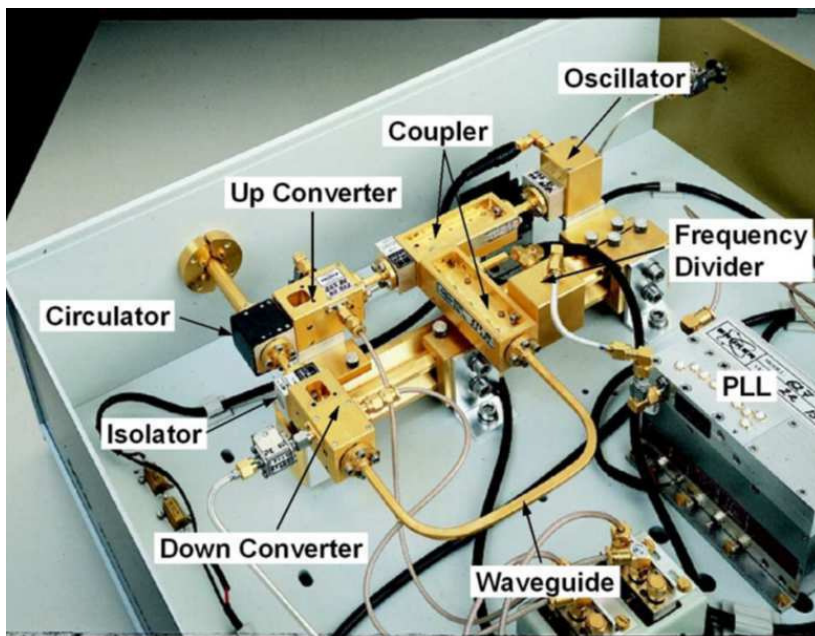
Facilitated by the advent of the aforementioned laser-based technologies, terahertz measurements have become feasible with significant development in terahertz time-domain spectroscopy (THz-TDS) (Withayachumnankul, 2010), which has been crucial to promote terahertz technology toward practical applications. One remarkable application based on THz-TDS is material characterisation (Naftaly and Miles, 2007), where THz-TDS systems can be deployed to efficiently measure the amplitude and phase of terahertz signals that are linked to the absorption coefficients and refractive indices of the substances exhibiting unique characteristics at terahertz frequencies. With capabilities to characterise materials, applications based on THz-TDS have been extended to noninvasive imaging (Moriwaki *et al.*, 2017) and sensing (Balakrishnan *et al.*, 2009). Typically, THz-TDS systems are implemented in tabletop environments and consist of multiple optical components (Ung *et al.*, 2013), where one example can be seen in Fig. 1.1(a). Such systems feature broad bandwidth, high efficiency, and configuration flexibility for free-space operation. However, they were designed specifically for spectroscopy and are as such difficult to customise for other applications. Also their large volume and high cost are factors that limit their usability (Sengupta *et al.*, 2018).

A crucial drive towards compact economical terahertz systems is its applications in wireless communications (Song and Nagatsuma, 2011; Nagatsuma *et al.*, 2013, 2016; Withayachumnankul *et al.*, 2018a). Over the past decade, data traffic has grown exponentially with a dramatically increasing portion of the world population accessing online services (Cisco, 2017). This trend has been exacerbated by the rapid growth in

1.1 Terahertz technology



(a) © 2013 IEEE



(b) © 2010 IEEE

Figure 1.1. Conventional table-top terahertz systems. (a) Simultaneous reflection and transmission THz-TDS system (Ung *et al.*, 2013). (b) Microwave hollow-waveguide-based sub-millimetre wave system (Seok *et al.*, 2010).

usage of high-resolution multimedia content with huge data volume. Therefore, higher channel capacities in wireless transmission are in demand to support not only mobile links but also backhaul connectivity. However, an increased data throughput adds pressure to the already congested microwave and millimetre-wave channels (Nagatsuma *et al.*, 2016). According to the Shannon-Hartley theorem, the channel capacity can be improved by increasing the bandwidth, subject to signal quality (Goldsmith, 2005).

Owing to its ultra-wide absolute bandwidth, the terahertz spectrum is an ideal candidate to support wireless line-of-sight transmission (Nagatsuma *et al.*, 2016; Ma *et al.*, 2018). Theoretically, the prospective data rate carried by a terahertz channel can reach 1 Tbit/s over the distance of several kilometres (Koenig *et al.*, 2013). However, the biggest obstacle to reach such a theoretical capability is power loss, which could lower the signal-to-noise ratio (SNR), resulting in degraded channel capacities and limited transmission distance (Nagatsuma *et al.*, 2016). Specifically, the power losses suffered by terahertz waves in wireless communications mainly involve atmospheric attenuation, free-space path loss (FSPL), scattering loss, and material loss (Nagatsuma *et al.*, 2016; Withayachumnankul *et al.*, 2018a; Schneider *et al.*, 2012). As shown in Fig. 1.2(a), atmospheric attenuation that usually accounts for water vapour absorption under normal air condition is frequency-dependent leading to several transmission windows, e.g., 200–300 GHz, 625–725 GHz, and 780–910 GHz, within which the atmospheric attenuation is minimum. Additionally, as illustrated in Fig. 1.2(b), within a certain atmospheric window, the link budget mainly considers the free-space path loss, which can be compensated by adopting high gain antennas. For wireless transmission, the scattering loss is usually caused by fog/rain/mist droplets and increases with the frequency and the density of the droplets (Schneider *et al.*, 2012). Since such scattering losses can elevate the overall loss, they should be considered for the link budget for fixed wireless links (Schneider *et al.*, 2012). From a device level, material losses mainly comprise ohmic loss and dielectric substrate loss (Withayachumnankul *et al.*, 2018a). At microwave and millimetre-wave frequencies, the ohmic loss commonly exists in metallic transmission lines and components. However, it increases dramatically at terahertz frequencies due to the reduced conductivity and skin depth resulting in increased surface resistance. Furthermore, the ohmic loss will be exacerbated in resonant structures with strongly confined electromagnetic fields. Additionally, the dielectric loss is usually not negligible considering that only a limited number of materials are suitable for microfabrication. Typically, to mitigate the power loss caused by materials in transceiver chains, as shown in Fig. 1.1(b), bulky discrete components, e.g., rectangular-hollow-waveguide-based components are adopted, where the current density on metal is low. However, such a strategy imposes tradeoffs in terms of dispersion, fabrication complexity, and compactness (Seok *et al.*, 2010).

Based on strong demands towards practical applications, in recent years, a paradigm shift has been seen in terahertz technology that transits from physics-oriented to

1.1 Terahertz technology

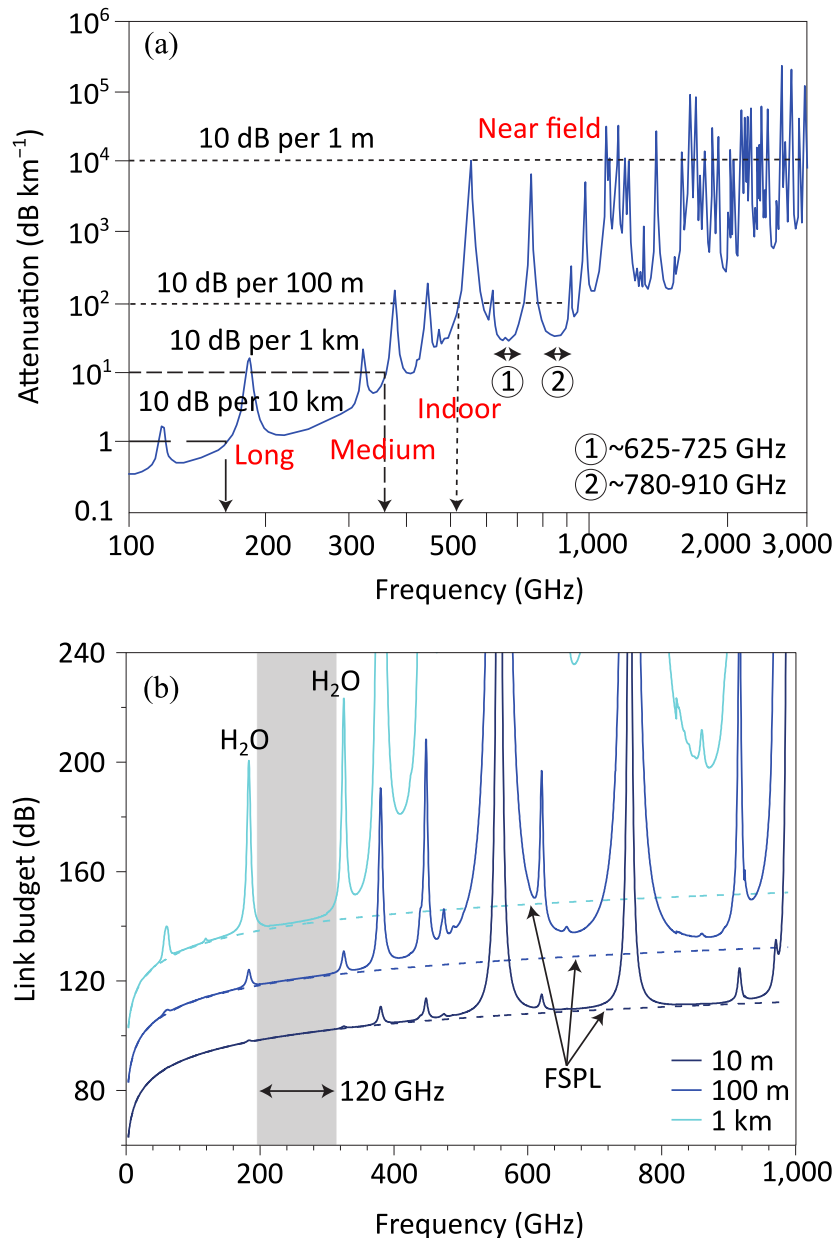


Figure 1.2. Impact of atmospheric attenuation and free-space path loss on terahertz waves.

(a) Atmospheric attenuation as a function of frequency. (b) Link budget at terahertz frequencies.

Adopted from Nagatsuma *et al.* (2016).

engineering-oriented, from spectroscopy-based to application-driven, and from free-space optics to integrated circuits (Withayachumnankul *et al.*, 2018a; Gao *et al.*, 2020a). Such a shift is not unexpected but is a natural evolution for any technology once physics quests have been reasonably completed. While optics-based THz-TDS systems are indispensable in spectroscopy, compared to integrated systems, they are bulky and costly, which makes them not readily amenable to widespread applications in communications,

imaging, radar, and sensing. Similar restrictions are applicable to the conventional microwave hollow-waveguide-based systems. With established knowledge in terahertz physics, it is the time to work on technical challenges towards terahertz integrated systems for widespread real-life applications (Kenneth *et al.*, 2019).

1.2 Existing terahertz integrated systems

To enable comprehensive terahertz integrated systems, recent efforts have been dedicated to exploiting solid-state semiconductor technologies based on III-V and silicon (Sengupta *et al.*, 2018). Essentially, for any radio frequency (RF) integrated circuits (ICs), the key elements include signal generators, receivers, interconnections, various active or passive components, and I/O interfaces, and there is no exception for terahertz integrated circuits (Yu, 2020).

In general, for silicon-based technologies such as CMOS, SiGe, or bipolar-CMOS (BiCMOS), terahertz power can be generated by two methods including harmonic extraction from an on-chip oscillator and frequency multiplication of fundamental signals that are generated either from the on-chip oscillators or from external sources (Pfeiffer *et al.*, 2018). One important quantitative figure of merit to characterise these electronics-inspired generators is f_{\max} , which represents the maximum frequency of the device for signal amplification (Sengupta *et al.*, 2018). Due to the limitation of f_{\max} , the generated power decreases with frequency increasing. It has been demonstrated that the f_{\max} can go up to 0.5 THz for SiGe-based BiCMOS transistors, followed by a f_{\max} of 0.3 THz for CMOS transistors (Sengupta, 2019). For III-V based transistors, e.g., InP high electron mobility transistors (HEMTs), the f_{\max} can reach 1.5 THz but with a compromised integration level compared to CMOS (Mei *et al.*, 2015; Sengupta *et al.*, 2018). Recently, beyond- f_{\max} continuous-wave generation has been realised by exploiting the frequency multiplication via the non-linearities of the devices (Park *et al.*, 2012; Katayama *et al.*, 2016). Other electronics-based generators include Gunn diodes (Khalid *et al.*, 2014), impact ionisation avalanche transit-time (IMPATT) diodes (Al-Attar and Lee, 2005), and resonant tunnelling diodes (RTD) (Izumi *et al.*, 2017) with a tradeoff in terms of maximum power and f_{\max} (Yu, 2020). It is worth mentioning that another efficient continuous terahertz wave generation scheme is to use photodiodes, where two lasers with different wavelengths are injected to be down-converted to terahertz signals. In particular, uni-travelling-carrier photonic diodes (UTC-PDs) have been developed for

1.2 Existing terahertz integrated systems

high-speed response and high-saturation current. It has been demonstrated that a UTC-PD can generate terahertz frequency over 2 THz (Ishibashi *et al.*, 2013).

Terahertz continuous wave receivers are usually realised through two methods, i.e., heterodyne and direct detections (Pfeiffer *et al.*, 2018). For the heterodyne detectors, an injection of local oscillator signal is required to downconvert the terahertz signal to an intermediate frequency. This coherent detection scheme allows to retrieve the signals with both amplitude and phase information but at an expense of a higher power consumption and a larger footprint due to the involvement of a local oscillator (LO) and a down-conversion mixer (Pfeiffer *et al.*, 2018). By contrast, the direct detectors rely on the device non-linearities for envelop detection leading to a simpler operation, smaller power consumption, and a higher integration level (Pfeiffer *et al.*, 2018). Common terahertz direct detectors include Schottky barrier diodes (SBD) (Hesler and Crowe, 2007), Fermi-level managed barrier diodes (FMBD) (Ito and Ishibashi, 2016), field-effect transistors (FET) (Knap *et al.*, 2009), and resonant tunnelling diodes (RTD) (Shiode *et al.*, 2011). Among those detectors, SBDs have been widely adopted and have become commercially available due to their broad bandwidth and good stability, however with a relatively low sensitivity due to the conversion loss (Hesler and Crowe, 2007). With a higher sensitivity, RTD has recently attracted attention for terahertz detection (Yu, 2020).

With the significant developments of the terahertz on-chip self-contained generators and detectors discussed above, many advanced terahertz integrated circuits have been proposed for various applications such as imaging, sensing, communications, and radar (Sengupta *et al.*, 2018; Pfeiffer *et al.*, 2018). These integrated systems employ comprehensive techniques leveraging RF passive components, high-speed transistors, scaling, and mixed signal integration capabilities (Pfeiffer *et al.*, 2018). As shown in Fig. 1.3(a), a 32×32 pixel terahertz camera in 65-nm CMOS technologies was proposed for focal-plane imaging (Al Hadi *et al.*, 2012). The pixel array constituted a ring antenna coupled to NMOS detectors, while the whole structure coupled to a hyper-hemispherical lens leading to a directivity of 41.7 dBi. The proposed terahertz camera operated in an active mode with a broad bandwidth covering 0.1 to 4.0 THz and a single-pixel sensitivity of 413 pW at 850 GHz with 1024 frame averaging at 30 fps (Al Hadi *et al.*, 2012). For sensing application, a terahertz on-chip spectroscopic receiver based on SiGe BiCMOS process was reported (Wu and Sengupta, 2018). As shown in Fig. 1.3(b), the main body of this sensor was composed of a log-period tooth-shaped antenna loaded

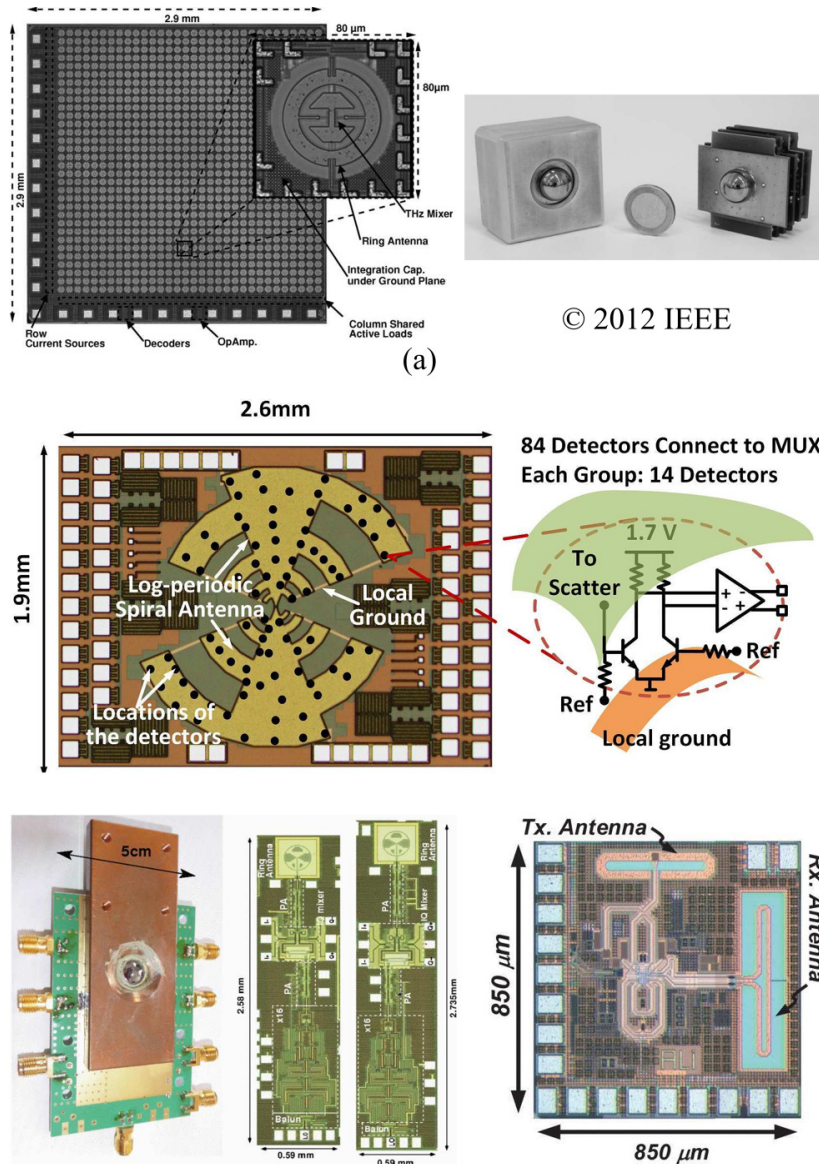


Figure 1.3. Terahertz integrated circuits for various applications. (a) 32×32 terahertz camera based on 65 nm CMOS technology for focal-plane imaging (Al Hadi *et al.*, 2012). (b) Single-chip source-free terahertz spectroscope for near-field sensing (Wu and Sengupta, 2018). (c) 220–260 GHz Tx and Rx RF front-ends implemented in a $0.13 \mu\text{m}$ SiGe HBT technology together with the packaged Tx/Rx module (Rodríguez-Vázquez *et al.*, 2018). (d) 170 GHz single-chip FMCW imaging radar with 3-D imaging capability (Mostajeran *et al.*, 2017).

with multiple HBT-based detectors to measure the spectrally-sensitive 2D distribution of terahertz near fields. The proposed chip eliminates bulky components required by the conventional optics-based spectroscopic systems and can operate at a room temperature

1.3 Existing terahertz waveguides

over 0.04 to 0.99 THz with an accuracy of 10 MHz in frequency resolution (Wu and Sengupta, 2018). Additionally, a terahertz on-chip transceiver for wireless communications (Rodríguez-Vázquez *et al.*, 2018) has been proposed as shown in Fig. 1.3(c). This Tx-Rx chip was based on SiGe technology and fully packaged with hyper-hemispherical lenses. The proposed RF front end can support a transmission data rate of 90 Gbit/s over a distance of 1 m with a bandwidth from 220 to 260 GHz (Rodríguez-Vázquez *et al.*, 2018). Furthermore, as shown in Fig. 1.3(d), a fully integrated single-chip heterodyne frequency modulated continuous-wave (FMCW) imaging radar was reported (Mostajeran *et al.*, 2017). This FMCW radar was based on a 130-nm SiGe BiCMOS technology with a bandwidth 27.5 GHz centered at the frequency of 168 GHz. The proposed radar allows for both 2D and 3D imaging with a range resolution of 7 mm together with a measured sensitivity of 87 fW and total dc power consumption of 67 mW (Mostajeran *et al.*, 2017).

Despite their magnificent capabilities, the conventional integrated circuits based on III-V and silicon technologies suffer significant ohmic and substrate losses (Song and Nagatsuma, 2011). For example, the traditional planar metallic transmission lines can impose significant transmission losses in the order of several dB/cm at terahertz frequencies (Yu, 2020). In contrary to that, the power available from terahertz sources is low, in order of 100 μ W (Withayachumnankul *et al.*, 2018a). To this end, it is in significant demand to design new integrated platforms with low loss together with broad bandwidth, while being able to accommodate various passive and active components (Withayachumnankul *et al.*, 2018a). One critical enabling technology for efficient integrated platforms is the interconnection (Gao *et al.*, 2019), as discussed in Section 1.3.

1.3 Existing terahertz waveguides

This section gives an overview about terahertz waveguides categorised into non-planar and planar types. The non-planar terahertz waveguides mainly focuses on the metallic rectangular waveguides and terahertz fibres, while for the planar waveguides, the microwave-inspired and photonics-inspired guiding structures are discussed in detail.

1.3.1 Non-planar waveguides

Before we look into integrated waveguides, it is necessary to review existing non-planar terahertz waveguides for their operation and design principles, which can be useful for terahertz integrated waveguides. Based on materials, the non-planar waveguides can be categorised into two types namely metallic waveguides and dielectric waveguides. The commonly used non-planar metallic waveguides for the terahertz spectrum include circular/rectangular hollow waveguides (McGowan *et al.*, 1999a; Gallot *et al.*, 2000) and parallel-plate waveguides (Mendis and Grischkowsky, 2001; Karl *et al.*, 2015). Considering the tradeoffs in terms of loss, dispersion, and applicability in measurement and packaging, here, the descriptions focus onto the rectangular hollow waveguides. The non-planar dielectric waveguides also known as fibres are mostly used at higher terahertz frequencies due to their low dissipation (Atakaramians *et al.*, 2013). The overview on this waveguide category provides an appropriate background for understanding the design and guiding principles of planar dielectric waveguides discussed in Section 1.3.2.

Metallic rectangular waveguides

Downscaled from microwave frequencies, rectangular hollow waveguides have been widely used in the terahertz spectrum (Ding *et al.*, 2017; Gonzalez and Kaneko, 2021b; Pérez-Escudero *et al.*, 2020). The waveguides are usually fabricated with copper based on a CNC milling process, while gold plating is employed on the waveguide channel to alleviate the oxidisation (Alonso-del Pino *et al.*, 2019). Compared to the metallic transmission lines, which strongly confines electromagnetic waves within metal and lossy substrate, rectangular waveguides can achieve much lower loss since the largest portion of wave energy propagates in air (Wu *et al.*, 2021). For example, the attenuation coefficient for a WR-3.4 rectangular waveguide ranges from 0.214 to 0.308 dB/cm over 220 to 330 GHz (VDI, 2010). With such a reasonably low loss, many terahertz passive and active components have been built based on the rectangular waveguides such as band-pass filters (Ding *et al.*, 2017), orthomode transducers (Gonzalez and Kaneko, 2021b), and mixers (Pérez-Escudero *et al.*, 2020). These components together with their host waveguides are crucial to functional systems with robust performance for applications such as communications and astronomy. In terahertz electronic-photonic measurement systems, the rectangular waveguides can offer an efficient interface for device under test (DUT) (Gao *et al.*, 2020b). Importantly, as shown in Fig. 1.4, these CNC milling machined hollow-waveguide-based structures can provide an efficient packaging solution for

1.3.1 Non-planar waveguides

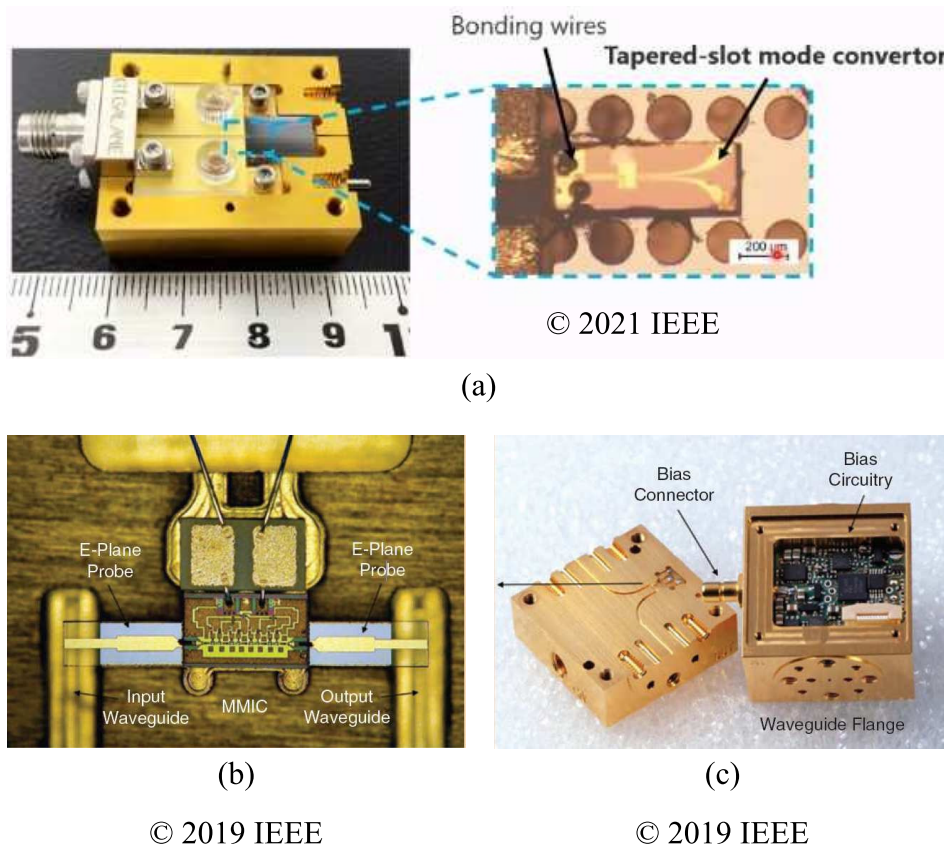


Figure 1.4. Terahertz waveguide packaging. (a) Integrated resonant tunnelling diode with rectangular waveguide I/O using photonic crystal interface (Kawamoto *et al.*, 2021). (b) A 300-GHz monolithic microwave integrated circuit (MMIC) housed in an *E*-plane split package. (c) The *E*-plane split package in (b) contains the waveguide flange, bias connector, and biasing printed circuit boards (Alonso-del Pino *et al.*, 2019).

terahertz integrated systems (Alonso-del Pino *et al.*, 2019). Practically, for integrated system testing purpose, each passive and active component can be packaged individually and then connected through waveguide flanges allowing for a component-level testing, which has more flexibility and lower packaging complexity compared to the “all-in-one” testing strategy (Alonso-del Pino *et al.*, 2019). Recently, fabrication technologies such as silicon deep reactive-ion etching (DRIE) (Beuerle *et al.*, 2018) and 3D printing (Otter *et al.*, 2017) together with metallisation have been employed to fabricate rectangular waveguides. These advanced fabrication technologies can effectively address the challenges faced by conventional CNC metal milling in terms of accuracy, complexity, and cost especially at higher terahertz frequencies. Benefiting from the micromachining, packaging consisting of multiple stacked metallised silicon wafers has been realised allowing for vertical integration in a compact manner (Alonso-del Pino *et al.*, 2019).

Terahertz fibres

Inspired by optical fibres, the terahertz fibres are usually formed in a hollow, solid, or porous core. The various realisations are governed by different guiding principles with tradeoffs in terms of loss and bandwidth (Atakaramians *et al.*, 2013). In 2005, a hollow-core waveguide clad by ferroelectric poly vinylidene fluoride (PVDF) was proposed (Hidaka *et al.*, 2005), and was demonstrated to achieve a low transmission loss with waves concentrated within the air core. However, its guiding mechanism strongly relies on the cladding material properties. Specifically, the frequency-dependent dielectric constant of PVDF can become negative at high terahertz frequencies leading to an imaginary refractive index, for which the dielectric material behaves as metal with complete reflection. As a result, the waveguide bandwidth is bounded by the frequency range of the cladding material exhibiting negative dielectric constant together with the cladding thickness, leading to a narrow bandwidth (Hidaka *et al.*, 2005). Instead, photonic bandgap claddings (Mosallaei and Rahmat-Samii, 2000a), where propagation modes are rejected, was introduced to surround the air core, so that the waves can be confined and propagate along the core. As shown in Figs. 1.5(a) and (b), typically, the bandgap claddings are in form of 2D photonic crystal (Correa and Knight, 2008; Vincetti, 2009) realised by periodic air holes or in the form of Bragg mirrors (Dupuis *et al.*, 2011) achieved by alternatively stacking multiple layers of materials with high refractive index contrast. Due to the strong in-band dispersion of the bandgap claddings, the bandwidth of this fibre type is narrow.

To increase the bandwidth, as shown in Fig. 1.5(c), solid-core waveguides clad by subwavelength air holes was reported (Han *et al.*, 2002; Goto *et al.*, 2004), where the subwavelength engineered claddings have lower refractive index with respect to the core. Consequently, due to the refractive-index contrast between the core and cladding, the wave can be guided through total internal reflection with a broad bandwidth (Han *et al.*, 2002; Goto *et al.*, 2004). It is noted that although these fibres are called photonic crystal fibres, their guiding mechanisms do not rely on the photonic bandgap effects implemented with photonic crystal claddings as shown in Fig. 1.5(a). Compared to the hollow-core fibres, the solid-core fibres have higher loss with more energy fraction in their materials (Atakaramians *et al.*, 2013). Additionally, due to the weaker boundary condition, the mode is less confined leading to radiation loss, and this can be alleviated by using a larger core with tradeoffs of material loss and potentially higher-order mode excitation (Atakaramians *et al.*, 2013).

1.3.1 Non-planar waveguides

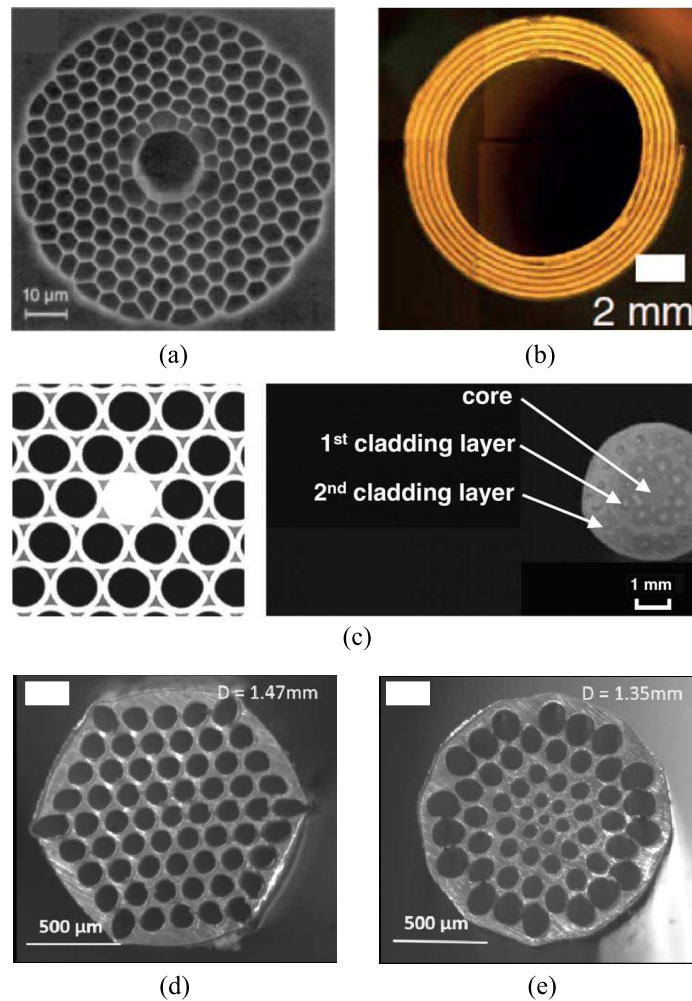


Figure 1.5. Fibres. (a) Optical fibre clad by photonic crystal bandgap claddings (Correa and Knight, 2008). (b) Terahertz Bragg fibre (polymer-doped polymer) (Dupuis *et al.*, 2011). (c) Terahertz solid-core fibres clad by subwavelength air holes (Han *et al.*, 2002; Goto *et al.*, 2004). Terahertz fibres with (d) uniform porous core and (e) graded-index porous core (Ma *et al.*, 2015).

To this end, porous-core waveguides (Atakaramians *et al.*, 2008; Ma *et al.*, 2015; Hasani *et al.*, 2008) were proposed. As shown in Figs. 1.5(d), the uniform porous waveguide is clad by a distribution of subwavelength air holes. As a result, the mode can be confined within the holes and guided through total internal reflection. Compared to the air-clad solid-core fibre with a subwavelength core width, the porous-core waveguide can offer better wave confinement and lower effective material loss (Atakaramians *et al.*, 2008). Furthermore, as shown in Fig. 1.5(e), by gradually increasing the hole diameters from the centre to the edge resulting in a gradually decreased effective refractive index distribution, a lower dispersion can be achieved (Ma *et al.*, 2015). It is noteworthy that

the evolution of terahertz fibres have provided valuable references for designing the integrated dielectric waveguides presented in this thesis.

1.3.2 Planar waveguides

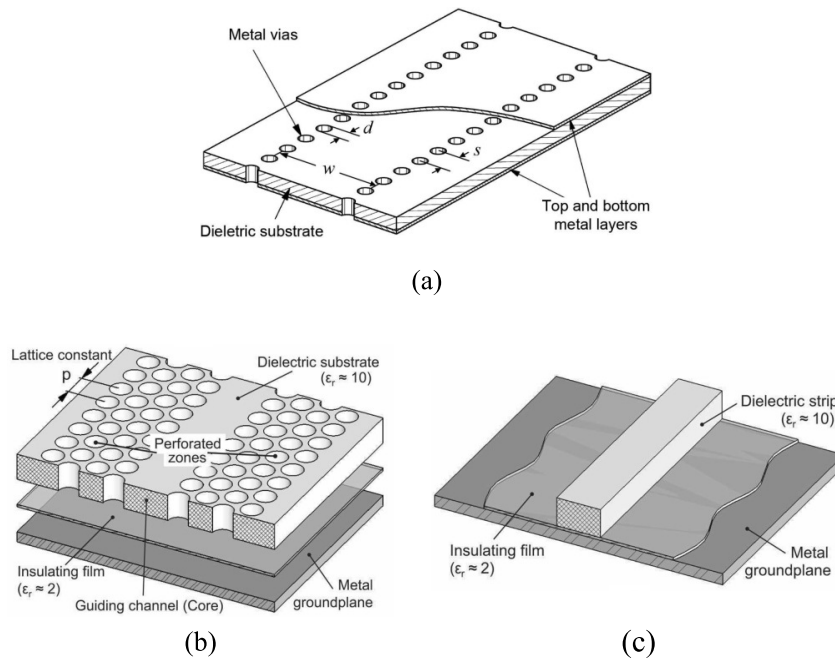
Planar waveguides and transmission lines are the most fundamental building blocks of integrated circuits and systems due to their structural compactness, low cost, and easy integration with active devices, such as diodes and transistors (Pozar, 2011).

Microwave-inspired guiding structures

In the microwave and millimetre-wave regimes, microstrip lines (Murano *et al.*, 2017), coplanar waveguides (CPW) (Frankel *et al.*, 1991; Zhang and Hsiang, 2005; Eblabla *et al.*, 2016), and substrate-integrated waveguides (SIW) (Wu *et al.*, 2003, 2021) have been widely used owing to their low cost, easy implementation, and convenient integration with active components. For the microstrip lines, one notable advantage is that they can support a quasi-TEM mode leading to negligible dispersion and broad bandwidth, together with a tailorable interface with active devices (Pozar, 2011; Wu *et al.*, 2021). However, the drawbacks of the quasi-TEM mode are their current singularities along the strip edges resulting in several issues such as strong magnetic couplings with adjacent lines and potential radiation loss (Pozar, 2011; Wu *et al.*, 2021). Additionally, due to the high current density on metal, the ohmic loss of microstrip lines is significant and exacerbated at high frequencies with a thinner substrate and a narrower strip line to suppress the undesired modes (Pozar, 2011; Wu *et al.*, 2021; Dolatsha, 2013). Similar issues occur in the other planar metallic transmission lines, e.g., CPWs.

Facilitated by substrate-integrated technologies, planar synthesis of non-planar rectangular waveguide becomes possible (Deslandes and Wu, 2001a,b; Wu *et al.*, 2003). Specifically, this technology aims to confine the waves in a substrate by implementing metallic via holes (Wu *et al.*, 2003) or air holes (Patrovsky and Wu, 2006) along the guiding channel. The SIWs are realised with metallic via-hole arrays that mimic two side walls of the rectangular waveguide as shown in as shown in Fig. 1.6(a), and as such they are dispersive, leading to narrower bandwidths compared to the microstrip lines. However, they can offer relatively low loss at frequencies up to around 400 GHz (Wang *et al.*, 2020). With the frequency increasing, the ohmic loss will rise dramatically mainly due to the electric current flowing along the metallised via holes. Furthermore, it is challenging

1.3.2 Planar waveguides



© 2006 IEEE

Figure 1.6. Millimetre-wave substrate integrated waveguide and image guides. (a) Substrate integrated waveguide (SIW) (Wu *et al.*, 2021). (b) Substrate-integrated-image guide (SIIG) (Patrovsky and Wu, 2006). (c) Conventional image guide. (Patrovsky and Wu, 2006).

to fabricate and arrange the miniature vias at high frequencies with microfabrication technologies, while the waveguide performance is strongly dependent on the via quality (Wu *et al.*, 2003). Although the through silicon via (TSV) technology allows for such miniature implementations at terahertz frequencies (Wang *et al.*, 2020), still the presence of metal limits their applications.

Another version of SIW also known as substrate-integrated image guide (SIIG) can be realised by creating air holes along the guiding channel (Patrovsky and Wu, 2006). This leads to a dielectric constant contrast between the core and the in-plane surroundings, so that the wave can be guided through total internal reflection. This technique resembles the one adopted in the terahertz fibres cladded by subwavelength air holes (Han *et al.*, 2002; Goto *et al.*, 2004). As shown in Fig. 1.6(b), the SIIG consists of a perforated high-permittivity substrate supported by a ground plane, between which an insulating film is introduced to reduce the ohmic loss in the ground plane (Patrovsky and Wu, 2006). Free of metallic vias, the SIIG has a much lower loss than the SIW does. Compared to the conventional image guide consisting of a single dielectric strip (Taeb *et al.*, 2016a; Taeb, 2015) as shown in Fig. 1.6(c), the SIIG offers several advantages in terms of

fabrication simplicity, alignment precision, design flexibility, and interconnections with other transmission lines (Patrovsky *et al.*, 2006; Dolatsha, 2013). Specifically, the dielectric strip in the conventional image guide is usually tiny and fragile at millimetre-wave frequencies or above, so it requires high-precision bonding on the ground plane, while a precise alignment between adjacent elements is also very demanding. As a result, the fabrication complexity is significantly increased especially for complex circuits. Additionally, a single strip is difficult to interconnect to other transmission lines, e.g., microstrip lines and CPWs, or active components. Nevertheless, the SIIG also suffers high ohmic loss at terahertz frequencies due to the existence of a ground plane, although recent efforts resulted in increasing the mode isolations from the ground plane (Dolatsha, 2013).

Photonics-inspired guiding structures

Inspired by guided-wave photonics, all-dielectric waveguides free of ohmic loss have been investigated at terahertz frequencies including rectangular dielectric waveguides (Malekabadi *et al.*, 2014; Akiki *et al.*, 2020; Ranjkesh *et al.*, 2015), silicon-on-insulator (SOI) waveguides (Amarloo *et al.*, 2018; Amarloo and Safavi-Naeini, 2021), dielectric microstrip lines (DML) (Zhu *et al.*, 2016b,a), and photonic crystal (PC) waveguides (Tsuruda *et al.*, 2015a; Yu *et al.*, 2019e; Headland *et al.*, 2019). In general, terahertz dielectric waveguides have similar guiding principles as optical dielectric waveguides, where the waveguide core dimensions are proportional to the operation wavelength. However, one notable difference is the refractive index contrast between the waveguide core and the surroundings. For optical waveguides, the refractive index contrast between the core and the claddings is usually small, i.e., the refractive index ratio between the core and the claddings Δ is around from 1.002–1.053, leading to the core dimensions on the order of several wavelengths for fundamental mode operation (Marcatili, 1969). By contrast, the refractive index contrast for terahertz dielectric waveguides is large, e.g., with a refractive index ratio Δ around 3.418 for an air-clad silicon waveguide, so that the wave can be tightly confined within the core in a compact footprint (Malekabadi *et al.*, 2014). It is noteworthy that most dielectric materials can introduce significant loss at terahertz frequencies, and therefore waveguides consisting of a few selected materials are preferred to alleviate the material loss.

Recently, several dielectric rectangular waveguides based on high-resistivity silicon have been proposed at terahertz frequencies. As shown in Fig. 1.7(a), the most fundamental

1.3.2 Planar waveguides

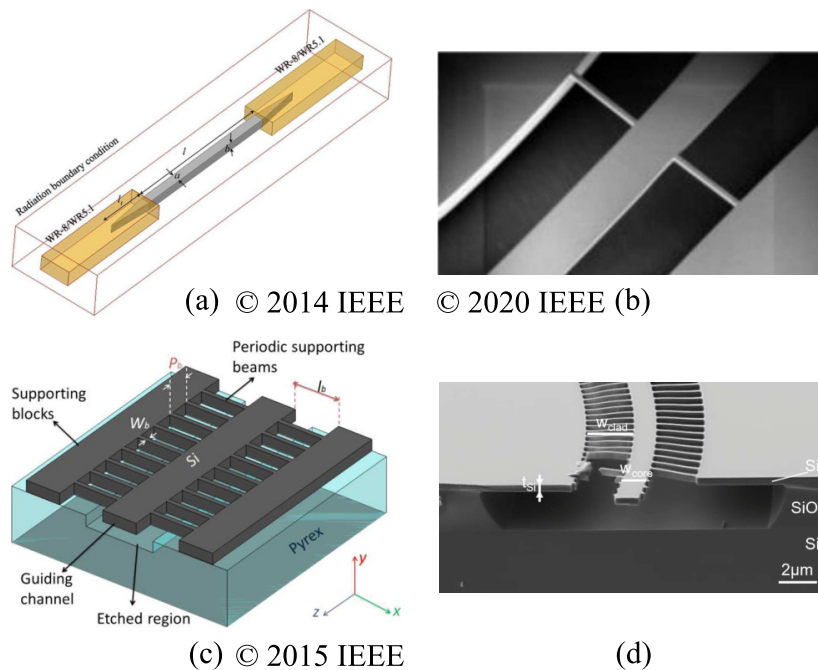


Figure 1.7. Rectangular dielectric waveguides. (a) Terahertz high-resistivity silicon dielectric waveguide (Malekabadi *et al.*, 2014). (b) Terahertz suspended silicon waveguide Akiki *et al.* (2020). (c) Terahertz suspended silicon-on-glass dielectric waveguide (Ranjesh *et al.*, 2015). (d) Mid-infrared suspended waveguide with subwavelength grating metamaterials Penades *et al.* (2016).

dielectric waveguide consists of a single silicon rod, which has extremely low loss, low dispersion, and broad bandwidth, while supporting two orthogonal fundamental modes (Malekabadi *et al.*, 2014). High-resistivity float-zone intrinsic silicon, as the only constituent material, has extremely low dissipation at terahertz frequencies (Dai *et al.*, 2004). With such benefits, a simple dielectric rectangular waveguide has been adopted as an interconnection for on-chip communications (Holloway *et al.*, 2017). However, such a bare waveguide has limitations in realising integrated systems since it lacks self-support and support for other components. To improve the integrability, several suspended dielectric waveguides have been reported. One example can be seen in Fig. 1.7(b), where thin cross beams are introduced to connect the waveguide core with the silicon slab for supporting purpose. However, such a structure has a relatively low mechanical strength and is affected by scattering loss by the beams (Akiki *et al.*, 2020). Similarly, a terahertz silicon-on-glass dielectric rectangular waveguide supported by grating beams was reported (Ranjesh *et al.*, 2015) as shown in Fig. 1.7(c). However, these sparsely distributed supporting gratings would introduce Bragg and/or leaky-wave effects leading to reflection and/or radiation losses. Consequently, the waveguide

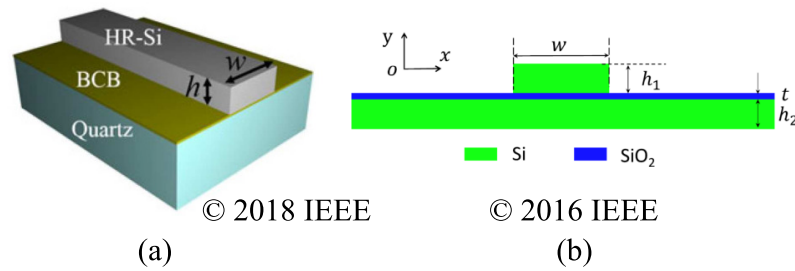


Figure 1.8. Terahertz silicon-on-insulator waveguides. (a) Silicon-BCB-quartz dielectric waveguide (Amarloo *et al.*, 2018). (b) Silicon-on-insulator-based dielectric microstrip line (Zhu *et al.*, 2016b).

bandwidth and efficiency are compromised. To further enhance the mechanical stability without introducing side effects, one may refer to an example of suspended silicon mid-infrared waveguide based on a silicon-on-insulator (SOI) platform (Penades *et al.*, 2016). As shown in Fig. 1.7(d), the waveguide core is supported by lateral subwavelength gratings (SWGs), whose period is much smaller than the Bragg period so as to avoid reflection and radiation (Penades *et al.*, 2016). Noticeably, the SWGs claddings can not only mechanically support the waveguide core but also can provide lateral refractive index contrast with respect to the core for guiding waves. Again, this technique together with the resultant guiding principle is similar with those involved in the subwavelength-holes-clad-solid-core fibres (Han *et al.*, 2002; Goto *et al.*, 2004) and SIIG (Patrovsky and Wu, 2006).

To further improve the integrability, silicon-BCB-quartz (SBQ) waveguide (Amarloo *et al.*, 2018) and dielectric microstrip line (Zhu *et al.*, 2016b) have been proposed. Figure. 1.8(a) shows a terahertz silicon-BCB-quartz waveguide, which consists of a high-resistivity silicon strip supported by a crystalline quartz. In this design, the adoption of quartz material can reduce the substrate loss (Amarloo *et al.*, 2018). To bond the waveguide to the substrate, an adhesive polymer called benzocyclobutene (BCB) was introduced. Such a SOI waveguide can achieve an average loss around 0.46 dB/cm over 500 to 580 GHz (Amarloo *et al.*, 2018). With structural resemblance, dielectric microstrip lines (DML) were reported as shown in Fig. 1.8(b). In contrast to the SBQ waveguide, the DML concentrates the energy in the low-index oxide spacer, while supporting only the out-of-plane polarisation with the loss varying from 0.23 to 1.2 dB/cm over 750 to 925 GHz (Zhu *et al.*, 2016b). Despite the improved integrability, for the SOI waveguides

1.3.2 Planar waveguides

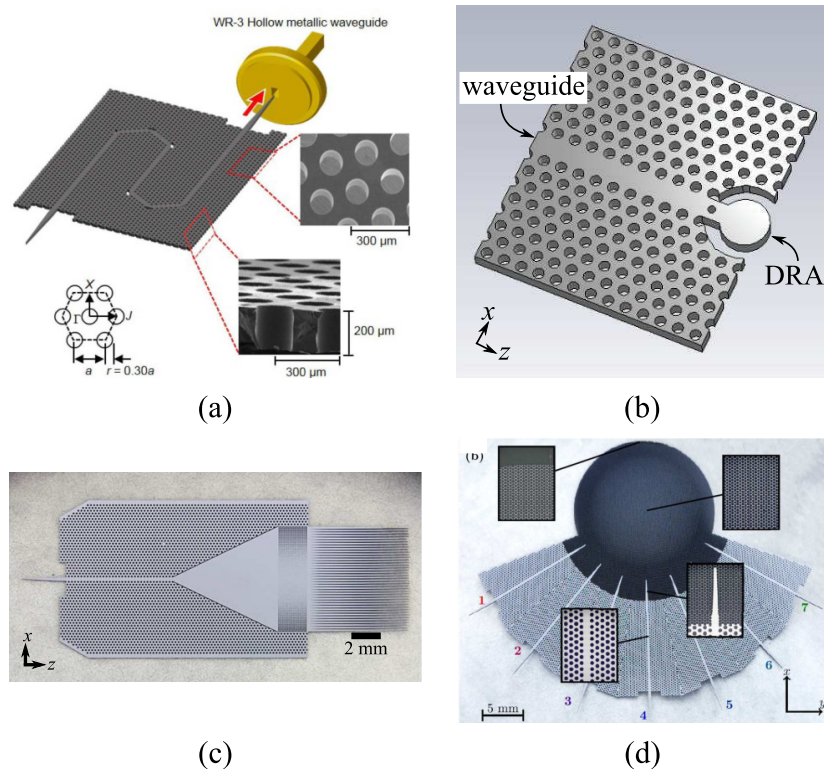


Figure 1.9. Terahertz photonic crystal waveguides and associated passive components. (a) All-silicon photonic crystal waveguide (Tsuruda *et al.*, 2015a). (b) All-dielectric resonator antenna (Withayachumnankul *et al.*, 2017). (c) All-dielectric rod antenna array (Withayachumnankul *et al.*, 2018b). (d) Luneburg lens antenna (Headland *et al.*, 2018b).

and DML, the dielectric loss caused by the required supporting substrate and spacer material is not negligible (Lee *et al.*, 2001).

To achieve an integrated platform with low loss and structural simplicity, all-dielectric 2D photonic crystal waveguides built from a single silicon wafer were proposed as shown in Fig. 1.9(a) (Tsuruda *et al.*, 2015a; Yu *et al.*, 2019e; Headland *et al.*, 2019). Here, the 2D photonic crystal waveguide can be treated as a planar realisation of the photonic crystal fibre utilising the photonic bandgap defect for wave guidance (Correa and Knight, 2008). As such, a propagation loss of less than 0.1 dB/cm was demonstrated from 319 to 337 GHz by Tsuruda *et al.* (2015a), while another similar design yielded an enhanced bandwidth of 324–361 GHz with comparable losses (Yu *et al.*, 2019e). Based on the photonic crystal waveguide integrated platform, various passive components have been proposed such as dielectric resonator antenna (Withayachumnankul *et al.*, 2017), rod antenna array (Withayachumnankul *et al.*, 2018b), and Luneburg lens (Headland *et al.*, 2018b) as shown in Fig. 1.9. Additionally, such an integrated

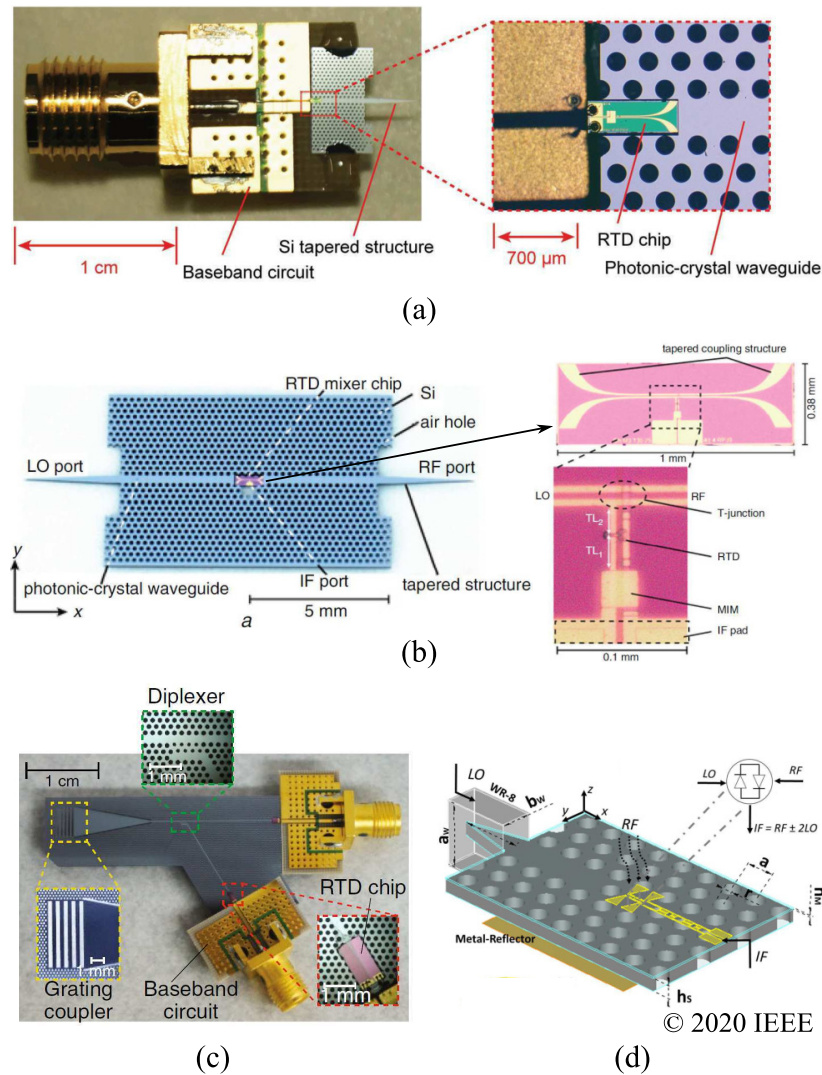


Figure 1.10. Terahertz photonic crystal waveguide connected with active components. (a) RTD integrated photonic crystal waveguide as a terahertz transceiver (Yu *et al.*, 2019b). (b) Waveguide-input RTD mixer for terahertz communications (Yu *et al.*, 2020). (c) Photonic crystal inspired terahertz diplexer (Fujita and Nagatsuma, 2016). (d) Silicon integrated subharmonic mixer on a photonic crystal platform (Torres-García *et al.*, 2020).

platform can also accommodate various active components, e.g., resonant tunnelling diode (RTD) and Schottky diode, leading to a series of functional devices such as terahertz transceiver (Yu *et al.*, 2019b), mixers (Yu *et al.*, 2020; Torres-García *et al.*, 2020), and frequency diplexer (Fujita and Nagatsuma, 2016) as shown in Fig. 1.10. However, the photonic crystal waveguides have relatively narrow bandwidths and strong in-band dispersion related to the intrinsic photonic bandgap (PBG) phenomenon (Mosallaei and Rahmat-Samii, 2000a). The same issues also arise in the all-silicon topological

1.3.3 Performance comparison of various waveguide designs

waveguide (Yang *et al.*, 2020), which allows for a sharp bend but with a much higher structural complexity.

1.3.3 Performance comparison of various waveguide designs

Various terahertz and millimetre-wave guiding structures based on different techniques are compared in Table 1.1. Although for the existing planar guiding structures, the all-dielectric waveguides have much lower losses compared to the metallic guiding structures as shown in Fig 1.11, there are tradeoffs in terms of bandwidth, loss, dispersion, and integrability as compared in Table 1.1. To this end, it is imperative to achieve a terahertz integrated platform with high efficiency, low dispersion, and broad bandwidth, while being able to accommodate various passive and active components (Withayachumnankul *et al.*, 2018a).

1.4 Thesis outline and original contributions

Up until recent years, there had been no platform uniquely designed for terahertz integrated systems. Existing platforms adopted either millimetre-wave or photonic integrated circuits into the terahertz range. However, all those adopted platforms exhibit limitations in this spectral range in terms of efficiency and bandwidth. In line with the practical needs of high-efficiency and wideband terahertz integrated systems, all-silicon effective-medium-clad dielectric waveguides and relevant components are proposed and demonstrated in this thesis to expand into a new terahertz integrated platform.

This thesis is composed of six chapters including four chapters for original contributions. The background for understanding the motivation of this thesis is provided in this chapter, while the final chapter provides a holistic conclusion and outlook. The details of each chapter can be found as follows:

Chapter 1 (Introduction) introduces the background knowledge for this thesis including terahertz technology, terahertz conventional integrated circuits, and waveguides operating at millimetre-wave and terahertz frequencies. In particular, a thorough literature review is focused on various guiding structures with comprehensive analysis of their performance, applicability, and limitations.

Table 1.1. Comparison of guiding structures at terahertz and millimetre-wave frequencies.

	Frequency (GHz)	Losses (dB/ λ_c)	Dispersions	Modes
Non-planar metallic waveguides				
Circular hollow waveguide (McGowan <i>et al.</i> , 1999b)	650–3500	0.09	High	TE ₁₁ , TM ₁₁ , TE ₁₂
Commercial hollow waveguide (VDI, 2010)	260–400	0.033	High	TE ₁₀
Parallel-plate waveguide (Mendis and Grischkowsky, 2001)	100–4000	0.02	Low	TEM, TE ₁
Terahertz fibres				
Solid-core photonic crystal fibre (Han <i>et al.</i> , 2002)	100–3000	0.042	Low	HE ₁₁
Hollow-core Bragg fibre (Dupuis <i>et al.</i> , 2011)	100–2000	0.037	High	Multimode
Porous-core fibre (Ma <i>et al.</i> , 2015)	300–1500	0.013	Low	Multimode
Hollow-core photonic bandgap fibre (Vincetti, 2009)	800–1000	0.0003	High	HE ₁₁
Microwave-inspired planar waveguides/transmission lines				
SIW (Wang <i>et al.</i> , 2020)	260–400	2	High	E_{11}^y
Coplanar waveguide (Frankel <i>et al.</i> , 1991)	200–400	1.35	Low	Quasi-TEM
Metallic microstrip line (Murano <i>et al.</i> , 2017)	220–330	0.475	Low	Quasi-TEM
SIIG waveguide (Patrovsky and Wu, 2006)	83–99	0.148	Low	E_{11}^y
SIIG waveguide (Taeb <i>et al.</i> , 2016a)	110–170	0.075	Low	E_{11}^y
Photonics-inspired planar waveguides				
Silicon-BCB-Quartz waveguide (Amarloo <i>et al.</i> , 2018)	500–580	0.026	Low	E_{11}^x
Dielectric microstrip line (Zhu <i>et al.</i> , 2016b)	750–925	0.025	Low	E_{11}^y
Ribbon waveguide (Malekabi <i>et al.</i> , 2014)	140–220	0.015	Low	E_{11}^x and E_{11}^y
PC waveguide (Yu <i>et al.</i> , 2019e)	324–361	0.009	High	TE

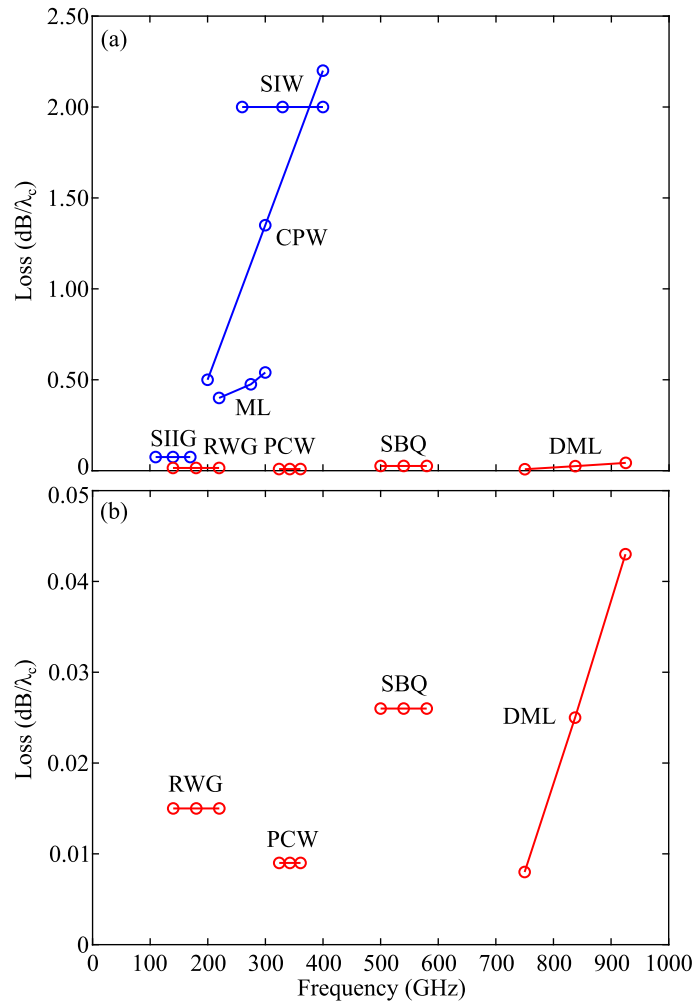


Figure 1.11. Loss comparison between microwave-inspired and photonics-inspired planar waveguides. (a) Losses of various planar waveguides based on microwave and photonic technologies. (b) Zoom-in showing losses of photonics-inspired all-dielectric waveguides. Microwave-inspired guiding structures include substrate integrated image guide (SIIG) (Taeb *et al.*, 2016a), microstrip line (ML) (Murano *et al.*, 2017), coplanar waveguide (CPW) (Frankel *et al.*, 1991), and substrate integrated waveguide (SIW) (Wang *et al.*, 2020). Photonics-inspired guiding structures include ribbon waveguide (RWG) (Malekabadi *et al.*, 2014), photonic crystal waveguide (PCW) (Yu *et al.*, 2019e), Silicon-BCB-Quartz (SBQ) waveguide (Amarloo *et al.*, 2018), and dielectric microstrip line (DML) (Zhu *et al.*, 2016b).

Chapter 2 (Original contribution) presents a class of integrated dielectric waveguides solely built into high-resistivity float-zone silicon wafer to achieve extremely low loss, and low dispersion. In-plane air-silicon effective medium is employed as waveguide cladding. Owing to the total internal reflection guiding mechanism, the waves can be guided with a broad bandwidth. Free of substrate, the dielectric

waveguides show an experimentally verified high efficiency compared with the conventional silicon-on-insulator (SOI) waveguides adopted from the photonics. To experimentally validate the performance in communications applications, real-time data error rate testing experiments are performed and uncompressed 4K resolution video data transmission is demonstrated. The content of this chapter is published in Gao *et al.* (2019).

Chapter 3 (Original contribution) presents comprehensive characteristics of the dielectric waveguides clad by effective medium, including transmission, dispersion, and crosstalk. Various fundamental building blocks are discussed including bends, crossing, and directional couplers. All the results are experimentally verified. The waveguide design process is generalised. With such in-depth investigations, it is expected that the effective-medium-clad dielectric waveguides will be a basis to build a terahertz integrated platform in analogy to microstrip lines in the microwave range and SOI waveguides in optics. The content of this chapter is published in Gao *et al.* (2020b).

Chapter 4 (Original contribution) presents a series of Bragg grating filters based on the effective-medium-clad waveguide platform, while various characteristics are discussed including transmission, 3-dB bandwidth, central frequency, and dispersion. Due to the controllable air-silicon effective medium permittivity, an additional degree of freedom can be accessed in the design of Bragg grating structures. In effect, the modal indices can be designed for a broadband operation. The results are experimentally validated. The techniques to improve the filter characteristics by controlling the effective medium are adaptable to the microwave and optics regimes. The content of this chapter is published in Gao *et al.* (2021).

Chapter 5 (Original contribution) presents a polarisation splitter integrated into the effective-medium-clad dielectric waveguide platform. The polarisation splitter is based on tapered directional couplers to enable a broad operation bandwidth. Owing to the concept of effective medium, the performance in terms of polarisation extinction ratio is significantly enhanced without introducing additional materials. Various characteristics of the proposed polarisation splitter are thoroughly investigated including transmission, crosstalk, isolation, higher-order mode conversion, and dispersion. It can be foreseen that such an all-silicon polarisation multiplexer can find wide use in terahertz integrated systems and benefit a broad range of

1.4 Thesis outline and original contributions

applications, especially for short-distance communications with increased channel capacity. A publication is under preparation.

Chapter 6 (Summary and outlook) concludes this thesis while providing an outlook for future developments based on the proposed terahertz integrated platform.

Effective-medium-clad dielectric waveguides: A proof of concept

TERAHERTZ integrated waveguides with high efficiency and broad bandwidth are essential to form integrated platforms. This chapter presents substrate-less all-dielectric waveguides defined by an effective medium realised with a subwavelength hole array. These self-supporting structures are built solely into a single silicon wafer to minimize significant absorption in metals and dielectrics at terahertz frequencies. In a stark contrast to photonic crystal waveguides, the guiding mechanism is not based on a photonic bandgap but on total internal reflection. Experimental results show that the realised waveguides can cover the entire WR-2.8 band (260–400 GHz) with fundamental dominant modes in orthogonal polarisations and an average measured attenuation around 0.05 dB/cm. Limited by the measurement setup, a maximum error-free data rate up to 30 Gbit/s is experimentally achieved at 335 GHz on a 3-cm waveguide. The transmission of uncompressed 4K-resolution video across this waveguide is demonstrated.

2.1 Introduction

Terahertz waveguides with planar structures are crucial to future terahertz systems (Withayachumnankul *et al.*, 2018a). Particular attention is required on efficiency, dispersion, and bandwidth. Conventional microwave transmission lines and waveguides such as microstrip lines, coplanar waveguides, and substrate integrated waveguides are not efficient and therefore not suitable for terahertz systems owing to their strong field confinements and significant ohmic loss at this high frequency range. Alternatively, waveguides constructed of purely dielectric materials, such as high-resistivity float-zone silicon can be ideal candidates for terahertz wave guidance (Dai *et al.*, 2004). High-resistivity-silicon-based waveguides clad by air are the simplest embodiments of dielectric waveguides and can achieve extremely low loss and low dispersion over a wide band (Malekabadi *et al.*, 2014). However, such bare waveguides are not useable in integrated systems due to a lack of self-support and support for other components. With better integrability, 2D photonic crystal (PC) waveguides built solely from high-resistivity silicon were proposed (Tsuruda *et al.*, 2015a; Yu *et al.*, 2019e; Headland *et al.*, 2019). However, the dispersion of such PC waveguides is high due to the nature of photonic bandgap (PBG) structures that are highly frequency dependent, thus limiting the operation bandwidth. Theoretically, dielectric waveguides with better integrability and broad bandwidth can be achieved by changing the air claddings to a material with a certain refractive index lower than the waveguide core. However, introducing an additional clad material in turn increases fabrication complexity and imposes additional transmission losses. To realise a self-supporting, planar, and single-material-based terahertz guiding structure, a class of effective-medium-clad waveguides are proposed.

The proposed substrate-less waveguides are constructed solely from a high-resistivity silicon wafer that has exceptionally low loss and low dispersion at terahertz frequencies (Dai *et al.*, 2004). A silicon waveguide core is surrounded by in-plane effective-medium claddings, which are realised by periodic perforation of the silicon slab. This pure-silicon platform allows integration of active and passive components, as demonstrated in photonic crystal waveguides (Yu *et al.*, 2019a,b). In a stark contrast to photonic crystal waveguides, the perforation period of the proposed waveguide is in the deep subwavelength region. In this way, the perforated medium behaves like a homogeneous material rather than a bandgap material (Cheben *et al.*, 2018). Compared with a bandgap material, this chosen cladding results in a great bandwidth enhancement with low dispersion in both orthogonal modes—the properties much needed in diverse

terahertz applications, but not available from photonic crystal waveguides. Compared to the substrate integrated images guides (SIIGs) (Patrovsky and Wu, 2006; Dolatsha, 2013; Taeb *et al.*, 2016b), the proposed design is free from metal thus achieving lower transmission losses, while being able to sustain two orthogonal dominant modes. Compared to the silicon-on-insulator (SOI) waveguides (Ranjesh *et al.*, 2015; Amarloo *et al.*, 2018; Amarloo and Safavi-Naeini, 2021; Zhu *et al.*, 2016b), the proposed design is self-supporting and does not require additional materials that would contribute to propagation losses. In Section 2.2, the waveguide design and the modal analysis are presented. Section 2.3 discusses the waveguide fabrication and measurements, where the low-loss, low-dispersion transmission and high-speed terahertz communications over this waveguide are demonstrated.

2.2 Waveguide design and analysis

2.2.1 Overview

As shown in Figs. 2.1(a)–(c), the proposed integrated all-dielectric waveguide comprises a waveguide solid core and in-plane effective medium claddings, both built monolithically into a silicon slab. The silicon slab with a thickness of $200\ \mu\text{m}$ has a relative permittivity ϵ_{Si} of 11.68 (an equivalent refractive index n_{Si} of 3.418) and a resistivity of $20\ \text{k}\Omega\text{-cm}$. Such high-resistivity silicon is nondispersive and offers extremely low loss, with power absorption coefficients less than $0.01/\text{cm}$ in the entire terahertz band (Dai *et al.*, 2004). The effective medium is realised by periodically perforating the silicon slab with cylindrical air holes in a hexagonal lattice, with a period a much smaller than the shortest guided wavelength λ_g as shown in Fig. 2.1(d). The effective relative permittivity of the effective medium falls between those of air and silicon, and is determined by the perforation period a and the hole diameter d . Owing to the refractive index contrast between the core and the claddings, i.e., between silicon and effective medium in plane, and silicon and air out of plane, the waves can be confined within the waveguide core and propagate through total internal reflection. For the in-plane effective-medium claddings, given a certain deep subwavelength perforation period, a lower effective relative permittivity achieved by a larger hole diameter can enhance wave confinement. Due to the low-index claddings in both transverse dimensions, the waveguide supports two orthogonal fundamental modes E_{11}^x and E_{11}^y , namely with the polarisation for the E_{11}^x mode being parallel to the slab, while being perpendicular to the

2.2.1 Overview

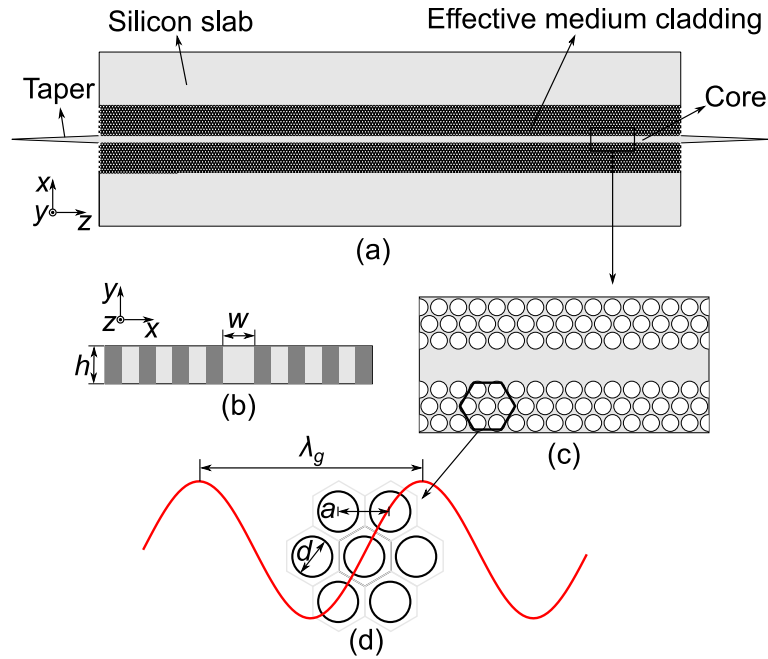


Figure 2.1. Effective-medium-clad dielectric waveguide. (a) Top view, (b) magnified cross-sectional view, (c) magnified view of waveguide core and claddings, and (d) hexagonal lattice of the effective medium cladding with perforation period a and hole diameter d . The period a is a quarter of the shortest guided wavelength λ_g . This effective-medium cladding is completely different from a photonic crystal cladding that requires a periodicity close to half a guided wavelength. As a result, the waveguide can be classified as a dielectric waveguide, not a photonic crystal waveguide. The tapers are coupling structures to be inserted into the hollow metallic waveguides required for simulations and measurements. The dimensions of the final design are: $h = 200 \mu\text{m}$, $w = 160 \mu\text{m}$, $a = 100 \mu\text{m}$, $d = 90 \mu\text{m}$. It is noted that the lateral unperforated silicon regions are for handling purpose, and they do not interfere with the guided modes.

slab for the E_{11}^y mode. Given properly designed waveguide width, perforation period, and hole diameter, the waveguide can operate with a single mode over 260 to 400 GHz (WR-2.8 band) for each polarisation.

Despite their similar appearances, the proposed effective-medium-clad dielectric waveguides are fundamentally different from the photonic crystal waveguides (Tsuruda *et al.*, 2015a; Yu *et al.*, 2019e) in terms of operation mechanism (Cheben *et al.*, 2018; Mosallaei and Rahmat-Samii, 2000b). Specifically, the guidance of the photonic crystal waveguides relies on the bandgap effects. The bandgap material prohibits propagation modes by means of interference and thus confines the waves within the core. The realization of the bandgap materials is based on a variation in refractive indices of two alternating

dielectric materials with the period equal to or longer than half of the guided wavelength to cause destructive interference. This guiding mechanism greatly limits the operation bandwidth, including strong in-band dispersion, and restricting the waveguide to a single polarisation. In contrast, the effective-medium-clad waveguides rely merely on the total internal reflection owing to the refractive index contrast between the waveguide core and the claddings. In this case, the purpose of the deep sub-wavelength perforation is to lower the effective refractive index of the silicon slab to create an effective medium (Cheben *et al.*, 2018; Birman *et al.*, 2009). As such, we can expect a vastly extended bandwidth with low dispersion for orthogonal dominant modes. The considerations for the effective medium and waveguide modal analysis will be discussed in Sections 2.2.2 and 2.2.3.

2.2.2 Effective medium

As shown in Fig. 2.1(d), the effective medium claddings are in the form of a hexagonal array of cylindrical thru-holes perforated into the silicon. The relative permittivity of the effective medium can be obtained by Maxwell–Garnett approximations (Subashiev and Luryi, 2006; Birman *et al.*, 2009), which are polarisation-dependent. These approximations are valid only when the periodicity is subwavelength, where wave diffraction and scattering are negligible. In this way, the effective medium can be treated as a homogeneous material with an equivalent anisotropic permittivity tensor $(\epsilon_x, \epsilon_y, \epsilon_z)$ with respect to the macroscopic electromagnetic field (Cheben *et al.*, 2018; Birman *et al.*, 2009). Specifically, the relative permittivities for the E -field perpendicular and parallel to the axis of the cylindrical air hole are defined as ϵ_x (ϵ_z) and ϵ_y respectively. They are given as (Subashiev and Luryi, 2006)

$$\epsilon_x = \epsilon_{\text{Si}} \frac{(\epsilon_{\text{air}} + \epsilon_{\text{Si}}) + (\epsilon_{\text{air}} - \epsilon_{\text{Si}})\zeta}{(\epsilon_{\text{air}} + \epsilon_{\text{Si}}) - (\epsilon_{\text{air}} - \epsilon_{\text{Si}})\zeta'} \quad (2.1)$$

$$\epsilon_y = \epsilon_{\text{Si}} + (\epsilon_{\text{air}} - \epsilon_{\text{Si}})\zeta, \quad (2.2)$$

$$\epsilon_z = \epsilon_x. \quad (2.3)$$

where ϵ_0 and ϵ_{Si} are the relative permittivities of the air and silicon respectively, while ζ represents the fill factor of the air volume in silicon. For a hexagonal lattice, the fill factor can be calculated from $(\pi d^2)/(2\sqrt{3}a^2)$, where d is the diameter of the cylindrical air hole and a is the period of the lattice. According to Eqs. (2.1)–(2.3), the effective relative permittivities for both polarisations are monotonously decreasing with the fill factor and varying between the values of silicon and air.

2.2.3 Modal analysis

In addition to the subwavelength periodicity, the design process for the effective-medium claddings needs to account for the following considerations: (i) single-mode operation for each polarisation (fundamental-mode operation), (ii) wave confinement, and (iii) structural integrity. Since the cutoff frequencies of the higher-order modes are affected by the claddings, the effective relative permittivity must be selected properly to enable a single-mode operation for each polarisation over the desired band. Specifically, a lower relative permittivity of the claddings would generate a lower propagation constant thus pushing the cutoff frequencies of higher-order modes upward. To obtain a well guided wave with its power mostly concentrated within the core, a higher refractive index contrast between the core and the claddings is preferred (Okamoto, 2007). These two conditions can be satisfied with an effective medium having a larger portion of air. As a trade-off, a larger air portion in the claddings compromises mechanical strength of the platform.

By considering all those factors mentioned above, the periodicity a is selected as $100 \mu\text{m}$ in this design, corresponding to about $0.46\lambda_{\text{Si}}$, where λ_{Si} is the wavelength in bulk silicon at 400 GHz. This estimation is the worst case, since the guided wavelength is always larger than that in the bulk material. The hole diameter is chosen as $90 \mu\text{m}$ generating ϵ_x and ϵ_y of 2.75 and 3.84 respectively. These effective relative permittivities are much lower compared with the relative permittivity of bulk silicon of 11.68. In this work, a hexagonal lattice is adopted for mechanical strength of the platform. It is noted that given a subwavelength period between adjacent holes, the effective medium claddings could be defined in any lattice, e.g., hexagonal or square lattice to match the profile of the waveguide core.

2.2.3 Modal analysis

Marcatili's theory (Marcatili, 1969) is applied here to investigate the dispersion characteristics of the waveguide, as will be elaborated in Section 3.2.2. According to this theory, the propagation constant β_z is a function of the operation wavelength λ , the width w and the height h of the waveguide core, as well as the relative permittivities of the core and effective medium claddings. In the specific design presented in this chapter, the height of the waveguide core is $200 \mu\text{m}$, while its width is selected as $160 \mu\text{m}$. Given the effective relative permittivity tensor of the claddings, the dispersion characteristics can be theoretically obtained. It is noted that Marcatili's theory has limitations in accurately predicting the dispersion behaviour of the fundamental modes at low frequencies

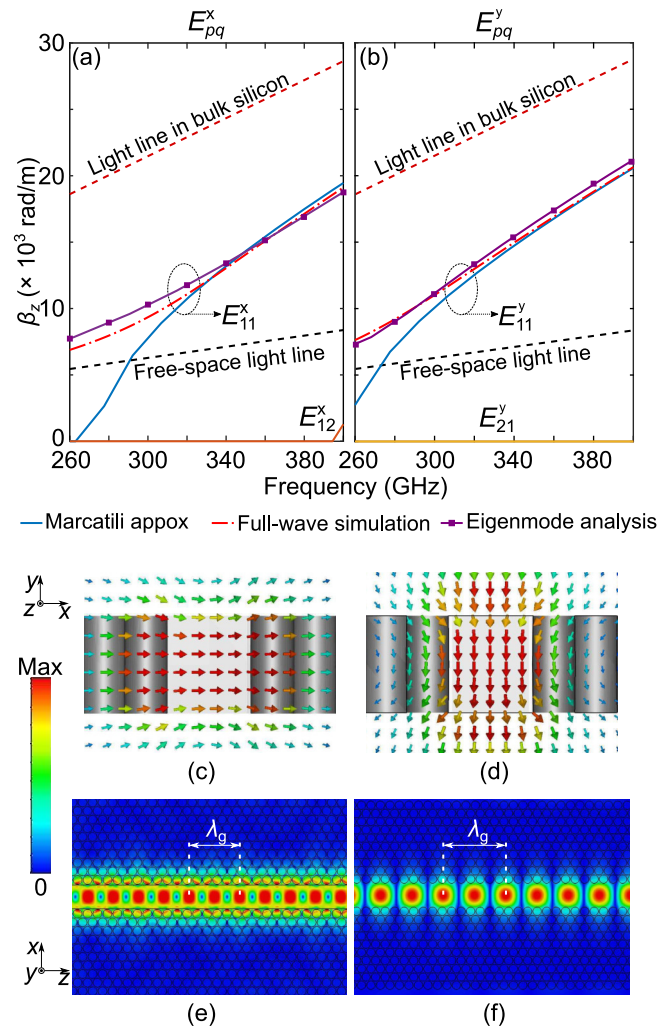


Figure 2.2. Characteristics of the waveguide. Dispersion characteristics for (a) E_{pq}^x and (b) E_{pq}^y modes. Simulated E -field distributions in linear scale at 330 GHz for (c, e) E_{11}^x and (d, f) E_{11}^y modes in the cross-sectional and top views, respectively. The propagation constants in the case of full-wave simulation and Eigenmode analysis are obtained from CST Microwave Studio. The propagation constants for higher-order modes are obtained from Marcatili approximation (Marcatili, 1969), and these modes remain below the cutoff in this frequency range.

owing to the mode approximations (Marcatili, 1969). Therefore, Eigenmode analysis and full-wave simulations are performed in CST Microwave Studios to complement the analytical results.

As shown in Figs. 2.2(a)–(b), the results from the three approaches for the fundamental modes are in good agreement, and converge at high frequencies. Within the operation frequency range from 260 to 400 GHz, the waveguide can work with low dispersion in single dominant modes for both polarisations. In addition, we can infer that the waves

2.2.3 Modal analysis

are tightly confined, as all the propagation constants for the E_{11}^x and E_{11}^y modes are well above the free-space light line. In addition, the higher-order mode appearing above 395 GHz for the horizontal polarisation will not interfere with the dominant modes, since they have propagation constants below the light line, i.e., the wave confinement is extremely weak. However, the higher-order mode might cause slight radiation loss and reduce the waveguide efficiency. In this way, the bandwidth of the waveguide might need to be reduced to 260–395 GHz in some particular scenarios. The simulated E -field distributions for both dominant modes at 330 GHz, i.e., at the centre frequency, are shown in Figs. 2.2(c)–(f).

It is observed that most of the power is concentrated within the waveguide core with evanescent fields extending a few rows into the claddings as shown in Figs. 2.2(e)–(f). Based on the dispersion characteristics, the effective modal indices for the two dominant modes can be obtained. As shown in Fig. 2.3(a), the effective modal index for the E_{11}^x mode is lower than that for the E_{11}^y mode. This disparity results from the differences between the width and height of the waveguide core and between the in-plane and out-of-plane claddings (Chrostowski and Hochberg, 2015). Based on these modal indices, the periodicity of the effective medium amounts to only $0.3\lambda_g$, where λ_g is the shortest guided wavelength at 400 GHz. Derived from the modal indices, the group index for the E_{11}^x mode is found to be higher than that for the E_{11}^y over 260–335 GHz, while the trend inverses over 335–400 GHz as shown in Fig. 2.3(b).

The calculated 3-dB dispersion bandwidths based on the group delay (Agrawal, 2012) of a 3 cm-waveguide for both the E_{11}^x and E_{11}^y modes are shown in Fig. 2.3(c). Owing to the low dispersion, the 3-dB bandwidth for each carrier frequency is high, i.e., the waveguide can support high-speed communications with ultra-broad bandwidth. The 3-dB dispersion bandwidth ranges from 80 to 185 GHz for the E_{11}^x mode, while it varies from 80 to 190 GHz for the E_{11}^y mode over the entire frequency range. The discrepancies of the bandwidth for the two modes are due to a slight difference in the dispersion characteristics. Compared to the bandwidth-enhanced photonic crystal waveguide (PCW) (Yu *et al.*, 2019e), the calculated 3-dB dispersion bandwidths of the proposed waveguide are much higher. This performance improvement is attributed to its extremely low in-band dispersion.

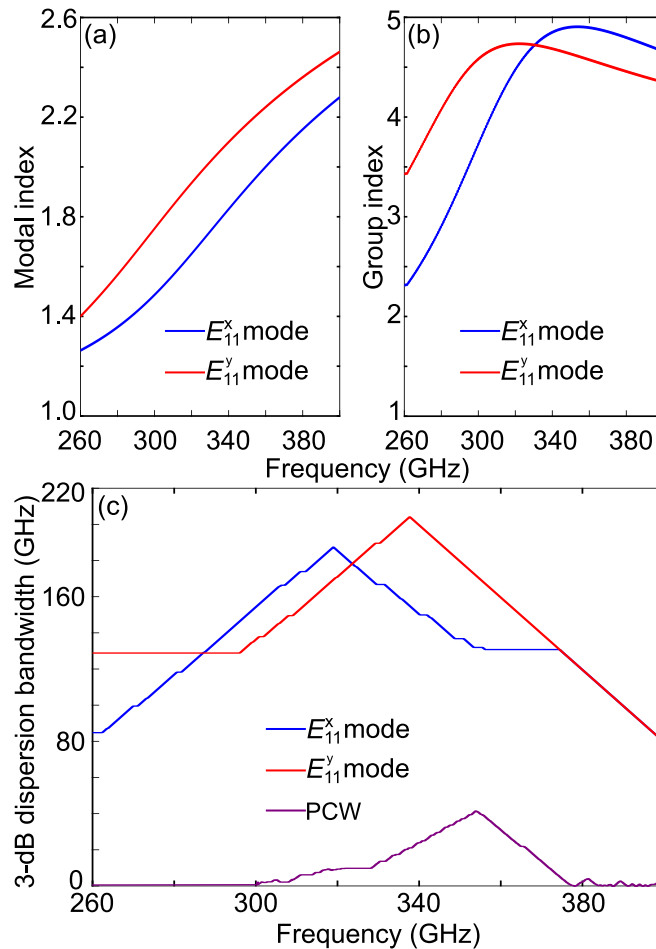


Figure 2.3. Simulated dispersion characteristics. (a) Modal indices, (b) group indices, and (c) calculated 3-dB dispersion bandwidth for the effective-medium-clad waveguide and photonic crystal waveguide. The lengths of the effective-medium-clad waveguide and the bandwidth-enhanced photonic crystal waveguide (Yu *et al.*, 2019e) for 3-dB bandwidth calculation are 3 cm.

2.3 Experiments

To validate the design, waveguide samples with lengths of 1, 2 and 3 cm have been fabricated. The samples are obtained from a 4-inch intrinsic float-zone silicon wafer with a thickness of $200\ \mu\text{m}$ and a resistivity of $20\ \text{k}\Omega\text{-cm}$. The fabrication is based on a standard deep reactive-ion etching (DRIE) process. The waveguide core with height of $200\ \mu\text{m}$ and width of $160\ \mu\text{m}$ is surrounded by the effective medium claddings that are made of cylindrical air holes in a hexagonal lattice with period of $100\ \mu\text{m}$ and hole diameter of $90\ \mu\text{m}$. As mentioned earlier, the solid outer claddings are for handling purposes and do not interfere with the guided waves. To test the mechanical strength of the samples, the cladding on each side contains 24 rows of holes as shown in Fig. 2.4.

2.3.1 Transmission measurements

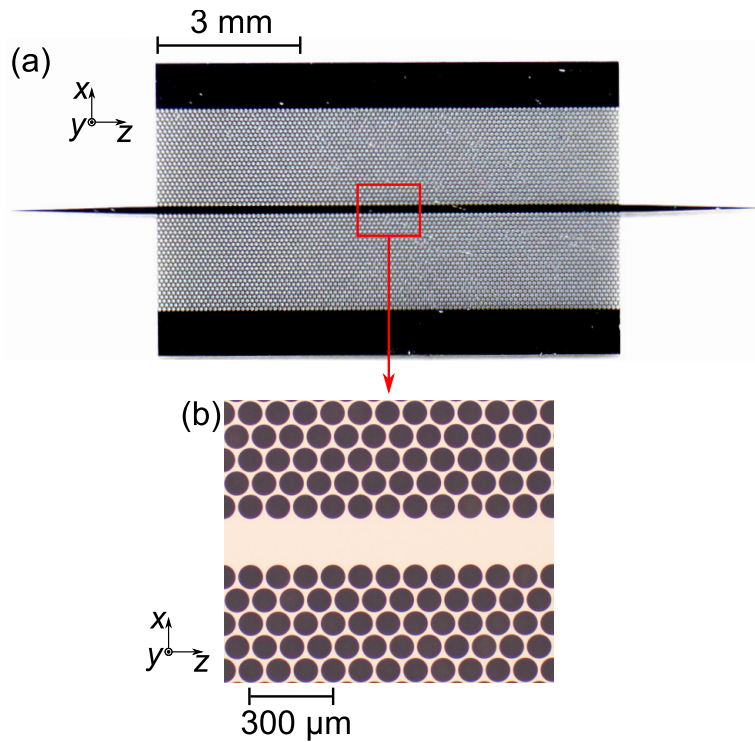


Figure 2.4. Fabricated effective-medium-clad dielectric waveguide. (a) 1 cm waveguide sample, and (b) magnified view of the effective-medium claddings. The design parameters are given in the caption of Fig. 2.1.

The fabricated samples with various lengths show good mechanical strength. However, such a row number is excessive, because the cladding size must be designed with the considerations of wave confinement, structural compactness and mechanical strength. As shown in Figs. 2.2(e)–(f), a minimal number of rows of around three is sufficient to accommodate the evanescent fields. It is noted that in measurement the impact of the feeding waveguide on coupling cannot be neglected, and in this case, seven rows of holes for the cladding are preferred.

2.3.1 Transmission measurements

As shown in Figs. 2.5(a)–(b), the transmission measurements are carried out using a terahertz electronic system. The continuous wave electronic source is constructed from a millimetre-wave signal generator and a nine-fold frequency multiplier. On the receiver side, a frequency mixer downconverts the terahertz signal to the intermediate frequency (IF) at 404.4 MHz by mixing with a local oscillator (LO) signal generated from the spectrum analyser. This setup works in the frequency range from 260 to 390 GHz.

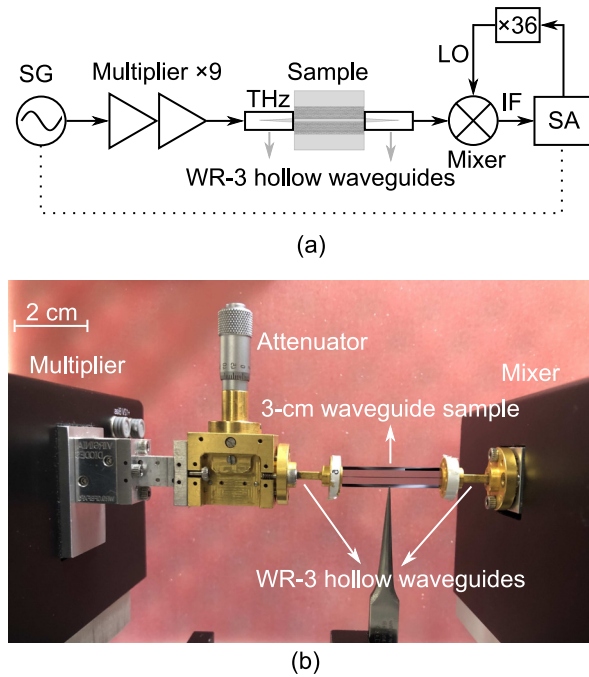


Figure 2.5. Transmission measurement setup. (a) Block diagram, and (b) actual setup. SG: signal generator, SA: signal analyser, THz: terahertz frequency, LO: local oscillator, IF: intermediate frequency. The present setup is for the E_{11}^x mode measurement, while the E_{11}^y mode can be measured by rotating the waveguide sample by 90° with respect to the propagation axis.

The system is equipped with WR-3 hollow metallic waveguide ports. Thus, to enable efficient transition, the tapered structures are inserted into the rectangular waveguides, so that the modes can couple between the hollow waveguides and the sample. In this way, a dielectric waveguide sample positioned between the transmitter and the receiver can be measured with minimal coupling losses.

The transmission coefficients $|S_{21}|$ of the fabricated waveguides displayed in Fig. 2.4 for both polarisations are measured with the waveguide length varying from 1 to 3 cm as shown in Fig. 2.6. The measurements agree well with the simulations in terms of the transmission levels. From the results shown in Figs. 2.6(c)–(d), the measured transmission for the E_{11}^x mode for each length varies from -2.5 to -0.1 dB over 260 to 390 GHz and from -2 to -0.05 dB for the E_{11}^y mode over the band. Both the simulated and measured transmission levels are lower at the lower frequencies because of the higher coupling losses caused by the slight impedance and mode mismatches between the sample and the feed. Due to the evanescent fields of the dielectric waveguide, the transmission measurements are highly sensitive to the alignment with respect to the feeding hollow waveguides. Despite the aid of micromechanical positioners in

2.3.1 Transmission measurements

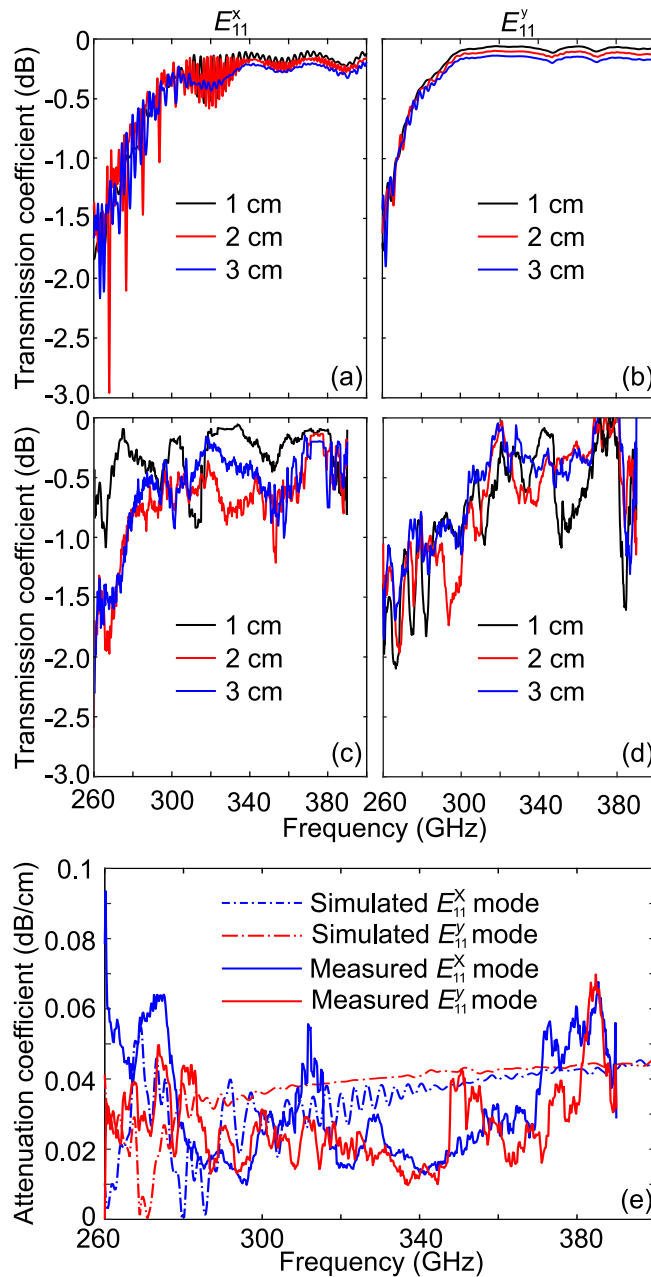


Figure 2.6. Transmission and attenuation coefficients of the waveguides. (a, b) Simulated, (c, d) measured transmission coefficients, and (e) simulated and measured attenuation coefficients extracted from (a–d). The E_{11}^x and E_{11}^y modes are represented in (a, c) and (b, d), respectively. A realistic loss tangent of 3×10^{-5} for the silicon is used in full-wave simulation by CST Microwave Studio.

the alignment, the measured transmission profiles exhibit larger fluctuations than that of simulations, while the details of the transmission sensitivity to the misalignment can be found in Appendix A. In view of this fact, we conclude that the attenuation of the waveguide is too small to be extracted directly, but can be approximated by

comparing and averaging the losses of waveguides with multiple lengths. As shown in Fig. 2.6(e), the simulated attenuation coefficient varies from 0.003 to 0.055 dB/cm for the E_{11}^x mode, while it ranges from 0.003 to 0.048 dB/cm for the E_{11}^y mode over 260 to 400 GHz. However, the measured attenuation coefficient varies from 0.01 to 0.09 dB/cm for the E_{11}^x mode, and from 0.01 to 0.07 dB/cm for the E_{11}^y mode over 260 to 380 GHz with an average value of around 0.05 dB/cm.

This level of loss for the proposed effective-medium-clad waveguides is comparable to the extremely low-loss photonic crystal waveguides (Tsuruda *et al.*, 2015a; Yu *et al.*, 2019e) and bare high-resistivity dielectric waveguides (Malekabadi *et al.*, 2014), which exhibited less than 0.1 dB/cm attenuation over their operation band. However, the loss of the proposed waveguides is more than one order of magnitude lower than a commercial WR-2.8 rectangular waveguide (0.287 – 0.436 dB/cm) (VDI, 2010). In addition, the radiation loss caused by a 90° bending with a radius of 2 mm is simulated in CST Microwave Studio. An average bending loss of less than 0.1 dB per bending for the two modes is achieved over 310–400 GHz and it is comparable to that of the photonic crystal waveguide (Tsuruda *et al.*, 2015a) with a bending loss of about 0.2 dB per bending around 323–331 GHz. However, at the lower frequencies from 260 to 310 GHz, the bending loss varies from 5.5 to 0.5 dB per bending for the E_{11}^x mode and from 3.1 to 0.1 dB per bending for the E_{11}^y mode. The higher bending losses can be compensated by increasing the bending radius at the expense of structural compactness. A comparison between the proposed dielectric interconnect and other guiding structures based on microwave and photonic technologies is shown in Table 2.1. The comparison demonstrates that at terahertz frequencies the proposed waveguides exhibit broad bandwidth, low loss, and low dispersion, while supporting two orthogonal fundamental modes.

2.3.2 Communications measurements

To validate the waveguide performance in terahertz communications, bit-error-rate testing experiments are performed and an uncompressed 4K-resolution video transmission is demonstrated. A diagram of the measurement system is shown in Fig 2.7. On the transmitter side, two tunable near-infrared laser sources generate a beat optical signal that is modulated with the signal from a pulse-pattern generator or a 4K-resolution video player. Amplified by the EDFA, the modulated signal is down-converted to the terahertz signal by a UTC-PD and then coupled to the dielectric waveguide through a WR-3 hollow waveguide. On the receiver side, a SBD is used to retrieve the modulating

2.3.2 Communications measurements

Table 2.1. Comparison of interconnects inspired by microwave and photonic technologies .

	Frequency (GHz)	Bandwidth ^a	Losses (dB/cm)	Dispersions	Modes	Integrability
Microwave-based						
Coplanar waveguide (Frankel <i>et al.</i> , 1991)	200–400 ^b	–	5–22	Low	Quasi-TEM	Yes
Metallic microstrip line (Murano <i>et al.</i> , 2017)	220–330 ^b	–	3.7–5.0	Low	Quasi-TEM	Yes
Commercial hollow waveguide	260–400	42.4%	0.287–0.436	High	TE ₁₀	No
SIIG waveguide (Patrovsky and Wu, 2006)	83–99	17.6%	0.45	Low	E_{11}^y	Yes
SIIG waveguide (Taeb <i>et al.</i> , 2016a)	110–170	42.9%	0.35	Low	E_{11}^y	Yes
Photonics-based						
Dielectric microstrip line (Zhu <i>et al.</i> , 2016b)	750–925	20.9%	0.23–1.2	Low	E_{11}^y	Yes
SOI waveguide (Amarloo <i>et al.</i> , 2018)	500–580	14.8%	0.46	Low	E_{11}^x	Yes
PC waveguide (Yu <i>et al.</i> , 2019e)	324–361	10.8%	< 0.1	High	TE	Yes
Ribbon waveguide (Malekabadi <i>et al.</i> , 2014)	140–220	44.4%	0.087	Low	E_{11}^x and E_{11}^y	No
This work	260–400	42.4%	0.05	Low	E_{11}^x and E_{11}^y	Yes

^a The bandwidth is for dominant modes.

^b The frequency range is limited by the bandwidth of measurement system.

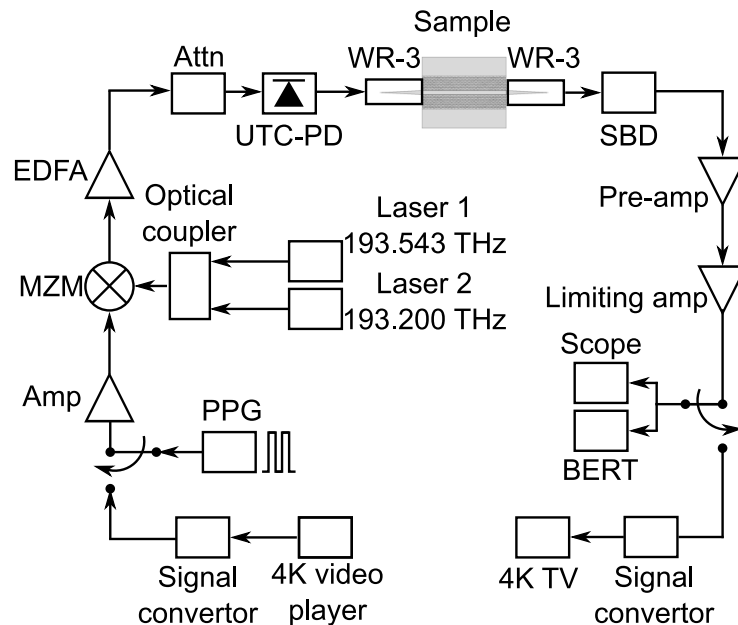


Figure 2.7. Communications measurement diagram. PPG: pulse-pattern generator, Amp: amplifier, MZM: Mach-Zehnder modulator, EDFA: erbium-doped fibre amplifier, Attn: attenuator, UTC-PD: uni-travelling carrier photodiode, WR-3: WR-3 hollow waveguide, SBD: Schottky barrier diode, Scope: oscilloscope, and BERT: bit-error-rate tester.

data from the received terahertz signal. The data signal is then reshaped by a preamplifier and a limiting amplifier. The data quality is then measured by a bit-error rate

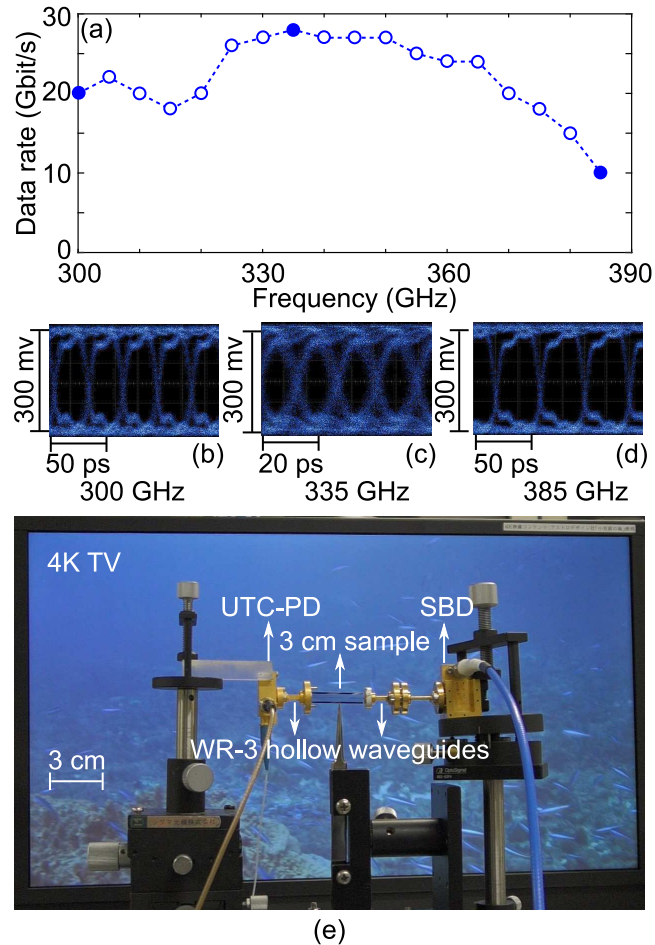


Figure 2.8. Communications measurement results. (a) Measured error-free data rate as a function of frequency over 300 to 385 GHz. The results are discrete and the lines are for visual guidance. Eye diagrams at the carrier frequencies of (b) 300 GHz (20 Gbit/s), (c) 335 GHz (28 Gbit/s), and (d) 385 GHz (10 Gbit/s). (e) Uncompressed 4K-resolution video transmission demonstration (See Visualization).

tester and an oscilloscope, while for the uncompressed 4K-resolution video transmission measurement, the signal can be displayed on a 4K television after a digital signal converter.

A bit-error-rate test is conducted with a 3-cm waveguide sample for the E_{11}^x mode over 300 to 385 GHz. As shown in Fig. 2.8(a), the error-free data rate is reasonably stable over a relatively wide bandwidth (310–370 GHz), which is attributed to the extremely low loss and low dispersion of the waveguide. At 335 GHz, the maximum measured data rate of 28 Gbit/s is achieved corresponding to the highest 3-dB bandwidth shown in Fig. 2.3(c). The measurable maximum data rates are limited by the bandwidths of various components in the measurement setup. Specifically, the degradations of

2.4 Conclusion

the data rate at lower and higher frequencies are due to the roll-off effects of the uni-travelling carrier photodiode (UTC-PD) and Schottky barrier diode (SBD). Meanwhile, the eye-diagrams have clear opening as shown in Figs. 2.8(b)–(d) for 330, 335 and 385 GHz. An uncompressed 4K-resolution video transmission is performed as shown in Fig. 2.8(e). It demonstrates that the proposed waveguide can support a real-time uncompressed 4K video data transmission at the speed of 6 Gbit/s. The 3-cm sample in this study is mainly for a proof of the concept, and this type of waveguide is not intended for long-range transmission. The proposed interconnects are rather for a terahertz integrated platform or frontend to accommodate various passive and active components for different terahertz applications. For example, such a frontend can be used to interface with wireless and fiber links similar to the photonic crystal waveguide (Yu *et al.*, 2019d).

2.4 Conclusion

A design of low-loss, low dispersion dielectric waveguides based on effective medium claddings has been proposed. The waveguides are created from a single silicon wafer and do not include other materials. The effective medium claddings enable a self-supporting and integrated platform while yielding a totally different guiding mechanism compared with photonic bandgap claddings. The designed waveguides can support fundamental modes for each polarisation namely the E_{11}^x and the E_{11}^y modes over 260 to 400 GHz, which is equivalent to a relative bandwidth of 42.4%. An average measured attenuation coefficient of around 0.05 dB/cm is achieved for both E_{11}^x and E_{11}^y modes over the operation frequency range. To characterize the transmission and communications performance, waveguide samples with various lengths have been fabricated. The measurement shows a system-limited maximum error-free data rate of 28 Gbit/s at 335 GHz. Importantly, the proposed waveguide delivers much needed bandwidth, dispersion, and mode orthogonality that are not available from photonic crystal waveguides. With demonstrated performance and form-factor, the proposed waveguide concept can be used as a platform to accommodate various passive/active devices in future terahertz more general systems (Withayachumnankul *et al.*, 2018a; Yu *et al.*, 2019a,b). The concept of the waveguide is applicable to operation at infrared and optical frequencies.

Analysis of effective-medium-clad waveguides and peripherals



THIS chapter extends the investigations of the effective-medium-clad dielectric waveguides by analysing their dispersion, cross-polarisation, and crosstalk, as well as the characteristics of bends and crossings over an operation frequency range of 220 to 330 GHz (WR-3.4 band). Taking the E_{11}^x mode as an example, the experimental results show an average measured attenuation coefficient of 0.075 dB/cm and a group velocity dispersion ranging from around ± 10 ps/(THz · mm) across the whole band. A crosstalk level below -10 dB is measured for parallel waveguides with a separation of $0.52\lambda_0$ and a coupler length of 1.2 cm at 300 GHz. The realised waveguides show a bending loss ranging from 0.500–0.025 dB per bend and a crosstalk at crossing below -15 dB from 220 to 330 GHz. Due to the different dispersion characteristics, the E_{11}^y mode has similar performances but with its operation frequency range reduced to 260–330 GHz. Limited by the measurement setup, a cross coupling between the E_{11}^x and the E_{11}^y modes is measured to be below -20 dB over the whole band. This in-depth investigation of effective-medium-clad waveguides will form a basis for terahertz integrated platforms.

3.1 Introduction

Chapter 2 has presented a type of substrate-free dielectric waveguides cladded by in-plane effective media, which are defined by sub-wavelength periodic perforations. Accordingly, the relative permittivity of the cladding can be controlled by designing the perforations. The waveguides can then be solely built into a single high-resistivity float-zone silicon wafer and thus achieve extremely low loss and low dispersion over 260 to 400 GHz. It has been demonstrated that a straight waveguide could carry terahertz communications signals with a data rate up to 30 Gbit/s. The preliminary investigation focused on the transmission of the straight waveguides. This chapter comprehensively investigates the dispersion, cross-polarisation, and crosstalk of this waveguide type over the frequency range of 220 to 330 GHz (WR-3.4 band). It is noted that the WR-3.4 band is selected mainly because it aligns with an atmospheric window with minimum terahertz wave attenuation, which is beneficial for communications applications (Nagatsuma *et al.*, 2016). Modal characteristics are discussed, and the design process is generalised. Furthermore, the waveguide bends and crossings are implemented and characterised. Such comprehensive investigations are critical to the development of a terahertz integrated platform. In Section 3.2, the waveguide design is discussed in terms of the modal analysis and parametric studies. Section 3.3 discusses the characteristics of the waveguides in terms of dispersion, cross-polarisation, crosstalk, bending loss, and crosstalk in parallel and intersecting waveguides, together with the experimental results, while concluding remarks are given in Section 3.4.

3.2 Design principle

3.2.1 Overview

The various components demonstrated and characterised in this chapter are developed based on the straight interconnect shown in Fig. 3.1(a), which consists of a waveguide core surrounded by in-plane effective-medium claddings (Gao *et al.*, 2019). The waveguide is monolithically made of a single silicon wafer with the resistivity of >10 k Ω cm and relative permittivity ϵ_{Si} of 11.68 to achieve extremely low loss and low dispersion. The effective media are defined by periodically perforating the silicon slab in an hexagonal lattice as shown in Fig. 3.1(b–c), with the perforation period being in the deep subwavelength region, i.e, the period a is markedly smaller than the shortest

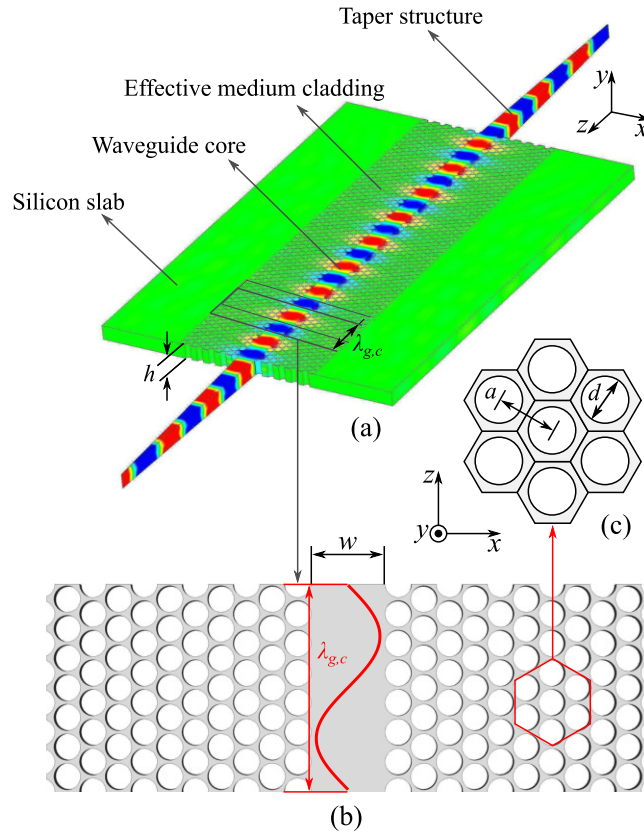


Figure 3.1. Schematic of the effective-medium-clad dielectric waveguide operating over 220 to 330 GHz. (a) Perspective view with instantaneous E -field distribution of a straight waveguide operating at 275 GHz. (b) Magnified view of the waveguide core and the in-plane effective medium claddings. (c) Magnified view of the hexagonal lattice of the effective medium cladding with perforation period $a = 100 \mu\text{m}$, and hole diameter $d = 90 \mu\text{m}$. The perforation period a is $0.17\lambda_{g,c}$ and $0.25\lambda_{g,h}$, where $\lambda_{g,c}$ and $\lambda_{g,h}$ are the guided wavelengths at 275 GHz and 330 GHz. The waveguide is built into a high-resistivity silicon wafer with a thickness $h = 200 \mu\text{m}$. The waveguide core width is $w = 240 \mu\text{m}$. The unperforated silicon slab is for handling purpose, while the taper structures are for mode transition between the sample and the feeding hollow waveguides in measurements.

guided wavelength $\lambda_{g,h}$ over the operation frequency range. It is noted that these effective medium cladding materials are physically completely different from the bandgap materials whose perforation period is defined in the Bragg reflection region (Mosallaei and Rahmat-Samii, 2000a; Cheben *et al.*, 2018). Because of the small scale of the period, the effective medium can be treated as a homogeneous material with its relative permittivity designable between that of air and bulk silicon (Cheben *et al.*, 2018), while the anisotropic permittivity tensor is dependent on the polarisation and can be obtained according to the Maxwell-Garnett effective medium theory (Subashiev and

3.2.2 Modal analysis

Luryi, 2006; Birman *et al.*, 2009). The contrast in the relative permittivities between the core and the claddings allows waveguiding through total internal reflection. Earlier realisations of effective medium theory in the terahertz regime can be found in fibers (Hassani *et al.*, 2008; Ma *et al.*, 2015), flat optics (Guerboukha *et al.*, 2019), and integrated optics (Withayachumnankul *et al.*, 2018a; Headland *et al.*, 2018b, 2020a).

3.2.2 Modal analysis

Marcatilli's theory is employed to investigate the dispersion characteristics of the waveguide platform (Marcatili, 1969). As shown in Fig. 3.2(a–b), the cross-sectional view of a straight waveguide can be divided into five regions, where the waveguide core is in the center surrounded by the vertical air claddings and horizontal effective medium claddings. The relative permittivities for the silicon core and the air are $\epsilon_{\text{Si}} = 11.68$ and $\epsilon_{\text{air}} = 1.0$ respectively. The relative permittivity for the effective medium is defined as a tensor $(\epsilon_x, \epsilon_y, \epsilon_z)$ depending on the polarisation of the wave with respect to the hole array as shown in Fig. 3.2(c). According to the effective medium theory (Subashiev and Luryi, 2006; Birman *et al.*, 2009), these relative permittivities can be obtained by Maxwell-Garnett approximations as shown in Eqs. (2.1)–(2.3). In this way, apart from varying the core dimensions, the modal index of the waveguide can be designed by changing the configuration of the hole array namely (a, d) without introducing any other additional materials or structures, where a is the period of the lattice and d is the diameter of the cylindrical air hole. Such a feature benefits the structural simplicity and design flexibility.

Marcatilli's theory assumes that most of the power is concentrated within the core with the evanescent fields exponentially decaying into the claddings with a minor penetration depth, while there is no electromagnetic field in the shaded areas as shown in Fig. 3.2(b) (Marcatili, 1969). To match these boundary conditions, two families of modes namely E_{pq}^x and E_{pq}^y are introduced with their polarisations corresponding to E_x and E_y respectively. Based on these assumptions, and by solving the Maxwell equations, the propagation constants β_z^x for the E_{pq}^x modes can be derived as (Marcatili, 1969)

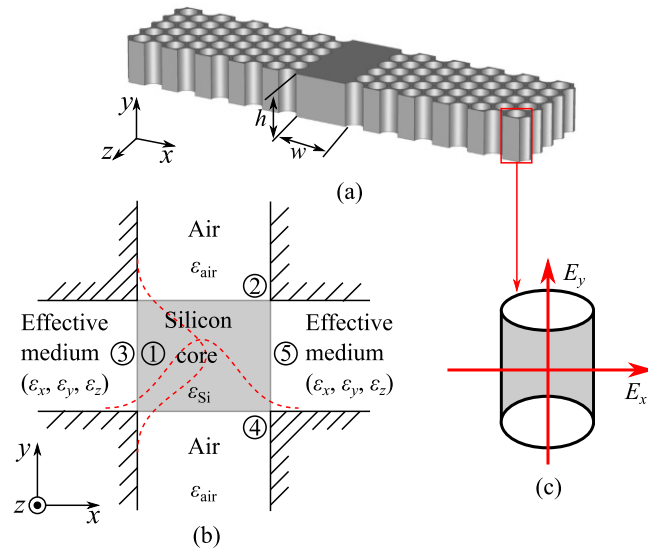


Figure 3.2. Analysis of the straight waveguide. (a) Perspective view of the effective-medium-clad waveguide. (b) Cross-sectional view revealing the approximated boundary conditions. It is assumed that most of the power is concentrated within the core with the evanescent fields in the claddings with a short penetration depth, while there is no electromagnetic fields in the shaded regions. (c) Definition of polarisation relative to the cylindrical hole.

$$\beta_z^x = \sqrt{k_{\text{Si}}^2 - k_x^{x2} - k_y^{x2}}, \quad (3.1)$$

$$k_x^x = \frac{p\pi}{w} \left(1 + \frac{4\epsilon_x c}{\omega \epsilon_{\text{Si}} w \sqrt{\epsilon_{\text{Si}} - \epsilon_x}} \right)^{-1}, \quad (3.2)$$

$$k_y^x = \frac{q\pi}{h} \left(1 + \frac{4c}{\omega h \sqrt{\epsilon_{\text{Si}} - \epsilon_{\text{air}}}} \right)^{-1}. \quad (3.3)$$

Similarly, the propagation constants β_z^y for the E_{pq}^y modes can be derived as (Marcatili, 1969)

$$\beta_z^y = \sqrt{k_{\text{Si}}^2 - k_x^{y2} - k_y^{y2}}, \quad (3.4)$$

$$k_x^y = \frac{p\pi}{w} \left(1 + \frac{4c}{\omega w \sqrt{(\epsilon_{\text{Si}} - \epsilon_y)}} \right)^{-1}, \quad (3.5)$$

$$k_y^y = \frac{q\pi}{h} \left(1 + \frac{4\epsilon_{\text{air}} c}{\omega \epsilon_{\text{Si}} h \sqrt{\epsilon_{\text{Si}} - \epsilon_{\text{air}}}} \right)^{-1}. \quad (3.6)$$

Here, p and q are integers denoting the mode order, while c and ω represent the speed of light in free space and angular frequency respectively, w and h are the width and height of the waveguide core, and $k_{\text{Si}} = \omega \sqrt{\epsilon_{\text{Si}}}/c$ is the wavenumber in silicon. Given ϵ_{air}

3.2.3 Parametric study

and ϵ_{Si} , the propagation constants will be dependent on w , h , a and d . Accordingly, the waveguide bandwidth for the dominant modes can be adjusted by properly selecting those parameters.

3.2.3 Parametric study

To enable the waveguide platform to operate over the designated band from 220 to 330 GHz with fundamental dominant modes, i.e., the E_{11}^x and E_{11}^y modes, the effects of waveguide dimensions on dispersion characteristics are investigated based on the modal analysis described above. An attention will be on higher-order modes that can degrade the waveguide performance in terms of modal dispersion and propagation loss (Selvaraja and Sethi, 2018). Specifically, the higher-order modes have different propagation constants with respect to the fundamental modes at a given frequency, thus increasing the modal dispersion, and reducing the communications bandwidth. Compared to the fundamental modes, the higher-order modes are loosely confined, and the power carried by the higher-order modes is more susceptible to radiation especially at waveguide bends, thus increasing the propagation loss. In addition, the extended evanescent fields of the higher-order modes will increase coupling between waveguides, thus forcing a reduction of the circuit density.

Waveguide core width w and height h

According to Marcatili's theory (Marcatili, 1969), the maximum thickness of a slab waveguide immersed in air to support only the fundamental modes is $h_{\text{max}} = \lambda_0 / (2\sqrt{\epsilon_{\text{Si}} - \epsilon_{\text{air}}})$, where λ_0 is the shortest operation wavelength in vacuum, while ϵ_{Si} and ϵ_{air} are the relative permittivities of silicon and air. In this case, $\lambda_0 = 909 \mu\text{m}$ the wavelength at 330 GHz is selected, and given $\epsilon_{\text{Si}} = 11.68$ and $\epsilon_{\text{air}} = 1$, the initial value of h is obtained as $139 \mu\text{m}$. For the waveguide width w , the starting value can be any value larger than 0, and a straightforward value is to select $w = h$ for symmetric considerations to support both fundamental orthogonal modes. However, from the initial investigations, it is found that the waves at lower frequencies are not well guided with such waveguide core dimensions. Therefore, we increase h and w to $200 \mu\text{m}$ as the starting values. It is noteworthy that the increasing thickness could result in higher-order modes for a slab waveguide, where the width is infinity. However, for a dielectric waveguide, the higher-order modes are determined by the combination

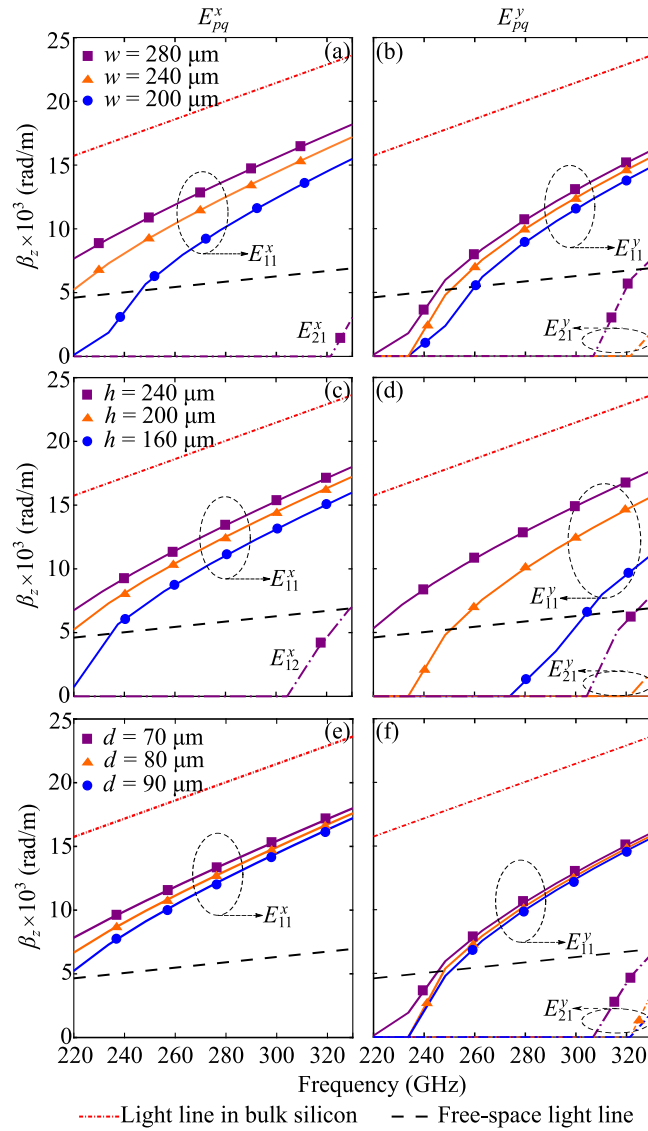


Figure 3.3. Dispersion characteristics based on Marcatilli's theory. The dispersion characteristics are achieved by varying waveguide core width w , height h , and hole diameter d of the effective medium claddings for (a,c,e) E_{pq}^x and (b,d,f) E_{pq}^y modes. The nominal values for the waveguide core width w , height h , perforation period a , and hole diameter d are $240 \mu\text{m}$, $200 \mu\text{m}$, $100 \mu\text{m}$, and $90 \mu\text{m}$, respectively. The investigations are based on Marcatili's theory (Marcatili, 1969).

of core width and height together with the relative permittivities of the surrounding claddings. Thus, such a selection of w and h allows the proposed waveguide to operate in fundamental modes for the initial parametric study.

To investigate the effect of w on the dispersion characteristics, h is selected as $200 \mu\text{m}$ as discussed above. The cladding period a and the hole diameter d are selected as $100 \mu\text{m}$ and $90 \mu\text{m}$, so that a is about $0.375\lambda_{g,330}$, where $\lambda_{g,330}$ is the wavelength in bulk silicon

3.2.3 Parametric study

at 330 GHz. Based on the Eqs. (2.1) and (2.2), this configuration generates effective relative permittivities ϵ_x and ϵ_y of 2.75 and 3.84, which are both much smaller than that of silicon. As shown in Fig. 3.3(a), the propagation constant of the E_{11}^x mode increases steadily when w varies from 200 to 280 μm . It is noticed that when w is 200 μm , β_z^x is below the free-space light line at lower frequencies. This is not physical but arises from the calculations due to the approximations of the boundary conditions. In reality, the propagation constant converges to the free-space light line at low frequencies, thus indicating that the wave is loosely confined (Gao *et al.*, 2019). Thus, a larger w is preferred to improve the wave confinement at lower frequencies. However, when w further increases, the second-order mode E_{21}^x can be observed at higher frequencies, and could lead to mode conversion. On the other hand, for the E_{11}^y mode, as shown in Fig. 3.3(b), a wider waveguide core does not significantly improve the wave confinement at lower frequencies, but results in an earlier appearance of second-order mode E_{21}^y at higher frequencies. Therefore, considering the trade-offs between the wave confinement and the presence of higher-order modes for both polarisations, w is selected as 240 μm , in spite of the E_{21}^y mode.

It should be noted that, while sacrificing some accuracies at lower frequencies, the analysis based on Marcatili's approximations is beneficial to accurately and rapidly estimate the appearance of higher-order modes at higher frequencies. This high-frequency part is crucial to designing a waveguide operating only at its fundamental dominant modes.

To investigate how the waveguide core height affects the dispersion characteristics, h is increased from 160 to 240 μm , while w is set as 240 μm with the same cladding parameters as in the width study. As shown in Fig. 3.3(c), the E_{pq}^x mode is less sensitive to a change in the height with E_{12}^x mode appearing above 300 GHz when h increasing to 240 μm . By contrast, as shown in Fig. 3.3(d), the E_{pq}^y mode varies more significantly with h , where the second-order mode appears with h growing from 160 μm to 240 μm . To achieve the fundamental-mode operation with good wave confinement for both polarisations across the whole band, the value for h is selected as 200 μm .

Perforation period a and hole diameter d of the claddings

The criteria for selecting the perforation period a of the cladding are based on two considerations. Firstly, for the upper boundary, a must be in the deep subwavelength region across the whole band, so that the perforated silicon behaves as a homogenous material. Secondly, for the lower boundary, the dimension of a needs to be larger than

the feasible hole size d , which is informed by a fabrication limit of around $20\ \mu\text{m}$ for a standard deep reactive-ion etching (DRIE) process. However, if the period a is close to $20\ \mu\text{m}$, the varying range of d is limited, thus limiting the possible range of the relative permittivity for the effective medium claddings. Therefore, in this work, we select a as $100\ \mu\text{m}$, which is around $0.28\lambda_{g,x}$ and $0.25\lambda_{g,y}$ at 330 GHz, where $\lambda_{g,x}$ and $\lambda_{g,y}$ are the guided wavelengths for the E_{11}^x and E_{11}^y modes, respectively. Such a selection of a does not only meet the criteria mentioned above, but also enables the effective relative permittivity of the claddings to be designable in a reasonable range. Specifically, with a fixed as $100\ \mu\text{m}$, the effective relative permittivity tensor $(\epsilon_x, \epsilon_y, \epsilon_z)$ can be tailored from $(10.98, 11.29, 10.98)$ to $(2.75, 3.83, 2.75)$ by increasing the hole diameter from 20 to $90\ \mu\text{m}$. Thus, with fixed waveguide core dimensions, by varying the hole diameter of the effective medium cladding, the modal index of the waveguide can be designed in a wide range to adapt to various scenarios for future applications.

It is seen in Figs. 3.3(e)–(f), that the propagation constants for both E_{11}^x and E_{11}^y modes increase when d decreases from 90 to $70\ \mu\text{m}$. This phenomenon means that a higher volume percentage of silicon in the effective medium claddings leads to the mode approaching that in a slab waveguide. To enable a better wave confinement to the core, a larger refractive index contrast between the core and the claddings is preferred with a larger hole diameter d . However, to ensure the mechanical strength and structural integrity of the waveguide, d can not be too large, and is therefore selected as $90\ \mu\text{m}$. It is noteworthy that a small fabrication tolerance of d has a minor impact on the dispersion characteristics.

3.3 Characteristics of waveguide

In this section, the characteristics of straight waveguides are investigated including transmission, dispersion, cross polarisation, and crosstalk between two parallel waveguides. In addition, the loss due to waveguide bends and the leakage at crossing waveguides are studied. As illustrated in Fig. 3.4, the straight waveguides are solely built into a single high-resistivity float-zone silicon wafer with a thickness of $200\ \mu\text{m}$, resistivity of $>10\ \text{k}\Omega\text{cm}$ and relative permittivity of 11.68. According to the analysis in Section 3.2, to maintain fundamental dominant modes for both polarisations, the width w and height h of the waveguide core are 240 and $200\ \mu\text{m}$, while the perforation period a and hole diameter d are selected as $100\ \mu\text{m}$ and $90\ \mu\text{m}$. To avoid the unperforated slab interfering

3.3.1 Transmission

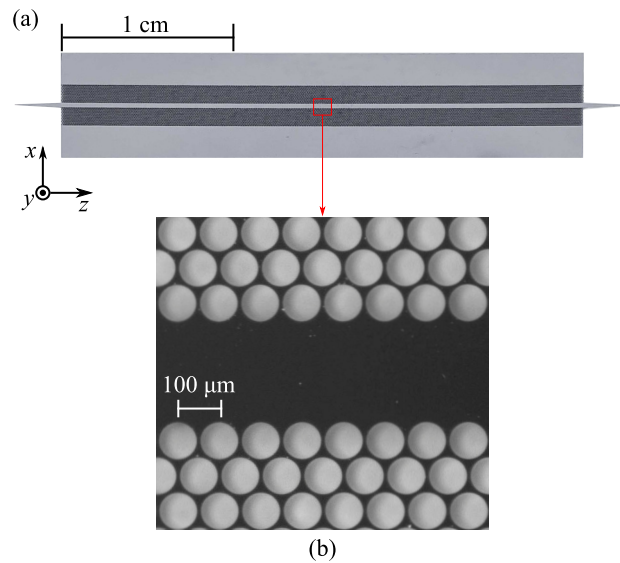


Figure 3.4. Fabricated straight waveguide at WR-3.4 band. (a) 3-cm straight waveguide sample. (b) Microscope image around the core. The dimensions of the waveguide core and effective medium are given Fig. 3.1. Each taper is with the length of 3 mm.

with the propagating waves, twelve rows of holes are employed on each side of the in-plane claddings. The fabrication is based on the standard deep reactive-ion etching (DRIE) process. The simulation is performed with CST Microwave Studio 2019. A realistic loss tangent of 3×10^{-5} for silicon is adopted in CST full-wave simulations. In the simulation, the waveguide under test is excited by the WR-3.4 rectangular hollow waveguides into which the tapered ends are inserted, as visible in Fig. 3.4(a). The measurements are carried out by using a Keysight PNA with VDI WR-3.4 extension modules spanning 220–330 GHz. As shown in Fig. 3.5, the samples are fed in the same way as in the simulations. While the samples are fixed onto the holder at the unperforated silicon slab, the waveguide core and the claddings are exposed to the air, so that there is no field disturbance in the y -direction. To realise the integration for future applications, a hollow package is proposed, and a possible implementation can be found in Appendix B together with simulated results.

3.3.1 Transmission

To investigate the transmission and attenuation coefficients of the straight waveguides, samples with lengths of 1, 2, 3 and 5 cm are measured. From the measured results illustrated in Figs. 3.6(a)–(b), the transmission coefficients for the E_{11}^x mode amount

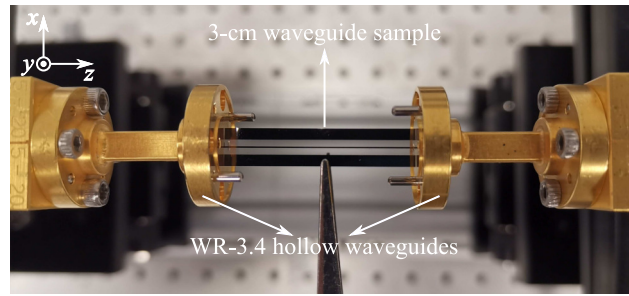


Figure 3.5. Measurement setup. For the E_{11}^y mode measurement, the sample is fed by straight WR-3.4 rectangular waveguides, while for the E_{11}^x mode measurement, extra WR-3.4 twist waveguides are added to rotate the polarisation. The opening of the hollow waveguide measures $431.8 \mu\text{m}$ by $863.6 \mu\text{m}$.

to around -1 dB, while the E_{11}^y mode shows higher loss. As shown in Fig. 3.6(a), the measured transmission level of the 2-cm sample is lower than that of the 3-cm one for the E_{11}^x mode. This is mainly caused by the waveguide-feed alignment that is more challenging for shorter waveguides due to the clearance for observation and manipulation. The measured transmissions for both orthogonal modes are in good agreements with the simulations shown in Figs. 3.6(c)–(d). The decrease of the transmission level at lower frequencies for both modes is mainly attributed to (i) the coupling loss due to mode mismatching with the feeding hollow waveguides as detailed in Appendix C, and (ii) the relatively low propagation constants resulting in weaker wave confinement as discussed in Section 3.2. The transmission level appears lower for the E_{11}^y mode due to weaker confinement.

The relatively stronger fluctuations in the measurements represent standing waves caused by the misalignment between the inserted tapers and the feeding hollow waveguides (Gao *et al.*, 2019). As such, the attenuation coefficients cannot be accurately extracted from the measurement directly, but reliable values can be obtained by cross-comparing and averaging the results from multiple waveguide lengths. As shown in Fig. 3.6(e), for the E_{11}^x mode, the simulated attenuation coefficients shows an average value around 0.03 dB/cm, while the measured attenuation coefficients is with an average value about 0.075 dB/cm across the band. The loss level is more than one order of magnitude lower than that of the commercial WR-3.4 rectangular waveguides with the attenuation coefficient ranging from 0.308–0.214 dB/cm (VDI, 2010). However, as shown in Fig. 3.6(f), for the E_{11}^y mode, the simulated attenuation coefficients are with an average value of 0.185 dB/cm over the frequency range of 220 to 330 GHz,

3.3.2 Dispersion

while the measured attenuation coefficient has a higher average value of 1.225 dB/cm over the frequency range of 220 to 260 GHz, and an average loss of 0.135 dB/cm over 260 to 330 GHz. The relatively greater discrepancies between the measurements and simulations at the lower frequencies for the E_{11}^y mode are mainly due to the loosely confined waves that are more sensitive to the sample alignment. Similarly, the coupling loss between the proposed dielectric waveguide and a WR-3.4 hollow waveguide is also related to the wave confinement and sample alignment, and it can be found in Appendix C.

3.3.2 Dispersion

The dispersion characteristics of the straight waveguides are simulated and measured as shown in Figs. 3.7(a)–(b). The propagation constants β_z for both simulation and measurement are derived from the unwrapped phase of the waveguides with multiple lengths. To prove the accuracy of the derivation, a port-mode simulation is also conducted and given. As shown in Fig. 3.7, the measured dispersion curves overlap with the simulated ones for both of the E_{11}^x and the E_{11}^y modes. While the curves exhibit the same slopes, the dispersion curves derived from the unwrapped phase have an offset with respect to the port-mode ones due to phase ambiguities.

Accordingly, as illustrated in Figs. 3.8(a)–(b), the group velocities for the two fundamental modes are calculated based on the dispersion characteristics shown in Fig. 3.7. The measured group velocity varies lightly across the whole band for the E_{11}^x mode, while it has a relatively larger slope at low frequencies for the E_{11}^y mode. All the measured results agree well with the simulations, and the slight discrepancies are due to the fabrication and measurement tolerances. Based on the group velocities, the group velocity dispersions (GVD) are derived as shown in Figs. 3.8(c)–(d). For the E_{11}^x mode, the measured GVD varies between ± 10 ps/(THz · mm) representing a low dispersion over a broad band. However, for the E_{11}^y mode, the measured GVD changes relatively significantly over the operation frequency range. According to the discussions in Section 3.2, to reduce the dispersion of the E_{11}^y mode, a thicker waveguide core is required depending on the specific applications. However, a thicker waveguide could invoke higher-order modes for both polarisations and would require a modification of the waveguide width to suppress these higher-order modes. Here, with a fixed cladding configuration, in the simulation we increase the waveguide thickness from 200 to 250 μm , and decrease the waveguide width to 225 μm . As shown in Fig. 3.9, with the waveguide thickness

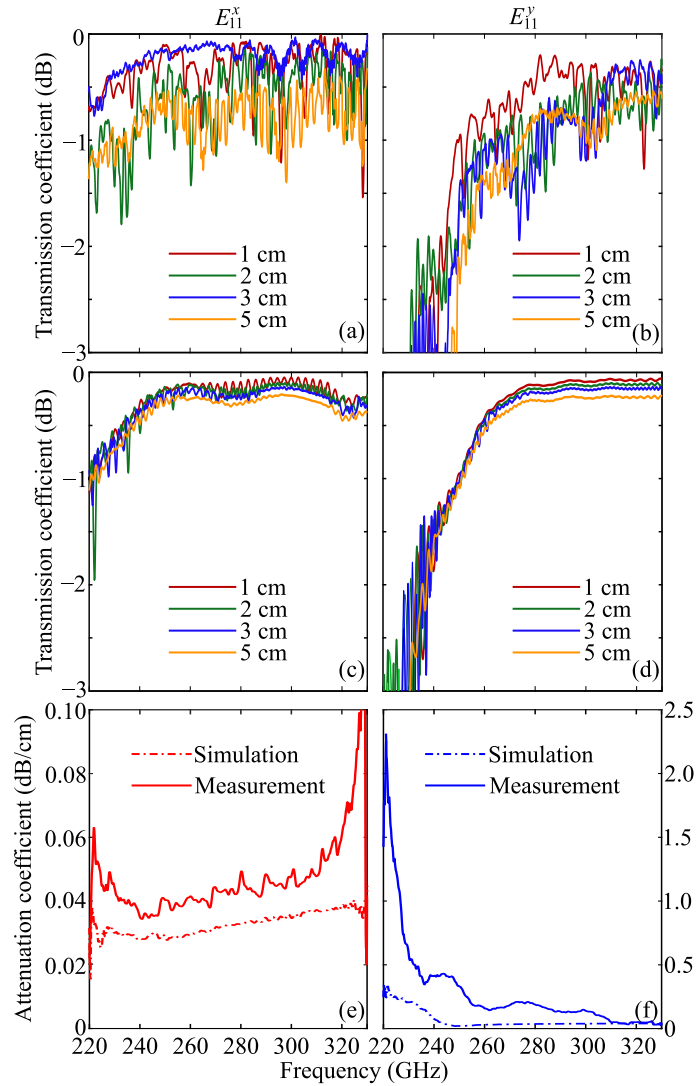


Figure 3.6. Transmission and attenuation coefficients of the straight waveguides. Measured (a–b) and simulated (c–d) transmission coefficients for straight waveguides with various lengths for E_{11}^x and E_{11}^y modes, and simulated and measured attenuation coefficients for (e) E_{11}^x and (f) E_{11}^y modes that are extracted from (a–d). The loss tangent of silicon adopted in the CST full-wave simulations is 3×10^{-5} .

increasing, the simulated GVD for the E_{11}^y mode approaches 0 ps/(THz · mm) across the whole frequency range.

3.3.3 Cross polarisation

To ensure polarisation purity, the cross coupling between the E_{11}^x and E_{11}^y modes are investigated. The measurements are carried out as shown in Fig. 3.10, where the sample

3.3.4 Crosstalk between parallel waveguides

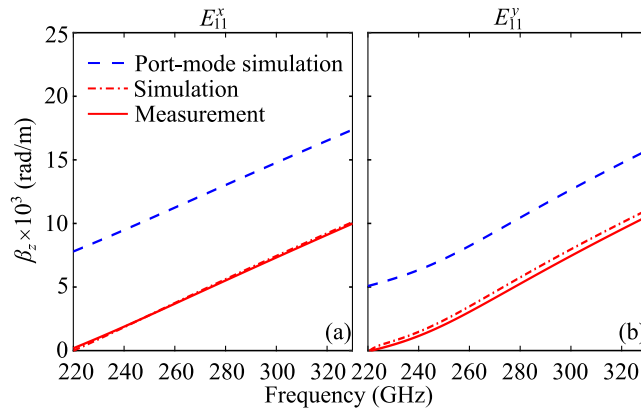


Figure 3.7. Dispersion characteristics of the straight waveguides. Simulated and measured dispersion characteristics for (a) the E_{11}^x , and (b) the E_{11}^y modes. The port-mode results are obtained by full-wave port-mode simulation in CST, while the simulated and measured propagation constant β_z are derived from the unwrapped phase of the waveguides with multiple lengths.

is fed with E_x polarisation, and the E_y polarisation is measured at the receiver side. The waveguide samples with lengths of 1 and 3 cm are measured with the resulting transmission coefficients as shown in Fig. 3.11. The average value for the 1-cm sample is around -20 dB, while it is about -30 dB for the 3-cm sample. In the ideal case, cross-polarisation conversion is non-existent (negative infinity in dB), as can be understood from symmetry considerations. However, the presence of cross-polarisation can be explained by several factors such as the imperfections in the waveguide samples, and the sample misalignment relative to the feeding waveguides. To investigate the effects of the misalignment on the cross polarisation, a 1-cm waveguide is simulated with 1 degree rotation around the z -axis relative to the hollow waveguides. As shown in Fig. 3.11, the simulated cross-polarisation coefficient for the imperfectly aligned waveguide almost overlaps with the measured result. It is confirmed that a slightly imperfect alignment introduces observable cross polarisation. However, such a low level of cross coupling is not expected to impact the operation of the waveguide in most applications.

3.3.4 Crosstalk between parallel waveguides

For terahertz integrated circuits, it is important to ensure that signals in adjacent traces will not interfere with each other. To investigate the minimum clearance between straight waveguides, we have implemented two sets of parallel straight waveguides with a coupling length of $l_c = 12$ mm. Each pair is separated by five or seven rows of

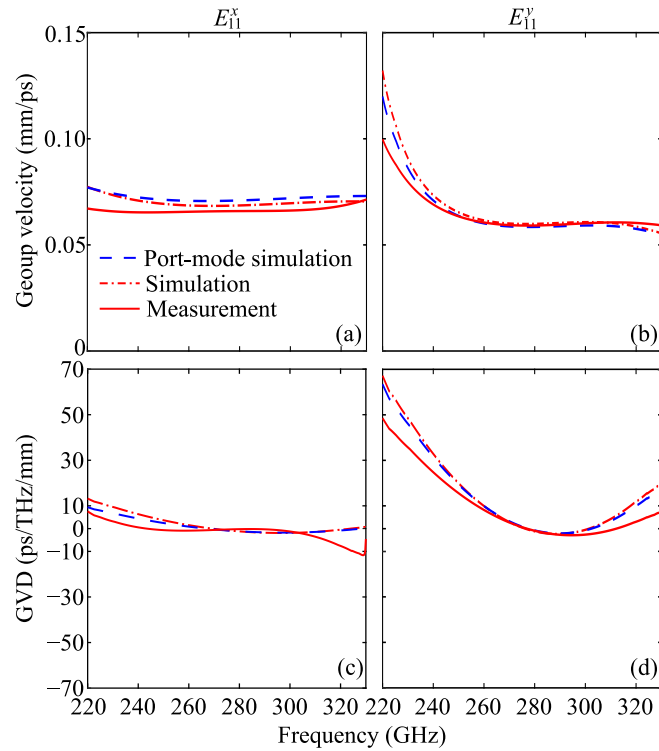


Figure 3.8. Group velocity and group velocity dispersion (GVD). Simulated and measured group velocities of (a) E_{11}^x , and (b) E_{11}^y modes. The group velocities are calculated from the dispersion characteristics shown in Fig. 3.7. To remove the noise, fifth-order polynomial curve fitting is carried on the dispersion characteristics. Simulated and measured group velocity dispersions of (c) the E_{11}^x , and (d) the E_{11}^y modes. The group velocity dispersions are derived from group velocities shown in (a)–(b).

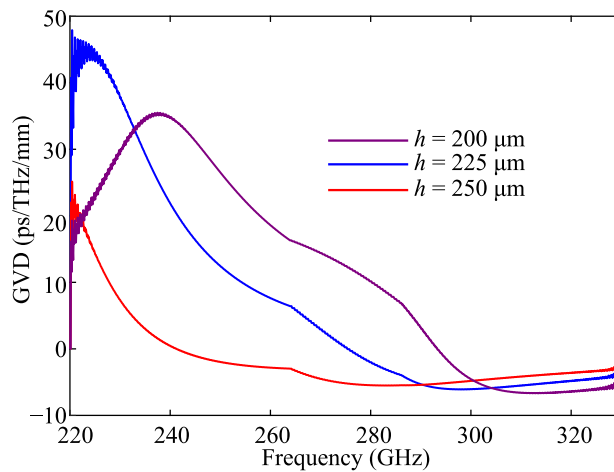


Figure 3.9. Simulated GVD for the E_{11}^y mode with increasing waveguide thickness. To suppress the high-order modes for both polarisations, the waveguide width is reduced to 225 μm .

3.3.4 Crosstalk between parallel waveguides

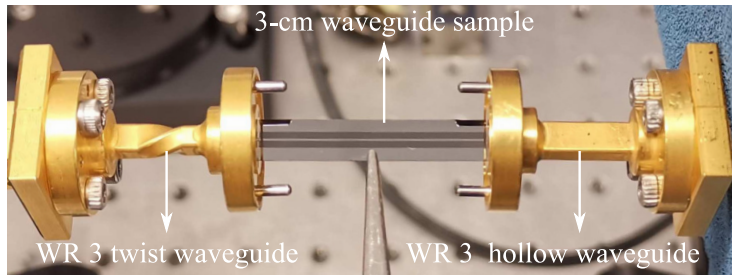


Figure 3.10. Cross polarisation measurement setup. At the excitation port on the left, a WR-3.4 twist waveguide is adopted for E_x polarisation, while at the receiving port, a WR-3.4 straight waveguide is implemented for E_y polarisation.

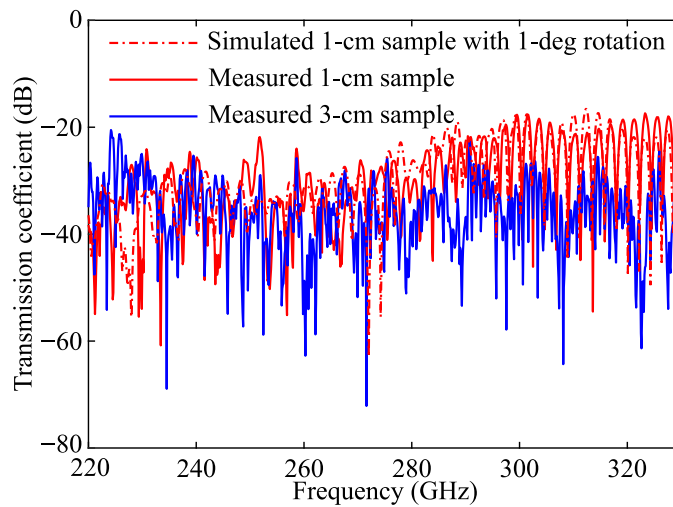


Figure 3.11. Simulated and measured transmission coefficients for the cross polarisation of straight waveguide samples. An artificially misaligned waveguide is simulated for comparison. In simulation, the polarisation for the excitation port is E_x , while at the receiving port, the polarisation is E_y .

perforations, or 0.35 mm and 0.52 mm respectively as shown in Figs. 3.12(a)–(c). One fabricated sample is shown in Fig. 3.12(d).

From the theory of directional couplers, a pair of dielectric waveguides is able to accommodate symmetric or antisymmetric mode, while the coupling coefficient between the waveguides should decrease exponentially with the ratio of g/ζ , where g is their separation, and ζ is the $1/e$ evanescent field penetration depth in the in-plane claddings (Marcatili, 1969). In other words, a larger distance and a smaller field penetration depth will lead to a weaker coupling between the two parallel waveguides. According to (Marcatili, 1969), ζ is inversely proportional to the lateral wavenumber k_x^x or k_x^y that is determined by the waveguide core width, and the refractive index contrast

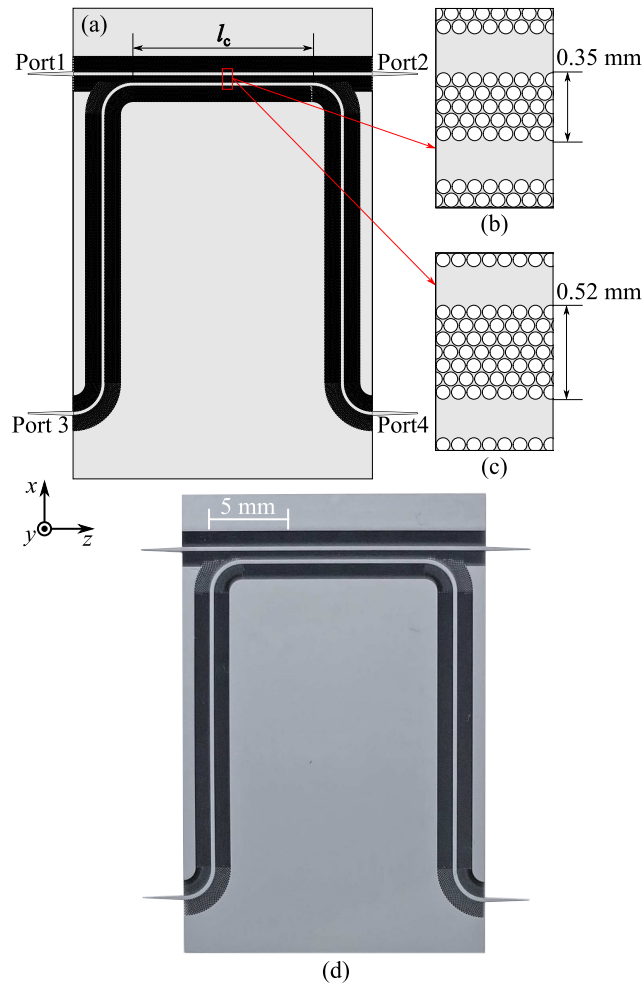


Figure 3.12. Two parallel waveguides. (a) Schematic of the two parallel waveguides model, and magnified view with separation of (b) 0.35 mm (five rows of holes) and (c) 0.52 mm (seven rows of holes). (d) Fabricated sample with waveguides' separation of 0.35 mm and a coupling length l_c of 12 mm. The layout is to expedite the measurement by having pairs of ports pointing in the same direction. The relatively large distance for Ports 1–3 and Ports 2–4 is to accommodate the flanges of the hollow waveguide feeds. During the measurement, the unused ports generate minimal reflections due to the good impedance matching of the tapers to free space.

between the core and the claddings as represented in Eqs. 3.2 and 3.5. Specifically, at a certain frequency, a wider waveguide core together with a larger refractive index contrast results in a larger k_x^x or k_x^y thus a smaller penetration depth, with most of the power concentrated within the core. In this case, given a certain waveguide configuration, the coupling coefficient is primarily determined by the separation g .

3.3.4 Crosstalk between parallel waveguides

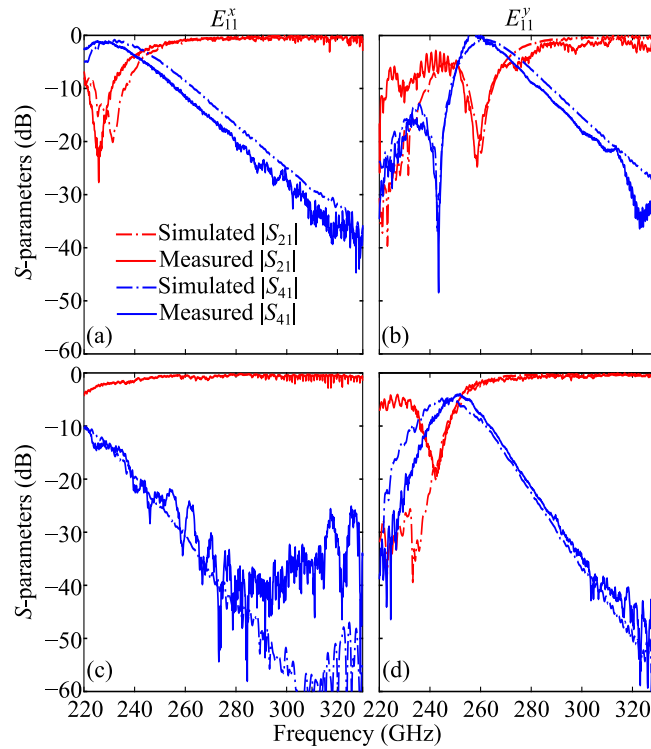


Figure 3.13. Simulated and measured S-parameters of the parallel waveguides. (a) E_{11}^x mode, and (b) E_{11}^y mode with a waveguides' separation of 0.35 mm (five rows of holes). (c) E_{11}^x , and (d) E_{11}^y modes with a waveguides' separation of 0.52 mm (seven rows of holes).

The S-parameters for the E_{11}^x and the E_{11}^y modes for two parallel waveguides with a separation of 0.35 mm (five rows of holes) are measured as shown in Figs. 3.13(a)–(b). For the E_{11}^x mode, the coupling coefficient is high in the range of 220 to 240 GHz, while it decreases monotonically over 240 to 330 GHz with wavelength decreasing. For the E_{11}^y mode, from 220 to 250 GHz, both the through and cross levels are low due to the loosely confined waves, while from 250 to 270 GHz, the crosstalk becomes stronger with an improved wave confinement. The coupling drops dramatically over 270 to 330 GHz with the same reason as for the E_{11}^x mode. On the other hand, for the waveguides separated in 0.52 mm, the wave can propagate with a high through level and the crosstalk below -10 dB for the E_{11}^x mode. However, for the E_{11}^y mode, a relatively stronger coupling happens over 230 to 250 GHz, while it decreases sharply over 250 to 330 GHz with wavelength decreasing. All the measured results agree well with the simulations, and the slight discrepancies are caused by the fabrication and measurement tolerances.

The results show that the crosstalk is frequency-dependent. This is because given a certain coupling length and gap width, the crosstalk level is related to the wavenumber

difference Δk between the symmetric and antisymmetric modes, and this Δk varies with frequency (Fujita and Nagatsuma, 2016). Specifically, the strongest crosstalk happens when Δk is equal to π/l_c (Fujita and Nagatsuma, 2016). In addition, the crosstalk for the E_{11}^y mode is larger because of its weaker wave confinement seen from the propagation constant β_z^y illustrated in Fig. 3.3. On the contrary, in Fig. 3.13(b) the crosstalk for the E_{11}^y mode from 240 to 250 GHz is lower than that from 220 to 230 GHz. This is because the coupling response is periodic with frequency leading to the different crosstalk levels. Specifically, at 243 GHz, the coupling length $l_c = 12$ mm is 50 times of $\lambda_{g,243}$, where $\lambda_{g,243}$ is the guided wavelength at 243 GHz. According to the quarter-wavelength directional coupler theory (Jones and Shimizu, 1958), the waves will take the through path leading to a low crosstalk. In general, a higher isolation level could be achieved by enlarging the separation depending on specific applications.

3.3.5 Bend

As illustrated in Figs. 3.14(a)–(b), a bent waveguide with multiple successive 90° bends clad by the in-plane effective media is designed and fabricated. Considering the trade-off between the radiation loss and the structural compactness, the optimal bend radius of the core r_b is selected as 2 mm, which corresponds to about twice the free-space wavelength at 300 GHz. To maintain the effective permittivity of the claddings, the fill factor of the bent claddings remains the same as in its straight counterpart. To satisfy this condition, as shown in Figs. 3.14(c)–(d), the effective medium claddings are divided into inner and outer parts with respect to the core. Both parts of the cladding are then divided into annular sectors by a series of arcs with an adjacent radius difference of $\Delta r_b = a \sin(\pi/3)$, where $a = 100 \mu\text{m}$. It is noted that the first row of holes starts from the edge of the waveguide core, so $r_{1(\text{in})}$ and $r_{1(\text{out})}$ are defined as $r_{1(\text{in})} = r_b - w_b/2 - d$ and $r_{1(\text{out})} = r_b + w_b/2 + d$ respectively, where w_b is the width of the bent waveguide core, and $d = 90 \mu\text{m}$ is the axis of the elliptical holes. In addition, each annular sector is sectioned in the azimuthal direction with an angular step of $\theta = a/(r_b - w_b/2 - d/2)$ in radians. As a result, the area of the cell in each sector can be obtained as $A_n = |r_{n+1}^2 - r_n^2|\theta/2$ accounting for both inner and outer claddings, while the cells in the even sectors are displaced by an angle $\theta/2$ relative to their counterparts in the odd sectors. To fit each annular sector cell, each hole needs then to be distorted into an ellipse with its area calculated as $A_{en} = A_n\zeta$. For the inner claddings, the major axis of the ellipse $d_{e,\text{major}}$ in each cell is fixed to $d = 90 \mu\text{m}$, so that the minor

3.3.5 Bend

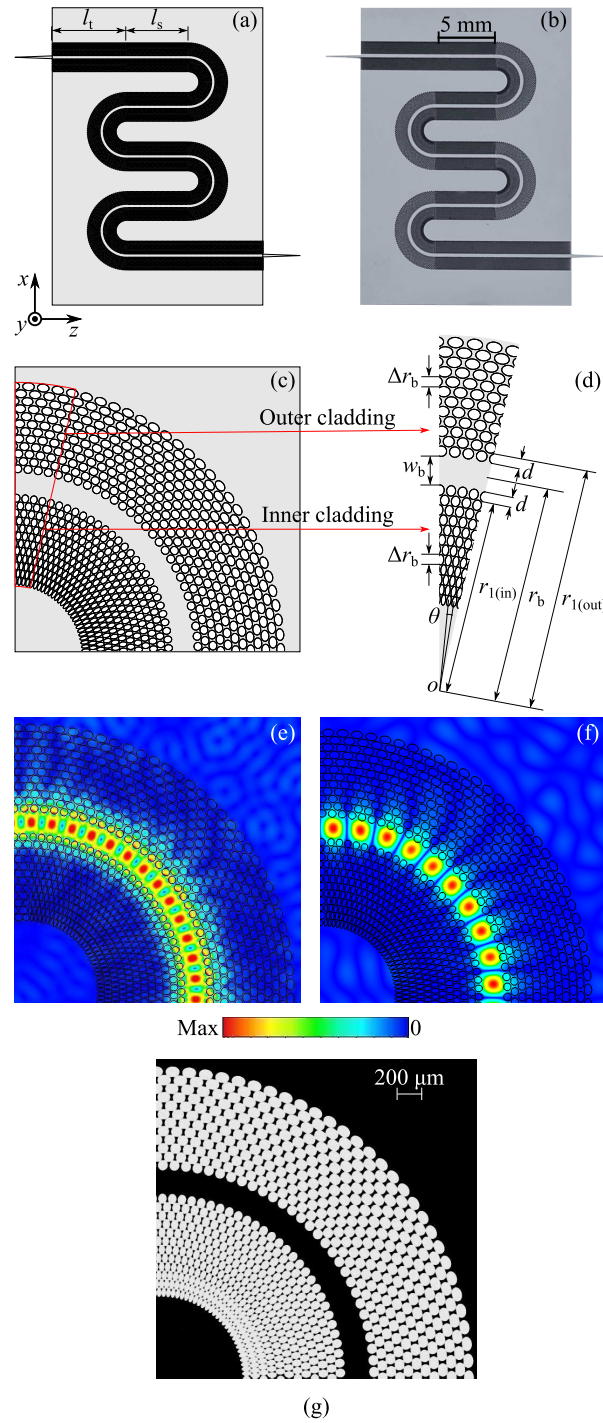


Figure 3.14. Bent waveguides. (a) Schematic of the multiple successive bends model. (b) Fabricated sample with multiple successive bends with a total length of 62 mm. (c) 90° bending model. (d) Magnified view of bent claddings. Simulated E -field distributions for (e) E_{11}^x and (f) E_{11}^y modes at 275 GHz. (g) Microscope image of the fabricated 90° bend. $d_e = 90 \mu\text{m}$, $w_b = 240 \mu\text{m}$, $r_b = 2 \text{ mm}$, $\Delta r_b = 86.6 \mu\text{m}$, $\theta = 3.13^\circ$.

axis $d_{e,\text{minor}}$ can be derived as $d_{e,\text{minor}} = A_{en}/(\pi d_{e,\text{major}})$. This is correspondingly done using a fixed minor axis and calculated major axis for the outer cladding. The simulated E -field distributions for the E_{11}^x and E_{11}^y modes at 275 GHz are shown in Figs. 3.14(e)–(f). It can be seen that most of the power concentrates within the core and the field penetration extends to about 5 rows of holes in the outer cladding due to the bending effects, resulting in some radiation loss.

To investigate the bending loss as a function of the bending radius, the radius for a single 90-deg bend clad by homogeneous artificial material is increased from 0.5 mm to 3.5 mm with a step width of 1.5 mm. As shown in Fig. 3.15, the bending losses for both E_{11}^x and E_{11}^y modes are decreased with the bending radius r_b increasing, with no significant improvement when the radius goes beyond 3.5 mm. The relatively high bending loss for the E_{11}^y mode is mainly due to its weaker wave confinement. To maintain a compact footprint, a 2-mm bending radius is selected.

To experimentally validate the bend design, two waveguides consisting of five straight sections and eight 90° bends are fabricated. The difference between the two waveguides is the length of each straight section represented by l_s , namely 5 mm and 10 mm, and the fabricated single 90° bend is illustrated in Fig. 3.14(g). Given the transition length l_t of 6 mm, the total lengths for the two samples are 62 mm and 87 mm. As shown in Figs. 3.16(a)–(d), for both the E_{11}^x and E_{11}^y modes, the measured and simulated transmission coefficients of the two samples agree well. The low transmission level at lower frequencies is mainly attributed to coupling loss as in straight waveguides. The loss per bend L_B can be approximately extracted by comparing and averaging the transmission coefficients of straight and bending waveguides as

$$L_B = \frac{L_{(\text{bending})} - L_{(\text{straight})} - \Delta l L_S}{8} \quad (3.7)$$

where $L_{(\text{bending})}$ and $L_{(\text{straight})}$ are the losses of a sample with multiple bends and a straight sample, and Δl is the length difference between the straight section of the two waveguides. L_S is the average loss of the straight waveguide shown in Fig. 3.6(e).

As illustrated in Fig. 3.16(e), for the E_{11}^x mode, the measured average bending loss is approximately 0.250 dB per bend over 220 to 260 GHz and 0.025 dB per bend over the operation frequency range from 260 to 330 GHz. With a much broader bandwidth, the proposed waveguide has a lower bending loss than that of the photonic crystal waveguide, which has a bending loss around 0.2 dB per bend from 323 to 331 GHz (Tsuruda *et al.*, 2015b). However, for the E_{11}^y mode, the measured bending loss is with an

3.3.6 Crossing

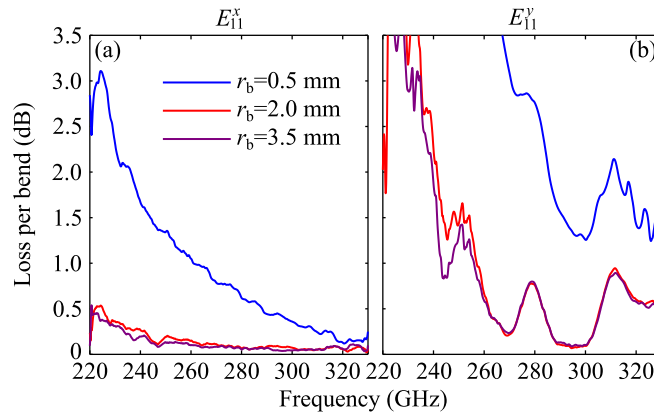


Figure 3.15. Simulated bending loss with various bending radius r_b . Simulated bending loss for (a) the E_{11}^x and (b) the E_{11}^y modes. Here, a single 90-deg bend model cladded by homogeneous artificial material is adopted in CST simulations, where the relative permittivity tensor $(\epsilon_x, \epsilon_y, \epsilon_z)$ for the homogeneous material is (2.75, 3.83, 2.75).

average value of 1.450 dB per bend over 220 to 260 GHz, and 0.250 dB per bend from 260 to 330 GHz. The measured results agree well with the simulations. The relatively higher bending loss for the E_{11}^y mode is primarily caused by the weaker wave confinement. It is observed that the bending loss decreases with frequency increasing for both modes, since the wavelength becomes shorter with improved wave confinement. Accordingly, to reduce the bending loss at lower frequencies, a greater wave confinement is required. To realise a sharper bending with low loss, one technique is to widen the bending core to achieve better confinement, while a slight lateral offset with respect to the straight sections is required to obtain a better mode matching so as to further reduce the bending loss (Kitoh *et al.*, 2002; Song *et al.*, 2016a).

3.3.6 Crossing

For terahertz integrated circuits, crossings allow a denser layout with low crosstalk. As shown in Fig. 3.17(a), a crossing is constructed from two orthogonal straight waveguides with different lengths. As illustrated in Fig. 3.17(b), to ensure the lattice integrity around the crossing, the adjacent holes along the horizontal arm are complete, while they are halved along the vertical arm. Such a configuration will not affect the transmission, since the fill factor remains unchanged resulting in the same effective relative permittivities. The simulated E -field distributions for wave propagating rightward at 275 GHz for the E_{11}^x and E_{11}^y modes are illustrated in Figs. 3.17(c)–(d), which demonstrate that

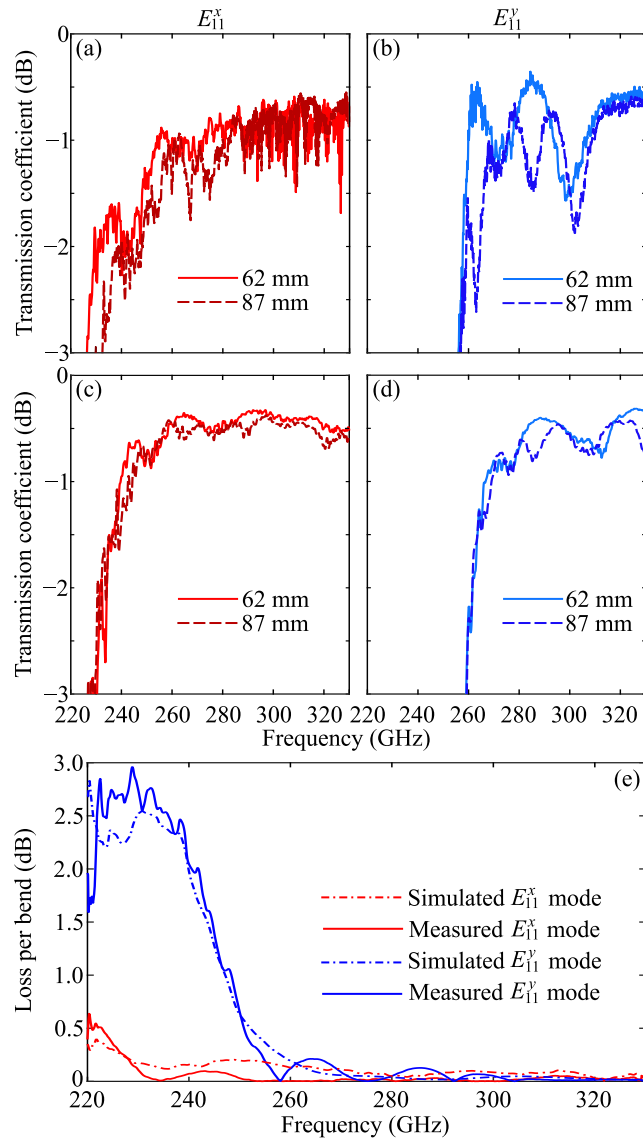


Figure 3.16. Transmission coefficients and bending loss of cascaded waveguide bends with two different total lengths of 62 mm and 87 mm. Measured transmission coefficients for (a) the E_{11}^x and (b) the E_{11}^y modes, and simulated transmission coefficients for (c) the E_{11}^x and (d) the E_{11}^y modes. (e) Measured and simulated bending loss per bend extracted from (a–d).

generally the waves are confined well within the transmitting channel. However, the field distributions of the E_{11}^x mode shown in Fig. 3.17(c) suggests higher cross-talk at the crossing due to the scattering effect.

Figures. 3.17(e–f) show a fabricated crossing with a magnified view around the center. The results are shown in Figs. 3.18(a)–(b). The transmission levels for both E_{11}^x and E_{11}^y modes are close to that of a straight waveguide with the same length across the whole band, while the crosstalk levels in terms of the $|S_{31}|$ for both modes are below

3.3.6 Crossing

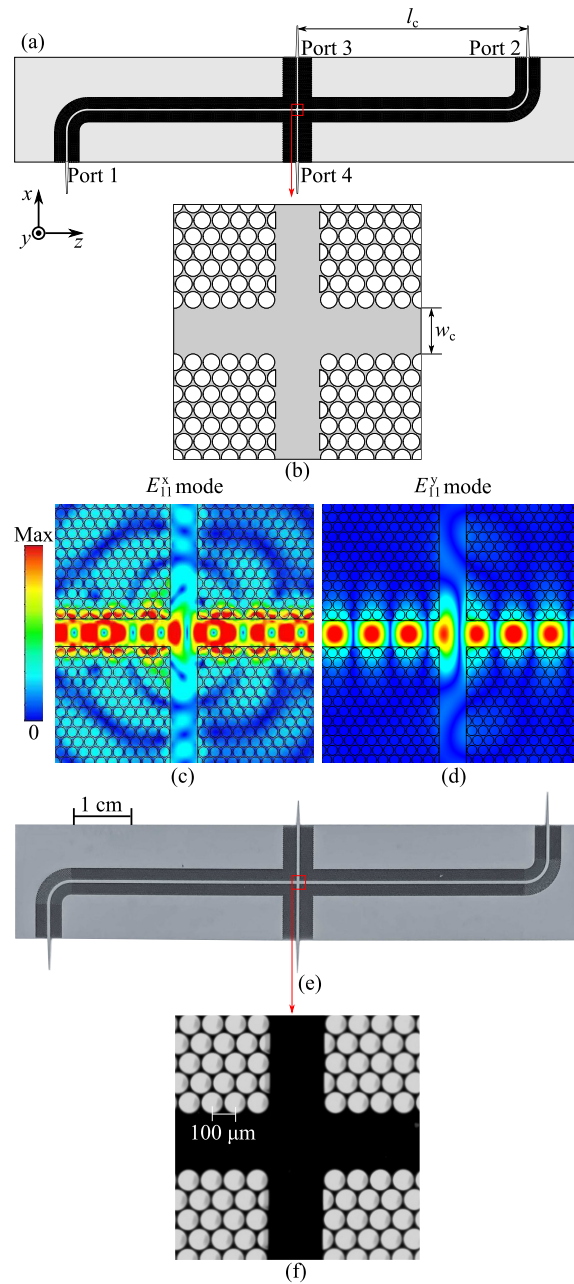


Figure 3.17. Waveguide crossing. (a) Model of the crossing. (b) Magnified view around the intersection, simulated E -field distributions for (c) E_{11}^x and (d) E_{11}^y modes at 275 GHz. (e) Fabricated crossing sample. (f) Microscope image of the fabricated waveguide crossing. The layout is to expedite the measurement by having pairs of ports pointing in the same direction. The relatively wide distance for Ports 1–4 and Ports 2–3 is to accommodate the flanges of the feeds. During the measurement, the unused ports are terminated by the tapers with good impedance matching to air.

–15 dB. All the measured results agree well with the simulations. As illustrated in Figs 3.18(a–b), the crosstalk level for the E_{11}^x mode is slightly higher than that of

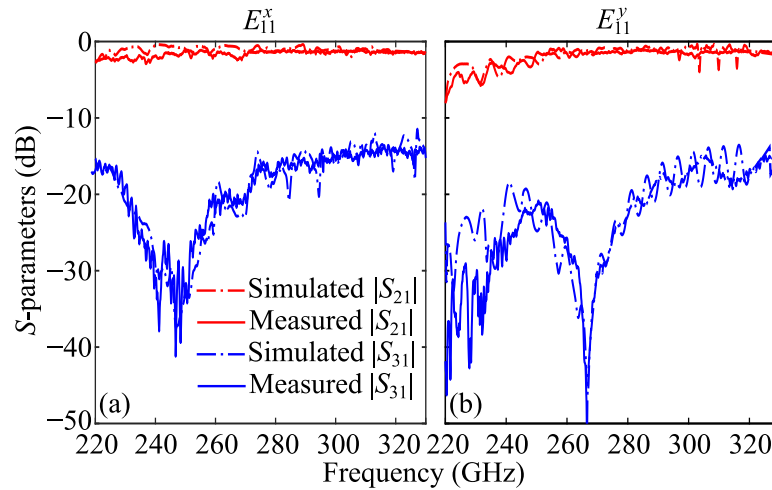


Figure 3.18. Simulated and measured S -parameters of the crossing. (a) E_{11}^x and (b) E_{11}^y modes. Since the structure is symmetric, $|S_{31}|$ and $|S_{41}|$ are identical.

the E_{11}^y mode. This is mainly attributed to the scattering effects associated with the relatively deeper in-plane field penetration of the E_{11}^x mode as shown in Figs. 3.17(c)–(d). According to Bogaerts *et al.* (2007), the scattering could be minimised by suppressing the E_x -field component through widening the waveguides at the intersection or varying the effective refractive index to flatten the wavefronts. Based on this principle, recently an improved crossing design based on the effective-medium-clad platform has been reported (Lees *et al.*, 2021b).

3.4 Conclusion

The characteristics of the effective-medium-clad dielectric waveguides including dispersion, cross-polarisation, crosstalk between parallel waveguides, bending loss, and wave leakage at crossing have been comprehensively investigated and measured over the frequency range of 220 to 330 GHz (WR-3.4 band). Benefiting from a low loss and low dispersion, the waveguides have an average measured attenuation coefficient about 0.075 dB/cm for the E_{11}^x mode over 220 to 330 GHz, while it is around 0.135 dB/cm over 260 to 330 GHz for the E_{11}^y mode. Within the same operation frequency ranges, a measured GVD of around ± 10 ps/(THz · mm) is obtained. A measured cross-coupling between the E_{11}^x and E_{11}^y modes is below -20 dB within measurement tolerance over the whole band. A minimum separation between two parallel straight waveguides is $0.52\lambda_0$ at 300 GHz. The experimental results show an average measured bending loss of around 0.250 dB per bend for the E_{11}^x mode and 1.450 dB per bend for the E_{11}^y mode

3.4 Conclusion

over 220 to 260 GHz, while from 260 to 330 GHz, an average measured bending loss is about 0.025 dB per bend for the E_{11}^x mode and 0.250 dB per bend for the E_{11}^y mode. A crosstalk level below -15 dB at the crossing is obtained for both E_{11}^x and E_{11}^y modes across the whole WR-3.4 band.

The proposed characteristics show the potential of the effective-medium-clad dielectric waveguides to establish terahertz integrated platforms with a high level of design flexibility. Specifically, to vary the refractive indices of the components, it is not necessary to introduce additional materials or multi-layered structures, which would cause additional dielectric loss and increase fabrication complexity considerably. Alternatively, an arbitrary refractive index can be defined by changing the configuration of the hole arrays along with the core dimensions to adapt to different guiding scenarios. The proposed waveguide platform is promising in various applications, since it is able to integrate various passive and active components in a similar way as the photonic crystal waveguide platform (Yu *et al.*, 2019c), however with much broader bandwidth. It can also be scaled to operation at higher terahertz frequencies without incurring higher losses. The concepts can benefit terahertz integrated circuits at large, in analogy to the SOI waveguides for integrated optics.

Effective-medium-clad Bragg grating filters

THIS chapter presents a series of integrated Bragg grating filters with performance enhancement via the concept of effective medium. The bandstop filters are built into a high-resistivity silicon wafer and operate over the WR-3.4 band (220–330 GHz) with in-plane polarisation. The proposed designs exploit an additional degree of freedom in controlling the effective refractive index so as to fully exploit the potentials of the Bragg grating structures. As a result, the high insertion loss typically observed at the low-frequency bound of the filters due to weak wave confinement can be reduced, while radiation caused by leaky-wave effect at the high-frequency bound is minimised, allowing for a 40% operation fractional bandwidth. These features are not achievable with conventional waveguide Bragg grating filters. All-silicon prototypes of filter samples are experimentally validated demonstrating promising performance for a wide range of terahertz applications. The demonstrated techniques to improve the filter characteristics by controlling the effective medium can be adopted in both microwave and optics domains.

4.1 Introduction

Terahertz integrated systems have attracted great attention for their compactness, portability, and low cost compared to the conventional quasi-optical systems, while promising a wide range of applications from imaging to communications (Sengupta *et al.*, 2018; Withayachumnankul *et al.*, 2018a). In particular, technologies from both electronics and photonics have accelerated the progress to form terahertz integrated circuits enabling comprehensive functionalities from signal generation, transmission, processing, to detection with moderately high efficiency (Sengupta *et al.*, 2018). To this end, effective-medium-clad dielectric waveguide platform with high efficiency, low dispersion, and broad bandwidth are proposed as discussed in Chapters 2 and 3. However, filters as one of the most essential components for terahertz integrated circuits are still not available on this platform. In line with practical needs of wideband terahertz systems, this chapter focuses on investigation of filters based on the effective-medium-clad waveguide platform (Gao *et al.*, 2020a).

To realise passive filters, one common approach is to periodically alternate high and low impedance segments or equivalently high and low modal indices along a guiding structure. This allows to effectively control the interference in transmitted and reflected waves thus generating the desired stopband or passband response over a particular frequency range (Pozar, 2011; Macleod, 2017). Accordingly, a number of terahertz filters based on microwave (Wang *et al.*, 2020; Chen *et al.*, 2013; Xing-Hai *et al.*, 2012) and optical (Withayachumnankul *et al.*, 2008; Li *et al.*, 2018; Akiki *et al.*, 2020) waveguiding structures have been proposed. However, microwave-technology-based filters suffer from high metallic loss at terahertz bands. An exception includes rectangular-waveguide-based filters (Chen *et al.*, 2013), which achieve relatively low loss due to low current density on metal. Nevertheless, the manufacturing complexity of metallic waveguide filters increases significantly with frequency, while their bulky form factor is not compatible to integrated systems. For optics-inspired terahertz structures, thin-film filters consisting of multi-layer dielectrics (Withayachumnankul *et al.*, 2008) are also not integratable despite their structural and design simplicity. Furthermore, although one dimensional photonic crystal cavities (Akiki *et al.*, 2020) have good integrability, the passband has significant fluctuations resulting from the strong refractive index contrast between air and silicon. In addition, the 3-dB bandwidth tends to be large due to the same reason thus limiting designability. Recently, a Bragg grating filter based on a polymer ribbon waveguide was proposed (Li *et al.*, 2018). This filter features structural

simplicity, but however, it lacks of a supporting structure for integration. Similar to the concept of Bragg grating structure, an optical bandstop filter realised by varying the parasitic elements along a waveguide core was reported (Tan *et al.*, 2009). However, its rejection performance was modest, while the passband response exhibited significant ripples.

In essence, all open dielectric-waveguide-based Bragg filters suffer limits in broadband operation, much needed for terahertz applications. The insertion loss rises with increasing frequency because of radiation resulting from the grating period close to one guided wavelength (Cheben *et al.*, 2018). Moreover, the transmission levels at lower frequencies tend to be reduced due to weak confinement of guided waves. These effects limit the filter operation bandwidth, which is generally not an issue for typical narrow-band operation at optical frequencies, e.g., with relative bandwidth of around 2.3% at C-band or 3.8% at L-band. In contrast, these effects become an issue at a terahertz band, which occupies a much larger fractional bandwidth, e.g., 40% for WR-3.4 band. Therefore, it is impractical to directly scale the existing optical waveguide Bragg grating filters down to the terahertz frequencies band.

This chapter presents a class of terahertz Bragg grating filters based on the effective-medium-clad waveguide (Gao *et al.*, 2020b, 2019). This waveguide platform allows the modal index to be modified by varying the waveguide core dimensions and/or the claddings configuration. Compared to conventional filters with physical corrugation of the waveguide core (Wang *et al.*, 2010, 2012, 2013), this technique offers an additional level of flexibility to control the filter characteristics, e.g., reducing insertion loss and allowing for broadband operation with a compact footprint. These features are very desirable in terahertz applications that typically leverage a vast available bandwidth with limited source power. This chapter is organized as follows: the design principles and considerations to select filter dimensions are given in Section 4.2, while the filter characteristics including transmission performance, bandwidth, central frequencies, and dispersion are presented in Section 4.3. The filter applicability at high terahertz frequencies is discussed in Section 4.4 followed by the conclusion in 4.5.

4.2 Design principles

4.2.1 Overview

As shown in Fig. 4.1(a), the proposed Bragg grating filter is built into a substrateless effective-medium-clad dielectric waveguide, which consists of a silicon waveguide core and in-plane effective medium claddings with lower relative permittivity, allowing for waveguiding through total internal reflection. The claddings are realised by periodically perforating the silicon slab with subwavelength spacing. Consequently, based on the Maxwell-Garnett effective medium theory, (Subashiev and Luryi, 2006) the effective relative permittivity tensor of the cladding material can be locally controlled by adjusting the ratio between air and silicon. The Bragg gratings are realised by corrugating the waveguide core laterally in a period of Λ , which is equal to half of a Bragg wavelength, i.e., the central operation wavelength of the Bragg grating filter. Importantly, the proposed Bragg grating filter has access to an additional degree of freedom by varying the cladding to modify the modal indices of the gratings. It will be shown through various designs that this additional control of the effective-medium claddings can yield benefits in terms of passband transmission levels, stop-band bandwidth, and device footprint.

4.2.2 Design considerations

To begin with, a simple uniform Bragg grating filter is implemented on the effective-medium-clad waveguide platform. We design the Bragg grating filter based on a single 250 μm thick high-resistivity silicon wafer with a relative permittivity of $\epsilon_{\text{Si}} = 11.68$ and resistivity of $>10 \text{ k}\Omega\cdot\text{cm}$. The filter is designed to operate in the E_{11}^x mode with in-plane polarisation, which is compatible with most of available terahertz devices. The full-wave simulations are performed with CST Microwave Studio 2019, where a realistic loss tangent of 3×10^{-5} is adopted for the silicon material. To save computational resources, as shown in Fig. 4.1(c), homogeneous cladding materials are adopted in simulations for initial investigations. It is noted that due to the approximations of the cladding relative permittivity used in the simulations, the calculated parameters (Λ , a , d) need to be slightly optimised for the final design.

A critical step is to properly select the waveguide width for each section and to control the relative permittivity tensor ($\epsilon_x, \epsilon_y, \epsilon_z$) of the effective medium claddings. This tensor is determined by the perforation period a and hole diameter d , and can be calculated

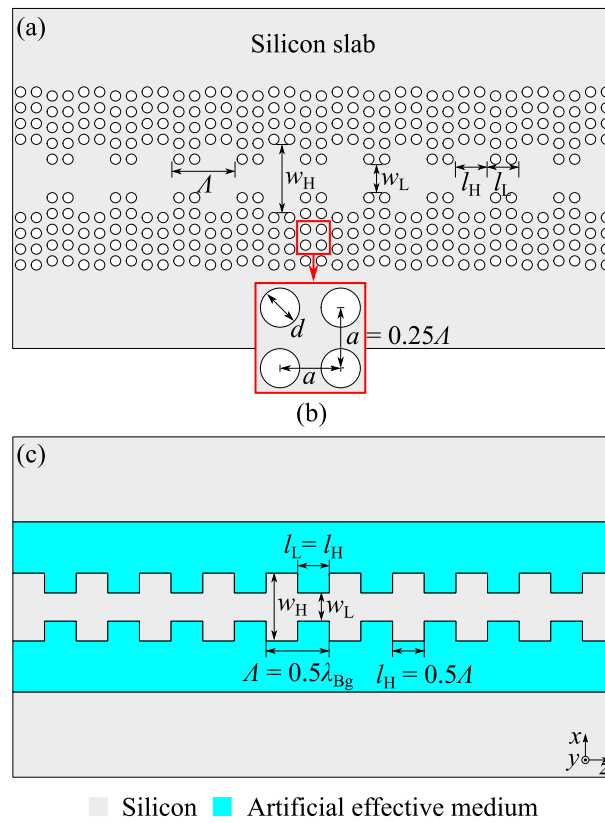


Figure 4.1. Effective-medium-clad Bragg grating filter. (a) Filter clad by air-silicon effective medium realised by perforating the silicon slab. (b) Magnified view of effective medium cladding in square lattice with a perforation period a and a hole diameter d . (c) Same filter with the cladding replaced by artificial anisotropic material. The artificial material is equivalent to the air-silicon effective medium with effective relative permittivity tensor $(\epsilon_x, \epsilon_y, \epsilon_z) = (6.642, 8.193, 6.642)$. The realised filter is based on a $250 \mu\text{m}$ thick high-resistivity intrinsic float-zone silicon wafer with a relative permittivity $\epsilon_{\text{Si}} = 11.68$. The unpatterned silicon slab is for handling purpose.

based on the Maxwell-Garnett effective medium theory (Subashiev and Luryi, 2006) as represented in Eqs. (2.1)–2.3. For a square lattice, the fill factor can be calculated from $(\pi d^2)/(4a^2)$. Since the filter operates in the E_{11}^x mode with in-plane polarisation, only ϵ_x is considered for the cladding relative permittivity to calculate the waveguide modal index. The average modal index $n_{\text{eff}} = (n_H + n_L)/2$ and the modal index difference $\Delta n = n_H - n_L$ are determined by ϵ_x and the waveguide widths, where n_H and n_L are the modal indices for the high- and low-index waveguide sections. Here, the modal indices can be calculated based on the Marcatili's approximations as indicated in Eqs. (3.1)–(3.3), while for precision they are obtained by CST port mode simulations in this work. Specifically, a larger ϵ_x , which can be achieved by a smaller d given a certain

4.2.2 Design considerations

subwavelength a , will lead to a higher n_{eff} thus a smaller grating period Λ (Gao *et al.*, 2020b; Chrostowski and Hochberg, 2015). Such a smaller Λ can avoid the radiation caused by the leaky-wave effect at higher frequencies, and thus promising a broadband operation of the device. However, a higher ϵ_x could reduce the modal index difference Δn leading to a smaller reflection depth and a narrower 3-dB bandwidth (Gao *et al.*, 2020b; Chrostowski and Hochberg, 2015). Additionally, a higher ϵ_x can lead to wave leakage into the slab. Therefore, the trade-offs for selecting the various parameters (w_H, w_L, a, d) must be considered in terms of operation bandwidth, device footprint, rejection level, 3-dB bandwidth, and wave confinement.

Considering the trade-offs mentioned above with a priority to minimise the radiation at the upper bound of this WR-3.4 band, a larger relative permittivity for the cladding is preferred. To accommodate the grating profile well, a square lattice is adopted for the filter design as shown in Fig. 4.1(b). Thus, the perforation period together with the hole diameter for the square lattice has to be selected according to the grating period. To satisfy the subwavelength perforation period condition (Gao *et al.*, 2019, 2020b; Subashiev and Luryi, 2006; Cheben *et al.*, 2018), the initial perforation period a for the square lattice is selected as $\Lambda/4$ or equivalently $\lambda_{\text{Bg}}/8$, where λ_{Bg} is the guided Bragg wavelength (Chrostowski and Hochberg, 2015). Given $l_H = l_L = \Lambda/2 = \lambda_{\text{Bg}}/4$, where l_H and l_L are the lengths for the high- and low-index sections, (Chrostowski and Hochberg, 2015) each waveguide section can hold two columns of holes along the z -direction. Given a certain ϵ_x and a , the hole diameter d can be calculated based on Eq. (2.1). Further reduction of a to obtain more holes per Bragg period would lead to too small holes, beyond the fabrication limit of around $20 \mu\text{m}$ based on the standard deep reactive ion-etching (DRIE) process (Gao *et al.*, 2020b). On the other hand, increasing a to $\lambda_{\text{Bg}}/4$, where only one column of holes would be accommodated by each waveguide section, a larger hole diameter d would be required to maintain the same air-in-silicon fill factor. However, the larger material discontinuities between air and silicon could cause wave scattering, while the device mechanical strength could be degraded.

To design a filter working at a Bragg frequency of 275 GHz with a 3-dB bandwidth around 16 GHz, we select the waveguide widths as $w_H = 240 \mu\text{m}$ and $w_L = 100 \mu\text{m}$. Given $(\epsilon_x, \epsilon_y, \epsilon_z) = (6.64, 8.19, 6.64)$, the corresponding modal indices of n_H and n_L for the E_{11}^x mode are obtained as 2.66 and 2.32, respectively based on port-mode simulations in CST. Correspondingly, the length for each waveguide section is calculated with approximations as $l_H = l_L = 111.5 \mu\text{m}$ together with the perforation period $a = 55.8 \mu\text{m}$

and hole diameter $d = 36 \mu\text{m}$. In this case, both waveguide sections have low insertion loss at lower frequencies (Gao *et al.*, 2020b), while based on the initial investigations, such a waveguide difference allows for a strong rejection band with a relatively short total grating length, e.g., 1 cm. The detailed criteria on the selection of waveguide difference can be found in Section 4.2.3 as below.

4.2.3 Impact of different waveguide width Δw

To investigate the impact of $\Delta w = w_{\text{H}} - w_{\text{L}}$ on the grating diffraction strength, several key parameters have been studied including the average modal index n_{eff} , modal index difference Δn together with the minimal transmission coefficient and 3-dB bandwidth as a function of Δw . Here, the high-index waveguide segment width w_{H} is fixed as $240 \mu\text{m}$, while the low-index waveguide segment width w_{L} is varied from $230 \mu\text{m}$ to $10 \mu\text{m}$ with a step width of $10 \mu\text{m}$. The investigations of n_{eff} and Δn are achieved through the port-mode simulations in CST, while the minimal transmission coefficients and 3-dB bandwidth are calculated by using the transfer matrix method (Chrostowski and Hochberg, 2015). It is noteworthy that given the design requirements, the combination of the two methods allows for a quick selection of starting values for the waveguide segment dimensions at the initial stage. As shown in Figs. 4.2(a)–(b), the average refractive index decreases with Δw increasing, while Δn increases with Δw increasing. In addition, given a fixed grating number N_{g} , as shown in Fig. 4.2(c), the minimum transmission coefficient decreases with Δw increasing showing an increased diffraction strength. Furthermore, a larger Δw can lead to a broader 3-dB bandwidth as shown in Fig. 4.2(d). It is noted that the jagged 3-dB bandwidth with a larger Δw and N_{g} is mainly due to the strong diffraction strength leading to the positions of the first nulls varied at the transition bands. Based on these studies, to achieve a uniform filter with a rejection level below -30 dB and 3-dB bandwidth of 16 GHz in Section 4.3.1, w_{L} is selected as $100 \mu\text{m}$ with a grating number $N_{\text{g}} = 40$.

4.3 Characteristics of filters

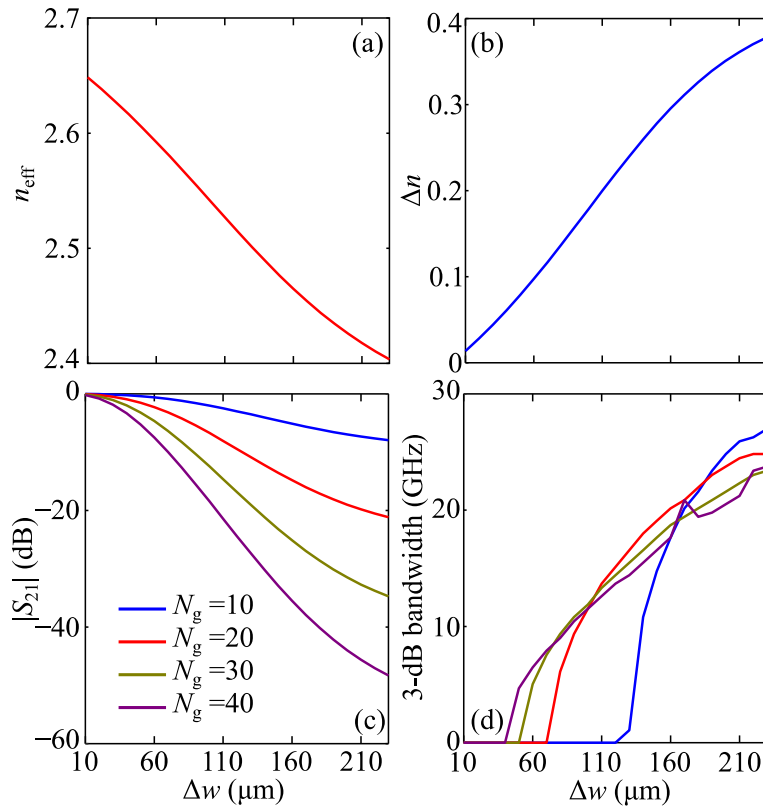


Figure 4.2. Characteristics of a uniform Bragg grating as a function of waveguide segment width difference. (a) Average modal index. (b) Modal index difference. (c) Minimal transmission coefficients. (d) 3-dB bandwidth. The high-index waveguide width is fixed as $240 \mu\text{m}$, while the effective relative permittivity for the effective medium cladding for the in-plane polarisation is selected as $\epsilon_x = 6.64$. (a) and (b) are simulated based on the port-mode simulations in CST, while (c) and (d) are calculated by using the transfer matrix method.

4.3 Characteristics of filters

In this section, various characteristics of the proposed filters are discussed including transmission, 3-dB bandwidth, central frequency, and dispersion. Furthermore, the impacts of fabrication tolerances on the filter performance are studied. A lateral multi-layer cladding is introduced for the first time to reduce the transmission fluctuation, while apodisation is employed to mitigate the band transition ripples. The fabrication for various filters is based on the standard deep reactive-ion etching (DRIE) process, while several illustrative designs are experimentally validated.

4.3.1 Transmission performance

Uniform waveguide Bragg grating

Based on the descriptions in Section 4.2, a uniform waveguide grating filter is realised as shown in Fig. 4.3. The filter consists of four major elements including a tapered coupling structure, a regular waveguide, a transition waveguide, and a Bragg grating with a grating number of $N_g = 40$. The 3-mm coupling tapers are introduced for excitation purpose, i.e., they are inserted into the WR-3.4 rectangular hollow waveguides in both simulations and measurements, so that the waves can be gradually coupled from the feed to the device. As shown in Figs. 4.3(b–c), a regular waveguide with a cladding effective relative permittivity of 2.75 is employed, because it has a tight wave confinement thus a better mode matching to the hollow waveguide than that of the waveguide cladded by the higher-index claddings. Thus, it can enhance the coupling between the filter and the feed. Additionally, the regular waveguides allow consistent interconnection between the filter and other components on the same platform.

To provide a good impedance matching between the regular waveguide section and the grating, a transition waveguide is adopted as illustrated in Figs. 4.3(d–e). Specifically, the hole diameter in the transition cladding decreases gradually leading to increasing modal index towards the grating. As shown in Fig. 4.3(f), the Bragg gratings are implemented with $w_H = 240 \mu\text{m}$ and $w_L = 100 \mu\text{m}$, while the optimised grating period Λ is $223 \mu\text{m}$. Correspondingly, the cladding configuration is $(a, d) = (55.8 \mu\text{m}, 36 \mu\text{m})$. Given $N_g = 40$, the total grating length is 8.92 mm. The claddings extend to 12 rows on both sides of the waveguide to accommodate the evanescent fields.

The fabricated sample is shown in Fig. 4.4. It is observed that the adjacent holes are slightly connected in the first two columns for the transition claddings due to the fabrication tolerance. Owing to the concept of effective medium, this imperfection has negligible impact on the effective relative permittivity. The measurements are accomplished with the arrangement shown in Fig. 4.5 by using a Keysight vector network analyser with VDI WR-3.4 extension modules spanning from 220 to 330 GHz. The measured and simulated S -parameters are shown in Figs. 4.6(a–b) with good agreements. However, it is observed that the Bragg frequency is shifted to 280 GHz from the designed frequency of 275 GHz, while the 3-dB bandwidth is slightly broadened by around 1 GHz. We found that such a 5-GHz blue shift and the increasing 3-dB bandwidth happen to all the samples presented in this chapter, and they are mainly

4.3.1 Transmission performance

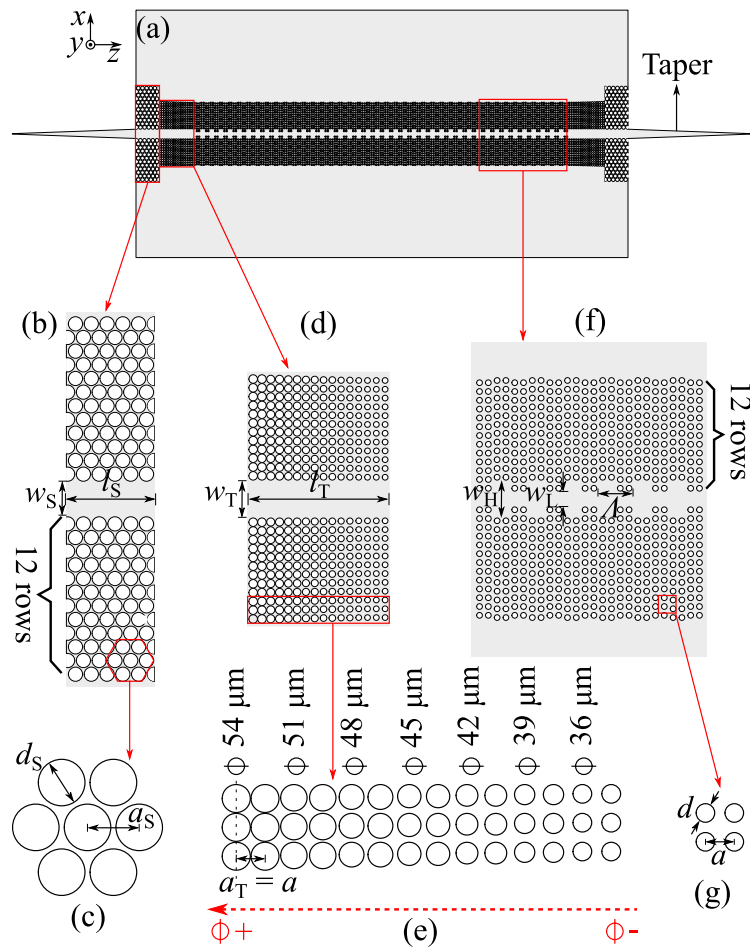


Figure 4.3. Uniform effective-medium-clad waveguide Bragg grating filter. (a) Top view. (b) Regular effective-medium-clad waveguide with core width $w_S = 225 \mu\text{m}$ and length $l_S = 500 \mu\text{m}$. (c) Hexagonal lattice of the effective medium cladding for the regular waveguide with lattice period $a_S = 100 \mu\text{m}$ and hole diameter $d_S = 90 \mu\text{m}$. (d) Transition waveguide between the regular feeding waveguide and the Bragg grating with core width of $w_T = 240 \mu\text{m}$ and length of $l_T = 781 \mu\text{m}$. (e) Effective medium cladding of the transition waveguide in square lattice. (f) Uniform waveguide Bragg grating with higher-index waveguide core width $w_H = 240 \mu\text{m}$, lower-index core width $w_L = 100 \mu\text{m}$, and grating period $\Lambda = 223 \mu\text{m}$. (g) Square lattice of the effective medium cladding for the Bragg grating with lattice period $a = 55.8 \mu\text{m}$ and hole diameter $d = 36 \mu\text{m}$. The tapered structures that are inserted into the WR-3.4 hollow waveguides in both simulations and measurements allow efficient coupling from the feed to the sample. The unpatterned silicon slab is for handling purpose. Slight systematic amendments of the dimensions are necessary to account for fabrication tolerances in the final results, as elaborated in Section 4.3.5.

caused by an observed reduced wafer thickness from $250 \mu\text{m}$ and slightly over-etched holes. These causes are confirmed in Section 4.3.5, where the relevant dimensions are

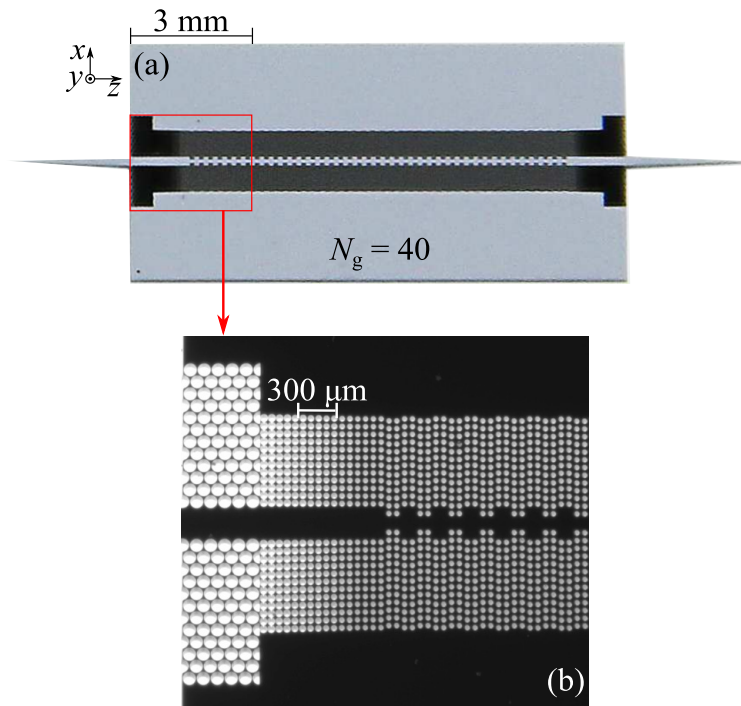


Figure 4.4. Fabricated uniform effective-medium-clad Bragg grating filter. (a) Filter sample. (b) Microscope image revealing a regular waveguide, transition waveguide, and Bragg grating.

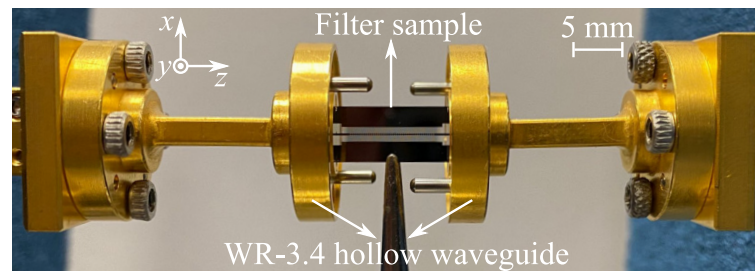


Figure 4.5. Measurement setup. The tapered structures are inserted into the WR-3.4 hollow waveguides for excitation, while the sample is fixed by a holder at the unpatterned silicon slab. The WR-3.4 waveguide operates in the TE_{10} mode, so that the E_{11}^x mode with polarisation in the x -direction is excited for the filter sample. The measurements are conducted by using a Keysight vector network analyser with VDI WR-3.4 extension modules spanning 220–330 GHz.

modified in simulation to compensate these systematic errors caused by the fabrication tolerances. It is noted that all the simulated results for various designs presented in this chapter have been systematically corrected accordingly, and the compensated dimensions can be found in the Section 4.3.5. From Fig. 4.6(a), a 3-dB bandwidth around 18 GHz is achieved with a stop-band rejection below -21 dB. There exists significant fluctuation in the pass bands especially at the lower frequencies and near the

4.3.1 Transmission performance

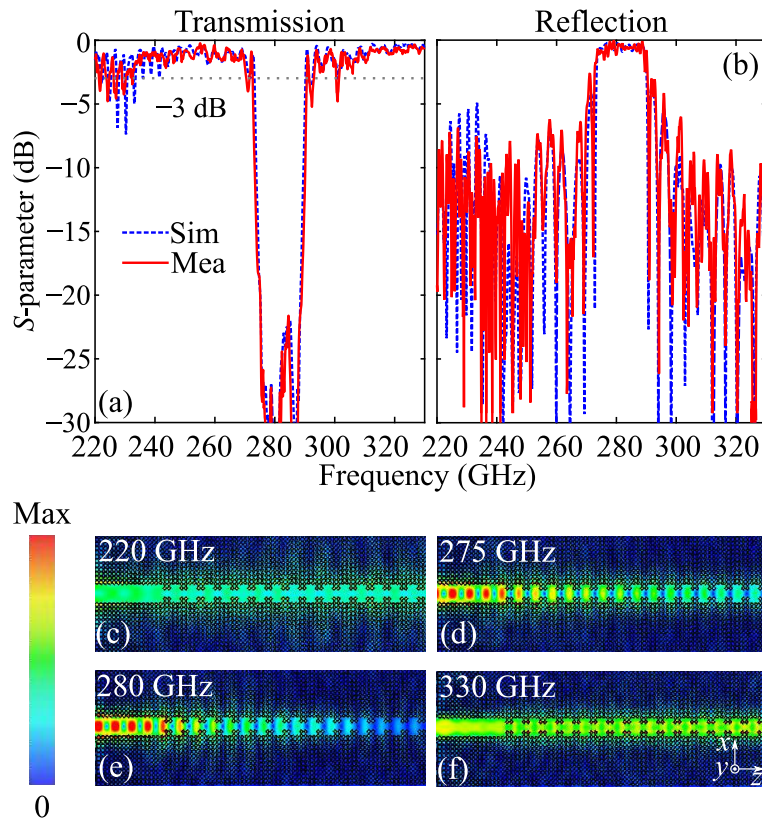


Figure 4.6. Simulated and measured S -parameters and simulated E -field amplitude distributions of the uniform waveguide Bragg grating filter. (a) Transmission. (b) Reflection. E -field distributions at (c) 220 GHz, (d) 275 GHz, (e) 280 GHz, and (c) 330 GHz. All the E -field distributions are normalised by the same factor.

transition shoulders. The fluctuation at the low frequency is mainly due to the weak wave confinement, as shown in Fig. 4.6(c), resulting in a large field penetration depth into the claddings. Correspondingly, the field is disturbed by the nearby unetched silicon slab. On the other hand, the ripples at the transitions are mainly because of the strong reflection among the gratings. These issues are resolved in the following two sections.

Cladding effects

The effects of the claddings on the passband transmission are investigated for the three gratings, which are cladded by air (Headland *et al.*, 2020b), by wider uniform effective medium claddings, and by two-layer mixed effective medium claddings, as shown in Figs. 4.7(a)–(c). For the air-clad filter, to maintain a comparable 3-dB bandwidth and

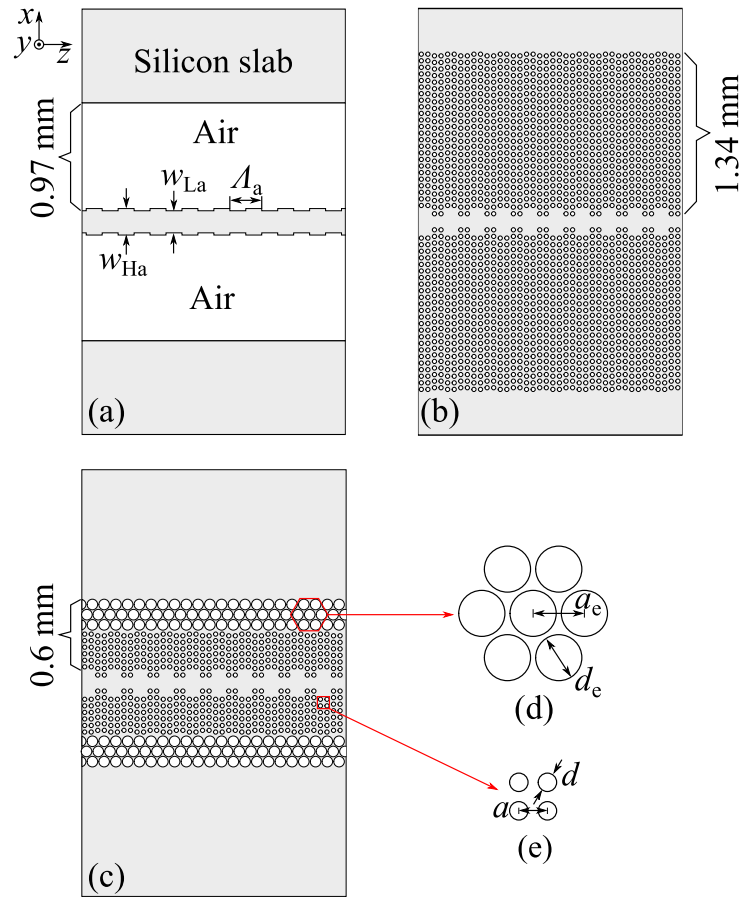


Figure 4.7. Schematics of Bragg grating filters with various claddings. (a) Air-clad filter with high-index waveguide width $w_{Ha} = 240 \mu\text{m}$, low-index waveguide width $w_{La} = 200 \mu\text{m}$ and grating period $\Lambda_a = 288 \mu\text{m}$. (b) Uniform effective-medium-clad filter with cladding width of 1.34 mm containing 12 rows of holes. (c) Two-layer mixed cladding filter with cladding width of 0.6 mm. (d) Hexagonal lattice of the outer cladding with lattice period $a_e = 100 \mu\text{m}$ and $d_e = 90 \mu\text{m}$. (e) Square lattice of the inner cladding with lattice period $a = 55.8 \mu\text{m}$ and $d = 36 \mu\text{m}$. The hole configuration of (b) is identical to that in Fig 4.3(f).

grating coupling strength, the waveguide widths are selected as $w_{Ha} = 240 \mu\text{m}$ and $w_{La} = 200 \mu\text{m}$ resulting in a modal index difference of 0.47 at 275 GHz and grating period Λ of $288 \mu\text{m}$. With a longer Λ , the grating number N_g is reduced to 20 to achieve a comparable rejection depth and roll-off rate. This air-clad Bragg grating filter is fed by a straight regular waveguide as shown in Fig. 4.8(a). Figure. 4.7(b) illustrates a uniform waveguide filter with wider cladding containing 24 rows of holes, while the other parameters are the same as in Fig. 4.3. For further investigation, the wide uniform cladding is replaced with a two-layer mixed cladding as shown in Figs. 4.7(c)–(e), where the outer layer with lower index is formed in a hexagonal lattice with

4.3.1 Transmission performance

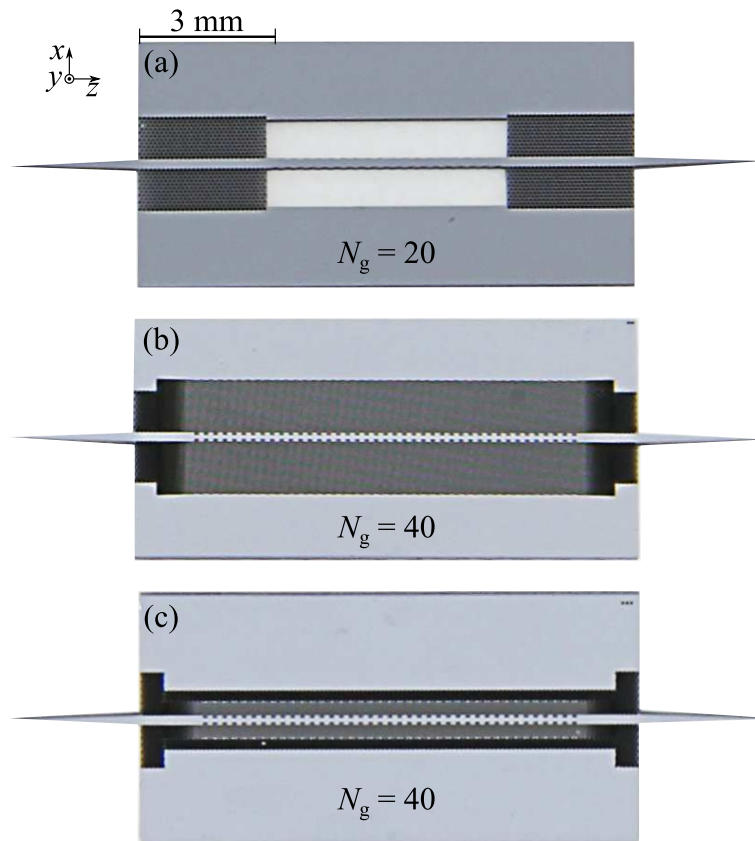


Figure 4.8. Fabricated waveguide Bragg gratings with various claddings. (a) Air-clad filter sample. (b) Wide uniform effective-medium-clad filter sample. (c) Mixed effective-medium-clad filter sample. All subfigures share the same scale.

$a_e = 100 \mu\text{m}$ and $d_e = 90 \mu\text{m}$, while the inner layer with a higher index is built in a square lattice with $a = 55.8 \mu\text{m}$ and $d = 36 \mu\text{m}$. Two types of cladding lattices adopted in this work account for structural completeness, mechanical strength, and fabrication tolerance. For the inner cladding, a square lattice is introduced to accommodate the square grating profile as discussed in the design considerations. For the outer cladding, a hexagonal lattice with a larger lattice period is adopted mainly because of the mechanical strength and fabrication tolerance. Specifically, the outer cladding has a much lower permittivity requiring larger air holes given a constant lattice period, which could lead to weakened mechanical strength. In this case, a hexagonal lattice is preferred to enhance the mechanical strength. Additionally, with an identical fill factor of air volume in silicon, a larger lattice period can result in a larger spacing between the edges of the adjacent holes so as to avoid hole merging due to the over-etching in fabrication. The fabricated samples of the three filters are shown in Fig. 4.8.

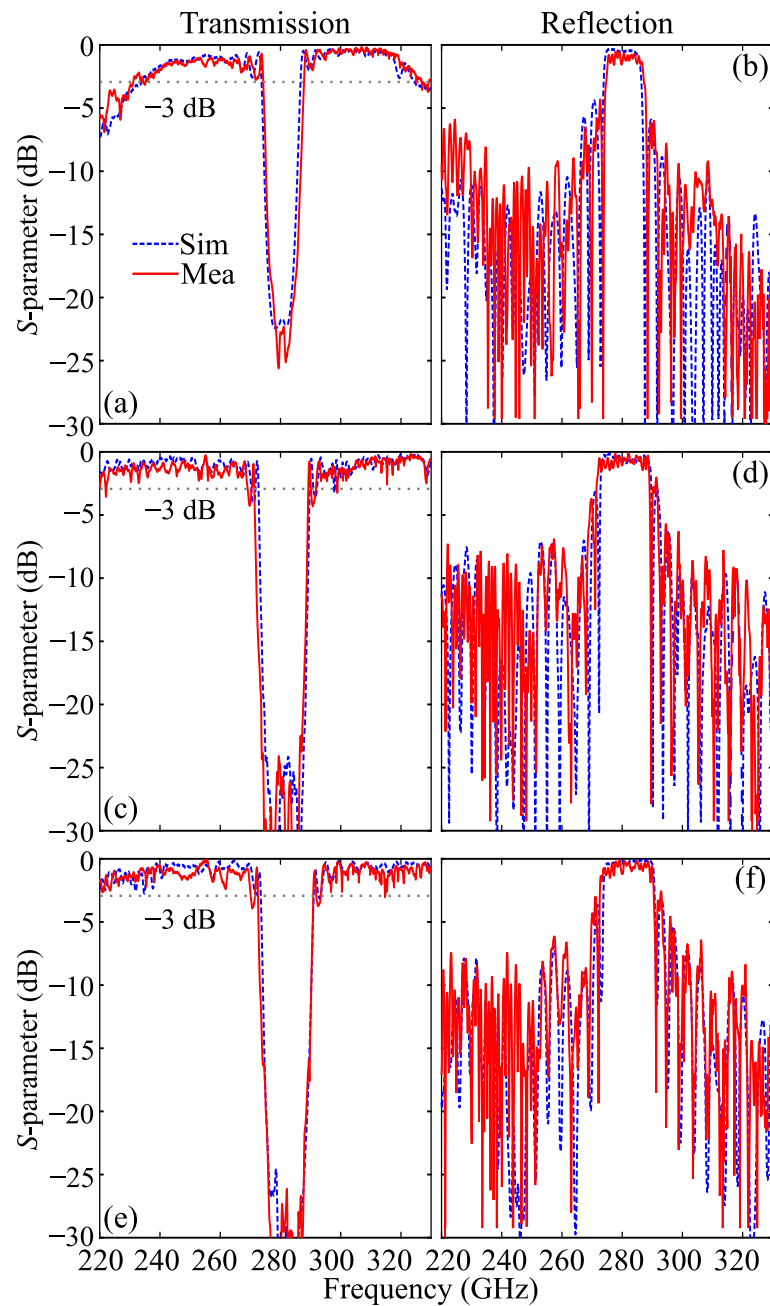


Figure 4.9. Simulated and measured S -parameters of the filters with different claddings. (a,b) for the air-clad filter. (c,d) for wide uniform cladding filter. (e,f) for two-layer mixed claddings filter.

The simulated and measured S -parameters of the air-clad filter are shown in Figs. 4.9(a)–(b). Obviously, the passband fluctuation is reduced significantly due to a stronger wave confinement resulting from a larger refractive index contrast between the air cladding and the silicon waveguide. Thus, there is negligible interference with nearby unetched silicon slab. Additionally, the transition level is improved to above -3 dB due to the smaller grating number resulting in weaker reflection. However, the transmission

4.3.1 Transmission performance

level at lower frequencies is decreased below -3 dB, which is caused by the impedance mismatch between the feeding and the grating waveguide with a modal index difference around 0.5 from 220 to 235 GHz. Meanwhile, a relatively stronger loss is also observed at higher frequencies. This is because the grating period is larger than the guided wavelength leading to radiation akin to a leaky wave antenna (Headland *et al.*, 2018a). In general, these effects are common for the conventional Bragg grating filters cladded by air or silicon dioxide, and they result in a reduced operation bandwidth. In the next case, as indicated in Figs. 4.9(c)–(d), a wider effective medium cladding that is able to accommodate extended evanescent fields can also alleviate the passband fluctuation. However, expanding the cladding reduces the structural compactness considerably. In contrast, as illustrated in Figs. 4.9(e)–(f), the two-layer mixed claddings can achieve a comparable transmission level but with only half the cladding width. Here, the outer layer confines the evanescent fields mainly within the two-layer claddings due to their relatively large refractive index contrast. In this case, the disturbance from the silicon slab is reduced resulting in a smoother transmission level. However, the transition shoulders are still lower than -3 dB with such configuration, and this issue is addressed in the next section on apodisation.

Apodised waveguide Bragg grating

To reduce the fluctuation around the transitions, an apodisation technique is employed to gradually increase the grating coupling coefficient (Murphy, 2001; Wang, 2013; Othonos *et al.*, 2006). Based on the coupled-mode theory, the coupling coefficient κ representing the amount of reflection per unit length is defined as (Chrostowski and Hochberg, 2015)

$$\kappa = \frac{2\Delta n}{\lambda_{B0}}, \quad (4.1)$$

where Δn is the grating modal index difference and λ_{B0} is the Bragg wavelength in free space. This apodisation technique has been widely used in designing optical fiber and waveguide grating structures, (Murphy, 2001; Wang, 2013; Othonos *et al.*, 2006) and there is a number of window functions with various roll-off rates available to taper the coupling strength such as linear ramp, raised-cosine, Hamming, or Gaussian functions. However, the trade-offs in terms of the transition level, filter roll-off rate, and device footprint have to be considered. A window function with a smaller roll-off rate can generate a smoother transition. However, it requires a large number of periods thus

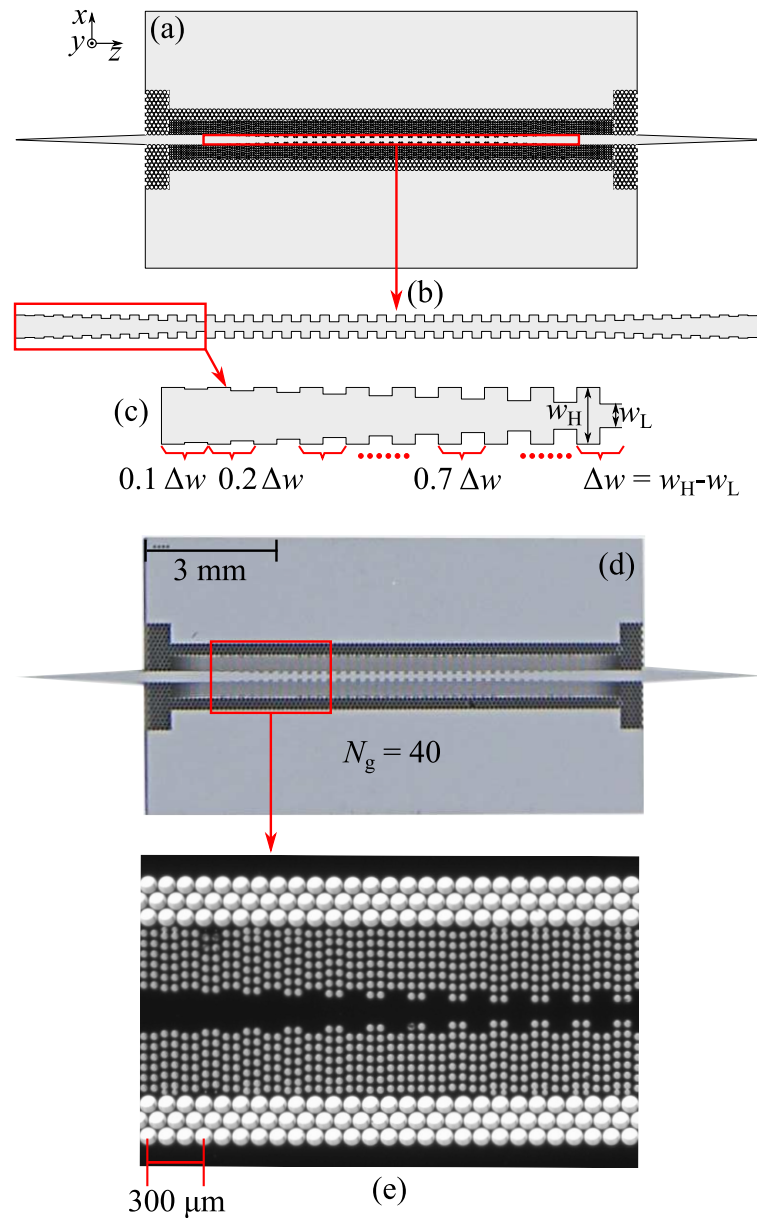


Figure 4.10. Bragg grating filter with apodisation. (a) apodised filter cladded by two-layer mixed effective medium cladding. (b) Bragg grating. (c) Apodised part. (d) Fabricated filter with apodisation. (e) Microscope image around the grating with apodisation.

a longer footprint to achieve a comparable stop-band level as its counterpart without apodisation.

Considering the trade-offs discussed above, in this work, a linear ramp function is used to taper the coupling strength. The realised filter with apodisation is shown in Figs. 4.10(a)–(c). The key parameters are kept the same as in the two-layer-cladding design in Fig. 4.7(c), while the grating in the first ten periods is apodised symmetrically. As depicted in Fig. 4.10(c), the waveguide width difference is gradually increased from

4.3.2 Bandwidth

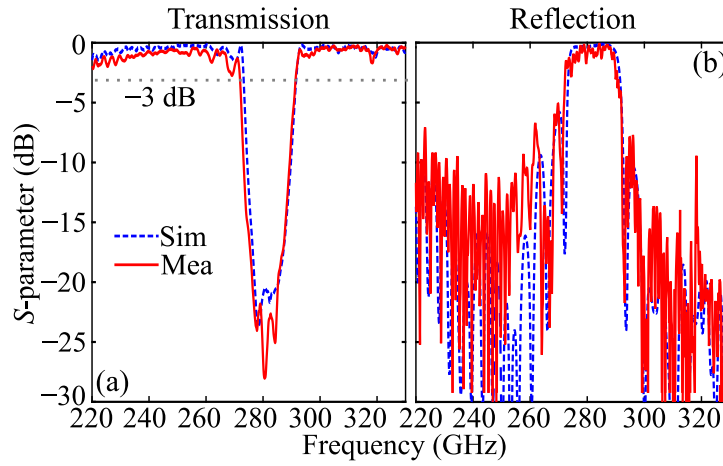


Figure 4.11. Simulated and measured S -parameters of the filter with apodisation and two-layer mixed cladding. (a) Transmission and (b) reflection.

$0.1\Delta w$ to Δw in a step of $0.1\Delta w$, where $\Delta w = w_H - w_L$. Therefore, the modal index difference Δn is gradually increased correspondingly. Thus, the coupling coefficient κ is tapered physically so as to achieve a moderately strong reflection at the transition band. The fabricated sample and a magnified view containing various critical features are shown in Figs. 4.10(d–e).

As shown in Fig. 4.11(a–b), when applying the apodisation, the filter can achieve the fluctuation near the transitions of around -2 dB, while the stopband level is reduced compared to the one without apodisation shown in Fig. 4.9(e). These results matches the expectations. Additionally, assisted by the mixed claddings, the filter achieves smooth passband transmission levels together with a 3-dB bandwidth of 18.5 GHz. The roll-off rate calculated between -3 dB and -20 dB is 4.42 dB/GHz resulting in a good frequency selectivity. Indeed, the transition level can be further enhanced by using a deeper apodisation function, e.g., cosine function, but at the expense of stopband level or structural compactness.

4.3.2 Bandwidth

To vary the 3-dB bandwidth, the grating modulation can be modified (Chrostowski and Hochberg, 2015). According to the bandwidth equation (Chrostowski and Hochberg, 2015)

$$\Delta\lambda = \frac{\lambda_{B0}^2 \kappa}{\pi n_g}, \quad (4.2)$$

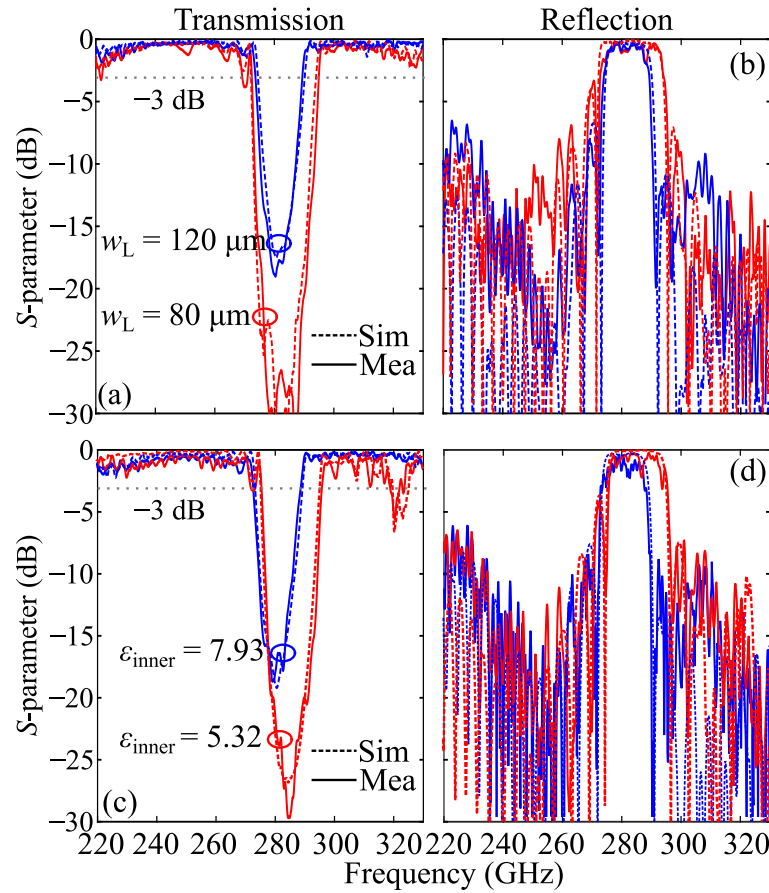


Figure 4.12. Simulated and measured S -parameters of the filters clad by mixed effective medium claddings with various bandwidths achieved by different strategies. (a) Transmission and (b) reflection for the filters with different widths of the lower-index waveguide section, while the higher-index waveguide width is maintained as $240 \mu\text{m}$. (c) Transmission and (d) reflection for the filters, where the inner cladding relative permittivity is varied, while the outer cladding has a constant relative permittivity of 2.75. For fair comparisons, all the gratings are linearly apodised and cladded by a two-layer mixed effective medium claddings with a grating number of $N_g = 40$.

where n_g is the group index, the filter bandwidth is mainly determined by the coupling coefficient κ that is proportional to the modal index difference Δn as expressed in Eq. 4.1. Accordingly, given a fixed w_H , a narrower and a broader bandwidth are obtained by increasing or decreasing w_L , respectively. As shown in Figs. 4.12(a)–(b), the filter with a broader bandwidth has a stronger stop band, while the transition level is steeper. These phenomena originate from a smaller average modal index n_{eff} that can lead to a larger grating period thus a longer total length L given an constant grating number (Chrostowski and Hochberg, 2015).

4.3.3 Central frequency

Alternatively, the 3-dB bandwidth also can be adjusted by varying the cladding relative permittivity, while maintaining the grating configuration. For the second strategy, we select $w_H = 240 \mu\text{m}$ and $w_L = 100 \mu\text{m}$ for both filters, while the effective relative permittivity of the inner cladding ϵ_{inner} is either 7.93 or 5.32. Here, the relative permittivity of the outer cladding is maintained as 2.75. The measured and simulated S -parameters as shown in Figs. 4.12(c)–(d) illustrate that the filter with a lower-index inner cladding achieves a broader bandwidth and stronger rejection depth. This is because a lower-index cladding can reduce the average waveguide modal index n_{eff} , while enhancing the modal index contrast Δn leading to a larger κ thus a broader bandwidth from Eqs. 4.1 and 4.2. However, a sudden drop of the S_{21} appears at around 320 GHz, which is mainly due to the mode radiation caused by the longer grating period. This could be remedied by optimizing the waveguide widths together with the cladding configuration.

4.3.3 Central frequency

To demonstrate that the proposed filter type is tailorable to operate across the whole WR-3.4 band, filter performances with Bragg frequencies shifted to 310 GHz and 250 GHz are presented. These filters are in the form of apodised grating cladded by the two-layer mixed claddings with a relative permittivity of 2.75 and 6.64 for the outer and inner claddings. To achieve comparable 3-dB bandwidth and rejection, the higher-index waveguide width w_H is maintained constant as $240 \mu\text{m}$, while the lower-index waveguide width w_L is set as $110 \mu\text{m}$ and $90 \mu\text{m}$ for the higher and lower Bragg frequencies, respectively. Accordingly, the grating periods are calculated as $192 \mu\text{m}$ and $264 \mu\text{m}$ for the higher and lower frequencies, respectively, while the grating number is kept as 40 for both designs. The simulated and measured S -parameters are shown in Figs 4.13(a)–(d). Attributed to its relatively small grating coupling strength, the filter operating at the higher frequency can achieve a smooth passband transmission level and a rejection depth below -17 dB. However, for the lower-frequency one, the transition level at the left shoulder is reduced below -3 dB due to the stronger coupling strength. It is noteworthy that the transmission level decreases with frequency increasing. This is mainly caused by the radiation loss due to the wavelengths becoming shorter than the grating period, thus leading to a leaky mode. This issue is typically not encountered in optical filters due to a much narrower bandwidth.

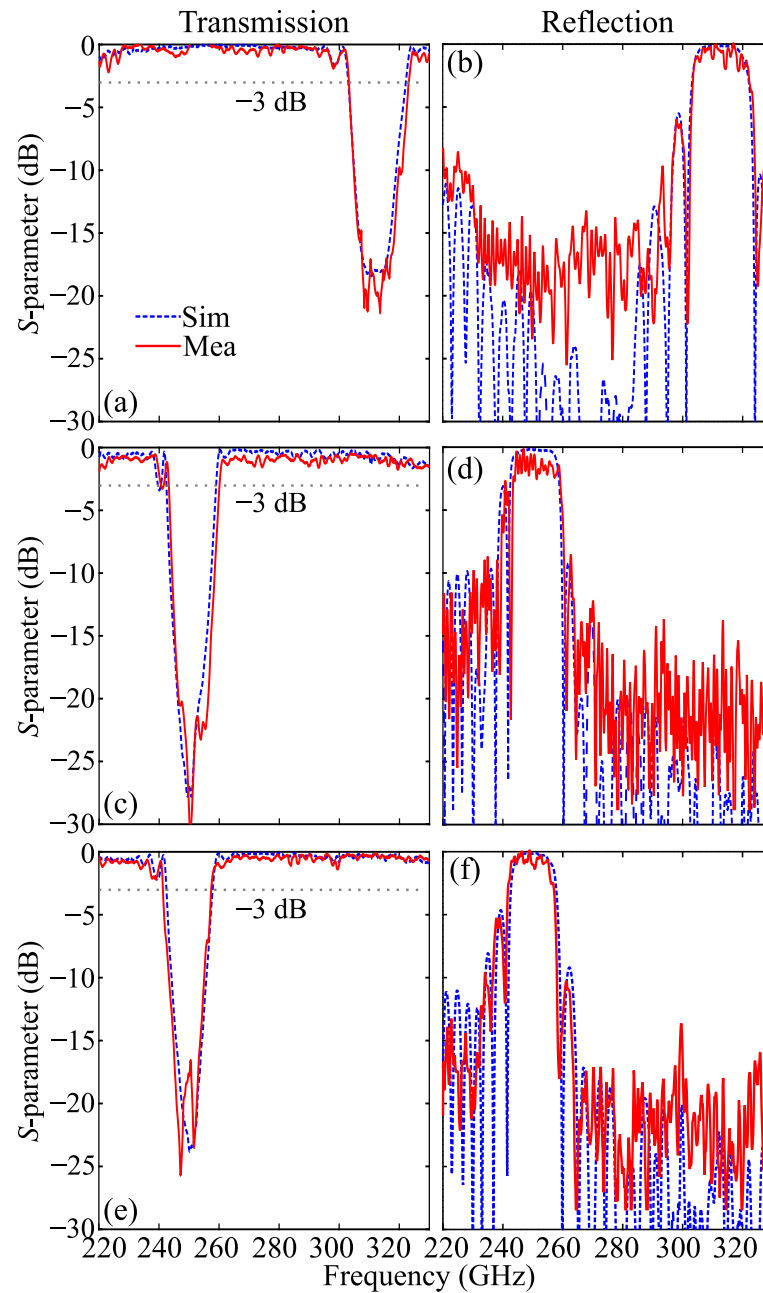


Figure 4.13. Simulated and measured S -parameters of the filters cladded by mixed claddings with various Bragg frequencies. (a) Transmission and (b) reflection of the filter working at 310 GHz. (c) Transmission and (d) reflection of the filter working at 250 GHz with an inner cladding relative permittivity of 6.64. (e) Transmission and (f) reflection of the filter working at 250 GHz with an inner cladding relative permittivity of 7.93.

To minimise the radiation, a smaller grating period is required together with wavelength shortening so to maintain the centre frequency. Accordingly, we implement a higher-index inner cladding with a relative permittivity of 7.93 and a reduced w_L of 80 μm to

4.3.4 Dispersion

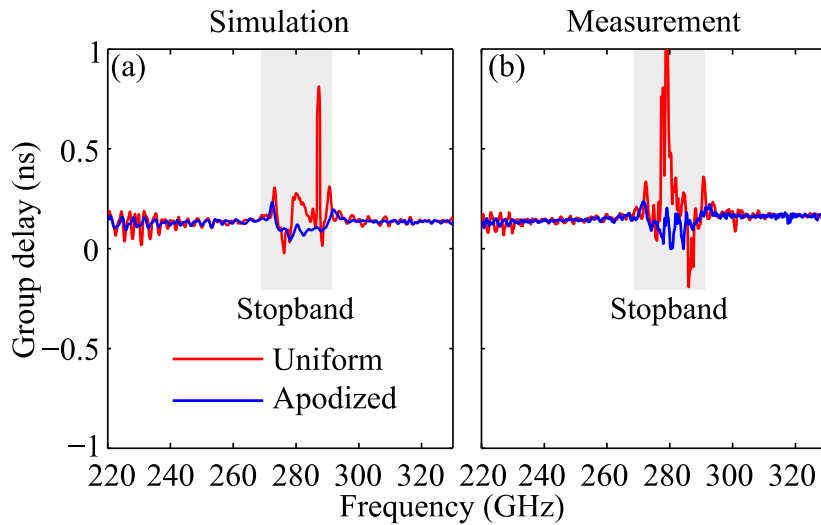


Figure 4.14. Simulated and measured group delay of the uniform filter shown in Fig. 4.3 and the apodised filter with mixed claddings shown in Fig. 4.10. (a) Simulation. (b) Measurement. The group delays in both simulations and measurements are derived from the unwrapped phase, where the phase contributions introduced by the hollow waveguides and straight waveguide sections are de-embedded by comparing the phase differences of the straight effective-medium-clad waveguides with multiple lengths. To mitigate the amplifying effects of the derivative operation on the phase noise, a smoothing function has been employed to process the measured data with a sliding window covering 1 GHz.

maintain a comparable 3-dB bandwidth. As a result, the grating period is reduced to $250 \mu\text{m}$, as opposed to $264 \mu\text{m}$. According to Figs. 4.13(e)–(f), the transmission levels at higher frequencies are improved with a transition level well above -3 dB . These results further show that the proposed filter type can operate in a 40% fractional bandwidth that is much larger than any practical optical band.

4.3.4 Dispersion

To investigate the dispersion characteristics of the proposed Bragg grating filters, simulations and measurements have been performed on the group delay for a uniform filter and an apodised filter with mixed claddings. As shown in Fig. 4.14, the measurements agree well with the simulations, where both filters show a small fluctuation in the group delay across the passband. The measured group delay for the apodised filter varies from 0.12 to 0.17 ns across the entire passband demonstrating an extremely low dispersion. For the uniform filter, the group delay is relatively higher with fluctuations at the

lower passband. This is mainly caused by the external disturbance, i.e., the interference with nearby unetched silicon slab. The results further show that the mixed claddings together with the apodisation can reduce the filter dispersion. In general, the proposed Bragg grating filters inherit the low dispersion of the effective-medium-clad waveguides allowing for broadband operation. This is crucial to terahertz communications with high-speed data transmission.

4.3.5 Fabrication tolerance and resultant effects

Informed by the manufacturers, the fabrication tolerance for the silicon wafer thickness is $\pm 10 \mu\text{m}$, while it is around $\pm 3 \mu\text{m}$ for the diameter of holes created using the standard deep reactive ion-etching process. To investigate the impact of the fabrication tolerance on the filter performance, simulations have been performed on the 3-dB bandwidth change and central frequency shift for a uniform filter as a function of wafer thickness and hole diameter. As shown in Fig. 4.15(a), given a certain hole diameter, the 3-dB bandwidth almost does not vary with the change of wafer thickness. However, the bandwidth increases with hole diameter increasing. On the other hand, the central frequency shift is determined by the combination of both factors as shown in Fig. 4.15(b). Specifically, given a fixed thickness, the central frequency shifts to a higher frequency with hole diameter increasing. Additionally, given a certain hole diameter, a reduced thickness can lead to a blue shift in the stop band.

In the measurements, it is found that the central frequencies for all the samples exhibit a blue shift of approximately 5 GHz compared to the design frequencies, while the 3-dB bandwidth is slightly broadened, e.g., by around 1 GHz. One example can be seen in Fig. 4.16. Based on the analysis on fabrication tolerance discussed above, it is believed that these discrepancies originate from material and device fabrication tolerances. It is known that the Bragg (central) wavelength λ_{B0} can be determined as $\lambda_{B0} = 2n_{\text{eff}}\Lambda$, where n_{eff} is the average modal index of the grating, while Λ is the grating period (Chrostowski and Hochberg, 2015). As such, the blue shift could be caused by a reduction in both n_{eff} and Λ with different weights. In this case, it is possible to get a smaller n_{eff} with a thinner wafer. The measured wafer thickness is around $245 \mu\text{m}$, which is within the fabrication tolerance $250 \pm 10 \mu\text{m}$. Furthermore, the deep reactive ion-etching (DRIE) process could result in over-etching, specifically with a large aspect ratio, which is around 10:1 in this work. This over-etching results in a lower cladding relative permittivity and a narrower waveguide core width thus a lower n_{eff} .

4.3.5 Fabrication tolerance and resultant effects

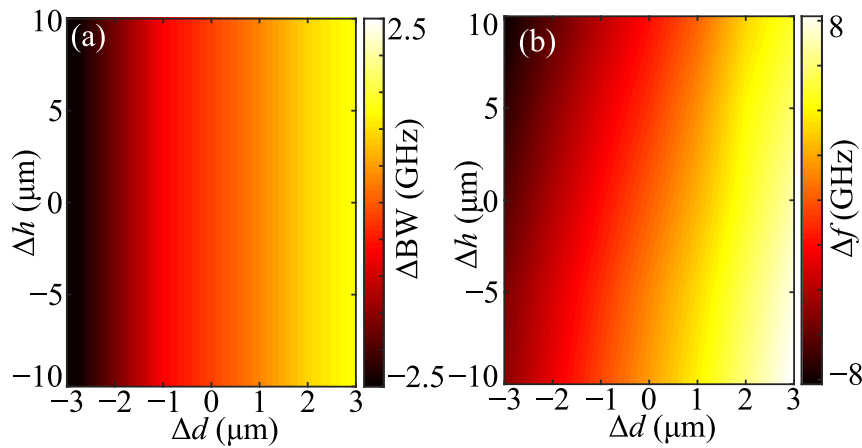


Figure 4.15. Simulated impact of fabrication tolerances on the performance of a uniform filter. (a) 3-dB bandwidth variation, and (b) frequency shift as a function of the variations of wafer thickness Δh and hole diameters Δd .

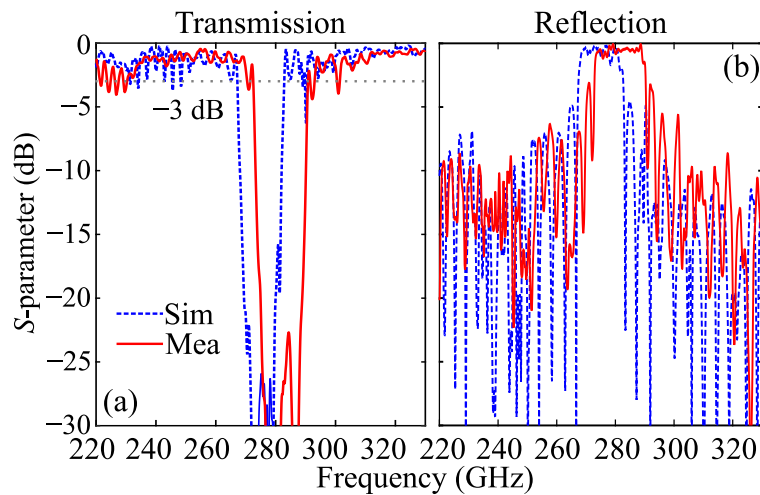


Figure 4.16. Simulated and measured S-parameters for the uniform waveguide Bragg grating filter shown in Fig. 4.4. The simulation is based on the originally designed dimensions with the central frequency at 275 GHz.

Based on the sample quality inspections, it is confirmed that most of the holes are over etched leading to a lower n_{eff} . Meanwhile, such effect could lead to a larger modal index difference Δn thus a broader 3-dB bandwidth (Gao *et al.*, 2020b; Chrostowski and Hochberg, 2015).

To verify these assumptions, the filters have been re-simulated by enlarging the hole diameters for only the grating claddings, while for the two-layer mixed cladding filters in Figs. 4.7(c) and 4.10(a), only the hole size for the inner claddings is varied. This is because the hole configuration for transition waveguides and the outer claddings do

Table 4.1. Compensated dimensions for various effective-medium-clad filters. (f : Designed central frequency; f' : Compensated central frequency; a : Perforation period; d : Designed hole diameter; Δd : Hole diameter error; d' : Compensated hole diameter; BBW: Broader bandwidth; NBW: Narrower bandwidth)

Design	f (GHz)	f' (GHz)	a (μm)	d (μm)	Δd (μm)	d' (μm)
Fig. 4.3(a)	275	280	55.8	36	2.7	38.7
Fig. 4.7(b)	275	280	55.8	36	2.5	38.5
Fig. 4.7(c)	275	280	55.8	36	2.7	38.7
Fig. 4.10(a)	275	280	55.8	36	2.3	38.3
Fig. 4.12(a)–(b) BBW	275	280	56.5	36	2.3	38.7
Fig. 4.12(a)–(b) NBW	275	280	54.8	35	2.7	37.7
Fig. 4.12(c)–(d) BBW	275	284	59.5	44.7	2.9	47.6
Fig. 4.12(c)–(d) NBW	275	280	52.5	28	2.7	30.7
Fig. 4.13(a)–(b)	305	310	48	31	2.7	33.7
Fig. 4.13(c)–(d)	245	250	66	41	2.7	43.7
Fig. 4.13(e)–(f)	245	250	62.5	33	2.7	35.7

Table 4.2. Compensated dimensions for air-clad filter. (w_{Ha} : Designed high-index waveguide width; w_{La} : Designed low-index waveguide width; Δw : waveguide width error; w'_{Ha} : Compensated high-index waveguide width; w'_{La} : Compensated low-index waveguide width)

Design	f (GHz)	f' (GHz)	w_{Ha} (μm)	w_{La} (μm)	Δw (μm)	w'_{Ha} (μm)	w'_{La} (μm)
Fig. 4.7(a)	275	280	240	200	5	235	195

not cause a Bragg frequency shift or a 3-dB bandwidth variation. It is noteworthy that the actual holes are conical. However, based on the initial simulations, conical holes have negligible effects on the relative permittivity tensor of the effective medium or the grating average modal index n_{eff} . To simplify the structural complexity in simulations, cylindrical holes are adopted. To compensate the frequency and 3-dB bandwidth errors, with the wafer thickness of 245 μm , hole diameters are swept with a step increment of 0.5 μm , and it is found that the errors range from 2.3 μm to 2.9 μm . These findings converge the results shown in Fig. 4.15. In particular, a thickness decrement of 5 μm together with a hole diameter increment of 2.7 μm results in a 5-GHz blue shift and

4.4 Applicability at high terahertz frequencies

increasing 3-dB bandwidth by around 1 GHz as shown in Fig. 4.16. It is noted that the waveguide width reduction of around $2.5 \mu\text{m}$ on each side for the air-clad filter shown in Fig. 4.7(a) also falls within this range. If such a compensation is introduced in the simulations, the results agree well with the measurements. The details of the compensated dimensions can be found in Tables 4.1 and 4.2.

4.4 Applicability at high terahertz frequencies

To investigate the applicability of the proposed Bragg grating filter type at high terahertz frequencies, two factors must be considered namely the material availability and fabrication capability. Essentially, the electromagnetic properties of the available materials should be unchanged with frequency increasing. This fact holds true for float-zone intrinsic silicon up to 2 THz (Dai *et al.*, 2004). Additionally, to enable the filter to operate in fundamental modes, the wafer thickness has to be reduced with increasing frequency. Nowadays, free-standing silicon substrates with minimal thickness reaching $10 \mu\text{m}$ are commercially available, which promises scalability to higher terahertz bands. Furthermore, with the operation wavelength decreasing, the subwavelength hole diameters have to be decreased. An etching process with fabrication tolerance less than a quarter of wavelength is required. Noticeably, since the accuracy of the deep reactive ion-etching process is closely related to the aspect ratio between the wafer thickness and hole diameter, simultaneously decreasing the wafer thickness and hole diameter will maintain a feasible aspect ratio range allowing for fabrication at higher terahertz bands. With these considerations, based on the Marcatili's theory (Marcatili, 1969), the fundamental-mode operation frequency range and hole diameter in the filter cladding as a function of wafer thickness are studied. To investigate the maximum fundamental-mode operation frequency range, the waveguide width scales with the thickness by a ratio of 0.9. As shown in Fig. 4.17(a), a $50\text{-}\mu\text{m}$ thick wafer thickness can support the operation frequency range from 1.02 to 1.67 THz. With such a thickness, as shown in Fig. 4.17(b), the required hole diameter is around $7.2 \mu\text{m}$ at 1.34 THz, which is feasible if electron-beam lithography is used to define patterns. To demonstrate the applicability of the filter operating above 1 THz, an effective-medium-clad Bragg grating filter is simulated, which works at WR-0.65 band (1.1-1.7 THz) with a fractional bandwidth of 42.9%. The filter is built into a $50\text{-}\mu\text{m}$ thick silicon on a footprint of $1.7 \times 0.2 \text{ mm}^2$. As shown in Fig. 4.18, the filter operates at the central frequency of 1.4 THz with a 3-dB bandwidth of 76 GHz, and rejection level below -24 dB showing a good

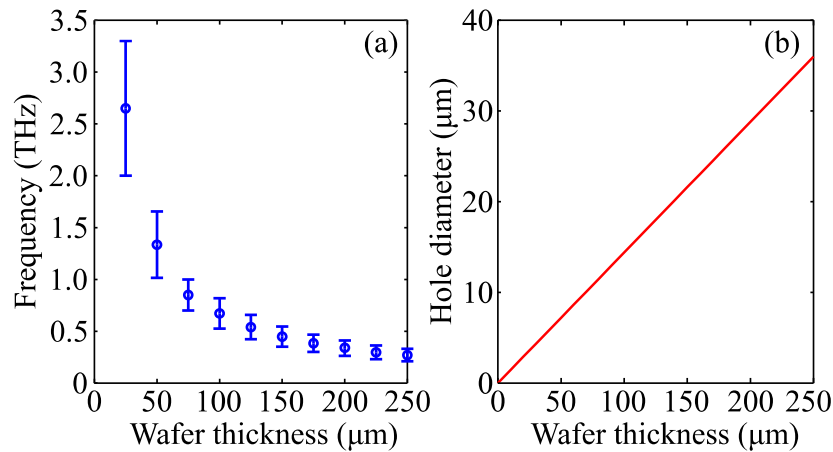


Figure 4.17. Operation frequency range and hole diameter for different wafer thicknesses.

(a) Fundamental-mode operation frequency range and (b) hole diameter as a function of wafer thickness. The operation frequency range is derived based on the Marcattili's theory. To enable a maximum bandwidth supporting only E_{11}^x and E_{11}^y modes, the waveguide width is normalised to the wafer thickness with a ratio of 0.9 and an effective relative permittivity tensor of (2.75, 3.83, 2.75) is adopted for the cladding of a straight waveguide. The given hole diameter is for the filter cladding with an effective relative permittivity tensor of (6.64, 8.19, 6.64), where the effective medium is formed in a square lattice with a lattice period of 0.125 guided Bragg wavelength at the central frequency for each band shown in (a).

frequency selectivity. With such a small footprint, it would be challenging to handle a single filter in measurement. However, it is feasible to handle an integrated platform containing such a filter and other components in a larger footprint. Nevertheless, the investigation shows the potential of the proposed filter type for high terahertz band operation with broad bandwidth and high efficiency.

4.5 Conclusion

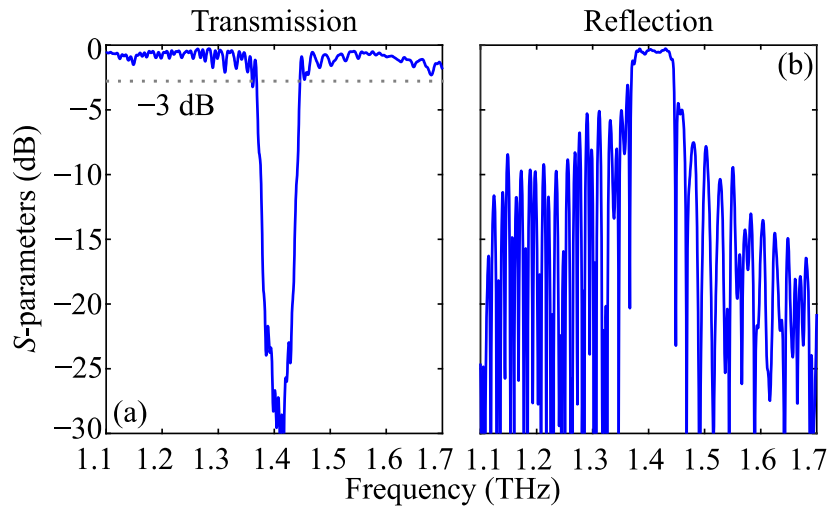


Figure 4.18. Simulated S-parameters of a uniform effective-medium-clad Bragg grating filter operating at WR-0.65 band. (a) Transmission and (b) Reflection. The filter is designed based on a thin silicon wafer with a thickness of $50\ \mu\text{m}$. The dimensions are given as $w_{\text{H}} = 48\ \mu\text{m}$, $w_{\text{L}} = 20\ \mu\text{m}$, $\Lambda = 42.8\ \mu\text{m}$, $(a, d) = (10.7\ \mu\text{m}, 6.9\ \mu\text{m})$. The grating number is 40 leading to a total grating length of 1.712 mm.

4.5 Conclusion

A class of integrated waveguide Bragg grating filters based on all-silicon effective-medium-clad waveguides has been comprehensively investigated. Various filter characteristics including transmission level, 3-dB bandwidth, and Bragg frequency have been considered over the wide operation frequency range from 220–330 GHz (WR-3.4 band). The filters are made into a substrateless high-resistivity float-zone silicon wafer based on the standard deep reactive-ion etching process. Relying on their tailorable effective medium claddings that are realised by periodically perforating the silicon slab, the proposed Bragg grating filter type has an additional degree of flexibility to control the performance compared with the conventional silicon-on-insulator (SOI) ones. By applying the apodisation technique, the transition level is improved above $-3\ \text{dB}$. Importantly, two-layer mixed effective medium claddings with different relative permittivities are introduced to improve the passband transmission levels above $-1.5\ \text{dB}$ with average ripples less than $0.5\ \text{dB}$, while maintaining the lateral footprint within one wavelength. Furthermore, the combination of hybrid claddings and apodisation can further reduce the dispersion with a measured group delay varying between 0.12 and $0.17\ \text{ns}$ across the whole passband. The radiation loss at higher frequencies for a grating with a long period is minimised by introducing higher-index effective

medium claddings, thus allowing for a broadband operation. With high efficiency, low dispersion, and broad bandwidth, the proposed filter type is applicable at high terahertz frequencies, e.g., above 1 THz. It can be foreseen that such Bragg grating structures can be implemented together with other components on this substrateless integrated platform for a wide range of terahertz applications. One important application for bandstop filters is to mitigate radiation interference from terahertz transmitters with passive astronomical observations. In addition, terahertz bandpass filters also can be realized by cascading multiple proposed Bragg grating filters with a certain spacing between two adjacent grating filters (Melloni and Martinelli, 2002). The presented effective medium techniques can be adopted in optics for enhancing filter performance.

Effective-medium-clad polarisation splitters

POLARISATION-division multiplexing is crucial to increasing channel capacity within a limited bandwidth. One enabling component for this technology is a polarisation splitter, which is able to separate/combine signals with orthogonal polarisations. In particular, terahertz polarisation splitters with low insertion loss, broad bandwidth, and high polarisation extinction ratio are in demand for various applications. The broadband operation can be satisfied by microwave-inspired orthomode transducers (OMTs), but the use of metallic waveguides to reach high extinction leads to high ohmic loss and bulky structures. On the other hand, optical integrated polarisation splitters have low loss and good integrability but narrow bandwidths. Therefore, terahertz polarisation splitter technology presents unique challenges with no directly scalable solution existing in these neighbouring spectral domains. To this end, this chapter presents a polarisation splitter based on the tapered directional couplers and effective medium. A 40% fractional bandwidth together with an average polarisation extinction ratio above 20 dB and an insertion loss below 1 dB is achieved at the WR-3.4 band extending over 220–330 GHz. This superior performance is due to the anisotropy of the effective medium claddings that affect the two guided modes differently. Various characteristics are comprehensively investigated including transmission, crosstalk, isolation, higher-order mode conversion, and dispersion. It can be foreseen that such a design can find a wide use in terahertz integrated systems, especially for short-range communications with increased channel capacities.

5.1 Introduction

All-silicon effective-medium-clad dielectric waveguides together with their peripherals have been demonstrated to be able to route the terahertz waves with low dissipation, low dispersion, and broad bandwidth, while supporting two orthogonal fundamental modes namely E_{11}^x mode (with in-plane polarisation) and E_{11}^y mode (with out-of-plane polarisation) (Gao *et al.*, 2019, 2020b). To enable an integrated platform allowing for functional systems, various capabilities for on-chip signal processing must be provided within this framework, such as filtering, modulation, multiplexing, and polarisation control (Withayachumnankul *et al.*, 2018a). Owing to the controllable relative permittivity of the effective medium, various passive components with different functionalities and high performance have been conceptualised and demonstrated (Gao *et al.*, 2019, 2020b, 2021; Liang *et al.*, 2021). The filters have been comprehensively studied in Chapter 4, where the effective medium plays a critical role in improving the device performance.

To manipulate on-chip polarisation states, polarisation rotators and splitters are indispensable components (Gao *et al.*, 2020a; Dai *et al.*, 2012; Barwicz *et al.*, 2007; Chen *et al.*, 2015; Dai *et al.*, 2021; Fang *et al.*, 2021; Komatsu *et al.*, 2009). In particular, polarisation splitters able to separate/combine signals with orthogonal polarisations are in demand for many applications especially for communications to achieve increased channel capacities (Pfau *et al.*, 2007; Sakaguchi *et al.*, 2011; Dong *et al.*, 2012b,a). Additionally, the polarisation splitters are crucial to building functional devices/systems for applications such as polarimetry (Fang *et al.*, 2021) and polarisation diversity (Pfau *et al.*, 2007; Barwicz *et al.*, 2007; Komatsu *et al.*, 2009; Chen *et al.*, 2015; Dai *et al.*, 2018, 2021).

In this context, a terahertz polarisation splitter implemented onto the effective-medium-clad waveguide platform is presented in this chapter. The proposed splitter is based on tapered directional couplers (Cook, 1955; Louisell, 1955; Milton and Burns, 1975; Kim and Ramaswamy, 1993; Cao *et al.*, 2010; Riesen and Love, 2013; Wang *et al.*, 2016) that can offer a much broader bandwidth compared to conventional directional couplers. Compared to the polarisation splitter involving out-of-plane stacked multiple materials to increase the birefringence (Sun *et al.*, 2016, 2017; Liu *et al.*, 2019), the proposed concept relies on in-plane effective medium, which can significantly enhance the polarisation birefringence while requiring a single-step fabrication process based on the standard deep reactive-ion etching without introducing additional materials. These concepts lead to a proposed design with a fractional bandwidth of 40% covering the whole WR-3.4 band over 220–330 GHz with a simulated average insertion loss below 1 dB, and an

5.2 Existing techniques for polarisation splitting

average polarisation extinction ratio above 20 dB for both the E_{11}^x and E_{11}^y modes on a footprint of $4.7\lambda_{0,275} \times 7.2\lambda_{0,275}$.

Section 5.2 reviews the existing techniques for polarisation splitting in both microwave and optical domains. Section 5.3 discusses the design principles, where a mathematical analysis shows bandwidth enhancement of the polarisation splitter through effective mediums. Section 5.4 presents various characteristics of the proposed polarisation splitter including transmission, path crosstalk, ports isolation, higher-order mode conversion, and dispersion. The conclusion is given in Section 5.5.

5.2 Existing techniques for polarisation splitting

To perform polarisation splitting in a dual-polarisation waveguide, techniques from both microwave and optical domains can be utilised but with tradeoffs in terms of integrability, bandwidth, efficiency, and fabrication complexity.

5.2.1 Microwave-based orthomode transducers

Inspired by microwave technologies, as shown in Fig. 5.1, the orthomode transducers (OMT) based on rectangular metallic waveguides have been proposed for terahertz operation (Asayama and Kamikura, 2009; Groppi *et al.*, 2010; Kamikura *et al.*, 2010; Reck and Chattopadhyay, 2013; Gonzalez and Asayama, 2018; Gomez-Torrent *et al.*, 2018; Gonzalez and Kaneko, 2021a). Typically, the OMTs are in form of 3D structures with broad bandwidth and low polarisation crosstalk due to the cut-off of the host waveguides. In one example by Gonzalez and Kaneko (2021a), as illustrated in Figs. 5.1(a) and (b), the OMT consisted of a square waveguide as a common port accepting both orthogonal modes. This port was connected to an in-plane Y-branch to split the horizontal polarisation and the vertical polarisation. By properly designing the waveguides' dimensions, good impedance matching between the input and output waveguides can be achieved for the desired mode, while the other mode below the cut-off frequency is strongly rejected (Gonzalez and Asayama, 2018; Gonzalez and Kaneko, 2021a). Such a polarisation splitting device can achieve an average insertion loss around 1 dB with a crosstalk level below -35 dB over a broad bandwidth from 275 to 500 GHz equivalent to a fractional bandwidth of 58% (Gonzalez and Kaneko, 2021a). However, the OMTs are not integratable due to their bulky 3D structures. Additionally, apart from the

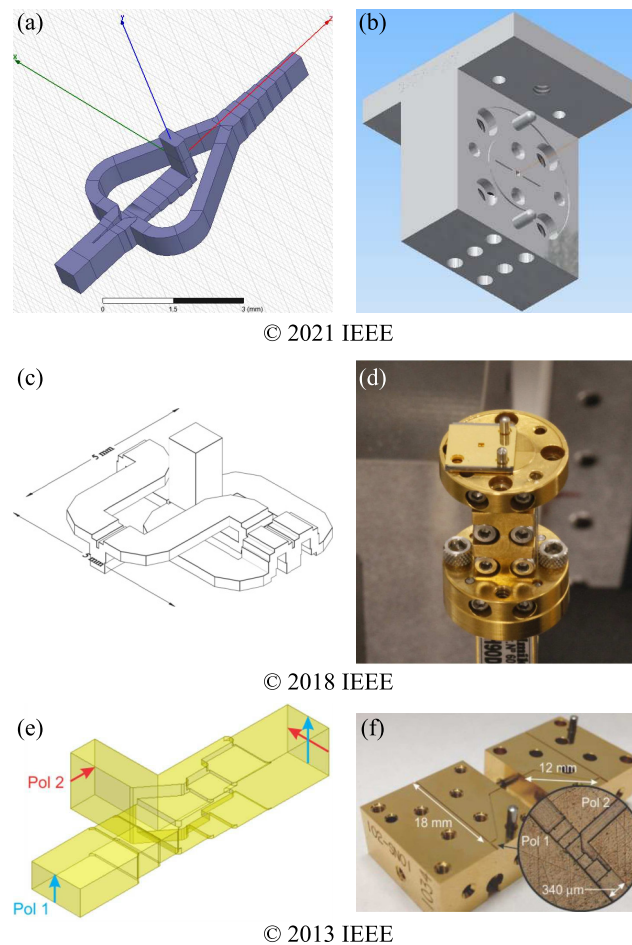


Figure 5.1. Microwave-based orthomode transducers (OMTs). (a) 3D schematic and (b) assembled structure of a double-ridged waveguide OMT operating over 275–500 GHz (Gonzalez and Kaneko, 2021a). (c) 3D schematic and (d) fabricated 220–330 GHz turnstile OMT based on micromaching process (Gomez-Torrent *et al.*, 2018). (e) 3D schematic and (d) fabricated structure of an asymmetrical OMT for 500–600 GHz operation (Reck and Chattopadhyay, 2013).

significantly increased ohmic loss of metallic waveguides with increasing frequency, the fabrication based on CNC machining is another challenge at this scale (Gomez-Torrent *et al.*, 2018; Gonzalez and Kaneko, 2021a). Although micromaching technologies can be adopted to fabricate a multi-layered OMT with a complicated structure as shown in Figs. 5.1(c) and (d), the fabrication complexity is high involving a multi-step process including lithography, deposition, deep reactive-ion etching, and gold sputtering for each layer of the OMT. Additionally, the geometrical symmetry required to achieve high performance over a broad bandwidth makes the fabrication more challenging. Simpler OMTs with no symmetries requirements, as shown in Figs. 5.1(e) and (f), can relax the fabrication requirements, at a cost of a narrower bandwidth and increased crosstalk

5.2.2 Optics-based polarisation splitters

levels due to the higher-order mode conversion (Uher *et al.*, 1993; Reck and Chattopadhyay, 2013). Nevertheless, such kind of polarisation splitting device is still useful for some special applications, e.g., radio astronomy receivers (Wootten and Thompson, 2009; Gonzalez and Asayama, 2018; Kojima *et al.*, 2020).

5.2.2 Optics-based polarisation splitters

Unlike in the terahertz domain where integrated polarisation splitters are still rarely available, they have been extensively studied in the optical regime especially for silicon integrated photonics (Dai *et al.*, 2012). In general, the optical polarisation splitters also known as polarisation beam splitters (PBSs) can be realised based on various methods including Mach-Zehnder interferometers (MZIs) (Soldano *et al.*, 1994; Liang and Tsang, 2005; Dai *et al.*, 2011a), multimode interferometers (MMIs) (Rahman *et al.*, 2001; Hong *et al.*, 2003; Zhang *et al.*, 2006; Jiao *et al.*, 2009; Hosseini *et al.*, 2011; Sun *et al.*, 2017; D’Mello *et al.*, 2018; Kudalippallyalil *et al.*, 2020), photonic crystals (PCs) (Kim *et al.*, 2003; Ao *et al.*, 2006; Zabelin *et al.*, 2007; Shi *et al.*, 2007), photonic inverse design (Shen *et al.*, 2015), and directional couplers (DCs) (Kiyat *et al.*, 2004; Augustin *et al.*, 2007; Komatsu *et al.*, 2009; Chang and Li, 2011; Zou *et al.*, 2011; Dai and Bowers, 2011; Dai *et al.*, 2011b; Dai, 2012; Lou *et al.*, 2012; Ding *et al.*, 2012; Sacher *et al.*, 2014; Kim *et al.*, 2015; Chen *et al.*, 2016; Wang *et al.*, 2016; Sun *et al.*, 2016, 2017; Wu *et al.*, 2017; He *et al.*, 2017; Ong *et al.*, 2017; Yin *et al.*, 2017; Li and Dai, 2018; Kim *et al.*, 2018; Cheng *et al.*, 2019; Liu *et al.*, 2019; Zhang *et al.*, 2020; Li *et al.*, 2020; Liu *et al.*, 2021; Deng *et al.*, 2021a). Despite their good integrability and low loss compared to the metallic structures mentioned above, again there exist tradoffs among these conventional optical PBSs in terms of operation bandwidth, insertion loss, structural compactness, and fabrication complexity. Mach-Zehnder interferometers with high structural simplicity have been widely used in optical modulators and sensors, while they also can be used as PBSs to split two orthogonal polarisations by leveraging the birefringence of the two waveguide arms (Dai *et al.*, 2011a). One example of the MZI-based PBS is shown in Fig. 5.2(a). The birefringence of such a polarisation splitter is small leading to a relatively low polarisation extinction ratio despite the introduction of additional highly birefringent materials, which would in turn increase the fabrication complexity and material loss (Dai *et al.*, 2012). Additionally, the footprint for the MZI-based PBS tends to be large due to the same reason, while the bandwidth is narrow (Soldano *et al.*, 1994; Liang and Tsang, 2005; Dai *et al.*, 2011a). For the MMI-based PBSs, the TE and TM modes can be separated into different through

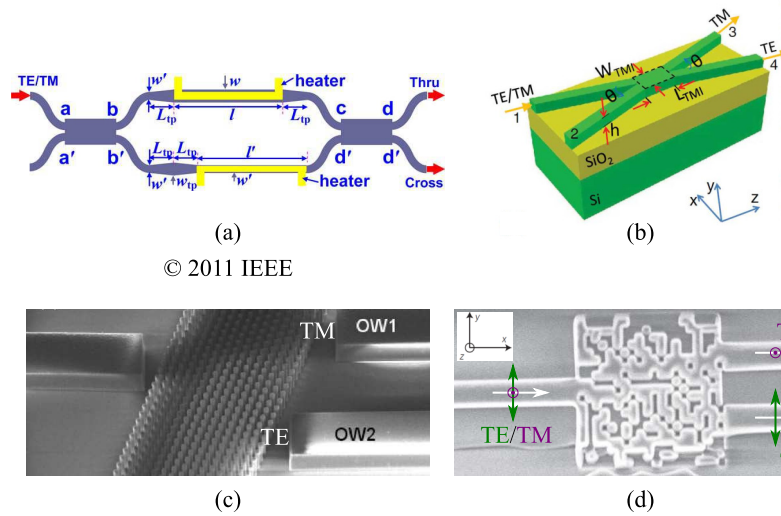


Figure 5.2. Optics-based polarisation beam splitters. (a) Schematic of a Mach-Zehnder-interferometer-based PBS operating over 1505–1595 nm (Dai *et al.*, 2011a). (b) Schematic of a multi-mode-interferometer-based PBS for 1525–1575 nm operation (Hosseini *et al.*, 2011). SEM images of fabricated PBSs based on (c) a photonic crystal of pillar type operating over 1550–1580 nm (Ao *et al.*, 2006) and (d) a photonic inverse design method operating over 1534–1566 nm (Shen *et al.*, 2015).

paths by utilising the difference in their self-imaging beat lengths (Hosseini *et al.*, 2011). Typically, the MMI length is chosen simultaneously as even and odd multiple beat lengths for the two polarisations, respectively (Hosseini *et al.*, 2011). However, due to a small birefringence of the MMI coupler, the structure is usually electrically quite long to achieve a sufficient polarisation extinction ratio. The device footprint can be shortened by using two-mode interference coupler (Hosseini *et al.*, 2011) or by cascading multiple MMI structures (Jiao *et al.*, 2009). Benefiting from such techniques, as shown in Fig. 5.2(b), an one-beat-length long MMI-based PBS has been reported (Hosseini *et al.*, 2011). Nevertheless, the bandwidth of such a PBS is narrow due to the mode interference mechanism that is strongly frequency dependent. Another strategy to realise the polarisation splitting function is to use photonic crystals as illustrated in Fig. 5.2(c), which are highly sensitive to the polarisation of light waves (Zabelin *et al.*, 2007). Typically, the PC-based structures can separate the TE and TM modes by leveraging their polarisation-dependent dispersion properties or bandgap difference between the two polarisations, so that the two modes can be refracted to different directions (Ao *et al.*, 2006; Kim *et al.*, 2003; Zabelin *et al.*, 2007; Shi *et al.*, 2007). However, the PC-based PBSs exhibit high insertion losses mainly due to the strong diffraction (Kim *et al.*, 2003;

5.2.2 Optics-based polarisation splitters

Zabelin *et al.*, 2007) and scattering (Ao *et al.*, 2006) at the PC interface. Additionally, owing to the strong in-band dispersion of the photonic crystals, their fractional bandwidths are only a few percent (Kim *et al.*, 2003; Ao *et al.*, 2006; Zabelin *et al.*, 2007; Shi *et al.*, 2007). Rather than relying on theoretical design concepts, a PBS has been proposed based on inverse photonic design method leading to an ultra compact footprint (Shen *et al.*, 2015) as shown in Fig. 5.2(d). However, the structure of such a PBS is highly complex with little insight into the details of the operation mechanisms, while the optimisation is computationally demanding.

With structural and design simplicity, directional couplers have been widely used for optical PBSs. Similar with the MMI-based structures, the operation principles of the directional-coupler-based PBS also rely on the beat length difference between the TE and TM modes (Kiyat *et al.*, 2004; Deng *et al.*, 2021a). Specifically, given a certain coupling length, the mode with a shorter beat length can be coupled from the input waveguide to its adjacent waveguide, while the one with a longer beat length can pass through the input waveguide with no coupling (Dai *et al.*, 2012). Therefore, a strong polarisation birefringence leading to a greater difference in beat length is demanded to achieve a compact PBS together with a high polarisation extinction ratio (Dai *et al.*, 2012). However, for a conventional silicon-based uniform directional coupler, the polarisation birefringence is usually weak leading to a quite long coupler length together with a relatively low extinction ratio. Furthermore, due to the coupling being strongly dependent on the frequency, the operation bandwidth is narrow, while the stringent requirements on the coupler dimensions result in a device performance that is highly sensitive to the fabrication tolerances (Dai *et al.*, 2012). Recently, an optics-inspired terahertz PBS based on a silicon directional coupler (Deng *et al.*, 2021a) was proposed, which operated over 445–475 GHz with a fractional bandwidth of 6.5% and an average polarisation extinction ratio of >8 dB on a footprint of $0.8\lambda_c \times 11.5\lambda_c$, where λ_c is the wavelength at central frequency. Another terahertz PBS design proposed by the same group adopted the existing optical techniques and showed slight improvements in the operation bandwidth and PER (Deng *et al.*, 2021b). However, a relatively high average insertion loss reaching around 3.7 dB and a narrow fractional bandwidth of around 7% together with a long footprint limited its applications.

To further increase the polarisation birefringence of the directional-coupler-based PBS, several approaches have been proposed by introducing asymmetric couplers (Dai *et al.*,

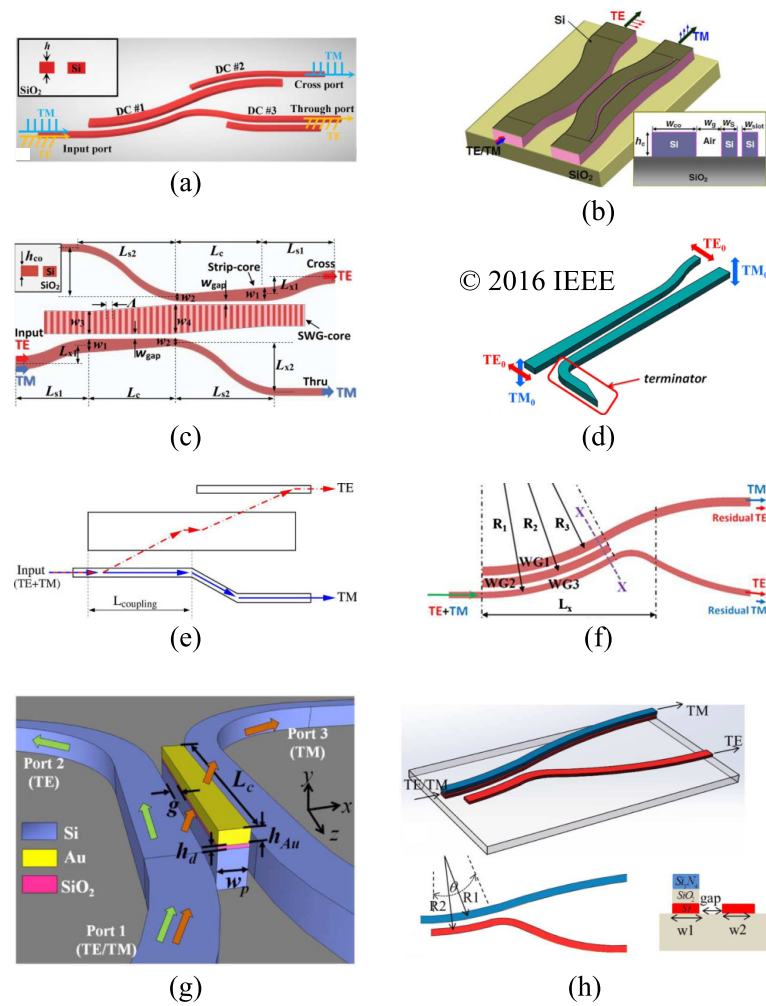


Figure 5.3. Optical polarisation beam splitters (PBSs) based on directional couplers. Schematic of a PBS based on (a) cascaded bent-waveguide couplers operating over 1475–1610 nm (Wu *et al.*, 2017), (b) bent-slot-waveguide coupler operating over 1470–1630 nm (Dai *et al.*, 2011b), (c) subwavelength grating-tapered waveguide coupler operating over 1435–1655 nm (Li *et al.*, 2020), (d) tapered directional coupler for 1520–1620 nm operation (Chen *et al.*, 2016), (e) multi-mode waveguide coupler operating over 1520–1620 nm (Augustin *et al.*, 2007), (f) triple-bent-waveguide coupler operating over 1520–1610 nm (Ong *et al.*, 2017), (g) dielectric-hybrid plasmonic-dielectric coupler operating over 1530–1565 nm (Lou *et al.*, 2012), and (h) bent silicon nitride-silica-silicon slot waveguide-silicon waveguide coupler operating over 1535–1575 nm (Liu *et al.*, 2019).

2011b) and hybrid-waveguide couplers (Lou *et al.*, 2012) as shown in Fig. 5.3. Both methods aim to achieve a good phase matching condition over a short coupling length for the mode propagating through cross-coupling, and simultaneously a phase mismatch for the other mode allowing it to propagate without significant coupling. In particular, for the asymmetric-directional-coupler-based PBSs, their performance can be improved

5.2.2 Optics-based polarisation splitters

with assistance of bent waveguides (Dai and Bowers, 2011; Dai *et al.*, 2011b; Wu *et al.*, 2017; Ong *et al.*, 2017; Liu *et al.*, 2019), slot waveguides (Komatsu *et al.*, 2009; Dai *et al.*, 2011b; Liu *et al.*, 2019), grating waveguides (Wang *et al.*, 2016; He *et al.*, 2017; Zhang *et al.*, 2020; Li *et al.*, 2020; Liu *et al.*, 2021), tapered waveguides (Ding *et al.*, 2012; Sacher *et al.*, 2014; Chen *et al.*, 2016; Yin *et al.*, 2017; Li *et al.*, 2020), triple waveguides (Augustin *et al.*, 2007; Komatsu *et al.*, 2009; Dai, 2012; Kim *et al.*, 2015; Li and Dai, 2018; Kim *et al.*, 2018; Cheng *et al.*, 2019; Sun *et al.*, 2017), and/or the combination of these techniques (Komatsu *et al.*, 2009; Dai *et al.*, 2011b; Ong *et al.*, 2017; Sun *et al.*, 2017; Liu *et al.*, 2019; Li *et al.*, 2020). However, it is still challenging to simultaneously achieve a broad bandwidth and a high extinction ratio on a compact footprint. Recently, as shown in Fig. 5.3(c), an optical PBS consisting of a subwavelength grating waveguide sandwiched between two tapered waveguides was reported with an average insertion loss less than 0.3 dB and a polarisation extinction ratio above 20 dB over a fractional bandwidth up to 16%, which was claimed as the largest bandwidth in the optical domain (Li *et al.*, 2020). However, it is impractical to directly scale such a PBS down to the terahertz band, since the footprint would be around $3 \times 55 \text{ mm}^2$ at the WR-3.4 band, while the bandwidth would be moderate considering a 40% fractional bandwidth required to cover the WR-3.4 band. To reduce the footprint, the hybrid-waveguide couplers can provide alternatives (Zou *et al.*, 2011; Chang and Li, 2011; Lou *et al.*, 2012; Sun *et al.*, 2016, 2017; Liu *et al.*, 2019). One popular method is to use the plasmonic-dielectric-waveguide coupler (Zou *et al.*, 2011; Chang and Li, 2011; Lou *et al.*, 2012) as shown in Fig. 5.3(g), where the metal-dielectric hybrid waveguide can support only a single polarisation that is perpendicular to the metallic walls and allowed to be cross coupled. Broadly, this leads to an infinite birefringence allowing for a compact footprint. However, the loss caused by the metal absorption is significant, which also limits the bandwidth (Zou *et al.*, 2011; Chang and Li, 2011; Lou *et al.*, 2012). Instead, all-dielectric hybrid waveguides can be adopted to remove the metallic loss (Sun *et al.*, 2016, 2017; Liu *et al.*, 2019). As illustrated in Fig. 5.3(h), such kind of hybrid waveguide usually constitutes vertically stacked multiple dielectric materials with various refractive indices so as to spatially separate the modes with only one of them cross coupled (Sun *et al.*, 2016, 2017; Liu *et al.*, 2019). For example, a silicon nitride-silica-silicon waveguide was utilised for a PBS, where the TE mode was confined within the bottom silicon layer and can be coupled to its adjacent silicon waveguide with an identical height, while the TM mode is concentrated within the middle silica layer and propagates through (Liu *et al.*, 2019). Such an all-dielectric-hybrid-waveguide-based PBS requires multi-step fabrication process with increased

complexity, while the additional dielectric material loss is not negligible (Sun *et al.*, 2017). Additionally, its relative bandwidth is only 2.6% based on the conventional coupling mechanism (Liu *et al.*, 2019). Therefore, so far there is no suitable solution scalable from either the microwave or optical domains that can provide a terahertz PBS with low insertion loss, broad bandwidth, high polarisation extinction ratio, and compact footprint.

5.3 Proposed design

5.3.1 Design principles

As shown in Fig. 5.4(a), the proposed polarisation splitter consists of multiple tapered directional couplers. The device is built on the effective-medium-clad dielectric waveguide platform to achieve a high efficiency, broad bandwidth, and high polarisation extinction ratios over the operation frequency range from 220 to 330 GHz. The specific design of the splitter is based on a 250- μm -thick silicon wafer with a relative permittivity of $\epsilon_{\text{Si}} = 11.68$ and resistivity $>10 \text{ k}\Omega \text{ cm}$. The effective medium claddings are realised by periodically perforating the silicon slab with deep subwavelength spacings, where the claddings are formed in hexagonal lattices to enhance the mechanical strength as shown in Figs. 5.4(b) and (c). The proposed PBS is designed to split the two fundamental modes with orthogonal polarisations, i.e., the E_{11}^x mode with in-plane polarisation and the E_{11}^y mode with out-of-plane polarisation, into two paths as illustrated in Figs. 5.4(d) and (e). Furthermore, regular waveguides cladded by lower index effective medium claddings are used to connect the tapering and the polarisation splitter so as to enhance the coupling between the device and the feed while allowing for a consistent interconnection with other components on the same platform (Gao *et al.*, 2021).

The proposed polarisation splitter can be understood by considering separately two paths namely the E_{11}^y -path and E_{11}^x -path as shown in Figs. 5.4(d) and (e). The E_{11}^y -path includes two tapered directional couplers connected by a 90° sharp bend. Here, the tapered directional couplers can achieve a much broader bandwidth compared to the conventional uniform directional couplers, and the details are given in Section 5.3.2. Furthermore, the effective medium claddings surrounding the couplers have to be properly selected so as to achieve a sufficiently high polarisation extinction ratio (PER), as discussed in more details in Section 5.3.2. For each coupler, the two evanescently

5.3.1 Design principles

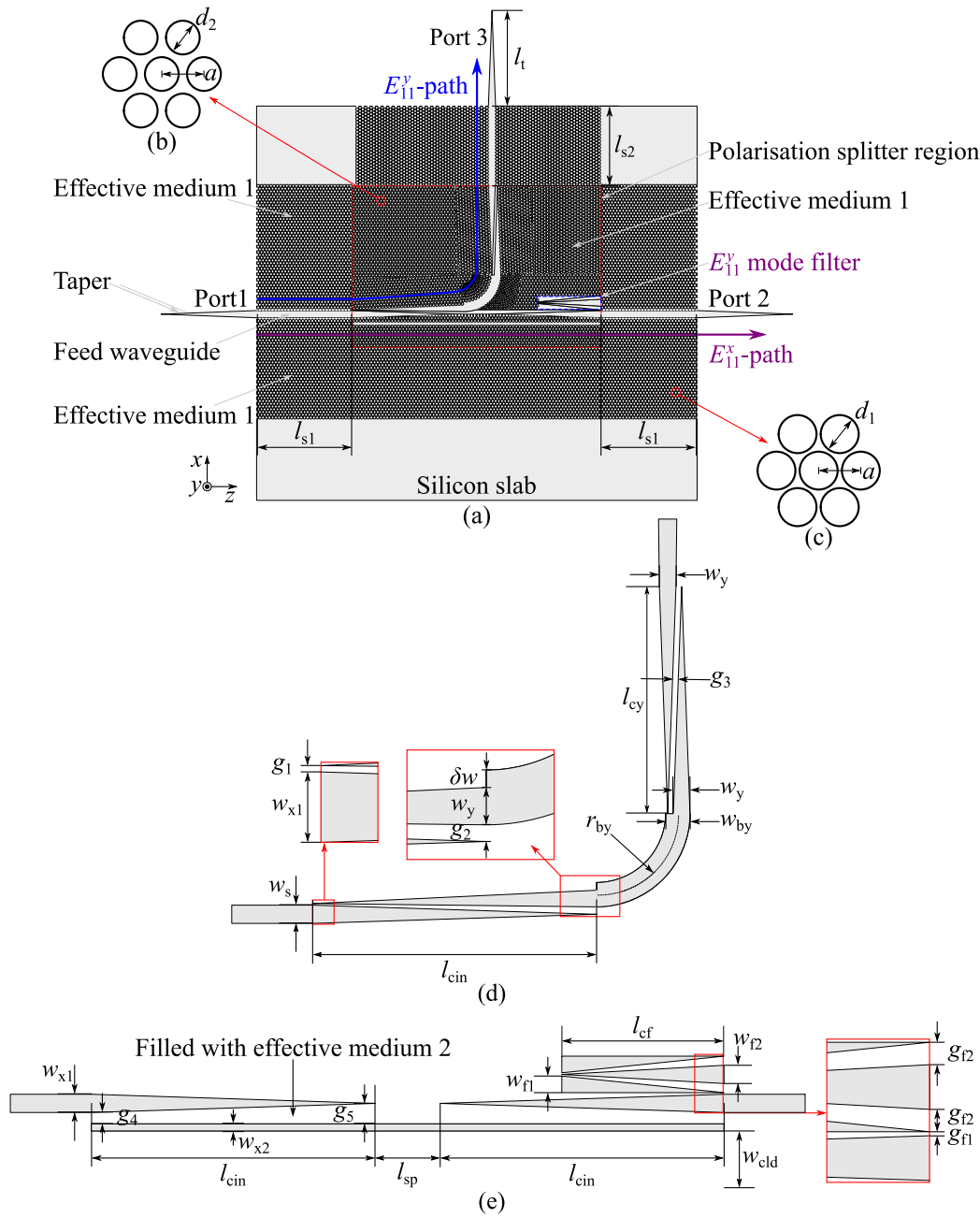


Figure 5.4. Schematic of the proposed integrated polarisation splitter. (a) Polarisation splitter based on air-silicon effective medium with a thickness of $250 \mu\text{m}$. Magnified views of the hexagonal lattices of the effective medium in the (b) Polarisation splitter region with a relative permittivity tensor of $(\epsilon_x, \epsilon_y, \epsilon_z) = (4.01, 5.48, 4.01)$ and (c) the non-polarisation-splitter region with $(\epsilon_x, \epsilon_y, \epsilon_z) = (2.75, 3.83, 2.75)$. Magnified views of the unclad components composing (d) the E_{11}^y -path and (e) the E_{11}^x -path. The unpatterned silicon slab in (a) is for handling purpose in measurements, while the tapering structure at each port is for coupling to the feeding hollow waveguide in both simulation and measurement. The dimensions are given in Table 5.1.

Table 5.1. Dimensions for the effective-medium-clad polarisation splitter.

a (μm)	d_1 (μm)	d_2 (μm)	g_1 (μm)	g_2 (μm)	g_3 (μm)	g_4 (μm)	g_5 (μm)	g_{f1} (μm)
100	90	80	20	75	70	140	252.5	20
g_{f2} (μm)	l_t (μm)	l_{s1} (μm)	l_{s2} (μm)	l_{cin} (μm)	l_{sp} (μm)	l_{cf} (μm)	l_{cy} (μm)	r_{by} (μm)
112.5	3000	3000	2500	3500	800	2000	2800	1000
w_s (μm)	w_{x1} (μm)	w_{x2} (μm)	w_y (μm)	w_{f1} (μm)	w_{f2} (μm)	w_{clid} (μm)	w_{by} (μm)	δw (μm)
225	225	87.5	205	205	225	700	300	95

coupled waveguides are laterally tapered and inversely positioned with a small coupling air gap along a sufficiently long coupling length. Such a design aims to achieve a high power transfer for the E_{11}^y mode while rejecting the E_{11}^x mode over the operation frequency range from 220 to 330 GHz (WR-3.4 band). The waveguide widths are selected for supporting only the fundamental mode of each polarisation. In this case, the double couplers can enhance performance by increasing the polarisation extinction ratio (PER). Introducing more couplers can further increase the PER but at the expense of higher complexity and coupling loss. The sharp bend with low bending loss is adopted to reduce the device footprint while minimising the interferences with the E_{11}^x -path Song *et al.* (2016b, 2020). The claddings surrounding the bend is based on the principles discussed in Chapter 3, where elliptical hole arrays are adopted with an identical effective refractive index in both inner and outer claddings.

The E_{11}^x -path consists of two symmetric tapered couplers bridged by a thin straight waveguide with a relatively wide coupling gap as shown in Fig. 5.4(e). To minimise the interference with the E_{11}^y -path, the two tapered waveguides are isolated with a certain distance l_{sp} . The bridging waveguide aids the coupling between the two tapered sections for the E_{11}^x mode. Typically, due to a larger in-plane field penetration depth of the E_{11}^x mode compared to the E_{11}^y mode (Marcatili, 1969), a combination of a wider coupling gap and a higher refractive index of filling material can support a high transmission for the E_{11}^x mode with a low crosstalk level for the E_{11}^y mode. Here, the effective medium with a tailorable refractive index is therefore crucial to the performance. Additionally, the core width of the bridging waveguide should be narrow so as to capture the gradually leaked E_{11}^x mode from the tapered waveguide or equivalently to provide a good mode matching over a broad bandwidth. To further enhance the PER, an E_{11}^y mode filter consisting of multiple tapered waveguides is introduced as shown in Fig. 5.4(e), so that the remaining power in the E_{11}^y mode is trapped in the filter while the E_{11}^x mode can pass through with a negligible impact. The mode filter leverages the

5.3.2 Effective-medium-clad tapered directional couplers

identical principle adopted in the E_{11}^y -path design relying on the polarisation dependence of the tapered couplers. It is noteworthy that as shown in Fig. 5.4(a), additional effective-medium claddings are introduced outside the polarisation splitter region with a lower relative permittivity compared to the one in the polarisation splitter region. This is mainly to minimise the leaked mode inference with the nearby silicon slab. With such a configuration, the leaked mode can be mainly confined within the cladding region due to the refractive index contrast between the claddings in the polarisation splitter and non-polarisation-splitter regions (Gao *et al.*, 2021).

5.3.2 Effective-medium-clad tapered directional couplers

The tapered directional couplers also known as tapered velocity or tapered mode couplers were first proposed several decades ago in the microwave regime for ultra-wideband applications (Cook, 1955; Louisell, 1955). Generally, the tapered directional coupler can be realised by tapering the geometries of the guiding structures and/or the refractive indices of the surrounding materials (Cook, 1955; Louisell, 1955; Milton and Burns, 1975; Kim and Ramaswamy, 1993; Riesen and Love, 2013). As a result, the tapered couplers can operate in the evanescent coupling regions without even and odd mode interference or critical beat length involved. This leads to a broad bandwidth but at a slight expense of a larger footprint compared to the conventional uniform directional couplers (Cook, 1955; Louisell, 1955). For a tapered directional coupler, it has been demonstrated that the power transfer between two individual waveguides is inversely proportional to $(d\Delta\beta/dz)/KK^*$, where $\Delta\beta = \beta_a - \beta_b$ with β_a and β_b being the propagation constants of the first and second coupled tapered waveguides, while K is the complex coupling coefficient between those two waveguides (Milton and Burns, 1975). Here, $\Delta\beta$ is a monotonically decreasing function of coupler position z , positive at one end of the coupler and negative at the other end. Milton and Burns (1975) have proved that nearly 100% power transfer will occur when

$$\frac{d\Delta\beta}{dz} \cdot \frac{1}{KK^*} \leq 1.5. \quad (5.1)$$

It is noted that a smaller $d\Delta\beta/dz$ can minimise the coupling between the quasi-even and odd modes allowing for a high total power transfer across the coupler with a single mode (quasi-even or quasi-odd mode). Otherwise, some power converted to the other mode (quasi-even or quasi-odd mode) could remain in the launching waveguide (Milton and Burns, 1975). Here, the quasi-modes are mainly due to the asymmetry of the coupler

at a certain position. A higher coupling coefficient usually can be achieved with a longer coupling length and a smaller coupling gap together with a sufficient evanescent field penetration depth (Louisell, 1955; Marcatili, 1969). Given a sufficiently large coupling coefficient K with across the coupler, the percentage of the total power transfer is mainly determined by $d\Delta\beta/dz$, where an appreciable power transfer requires a slowly varying $\Delta\beta$.

It has been observed through simulations that the power transfer across an air-clad tapered coupler varies with polarisation (Cao *et al.*, 2010). Below, it will be shown that the combination of the tapered coupler and effective medium can significantly enhance the polarisation discrimination with a great design flexibility. Specifically, the investigations will focus on how the effective medium affects $d\Delta\beta/dz$ and KK^* , respectively so as to improve the performance. The in-depth analysis provides insight into the design principles underpinning the superior performance of the proposed polarisation splitter.

Polarisation dependence: $d\Delta\beta/dz$

In this section, it will be proved that given a certain tapered directional coupler with high coupling coefficients for both orthogonal polarisations, $d\Delta\beta/dz$ varies with polarisation leading to a difference in power transfer. This is critical to the polarisation splitting and explains the main design principle for the E_{11}^y -mode path in the proposed polarisation splitter. Importantly, it will be shown that the introduction of the effective medium cladding can enhance such a difference.

In Chapter 3, the propagation constants of a uniform effective-medium-clad dielectric waveguide for both orthogonal polarisations have been derived. Without loss of generality, in this chapter, the original forms of the propagation constants are used. According to Marcatili's theory (Marcatili, 1969), the propagation constant β_z^x for the E_{pq}^x modes can be expressed as:

$$\beta_z^x = \sqrt{k_1^2 - k_x^2 - k_y^2}, \quad (5.2)$$

$$k_x^x = \frac{p\pi}{w} \left(1 + \frac{n_3^2 A_3 + n_5^2 A_5}{\pi n_1^2 w} \right)^{-1}, \quad (5.3)$$

$$k_y^x = \frac{q\pi}{h} \left(1 + \frac{A_2 + A_4}{\pi h} \right)^{-1}. \quad (5.4)$$

For the E_{pq}^y modes, the propagation constants β_z^y can be expressed as:

5.3.2 Effective-medium-clad tapered directional couplers

$$\beta_z^y = \sqrt{k_1^2 - k_x^{y2} - k_y^{y2}}, \quad (5.5)$$

$$k_x^y = \frac{p\pi}{w} \left(1 + \frac{A_3 + A_5}{\pi w} \right)^{-1}, \quad (5.6)$$

$$k_y^y = \frac{q\pi}{h} \left(1 + \frac{n_2^2 A_2 + n_4^2 A_4}{\pi n_1^2 h} \right)^{-1}; \quad (5.7)$$

and

$$A_{2,3,4,5} = \frac{\lambda}{2(n_1^2 - n_{2,3,4,5}^2)^{1/2}}. \quad (5.8)$$

For the effective-medium-clad waveguides, $A_{3(5)}$ is polarisation dependent due to the anisotropy of the effective medium claddings, i.e., n_{ix} is unequal to n_{iy} ($i = 3, 5$) based on the Maxwell-Garnett approximations. The above expressions were derived based on the model shown in Fig. 3.2. Here, p and q are integers denoting the mode order, while w and h are the width and height of waveguide core, k_i ($i = 1, 2, \dots, 5$) is the propagation constant in the i^{th} medium with a refractive index n_i ($i = 1, 2, \dots, 5$), $k_x^{x(y)}$ and $k_y^{x(y)}$ are the transverse propagation constants along the x and y directions, and λ is the wavelength in free space. Here, only the fundamental modes are considered, where $p = q = 1$.

In this work, the tapered directional couplers are realised by varying the waveguide core widths w along the wave propagation direction z leading to β_z^x and β_z^y varying with z , while the core height h and claddings effective properties remain unchanged. Based on the Eqs.(5.2)–(5.7), $\beta_z^x(z)$ and $\beta_z^y(z)$ are only affected by the transverse propagation constants $k_x^x(z)$ and $k_x^y(z)$, which are the functions of the core width w , while the other parameters are constants. In this case, the varying rate of $\Delta\beta_z(z)$ is proportional to the varying rate of $\Delta k_x(z)$ regardless of the polarisation. Additionally, since $d\Delta k_x/dz$ is differentiable, it can be represented as

$$\frac{d\Delta k_x}{dz} = \frac{dk_{xa}}{dz} - \frac{dk_{xb}}{dz}, \quad (5.9)$$

where k_{xa} and k_{xb} are the transverse propagation constants along the x -axis of the two individual waveguides. As shown in Fig. 5.4(d), the two identical tapered waveguides are inversely positioned. As a result, dk_{xb}/dz has an opposite sign relative to the dk_{xa}/dz , leading to the $d\Delta k_x/dz$ monotonically decreasing. Therefore, it is reasonable to determine the varying rate of Δk_x from a single tapered waveguide, i.e., from dk_x/dz .

For a effective-medium-clad tapered dielectric waveguide, based on Eqs. (5.3) and (5.6), the transverse propagation coefficients $k_x^x(z)$ and $k_x^y(z)$ for the E_{11}^x and E_{11}^y modes can be expressed as:

$$k_x^x(z) = \pi^2 n_1^2 \left(\frac{1}{\pi n_1^2 w(z) + n_{3x}^2 A_{3x} + n_{5x}^2 A_{5x}} \right), \quad (5.10)$$

$$k_x^y(z) = \pi^2 \left(\frac{1}{\pi w(z) + A_{3y} + A_{5y}} \right). \quad (5.11)$$

Correspondingly,

$$\frac{dk_x^x(z)}{dz} = \pi^3 n_1^4 w'(z) \left(\frac{1}{\pi n_1^2 w(z) + n_{3x}^2 A_{3x} + n_{5x}^2 A_{5x}} \right)^2, \quad (5.12)$$

$$\frac{dk_x^y(z)}{dz} = \pi^3 w'(z) \left(\frac{1}{\pi w(z) + A_{3y} + A_{5y}} \right)^2. \quad (5.13)$$

Since the waveguide is linearly tapered along z with a slope of m , here $w'(z) = m$ is a constant. The next step is to compare the varying rate of the transverse propagation constants between two orthogonal polarisations as:

$$\frac{dk_x^x(z)/dz}{dk_x^y(z)/dz} = \left(\frac{\pi n_1^2 w(z) + n_1^2 A_{3y} + n_1^2 A_{5y}}{\pi n_1^2 w(z) + n_{3x}^2 A_{3x} + n_{5x}^2 A_{5x}} \right)^2. \quad (5.14)$$

The distinctive terms in this ratio are $n_1^2 A_{3(5)y}$ and $n_{3(5)x}^2 A_{3(5)x}$. As discussed above, given a certain cladding configuration, A that can be obtained from Eq. (5.8) is polarisation dependent due to the anisotropy of the effective medium claddings. To analyse Eq. (5.14), a ratio η can be defined as:

$$\eta = \frac{n_1^2 A_{3(5)y}}{n_{3(5)x}^2 A_{3(5)x}} = \frac{n_1^2}{n_{3(5)x}^2} \left(\frac{n_1^2 - n_{3(5)x}^2}{n_1^2 - n_{3(5)y}^2} \right)^{1/2}, \quad (5.15)$$

where n_1 is the refractive index of the waveguide core, while $n_{3x(y)}$ and $n_{5x(y)}$ are the refractive indices of the lateral claddings for in-plane (out-of-plane) polarisation. Based on Eqs. (2.1)–(2.2) in Chapter 2, it is known that any air-silicon effective medium with a certain hole configuration has $n_{3(5)x} < n_{3(5)y}$ due to its inherent anisotropy, leading to the second item in Eq. (5.15) being greater than one. Thus, η in Eq. (5.15) is always greater than one for the coupler clad by effective medium, which means

$$n_1^2 A_{3y} > n_{3x}^2 A_{3x}, \quad (5.16)$$

$$n_1^2 A_{5y} > n_{5x}^2 A_{5x}. \quad (5.17)$$

5.3.2 Effective-medium-clad tapered directional couplers

Back to Eq. (5.14), this condition implies that for the effective-medium-clad tapered coupler

$$\frac{dk_x^x(z)}{dz} > \frac{dk_x^y(z)}{dz}. \quad (5.18)$$

As discussed previously, $d\Delta\beta/dz$ is proportional to $d\Delta k_x/dz$, which can be determined from a single tapered waveguide dk_x/dz . Therefore, it can be concluded that given an identical high coupling coefficient, the E_{11}^y mode will always have a higher power transfer compared to the E_{11}^x mode. This polarisation-dependent power transfer property forms a basis for polarisation splitting along the E_{11}^y -mode through path and for the E_{11}^y mode filter in the E_{11}^x path as shown in Fig. 5.4. Owing to the anisotropy, the effective medium can significantly enhance the polarisation discrimination, which does not exist in the silicon-on-insulator platforms with isotropic claddings.

Coupling coefficient: K

To achieve a sufficiently high PER, the cladding configuration has to be properly selected, since the resultant refractive indices also affect the coupling coefficient that is a critical parameter to determine the total power transfer. According to Marcatili's theory (Marcatili, 1969), the coupling coefficient K of a directional coupler decreases exponentially as a function of g/ζ , where g is the distance of the coupling gap, while ζ is the $1/e$ evanescent field penetration depth into the coupling gap and can be expressed as (Marcatili, 1969):

$$\zeta = \frac{1}{\sqrt{(\frac{\pi}{A_{\text{gap}}})^2 - k_x^2}}, \quad (5.19)$$

where A_{gap} and k_x can be obtained from Eqs. (5.8), (5.10), and (5.11). Specifically, a smaller coupling gap g and/or a larger field penetration depth ζ can result in a higher coupling coefficient K . Accordingly, for an effective-medium-clad tapered directional coupler with a slightly varying small air gap, reducing the outer cladding refractive index will lead to an increased k_x thus an increased field penetration depth ζ . This results in an increased coupling coefficient K for both polarisations. It can be concluded that a lower refractive index is preferred to improve the coupling and thus achieve a higher transmission level for the desired mode, e.g., the E_{11}^y mode, while a higher refractive index is required to reduce the crosstalk level for the unwanted mode, e.g., the E_{11}^x mode. To this end, the effective medium with a finely tailorable anisotropic refractive index tensor can be exploited to satisfy such a requirement. Specifically, a

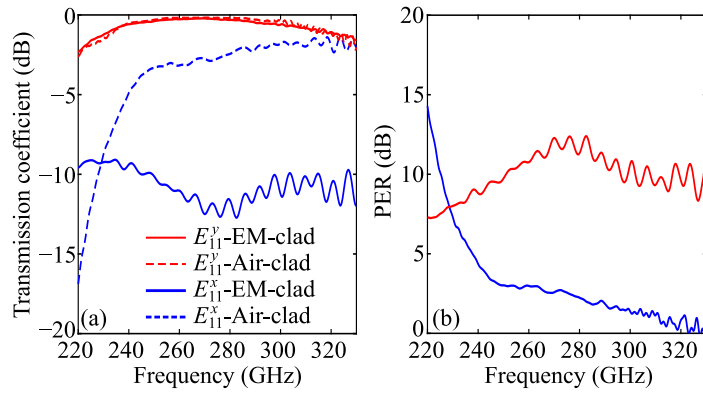


Figure 5.5. Performance comparison between a single tapered directional coupler cladded by effective medium (EM) and air, respectively. (a) Simulated transmission coefficient. (b) Simulated polarisation extinction ratio (PER). The PERs are derived by comparing the transmission coefficients between the E_{11}^y and E_{11}^x modes of a tapered coupler with an identical cladding as shown in (a). For both cases the coupler dimensions are identical with a sufficiently long coupling length ($3.5\lambda_0$) and a small coupling air gap (around $0.1\lambda_0$)

higher refractive index of the outer cladding for decreasing the coupling level of the E_{11}^x mode can be achieved with a small air fill factor, while a sufficiently high transmission for the E_{11}^y mode can be maintained due to a lower sensitivity to the refractive index change of the effective-medium-clad waveguide according to Eqs. (5.3) and (5.6).

Taking a single tapered directional coupler as an example, an optimal effective-medium cladding relative permittivity tensor $(\epsilon_x, \epsilon_y, \epsilon_z)$ has been obtained through CST simulation as $(4.01, 5.48, 4.01)$ resulting from a hole array configuration with $(a, d) = (100 \mu\text{m}, 80 \mu\text{m})$. As shown in Fig. 5.5, this cladding configuration can achieve an average transmission level of around -0.7 dB for the E_{11}^y mode and -11 dB for the E_{11}^x mode, leading to an average PER around 10 dB over the frequency range from 220 to 330 GHz. On the contrary, an air-clad coupler shows a comparable average transmission level for the E_{11}^y mode and around -3.7 dB for the E_{11}^x mode, resulting in an average PER around 3 dB. In this sense, compared to the case with air claddings, the effective medium claddings can provide an enhanced PER with a slightly decreased transmission level.

5.4 Characteristics of the polarization splitter

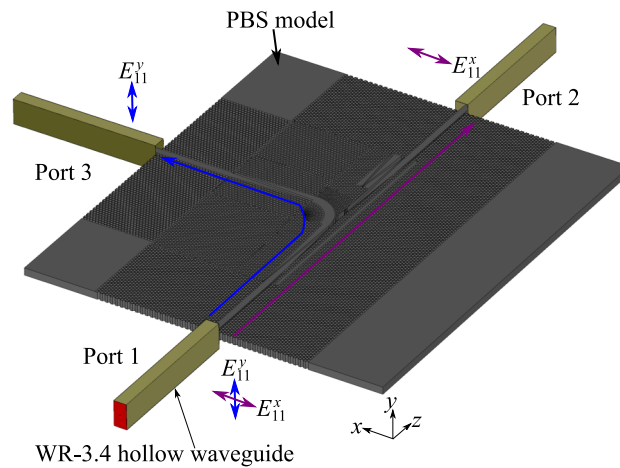


Figure 5.6. 3D model of the effective-medium-clad polarisation splitter fed by the WR-3.4 hollow waveguides. The presented setup is for E_{11}^x mode excitation, while the E_{11}^y mode can be excited by rotating the hollow waveguides by 90° . Similar feeding strategies are applicable to the measurements.

5.4 Characteristics of the polarization splitter

This section discusses the characteristics of the proposed polarisation splitter, including transmission, path crosstalk, ports isolation, higher-order mode conversion, and dispersion. Since the sample fabrication has been delayed due to COVID restrictions, all the results presented in this chapter are from simulations, which are performed with CST Microwave Studio 2021. A realistic loss tangent of 3×10^{-5} and a relative permittivity of 11.68 for silicon are adopted in CST full-wave simulations, where WR-3.4 hollow waveguides are used for excitation with the tapering structures inserted as shown in Fig. 5.6. Various polarisation splitter samples will be fabricated in the near future based on the standard deep reactive-ion etching (DRIE) process with a 4-inch high-resistivity float-zone silicon wafer that has a thickness of $250 \mu\text{m}$. The measurements will be conducted by using a Keysight vector network analyser (VNA) with VDI WR-3.4 extension modules spanning from 220–330 GHz, while the samples will be fed the same way as in the simulations in a setup similar to that presented in Chapters 3 and 4.

5.4.1 Transmission and path crosstalk

This section focuses on the transmission and path crosstalk of the proposed polarisation splitter by investigating the effects introduced by the accessories, i.e., the mode filter

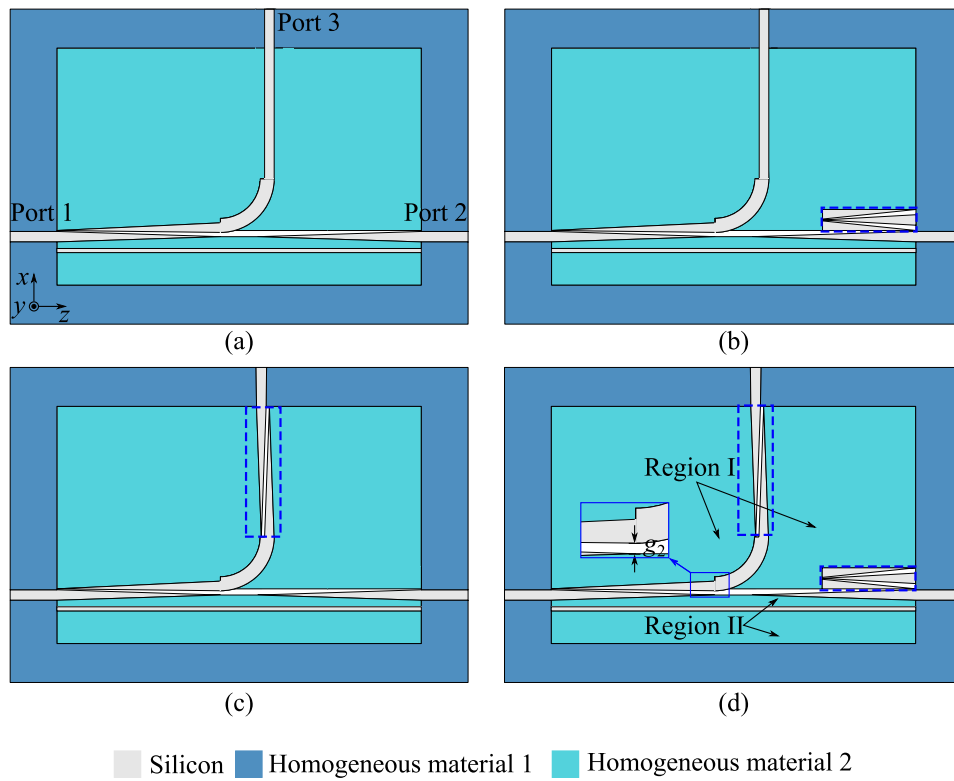


Figure 5.7. Evolution of polarisation splitter design based on the homogeneous artificial materials. (a) Bare polarisation splitter. (B) Polarisation splitter with a mode filter along the E_{11}^x -path. (c) Polarisation splitter with double tapered directional couplers along the E_{11}^y -path. (d) Final design. The dimensions are given in Fig. 5.4. The relative permittivity tensor $(\epsilon_x, \epsilon_y, \epsilon_z)$ is $(2.75, 3.83, 2.75)$ and $(4.01, 5.48, 4.01)$ for the homogeneous materials 1 and 2, respectively. The relative permittivity tensors are calculated based on the hole configurations shown in Figs. 5.4(b) and (c).

in the E_{11}^x -path and the additional tapered coupler in the E_{11}^y -path. The investigations correspond to the analyses given in Section 5.3.2.

Effects from the accessories

To investigate the effects from the accessories, as shown in Fig 5.7, homogeneous artificial materials are adopted to expedite the design process and save computing resources. The relative permittivity tensors of the homogeneous materials are calculated based on the Maxwell-Garnett effective medium theory (Subashiev and Luryi, 2006), and the results correspond to the hole configurations shown in Figs. 5.4(b) and (c). Various designs are considered including the bare polarisation splitter, the polarisation splitter with the mode filter along the E_{11}^x -path, and the polarisation splitter with double tapered

5.4.1 Transmission and path crosstalk

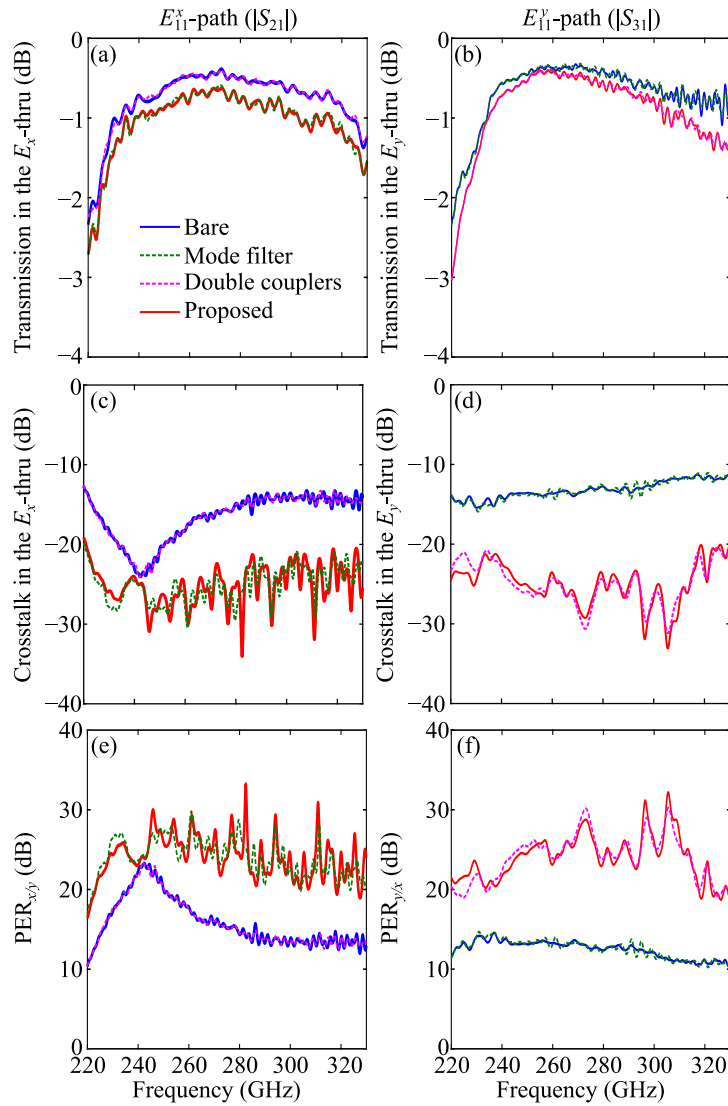


Figure 5.8. Simulated S -parameters of the polarisation splitter with various accessories as shown in Fig. 5.7. Transmission for (a) the E_{11}^x mode along the E_{11}^x -path and (b) the E_{11}^y mode along the E_{11}^y -path. Crosstalk for (c) the E_{11}^y mode in the E_{11}^x -path and (d) the E_{11}^x mode in the E_{11}^y -path. Polarisation extinction ratio for (e) the E_{11}^x -path and (f) the E_{11}^y -path.

directional couplers along the E_{11}^y -path. Their performance is compared to that of the final design as shown in Fig 5.7(d). As shown in Fig. 5.8, the bare polarisation splitter can achieve a comparable transmission level for the E_{11}^x and E_{11}^y modes ranging from -2.1 to -0.3 dB together with an average crosstalk level of -14 dB leading to average polarisation extinction ratios above 10 dB over the WR-3.4 band. To further reduce the crosstalk in the E_{11}^x -path, the E_{11}^y mode filter is introduced as shown in Fig. 5.7(b) leading to the average crosstalk decreased by around 10 dB as shown in Figs. 5.8(c). This is because the E_{11}^y component is coupled to the tapered coupler with most of power

trapped in the filter and eventually leaked into the claddings. As shown in Figs. 5.8(a), the filter slightly decreases the transmission level of the E_{11}^x mode by around 0.2 dB due to a small portion of power coupled to the filter. As a result, compared to the bare splitter, the polarisation extinction ratio for the E_{11}^x mode is improved by around 10 dB, as shown in Fig. 5.8(e). This filtering process further shows that the tapered coupler has a distinct effect on the power transfer for the two orthogonal polarisations as proved in Section 5.3.2.

To minimise the crosstalk of the E_{11}^x mode in the E_{11}^y -path, an additional tapered directional coupler is introduced along the E_{11}^y -path as shown in Fig. 5.7(c). Consequently, the crosstalk level is reduced by around 10 dB as shown in Fig. 5.8(d). It is noted that the additional coupler can slightly degrade the transmission of the E_{11}^y mode due to the additional coupling loss as illustrated in Fig. 5.8(b). However, the polarisation extinction ratio for the E_{11}^y mode is significantly improved compared to that of the bare polarisation splitter as shown in Fig. 5.8(f). Such an improvement also leverages the polarisation dependence of the tapered coupler that can support a much higher power transfer for the E_{11}^y mode than that for the E_{11}^x mode.

Consequently, the combination of the mode filter and the double tapered couplers leads to the optimal design as shown in Fig 5.7(d). Owing to these accessories, the final design achieves an average polarisation extinction ratio above 20 dB for both orthogonal modes as shown in Figs 5.8(e) and (f), while the transmission levels are slightly decreased due to these accessories as compared in Figs. 5.8(a) and (b). This well demonstrates that the polarisation extinction ratios for both E_{11}^x and E_{11}^y modes of the proposed polarisation splitter can be significantly enhanced by leveraging the polarisation dependence of the tapered directional couplers. It is noteworthy that a proper selection of the effective medium is critical to achieve such optimal performance.

Implementation on the effective medium platform

The polarisation splitter full model based on the air-silicon effective medium is shown in Fig. 5.6. To verify the implementation accuracy, the S -parameters of the polarisation splitters cladded by the artificial homogeneous materials and the air-silicon effective media are compared as shown in Fig. 5.9. Here, the coupling gap g_2 as indicated in Fig. 5.7(d) is reduced to 75 μm from 91.5 μm for the realised polarisation splitter. This is to compensate the discrepancies caused by the approximations of the effective refractive indices used in the homogeneous materials. With such an adjustment, the

5.4.1 Transmission and path crosstalk

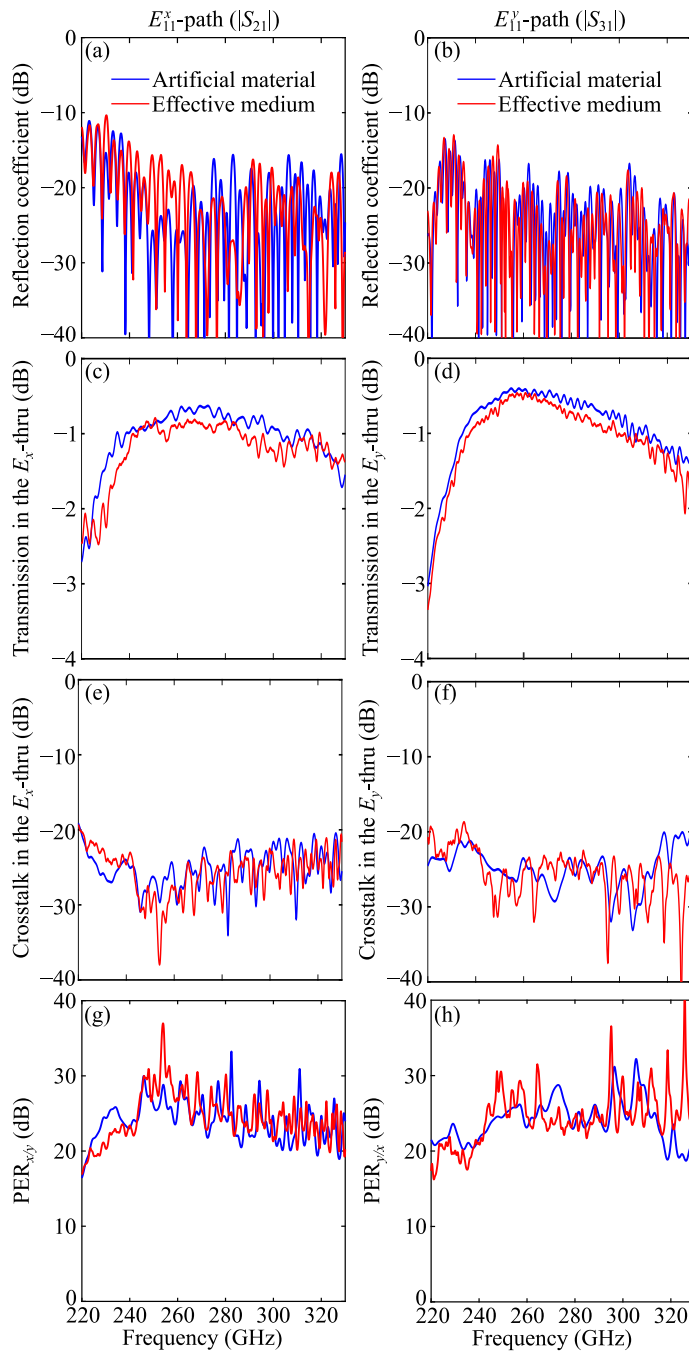


Figure 5.9. Simulated S -parameters of the polarisation splitters with artificial and effective medium claddings as shown in Figs. 5.4(a) and Fig. 5.7(d). Reflection coefficients for (a) the E_{11}^x mode and (b) the E_{11}^y mode at the input port. Transmission for (c) the E_{11}^x mode along the E_{11}^x -path and (d) the E_{11}^y mode along the E_{11}^y -path. Crosstalk for (e) the E_{11}^y mode in the E_{11}^x -path and (f) the E_{11}^x mode in the E_{11}^y -path. Polarisation extinction ratio for (g) the E_{11}^x -path and (h) the E_{11}^y -path.

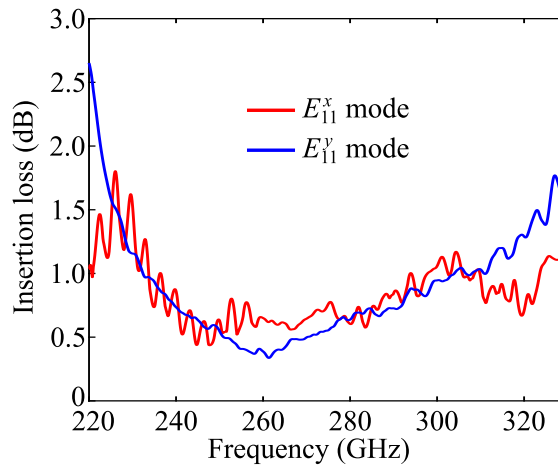


Figure 5.10. Simulated insertion losses of the effective-medium-clad polarisation splitter for the E_{11}^x and E_{11}^y modes. The insertion losses are extracted from the transmission coefficients of the E_{11}^x mode and the E_{11}^y mode as shown in Figs. 5.9(c) and (d), where the loss caused by the straight feeding waveguides are de-embedded.

S-parameters of the realised design agree well with those of the polarisation splitter clad by artificial homogeneous materials as shown in Fig. 5.9. It is observed that the transmission levels for both polarisations are slightly decreased by around 0.2 dB for the realised polarisation splitter due to the scattering loss of the effective medium. However, such a slight decrement in transmission has a negligible impact on the overall performance considering the average polarisation extinction ratios above 20 dB for both modes as illustrated in Figs 5.9(g) and (h). As shown in Fig. 5.10, the average insertion loss for both modes is below 1 dB. It is noted that the relatively high insertion loss at the lower frequency bound for the E_{11}^y mode is mainly due to the coupling loss of the tapered couplers together with the bending loss, and it can be improved by increasing the bending radius without changing other characteristics.

The simulated E -field distributions for the E_{11}^x and E_{11}^y modes at various frequencies are shown in Fig. 5.11. As shown in Figs. 5.11(a), (c), and (e), for the E_{11}^x mode, the waves can be transmitted well through the bridging coupling over the whole WR-3.4 band, while the waves coupled to the E_{11}^y -path are leaked into the claddings at the second tapered coupler leading to a low crosstalk level in the E_{11}^y -path. At the E_{11}^y mode filter side, there is a small portion of waves coupled to the air slots. Additionally, the discontinuity of the thin bridging waveguide at the interface between the tapered and straight waveguides causes wave leakage especially at the lower frequencies. These effects together can slightly reduce the transmission level of the E_{11}^x mode. For the E_{11}^y mode, as shown in

5.4.1 Transmission and path crosstalk

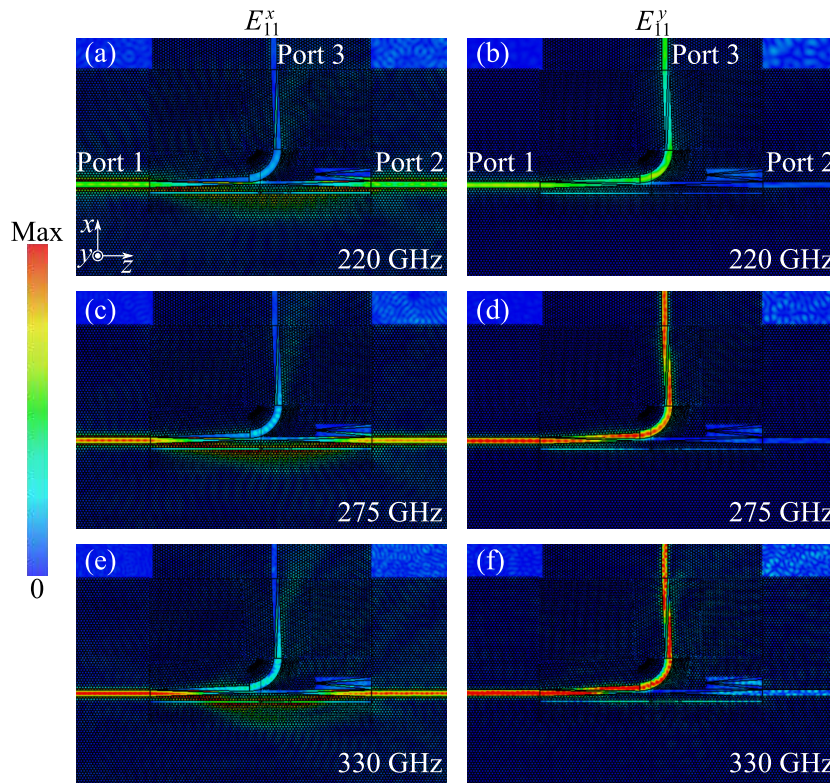


Figure 5.11. Simulated maximum E -field amplitude distributions of the effective-medium-clad polarisation splitter for the E_{11}^x and E_{11}^y modes at various frequencies. E -field distributions at 220 GHz, 275 GHz, and 330 GHz for (a, c, e) the E_{11}^x mode and (b, d, f) for the the E_{11}^y mode. All the E -field distributions are in linear scale and normalized by the same factor.

Figs. 5.11(b), (d), and (f), most of the power can be transmitted through the tapered couplers with a small portion of power leaking to the E_{11}^x -path and trapped by the mode filter eventually. Additionally, the radiation at the sharp bend is relatively strong at the lower frequencies leading to a higher insertion loss. In addition, the wave leakage at the second tapered coupler can lead to a gradually increased insertion loss with frequency increasing as shown in Fig. 5.10. This can be improved by reducing the coupling gap but at a slight expense of the polarisation extinction ratio due to an increased E_{11}^x mode crosstalk.

A comparison of various polarisation splitting devices at optical and terahertz frequencies is shown in Table 5.2. Compared to the microwave-inspired orthomode transducers, the proposed polarisation splitter has a good integrability and comparable broad bandwidth and insertion loss. In particular, the proposed polarisation splitter has a much simpler structure and lower fabrication complexity compared to the turnstile OMT operating at the WR-3.4 band (Gomez-Torrent *et al.*, 2018). Compared to the

Table 5.2. Comparison of polarisation splitting devices at optical and terahertz frequencies.
(λ_c : Central wavelength)

	Frequency (THz)	Bandwidth ^a	PER (dB) $E_{11}^x (E_{11}^y)$	Average IL (dB) $E_{11}^x (E_{11}^y)$	Footprint ^b
Microwave-inspired OMT (Unintegrated)					
Asymmetrical OMT (Reck and Chattopadhyay, 2013)	0.500–0.600	18.2%	>20 (>20)	2.5 (2.5)	3D
Turnstile OMT (Gomez-Torrent <i>et al.</i> , 2018)	0.220–0.330	40.0%	> 30 (>30)	0.3 (0.3)	3D
Double-ridged waveguide OMT (Gonzalez and Kaneko, 2021a)	0.275–0.500	58.0%	> 30 (>30)	<1.0 (<1.0)	3D
Optical PBS (Integrated)					
Photonic inverse design (Shen <i>et al.</i> , 2015)	191.57–195.57	2.1%	>10 (>10)	<1.5 (<1.5)	$1.6\lambda_c \times 1.6\lambda_c$
MMI-based (Hosseini <i>et al.</i> , 2011)	190.48–196.72	3.2%	>15 (>15)	0.8 (1.7)	$0.6\lambda_c \times 0.6\lambda_c$
PC-based (Zabelin <i>et al.</i> , 2007)	187.02–196.61	5.0%	> 10 (>10)	5.6 (4.6)	$11.7\lambda_c \times 11.7\lambda_c$
MZI-based (Dai <i>et al.</i> , 2011a)	188.09–199.34	5.8%	>10 (>10)	0.5 (0.5)	$3.1\lambda_c \times 580.7\lambda_c$
Directional-coupler-based					
Hybrid-plasmonic-waveguide coupler (Lou <i>et al.</i> , 2012)	191.69–196.08	2.3%	>15 (>15)	<1.5 (<1.5)	$1.3\lambda_c \times 3.3\lambda_c$
Hybrid-dielectric-waveguide coupler (Liu <i>et al.</i> , 2019)	190.47–195.44	2.6%	>20 (>20)	<0.4 (<0.15)	$0.8\lambda_c \times 3.4\lambda_c$
Triple-bent-waveguide coupler (Ong <i>et al.</i> , 2017)	186.34–197.37	5.8%	>20 (>20)	0.6 (0.3)	$3.8\lambda_c \times 8.3\lambda_c$
Tapered-waveguide coupler (Chen <i>et al.</i> , 2016)	185.19–197.37	6.4%	>15 (>15)	<0.4 (<0.4)	$0.9\lambda_c \times 18.5\lambda_c$
Multimode-tapered-waveguide coupler (Augustin <i>et al.</i> , 2007)	185.19–197.37	6.4%	>15 (>15)	3.5 (6.75)	$8.2\lambda_c \times 1718.0\lambda_c$
Bent-waveguide coupler (Wu <i>et al.</i> , 2017)	186.34–203.39	8.8%	>20 (>20)	<1.0 (<1.0)	$4.5\lambda_c \times 13.0\lambda_c$
Bent-slot-waveguide coupler (Dai <i>et al.</i> , 2011b)	184.05–204.08	10.3%	>10 (>10)	<0.3 (<0.3)	$0.9\lambda_c \times 4.6\lambda_c$
Grating-waveguide coupler (Li <i>et al.</i> , 2020)	181.26–209.06	15.6%	>20 (>20)	<1.0 (<1.0)	$2.8\lambda_c \times 50.0\lambda_c$
Terahertz PBS (Integrated)					
Conventional directional coupler based (Deng <i>et al.</i> , 2021a)	0.445–0.475	6.5%	>8 (>8)	<2.0 (<3.0)	$0.8\lambda_c \times 11.5\lambda_c$
Asymmetric directional coupler based (Deng <i>et al.</i> , 2021b)	0.438–0.470	7.1%	>10 (>10)	3.7 (3.7)	$0.3\lambda_c \times 23.5\lambda_c$
This work (Integrated)	0.223–0.330	38.7%	>20 (>20)	<1.0 (<1.0)	$4.7\lambda_c \times 7.2\lambda_c$

^a The bandwidth is defined based on the claimed minimum polarisation extinction ratio (PER).

^b The footprint for the OMT block is mainly determined by the flange size of the rectangular waveguide.

5.4.2 Port isolation and higher-order modes

existing optical and terahertz polarisation splitters, the proposed design has a much broader bandwidth together with a low insertion loss (IL), high polarisation extinction ratio (PER), and a reasonably compact footprint. Specifically, despite a similar PER and an insertion loss, the proposed polarisation splitter can achieve a more than twofold bandwidth on a much more compact footprint compared to the subwavelength-grating-waveguide-coupler based optical polarisation splitter (Li *et al.*, 2020). In addition, compared to the terahertz polarisation splitters that are directly scaled down from the optical domain (Deng *et al.*, 2021a,b), the proposed polarisation splitter has a bandwidth that is about six times as broad, with superior insertion loss and PER. Furthermore, owing to the effective medium increasing the polarisation birefringence, the proposed design has a much shorter footprint compared to those terahertz polarisation splitters based on the conventional silicon-on-insulator platforms (Deng *et al.*, 2021a,b).

5.4.2 Port isolation and higher-order modes

This section investigates the isolation between the E_{11}^x - and E_{11}^y -path together with the higher-order mode conversion across the device. As shown in Fig. 5.12, the isolation between the two output ports are good with an average $|S_{32(23)}|$ below -25 dB and below -20 dB for the E_{11}^x and E_{11}^y modes, respectively. The weaker isolation level for the E_{11}^y mode is mainly due to the interference between the two paths, and it can be improved by further increasing the isolation distance l_{sp} between the tapered waveguides along the E_{11}^x -path as shown in Fig. 5.4(e) but at an expense of a larger device footprint.

To investigate the higher-order mode conversion across the device due to the structural discontinuities, monitoring ports able to capture multiple modes are adopted at Ports 2 and 3 of the polarisation splitter in CST simulations. In this case, the hollow waveguides at the two output ports are removed, while the tapering structures are kept so as to achieve good impedance matching to air (Lees *et al.*, 2021a). It is noteworthy that these higher-order modes are not measurable in experiments since the WR-3.4 hollow waveguides can only accept the fundamental modes. The simulated results show that for the in-plane polarisation, there are two higher-order modes excited including E_{21}^x and E_{31}^x modes with their electromagnetic fields shown in Figs. 5.13(a)–(d), while for the out-of-plane polarisation, a quasi- E_{21}^y mode is excited as shown in Figs. 5.13(e) and (f). It is noted that the higher-order modes only can be converted from the fundamental modes with identical polarisations, while the cross-polarisation conversion does not

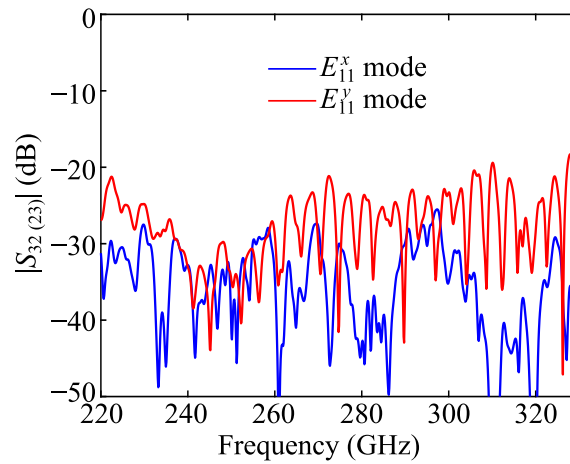


Figure 5.12. S -parameters for the port isolation for the effective-medium-based polarisation splitter model.

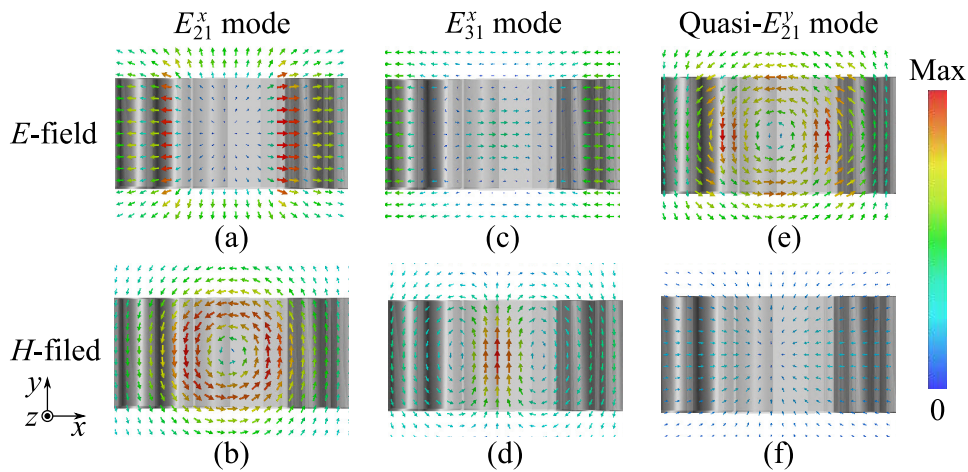


Figure 5.13. Simulated electromagnetic field distributions of higher-order modes. (a) E -field and (b) H -field distributions for the E_{21}^x mode. (c) E -field and (d) H -field distributions for the E_{31}^x mode. (e) E -field and (f) H -field distributions for the quasi- E_{21}^y mode.

exist. The simulated transmission coefficients of the higher-order modes for the two polarisations are shown in Fig. 5.14. At Port 2, the transmission level for the E_{31}^x mode is relatively high at the lower frequency bound compared to the E_{21}^x mode as illustrated in Fig. 5.14(a), and this would slightly decrease the power level of the fundamental mode at the lower frequencies. At Port 3, the transmission coefficients for both E_{21}^x and E_{31}^x modes are with an average level below -20 dB as shown in Fig. 5.14(c). For the quasi- E_{21}^y , the average $|S_{21}|$ is below -25 dB as shown in Fig. 5.14(b), which has a negligible impact on the overall performance. Additionally, the weak transmission

5.4.3 Dispersion

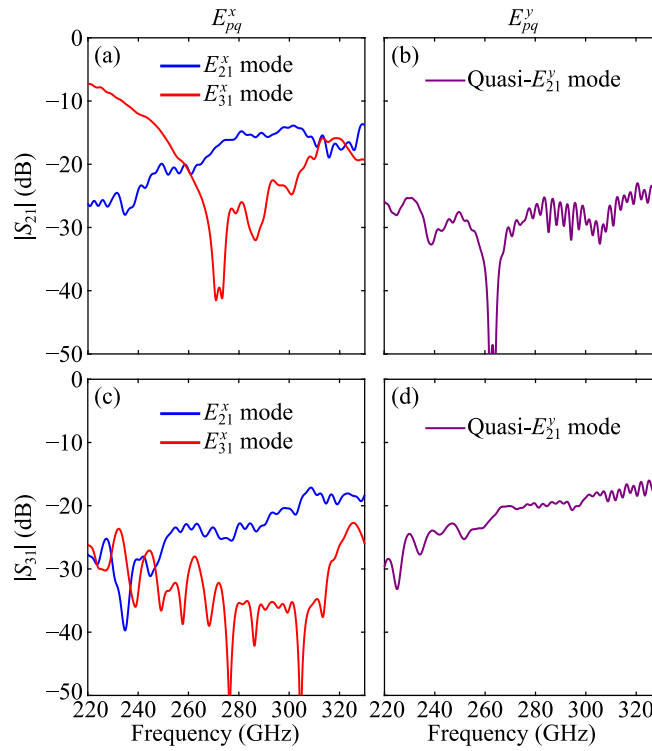


Figure 5.14. S-parameters for the higher-order modes conversion. Transmission coefficients for (a) E_{pq}^x and (b) E_{pq}^y modes at Port 2, and (c) E_{pq}^x and (d) E_{pq}^y modes at Port 3. The input is E_{11}^x at Port 1 for E_{pq}^x , and E_{11}^y at Port 1 for E_{pq}^y .

level for the quasi- E_{21}^y mode at Port 3 as shown in Fig. 5.14(d) would not degrade the transmission for the E_{11}^y mode.

5.4.3 Dispersion

To investigate the dispersion characteristics of the proposed effective-medium-clad polarisation splitter, the group velocity dispersions (GVDs) for both fundamental modes across the two paths are simulated as shown in Fig. 5.15. As shown in Fig. 5.15(a), the GVD along the E_{11}^x -path ranges from 6.8 to 1.5 ps/(THz mm) for the E_{11}^x mode. The mildly varying GVD for the E_{11}^x mode shows a low dispersion across its through path allowing for a high data rate. For the E_{11}^y -path, the GVD varies from 23 to 0 ps/(THz mm), the relatively high dispersion from 220 to 240 GHz is mainly due to the intrinsic dispersion of the straight waveguide and the two tapered couplers along the E_{11}^y path. Nevertheless, such a dispersion characteristic for the E_{11}^y mode is comparable to that of a single straight waveguide as discussed in Chapter 3.

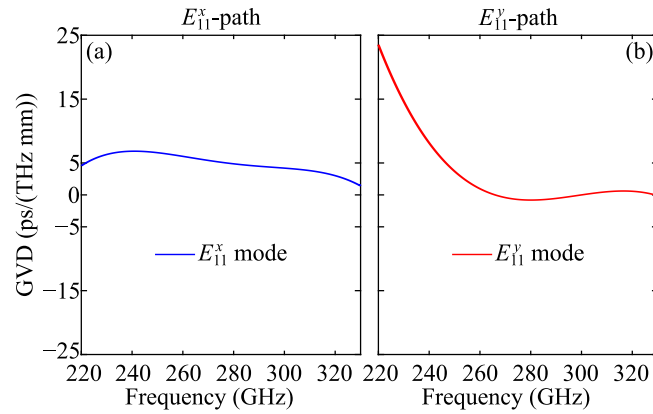


Figure 5.15. Simulated group velocity dispersions (GVDs) of the effective-medium-clad polarisation splitter. GVDs of (a) the E_{11}^x mode at Port 2 and (b) the E_{11}^y mode at Port 3. The group velocity dispersions are calculated from the simulated unwrapped phase. To remove the numerical phase noise, sixth-order polynomial curve fitting is carried out on the phase curves. The contributions by the regular straight waveguide sections are de-embedded.

5.5 Conclusion

This chapter has presented a terahertz polarisation splitter based on the effective-medium-clad dielectric waveguide platform over 220–330 GHz. The polarisation splitter has been comprehensively studied for various characteristics including transmission, crosstalk, isolation, higher-order modes, and dispersion. The simulated results show that the proposed polarisation splitter can achieve a 20-dB PER fractional bandwidth of 40% with an average insertion loss below 1 dB on a footprint of $4.7\lambda_{0,275} \times 7.2\lambda_{0,275}$. Furthermore, the proposed polarisation splitter has isolation levels above 25 dB. The average transmission level below -20 dB for the higher order modes dose not degrade the performance overall. The proposed polarisation splitter show a low dispersion with GVD ranging from 6.8 to 1.5 ps/(THz mm) for the E_{11}^x mode and from 23 to 0 ps/(THz mm) for the E_{11}^y mode. The thorough analysis shows that the combination of the tapered directional coupler and the effective medium can provide a high-performance polarisation splitter in terms of bandwidth and polarisation extinction ratio. In particular, the effective medium platform yields high design flexibility and low fabrication complexity, compared to the conventional silicon-on-insulator (SOI) platform based polarisation splitters. The 40% fractional bandwidth of the proposed polarisation splitter is nearly 20 times as wide as the optical C-band. This is much needed for terahertz applications especially for communications with increased channel capacities. Considering scalability, the proposed concepts can benefit integrated photonics at large.

Chapter 6



Summary and outlook

THIS chapter concludes the work presented in this thesis. Chapter 1 introduces the background and motivations of this doctoral thesis, while the original contributions are detailed in Chapters 2 to 5, including the effective-medium-clad dielectric waveguides, peripherals such as bends and crossings, Bragg grating filters, and polarisation splitters. The outlook for future developments on the proposed integrated platform is presented in this chapter.

6.1 Thesis conclusion

This doctoral thesis is centred around the development of a terahertz integrated platform with high efficiency, low dispersion, and broad bandwidth. Importantly, the proposed platform is envisaged to accommodate various passive and active components for a wide range of applications especially for high-volume short-range communications. Based on the Maxwell-Garnett effective medium theory, a series of all-silicon self-supporting substrateless terahertz integrated waveguides have been proposed, where the effective medium concept was shown to add significant design flexibility. To enable an integrated platform, various fundamental building blocks including bends, crossings, and directional couplers have been presented, while an in-depth analysis of the propagation characteristics has been performed. To demonstrate the on-chip signal processing capabilities of the proposed platform, two class of functional components have been proposed including filters and polarisation splitters. All these components feature high efficiency and broad bandwidth much needed for terahertz applications, while the effective medium plays a critical role in enhancing the device performance. This section provides a brief summary on the original contributions of the thesis.

Effective-medium-clad dielectric waveguides and peripherals

This part contains Chapters 2 and 3, and it presents the air-silicon effective-medium-clad dielectric waveguides and various peripherals including bends, crossings, and directional couplers. Based on the Maxwell-Garnett effective medium theory and Marcatili's theory, various characteristics have been comprehensively investigated including transmission, dispersion, cross polarisation, and crosstalk between two parallel waveguides together with the characteristics of bends and crossing. All the designs presented have been experimentally validated showing an extremely low loss, low dispersion, and broad bandwidth. To verify the performance of the proposed waveguides in terahertz communications, real-time bit-error-rate testing experiments have been performed, while an uncompressed 4K-resolution video transmission has been demonstrated.

Effective-medium-clad Bragg grating filters

This part consists of Chapter 4, which has discussed the Bragg grating filters implemented onto the effective medium waveguide platform. Owing to the effective medium, the proposed Bragg grating filters have been shown to break through the bandwidth limitations of this filter type based on the conventional

silicon-on-insulator platform. Various filter characteristics have been thoroughly investigated including transmission, bandwidth, central frequency, and dispersion. All the samples have been experimentally validated showing almost perfect agreements between the simulations and measurements. Additionally, fabrication tolerances and their effects have been investigated to provide insight into the details of the realised filter samples. The proposed Bragg grating filter type is potentially applicable at high terahertz frequencies above 1 THz. The proposed low-loss, low-dispersion, and broadband bandstop filters are much needed for communications applications, while the concept to enhance the filter performance by leveraging the effective medium can benefit both the microwave and optical domains.

Effective-medium-clad polarisation splitters

This part constitutes Chapter 5, where a planar effective-medium-clad polarisation splitter has been proposed. Attributed to the combination of the tapered directional couplers and effective medium, the proposed polarisation splitter can achieve a large fractional bandwidth with high polarisation extinction ratio and low insertion loss on a compact footprint. Various characteristics of the proposed polarisation splitter have been studied including transmission, crosstalk, isolation, higher-order mode conversion, and dispersion. It can be foreseen that such a polarisation splitter can benefit the short-distance communications toward increased channel capacities.

6.2 Outlook

This thesis has proposed a terahertz integrated platform based on the concept of effective medium and importantly provides a sound theoretical basis for future developments. To demonstrate the capabilities of this platform, spectral filtering and polarisation manipulation have been implemented, while more advanced functionalities can be further conceptualised and developed based on the achievements in this thesis. As a complement of the thesis, this section suggests further possibilities and list necessary advances to accelerate adoption of the proposed concepts, with the aim of resolving current research challenges and enabling practical applications of integrated terahertz technologies.

Broadside radiating antennas

Directional antennas with broadside radiation patterns are critical for communications. Although, the conventional microwave patch antennas can provide a simple solution, the significant ohmic loss introduced by the metal will significantly degrade the antenna efficiency at terahertz bands. To this end, it is necessary to investigate all-dielectric ground-plane-free broadside radiation antennas for terahertz applications. The proposed effective medium platform can provide an attractive support for such kind of antennas and further investigations are required to resolve the difficulties arising from the absence of a ground plane.

Beamforming networks

Wideband planar beamforming networks are crucial for many applications especially for passive antennas and radars capable of scanning their beams in a wide spatial angular range. This is critical for wireless communications to improve the channel diversity and capacity. To achieve a high-efficiency and broadband terahertz beamforming network, the effective medium waveguide platform is an ideal base, which can accommodate Butler matrix, Rotman lens, and Luneburg lens. However, there exist tradoffs in terms of structural compactness, port isolations, and bandwidth. Therefore, more investigations are needed for high-performance implementation of such constrained lenses/networks.

Bandpass filters

As one of the most fundamental and important components, bandpass filters are still not available on the proposed effective-medium platform. It is possible to realise a bandpass filter based on the platform by implementing photonic crystal cavities along the guiding channel, but the resulting bandwidth remains relatively narrow. Alternatively, the bandpass filtering function can be achieved by cascading multiple Bragg grating filters operating at various frequencies. However, this strategy can lead to a relatively large footprint. Furthermore, due to the relatively weak boundary conditions of the silicon material at the air interface, it is challenging to achieve a high-Q dielectric resonator to build the bandpass filters with good frequency selectivity. To overcome the material limitations, more advanced structures need to be investigated.

Polarisation rotators

Polarisation rotators together with the polarisation splitters are indispensable for polarisation diversity systems, which are critical for integrated circuits and

coherent receivers for communications. However, compared to the polarisation splitters, it is much more difficult to realise a waveguide-based polarisation rotator since, from symmetry considerations, it is challenging to rotate the optical axis of the dielectric waveguide. Although the conventional optical methodologies have offered possibilities in the open literature, the resultant achievable bandwidth is narrow. To this end, it is worth investing efforts to investigate a high-efficiency and broadband terahertz polarisation rotator based on the proposed platform.

Terahertz active devices

To realise an on-chip terahertz communications system, active and non-linear devices such as transceivers and mixers are indispensable. The highly efficient and broadband effective medium waveguide platform can be an ideal frontend to accommodate various active components such as RTDs and PIN diodes to realise such active devices. However, it is challenging to achieve an efficient interface between the dielectric waveguide and the active components due to the distinct difference in physical size and modal distributions. Thus, to achieve an efficient interface for high-density terahertz integrated circuits, further research efforts should be made.

In conclusion, it can be foreseen that the proposed effective-medium platform can greatly benefit terahertz integrated circuits and accelerate the practical applications of terahertz technologies, in analogy to the microstrip lines to microwave and silicon-on-insulator platform to photonic integrated circuits.

Transmission sensitivity to waveguide misalignment

Due to the evanescent fields, the proposed effective-medium-clad dielectric waveguides are sensitive to the alignment with respect to the feeding hollow waveguides. Typically, the mode with a weaker wave confinement that has a larger evanescent field penetration into the claddings is more sensitive to the misalignment. To investigate the sensitivity of the waveguide transmission to the misalignment, the transmission coefficients have been simulated for a 1-cm waveguide with various imperfect alignment over the WR-2.8 band. As shown in Fig. A.1(a), for the E_{11}^x mode a 5-deg rotation with respect to the propagation axis or a 0.1-mm shift with respect to the hollow waveguide can cause significant fluctuations. For the E_{11}^y mode, as shown in Fig. A.1(b), a 0.1-mm shift can lead to strong fluctuations in the transmission coefficient, while the performance is more robust to the rotation with slight fluctuations of the transmission coefficient at lower frequencies. Compared to the E_{11}^x mode, the E_{11}^y mode is less sensitive to the misalignment mainly due to its stronger wave confinement at the WR-2.8 band. It is noteworthy that given an identical wafer thickness, i.e., 200 μm , the wave confinement for the E_{11}^y mode will be degraded at the WR-3.4 band especially at the lower frequencies as discussed in Chapter 3, leading to a higher sensitivity to the waveguide misalignment compared to that of the E_{11}^x mode.

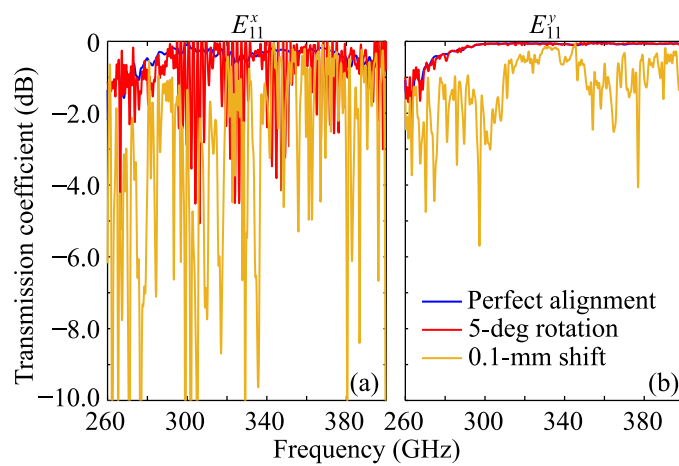


Figure A.1. Simulated transmission coefficients for waveguide misalignment investigation.

Simulated transmission coefficients for (a) the E_{11}^x mode and (b) the E_{11}^y mode over a 1-cm straight waveguide with perfect alignment, 5-deg rotation relative to the propagation axis, and 0.1-mm shift in the x -direction for the E_{11}^x mode and in the y -direction for the E_{11}^y mode with respect to the feeding hollow waveguides. The coordinates for the waveguide shift can be referred to Fig. 2.4, while the positions of the feeding hollow waveguides are fixed as shown in Fig. 2.5(b).

Packaging for practical applications



The proposed effective-medium-clad waveguide platform can realise various components with complex functions not achievable with typical metallic components. The introduction of the hollow-waveguide-based packaging would enable the components to stand alone and provide a good interface with WR-3.4 waveguide in measurement. Furthermore, the packaging allows for a component-level testing in a much more flexible manner compared to the “all-in-one” testing strategy.

A possible package consisting of a top and a base is shown in Fig. B.1(a-c). To avoid the influence of the package on the evanescent fields that extend around $100\ \mu\text{m}$ in the y -direction, an air cavity is created as shown in Fig. B.1(d). In addition, WR-3.4 hollow waveguides and flanges can be included for interfacing the platform with external components. To investigate the impact of the package on the waveguide performance, the transmission coefficients for a 1-cm waveguide with and without the package are simulated. As shown in Fig. B.2, the transmission levels for the waveguide with and without the package are comparable for both E_{11}^x and E_{11}^y modes. However, there are significant fluctuations at lower frequencies for the cases with package. These resonances mainly result from the cavity resonance effects, and the stronger resonance for the E_{11}^y mode is due to its weaker wave confinement leading to stronger radiation. To minimise the resonance, terahertz absorbers are needed inside the cavity.

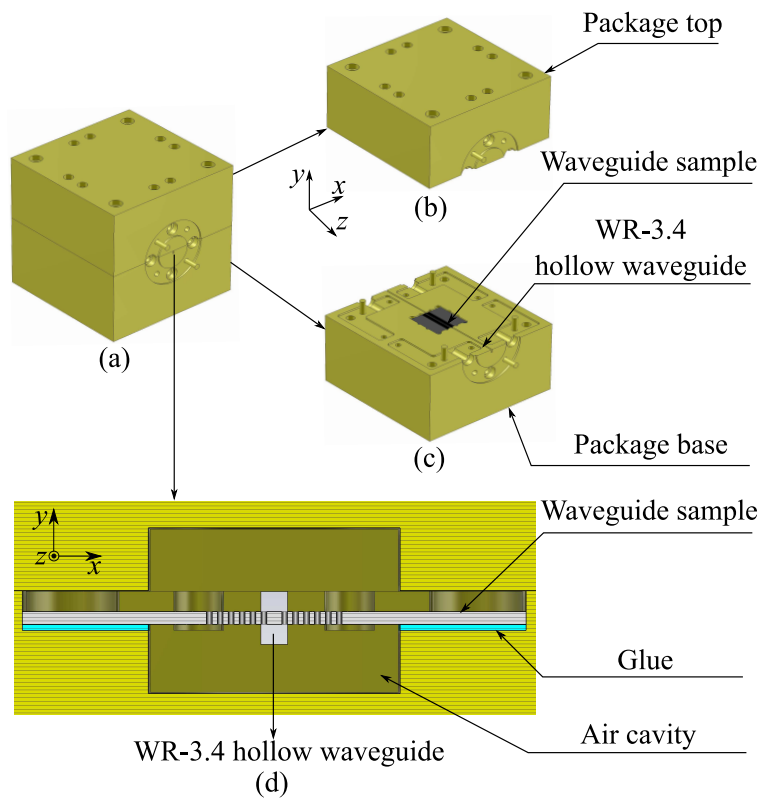


Figure B.1. Hollow waveguide package accommodating a 1-cm effective-medium-clad dielectric waveguide. Perspective view of (a) assembled package, (b) package top, and (c) package base. (e) Magnified cross-sectional view of the package.

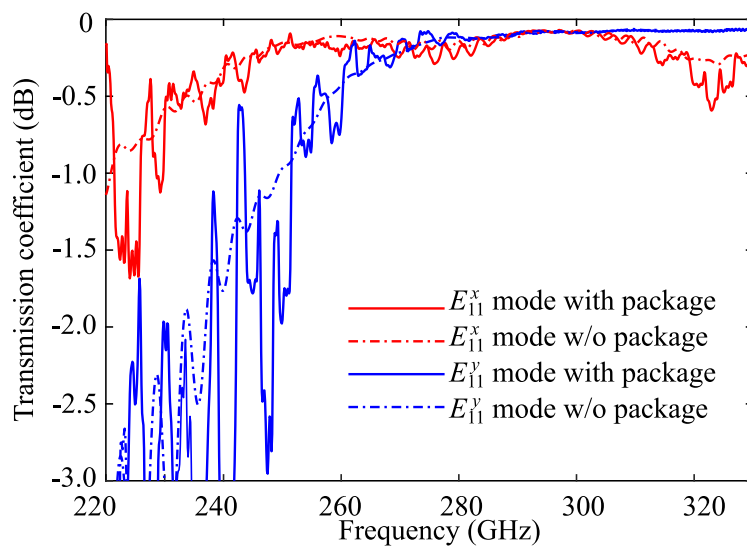



Figure B.2. Simulated transmission coefficients of 1-cm waveguide sample with and without package.

Coupling loss between effective-medium-clad waveguide and WR-3.4 hollow waveguide



The measured and simulated coupling losses between the straight waveguide and a WR-3.4 hollow waveguide are extracted by subtracting the loss of the straight section from the complete setup shown in Fig. 3.5. As illustrated in Fig. C.1, the measured coupling loss for the E_{11}^x mode is below 0.248 dB, and the measurement agrees well with simulation. This level of coupling loss is equivalent to that of the photonic crystal waveguide presented in Tsuruda *et al.* (2015b). However, for the E_{11}^y mode, due to the weaker wave confinement, the coupling loss is higher at lower frequencies. It is found that the sample alignment is more problematic for the E_{11}^y mode resulting in the relatively higher measured coupling loss across the band. This is related to the sample orientation with respect to the feed rectangular waveguide. As shown in Fig. C.2, the claddings along the E -field of the hollow waveguide are different for the two modes. For the E_{11}^x mode, it is the effective medium cladding, which could help the waveguide achieve a better wave confinement, so that it matches better the mode field distribution of the hollow waveguide that is strongly confined. However, for the E_{11}^y mode, the cladding along the y -direction is air, where the wave confinement is weaker and the mode matching between the sample and the hollow waveguide is worse leading to a relatively higher coupling loss.

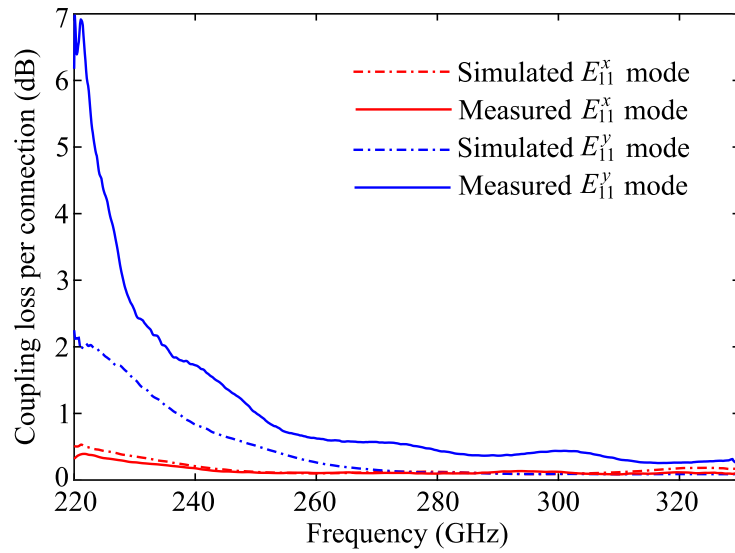


Figure C.1. Coupling loss between the effective-medium-clad waveguide and the WR-3.4 hollow waveguide for the E_{11}^x and the E_{11}^y modes.

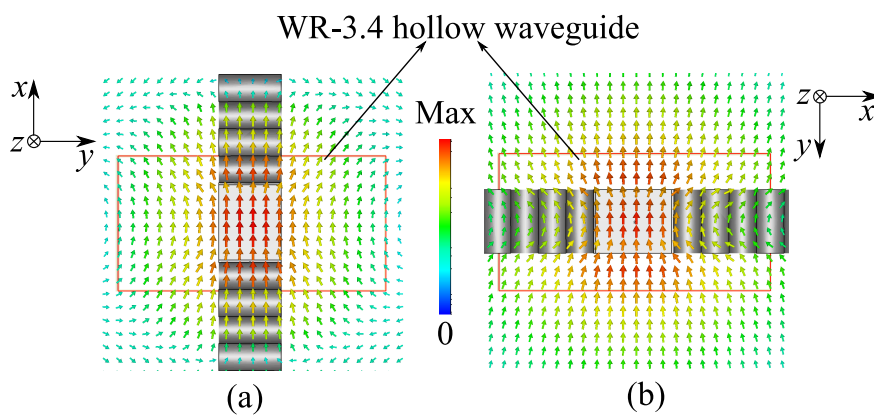


Figure C.2. Simulated E -field distributions at 275 GHz. (a) the E_{11}^x and (b) the E_{11}^y modes with different waveguide sample orientations with respect to the WR-3.4 hollow waveguide.

Bibliography

- AGRAWAL-G. P. (2012). *Fiber-Optic Communication Systems*, John Wiley & Sons.
- AKIKI-E., VERSTUYFT-M., KUYKEN-B., WALTER-B., FAUCHER-M., LAMPIN-J.-F., DUCOURNAU-G., AND VANWOLLEGHEM-M. (2020). High Q THz photonic crystal cavity on a low loss suspended silicon platform, *IEEE Transactions on Terahertz Science and Technology*, **11**(1), pp. 42–53.
- AL-ATTAR-T., AND LEE-T. H. (2005). Monolithic integrated millimeter-wave IMPATT transmitter in standard CMOS technology, *IEEE Transactions on Microwave Theory and Techniques*, **53**(11), pp. 3557–3561.
- AL HADI-R., SHERRY-H., GRZYB-J., ZHAO-Y., FORSTER-W., KELLER-H. M., CATHELIN-A., KAISER-A., AND PFEIFFER-U. R. (2012). A 1 k-pixel video camera for 0.7–1.1 terahertz imaging applications in 65-nm CMOS, *IEEE Journal of Solid-State Circuits*, **47**(12), pp. 2999–3012.
- ALONSO-DEL PINO-M., JUNG-KUBIAK-C., RECK-T., LEE-C., AND CHATTOPADHYAY-G. (2019). Micromachining for advanced terahertz: Interconnects and packaging techniques at terahertz frequencies, *IEEE Microwave Magazine*, **21**(1), pp. 18–34.
- AMARLOO-H., AND SAFAVI-NAEINI-S. (2021). Terahertz slot dielectric waveguide implemented on the silicon-BCB-quartz platform, *IEEE Transactions on Terahertz Science and Technology*, **11**(3), pp. 310–317.
- AMARLOO-H., RANJKESH-N., AND SAFAVI-NAEINI-S. A. (2018). Terahertz silicon-BCB-quartz dielectric waveguide: an efficient platform for compact THz systems, *IEEE Transactions on Terahertz Science and Technology*, **8**(2), pp. 201–208.
- AO-X., LIU-L., WOSINSKI-L., AND HE-S. (2006). Polarization beam splitter based on a two-dimensional photonic crystal of pillar type, *Applied Physics Letters*, **89**(17), art. no. 171115.

BIBLIOGRAPHY

- ASAYAMA-S., AND KAMIKURA-M. (2009). Development of double-ridged waveguide orthomode transducer for the 2 MM band, *Journal of Infrared, Millimeter, and Terahertz Waves*, **30**(6), pp. 573–579.
- ATAKARAMIANS-S., AFSHAR-S., FISCHER-B. M., ABBOTT-D., AND MONRO-T. M. (2008). Porous fibers: a novel approach to low loss THz waveguides, *Optics Express*, **16**(12), pp. 8845–8854.
- ATAKARAMIANS-S., V-S. A., MONRO-T. M., AND ABBOTT-D. (2013). Terahertz dielectric waveguides, *Advances in Optics and Photonics*, **215**, pp. 169–215.
- AUGUSTIN-L. M., VAN DER TOL-J. J., HANFOUG-R., DE LAAT-W. J., VAN DE MOOSDIJK-M. J., VAN DIJK-P. W., OEI-Y.-S., AND SMIT-M. K. (2007). A single etch-step fabrication-tolerant polarization splitter, *Journal of lightwave technology*, **25**(3), pp. 740–746.
- BALAKRISHNAN-J., FISCHER-B. M., AND ABBOTT-D. (2009). Sensing the hygroscopicity of polymer and copolymer materials using terahertz time-domain spectroscopy, *Applied Optics*, **48**(12), pp. 2262–2266.
- BARWICZ-T., WATTS-M. R., POPOVIĆ-M. A., RAKICH-P. T., SOCCI-L., KÄRTNER-F. X., IPPEN-E. P., AND SMITH-H. I. (2007). Polarization-transparent microphotonic devices in the strong confinement limit, *Nature Photonics*, **1**(1), pp. 57–60.
- BEUERLE-B., CAMPION-J., SHAH-U., AND OBERHAMMER-J. (2018). A very low loss 220–325 GHz silicon micromachined waveguide technology, *IEEE Transactions on Terahertz Science and Technology*, **8**(2), pp. 248–250.
- BIRMAN-J., EDWARDS-S. F., FRIEND-R., REES-M., SHERRINGTON-D., AND VENEZIANO-G. (2009). *Effective Medium Theory Principles and Applications*, II edn, Oxford Science Publications.
- BOGAERTS-W., DUMON-P., VAN THOURHOUT-D., AND BAETS-R. (2007). Low-loss, low-cross-talk crossings for silicon-on-insulator nanophotonic waveguides, *Optics Letters*, **32**(19), pp. 2801–2803.

- CAO-L., ELSHAARI-A., ABOKETAF-A., AND PREBLE-S. (2010). Adiabatic couplers in SOI waveguides, *Conference on Lasers and Electro-Optics*, Optical Society of America, art. no. CThAA2.
- CHANG-Y.-J., AND LI-W.-L. (2011). Directional-coupler-based polarization splitting in asymmetric metal/multi-insulator configuration for optical nanocircuitry, *IEEE Photonics Technology Letters*, **24**(6), pp. 458–460.
- CHEBEN-P., HALIR-R., SCHMID-J. H., ATWATER-H. A., AND SMITH-D. R. (2018). Subwavelength integrated photonics, *Nature*, **560**(7720), pp. 565–572.
- CHEN-D., XIAO-X., WANG-L., GAO-G., LIU-W., AND YANG-Q. (2016). Broadband, fabrication-tolerant polarization beam splitters based on a tapered directional coupler, *IEEE Photonics Technology Letters*, **28**(19), pp. 2074–2077.
- CHENG-Z., WANG-J., HUANG-Y., AND REN-X. (2019). Realization of a compact broadband polarization beam splitter using the three-waveguide coupler, *IEEE Photonics Technology Letters*, **31**(22), pp. 1807–1810.
- CHEN-S., SHI-Y., HE-S., AND DAI-D. (2015). Compact monolithically-integrated hybrid (de) multiplexer based on silicon-on-insulator nanowires for PDM-WDM systems, *Optics Express*, **23**(10), pp. 12840–12849.
- CHEN-Z., ZHENG-Y., KANG-X., LU-B., AND CUI-B. (2013). WR-2.8 band micromachined rectangular waveguide filter, *Journal of Infrared, Millimeter, and Terahertz Waves*, **34**(12), pp. 847–855.
- CHROSTOWSKI-L., AND HOCHBERG-M. (2015). *Silicon Photonics Design: from Devices to Systems*, Cambridge University.
- CISCO. (2017). *Cisco Visual Networking Index: Forecast and Methodology, 2016-2021*, Cisco.
- COOK-J. (1955). Tapered velocity couplers, *Bell System Technical Journal*, **34**(4), pp. 807–822.

BIBLIOGRAPHY

- CORREA-R. A., AND KNIGHT-J. (2008). Specialty fibers: novel process eases production of hollow-core fiber, *Laser Focus World*, **44**, pp. 67–71.
- DAI-D. (2012). Silicon polarization beam splitter based on an asymmetrical evanescent coupling system with three optical waveguides, *Journal of Lightwave Technology*, **30**(20), pp. 3281–3287.
- DAI-D., AND BOWERS-J. E. (2011). Novel ultra-short and ultra-broadband polarization beam splitter based on a bent directional coupler, *Optics Express*, **19**(19), pp. 18614–18620.
- DAI-D., BAUTERS-J., AND BOWERS-J. E. (2012). Passive technologies for future large-scale photonic integrated circuits on silicon: polarization handling, light non-reciprocity and loss reduction, *Light Science & Applications*, **1**(3), pp. 500–505.
- DAI-D., LI-C., WANG-S., WU-H., SHI-Y., WU-Z., GAO-S., DAI-T., YU-H., AND TSANG-H.-K. (2018). 10-channel mode (de) multiplexer with dual polarizations, *Laser & Photonics Reviews*, **12**(1), art. no. 1700109.
- DAI-D., WANG-Z., AND BOWERS-J. E. (2011a). Considerations for the design of asymmetrical Mach–Zehnder interferometers used as polarization beam splitters on a submicrometer silicon-on-insulator platform, *Journal of Lightwave Technology*, **29**(12), pp. 1808–1817.
- DAI-D., WANG-Z., AND BOWERS-J. E. (2011b). Ultrashort broadband polarization beam splitter based on an asymmetrical directional coupler, *Optics Letters*, **36**(13), pp. 2590–2592.
- DAI-D., ZHU-Z., ZHAO-W., XIE-Y., AND LIU-D. (2021). Silicon photonic devices for wavelength/mode-division-multiplexing, *Integrated Optics: Design, Devices, Systems and Applications VI*, Vol. 11775, International Society for Optics and Photonics, art. no. 117750E.
- DAI-J., ZHANG-J., ZHANG-W., AND GRISCHKOWSKY-D. (2004). Terahertz time-domain spectroscopy characterization of the far-infrared absorption and index of refraction of

- high-resistivity, float-zone silicon, *Journal of the Optical Society of America B*, **21**(7), pp. 1379–1386.
- DENG-W., CHEN-L., WANG-R., WANG-Z., YUAN-S., YU-Y., WU-X., AND ZHANG-X. (2021a). A compact terahertz polarization beam splitter based on directional coupler, *CLEO: Science and Innovations*, Optical Society of America, pp. STh2F–2.
- DENG-W., CHEN-L., YUAN-S., WANG-Y., WANG-R., WANG-Z., YU-Y., WU-X., AND ZHANG-X. (2021b). Silicon-based integrated terahertz polarization beam splitters, *Journal of Lightwave Technology*.
- DESLANDES-D., AND WU-K. (2001a). Integrated microstrip and rectangular waveguide in planar form, *IEEE Microwave and Wireless Components Letters*, **11**(2), pp. 68–70.
- DESLANDES-D., AND WU-K. (2001b). Integrated transition of coplanar to rectangular waveguides, *2001 IEEE MTT-S International Microwave Symposium Digest (Cat. No. 01CH37157)*, Vol. 2, IEEE, pp. 619–622.
- DING-J.-Q., SHI-S.-C., ZHOU-K., ZHAO-Y., LIU-D., AND WU-W. (2017). WR-3 band quasi-elliptical waveguide filters using higher order mode resonances, *IEEE Transactions on Terahertz Science and Technology*, **7**(3), pp. 302–309.
- DING-Y., LIU-L., PEUCHERET-C., AND OU-H. (2012). Fabrication tolerant polarization splitter and rotator based on a tapered directional coupler, *Optics Express*, **20**(18), pp. 20021–20027.
- D’MELLO-Y., EL-FIKY-E., SKORIC-J., KUMAR-A., HUI-M., WANG-Y., GUENIN-L., PATEL-D., AND PLANT-D. V. (2018). Compact, angled polarization splitter: characterization of broadband performance and fabrication tolerance, *IEEE Photonics Journal*, **10**(6), pp. 1–12.
- DOLATSHA-N. (2013). *Hybrid Integrated of Millimeter Wave Circuits based on Low-Loss Dielectric Waveguides*, PhD thesis, ETH Zurich.
- DONG-Z., LI-X., YU-J., AND CHI-N. (2012a). 6×128 -Gb/s Nyquist-WDM PDM-16QAM generation and transmission over 1200-km SMF-28 with SE of 7.47 b/s/Hz, *Journal of Lightwave Technology*, **30**(24), pp. 4000–4005.

BIBLIOGRAPHY

- DONG-Z., LI-X., YU-J., AND CHI-N. (2012b). 6×144 -Gb/s Nyquist-WDM PDM-64QAM generation and transmission on a 12-GHz WDM grid equipped with Nyquist-band pre-equalization, *Journal of Lightwave Technology*, **30**(23), pp. 3687–3692.
- DUPUIS-A., STOEFLER-K., UNG-B., DUBOIS-C., AND SKOROBOGATIY-M. (2011). Transmission measurements of hollow-core THz Bragg fibers, *Journal of the Optical Society of America B*, **28**(4), pp. 896–907.
- EBLABLA-A. M., LI-X., WALLIS-D. J., GUINEY-I., AND ELGAID-K. (2016). GaN on low-resistivity silicon THz high-Q passive device technology, *IEEE Transactions on Terahertz Science and Technology*, **7**(1), pp. 93–97.
- FANG-L., ZHENG-S., AND WANG-J. (2021). Design of on-chip polarimetry with stokes-determined silicon photonic circuits, *Optics Express*, **29**(20), pp. 31026–31035.
- FRANKEL-M. Y., GUPTA-S., VALDMANIS-J. A., AND MOUROU-G. A. (1991). Terahertz attenuation and dispersion characteristics of coplanar transmission lines, *IEEE Transactions on Microwave Theory and Techniques*, **39**(6), pp. 910–916.
- FUJITA-M., AND NAGATSUMA-T. (2016). Photonic crystal technology for terahertz system integration, *Terahertz Physics, Devices, and Systems X: Advanced Applications in Industry and Defense*, Vol. 9856, International Society for Optics and Photonics, art. no. 98560P.
- GALLOT-G., JAMISON-S., MCGOWAN-R., AND GRISCHKOWSKY-D. (2000). Terahertz waveguides, *Journal of the Optical Society of America B*, **17**(5), pp. 851–863.
- GAO-W., FUMEAUX-C., AND WITHAYACHUMNANKUL-W. (2020a). All-silicon terahertz components towards efficient integrated systems, *2020 45th International Conference on Infrared, Millimeter, and Terahertz Waves (IRMMW-THz)*, IEEE, pp. 1–2.
- GAO-W., LEE-W. S., FUMEAUX-C., AND WITHAYACHUMNANKUL-W. (2021). Effective-medium-clad bragg grating filters, *APL Photonics*, **6**(7), art. no. 076105.

- GAO-W., LEE-W. S., YU-X., FUJITA-M., NAGATSUMA-T., FUMEAUX-C., AND WITHAYACHUMNANKUL-W. (2020b). Characteristics of effective-medium-clad dielectric waveguides, *IEEE Transactions on Terahertz Science and Technology*, **11**(1), pp. 28–41.
- GAO-W., YU-X., FUJITA-M., NAGATSUMA-T., FUMEAUX-C., AND WITHAYACHUMNANKUL-W. (2019). Effective-medium-cladded dielectric waveguides for terahertz waves, *Optics Express*, **27**(26), pp. 38721–38734.
- GOLDSMITH-A. (2005). *Wireless Communications*, Cambridge University.
- GOMEZ-TORRENT-A., SHAH-U., AND OBERHAMMER-J. (2018). Compact silicon-micromachined wideband 220–330-GHz turnstile orthomode transducer, *IEEE Transactions on Terahertz Science and Technology*, **9**(1), pp. 38–46.
- GONZALEZ-A., AND ASAYAMA-S. (2018). Double-ridged waveguide orthomode transducer (OMT) for the 67–116-GHz band, *Journal of Infrared, Millimeter, and Terahertz Waves*, **39**(8), pp. 723–737.
- GONZALEZ-A., AND KANEKO-K. (2021a). High-performance wideband double-ridged waveguide OMT for the 275–500 GHz band, *IEEE Transactions on Terahertz Science and Technology*, **11**(3), pp. 345–350.
- GONZALEZ-A., AND KANEKO-K. (2021b). High-performance wideband double-ridged waveguide omt for the 275–500 GHz band, *IEEE Transactions on Terahertz Science and Technology*, **11**(3), pp. 345–350.
- GOTO-M., QUEMA-A., TAKAHASHI-H., ONO-S., AND SARUKURA-N. (2004). Teflon photonic crystal fiber as terahertz waveguide, *Japanese Journal of Applied Physics*, **43**(2B), art. no. L317.
- GROPPI-C., NAVARRINI-A., AND CHATTOPADHYAY-G. (2010). A waveguide orthomode transducer for 385–500 GHz, *Millimeter, Submillimeter, and Far-Infrared Detectors and Instrumentation for Astronomy V*, Vol. 7741, International Society for Optics and Photonics, art. no. 77412D.

BIBLIOGRAPHY

- GUERBOUKHA-H., NALLAPPAN-K., CAO-Y., SEGHILANI-M., AZAÑA-J., AND SKOROBOGATIY-M. (2019). Planar porous components for low-loss terahertz optics, *Advanced Optical Materials*, **7**(15), art. no. 1900236.
- HAN-H., PARK-H., CHO-M., AND KIM-J. (2002). Terahertz pulse propagation in a plastic photonic crystal fiber, *Applied Physics Letters*, **80**(15), pp. 2634–2636.
- HASSANI-A., DUPUIS-A., AND SKOROBOGATIY-M. (2008). Porous polymer fibers for low-loss terahertz guiding, *Optics Express*, **16**(9), pp. 6340–6351.
- HEADLAND-D., FUJITA-M., AND NAGATSUMA-T. (2019). Bragg-mirror suppression for enhanced bandwidth in terahertz photonic crystal waveguides, *IEEE Journal of Selected Topics in Quantum Electronics*, **26**(2), pp. 1–9.
- HEADLAND-D., FUJITA-M., AND NAGATSUMA-T. (2020a). Half-maxwell fisheye lens with photonic crystal waveguide for the integration of terahertz optics, *Optics Express*, **28**(2), pp. 2366–2380.
- HEADLAND-D., MONNAI-Y., ABBOTT-D., FUMEAUX-C., AND WITHAYACHUMNANKUL-W. (2018a). Tutorial: Terahertz beamforming, from concepts to realizations, *APL Photonics*, **3**(5), art. no. 051101.
- HEADLAND-D., WITHAYACHUMNANKUL-W., YAMADA-R., FUJITA-M., AND NAGATSUMA-T. (2018b). Terahertz multi-beam antenna using photonic crystal waveguide and luneburg lens, *APL Photonics*, **3**(12), art. no. 126105.
- HEADLAND-D., WITHAYACHUMNANKUL-W., YU-X., FUJITA-M., AND NAGATSUMA-T. (2020b). Unclad microphotronics for terahertz waveguides and systems, *Journal of Lightwave Technology*, **38**(24), pp. 6853–6862.
- HESLER-J. L., AND CROWE-T. W. (2007). NEP and responsivity of THz zero-bias Schottky diode detectors, *2007 Joint 32nd International Conference on Infrared and Millimeter Waves and the 15th International Conference on Terahertz Electronics*, IEEE, pp. 844–845.

- HE-Y., ZHANG-Y., WANG-X., LIU-B., JIANG-X., QIU-C., SU-Y., AND SOREF-R. (2017). Silicon polarization splitter and rotator using a subwavelength grating based directional coupler, *2017 Optical Fiber Communications Conference and Exhibition (OFC)*, IEEE, pp. 1–3.
- HIDAKA-T., MINAMIDE-H., ITO-H., NISHIZAWA-J.-I., TAMURA-K., AND ICHIKAWA-S. (2005). Ferroelectric PVDF cladding terahertz waveguide, *Journal of Lightwave Technology*, **23**(8), pp. 2469–2473.
- HOLLOWAY-J. W., BOGLIONE-L., HANCOCK-T. M., AND HAN-R. (2017). A fully integrated broadband sub-mmwave chip-to-chip interconnect, *IEEE Transactions on Microwave Theory and Techniques*, **65**(7), pp. 2373–2386.
- HONG-J. M., RYU-H. H., PARK-S. R., JEONG-J. W., LEE-S. G., LEE-E.-H., PARK-S.-G., WOO-D., KIM-S., AND BEOM-HOAN-O. (2003). Design and fabrication of a significantly shortened multimode interference coupler for polarization splitter application, *IEEE Photonics Technology Letters*, **15**(1), pp. 72–74.
- HOSSEINI-A., RAHIMI-S., XU-X., KWONG-D., COVEY-J., AND CHEN-R. (2011). Ultracompact and fabrication-tolerant integrated polarization splitter, *Optics Letters*, **36**(20), pp. 4047–4049.
- ISHIBASHI-T., MURAMOTO-Y., YOSHIMATSU-T., AND ITO-H. (2013). Continuous THz wave generation by photodiodes up to 2.5 THz, *2013 38th International Conference on Infrared, Millimeter, and Terahertz Waves (IRMMW-THz)*, IEEE, pp. 1–2.
- ITO-H., AND ISHIBASHI-T. (2016). InP/InGaAs Fermi-level managed barrier diode for broadband and low-noise terahertz-wave detection, *Japanese Journal of Applied Physics*, **56**(1), art. no. 014101.
- IZUMI-R., SUZUKI-S., AND ASADA-M. (2017). 1.98 THz resonant-tunneling-diode oscillator with reduced conduction loss by thick antenna electrode, *2017 42nd International Conference on Infrared, Millimeter, and Terahertz Waves (IRMMW-THz)*, IEEE, pp. 1–2.

BIBLIOGRAPHY

- JIAO-Y., DAI-D., SHI-Y., AND HE-S. (2009). Shortened polarization beam splitters with two cascaded multimode interference sections, *IEEE Photonics Technology Letters*, **21**(20), pp. 1538–1540.
- JONES-E., AND SHIMIZU-J. (1958). Coupled-transmission-line directional couplers, *IRE Transactions on Microwave Theory and Techniques*, **6**(4), pp. 403–410.
- KAMIKURA-M., NARUSE-M., ASAYAMA-S., SATOU-N., SHAN-W., AND SEKIMOTO-Y. (2010). Development of a submillimeter double-ridged waveguide ortho-mode transducer (OMT) for the 385–500 GHz band, *Journal of Infrared, Millimeter, and Terahertz Waves*, **31**(6), pp. 697–707.
- KARL-N. J., MCKINNEY-R. W., MONNAI-Y., MENDIS-R., AND MITTLEMAN-D. M. (2015). Frequency-division multiplexing in the terahertz range using a leaky-wave antenna, *Nature Photonics*, **9**(11), pp. 717–720.
- KATAYAMA-K., TAKANO-K., AMAKAWA-S., HARA-S., KASAMATSU-A., MIZUNO-K., TAKAHASHI-K., YOSHIDA-T., AND FUJISHIMA-M. (2016). A 300 GHz CMOS transmitter with 32-QAM 17.5 Gb/s/ch capability over six channels, *IEEE Journal of Solid-State Circuits*, **51**(12), pp. 3037–3048.
- KAWAMOTO-Y., SHIBATA-N., UEMURA-Y., IWAMATSU-S., NISHIDA-Y., FUJITA-M., AND NAGATSUMA-T. (2021). Integrated resonant tunneling diode with rectangular waveguide I/O using photonic crystal interface, *2021 46th International Conference on Infrared, Millimeter, and Terahertz Waves (IRMMW-THz)*, IEEE, pp. 1–2.
- KENNETH-K. O., CHOI-W., ZHONG-Q., SHARMA-N., AND KIM-I. (2019). Opening terahertz for everyday applications, *IEEE Communications Magazine*, **57**(8), pp. 70–76.
- KHALID-A., DUNN-G., MACPHERSON-R., THOMS-S., MACINTYRE-D., LI-C., STEER-M., PAPAGEORGIU-V., THAYNE-I., AND KUBALL-M. (2014). Terahertz oscillations in an In_{0.53}Ga_{0.47}As submicron planar Gunn diode, *Journal of Applied Physics*, **115**(11), art. no. 114502.

- KIM-D. W., LEE-M. H., KIM-Y., AND KIM-K. H. (2015). Planar-type polarization beam splitter based on a bridged silicon waveguide coupler, *Optics Express*, **23**(2), pp. 998–1004.
- KIM-H.-S., AND RAMASWAMY-R. V. (1993). Tapered, both in dimension and in index, velocity coupler: theory and experiment, *IEEE Journal of Quantum Electronics*, **29**(4), pp. 1158–1167.
- KIM-S., NORDIN-G. P., CAI-J., AND JIANG-J. (2003). Ultracompact high-efficiency polarizing beam splitter with a hybrid photonic crystal and conventional waveguide structure, *Optics Letters*, **28**(23), pp. 2384–2386.
- KIM-Y., LEE-M. H., KIM-Y., AND KIM-K. H. (2018). High-extinction-ratio directional-coupler-type polarization beam splitter with a bridged silicon wire waveguide, *Optics Letters*, **43**(14), pp. 3241–3244.
- KITOH-T., TAKATO-N., YASU-M., AND KAWACHI-M. (2002). Bending loss reduction in silica-based waveguides by using lateral offsets, *Journal of Lightwave Technology*, **13**(4), pp. 555–562.
- KIYAT-I., AYDINLI-A., AND DAGLI-N. (2004). A compact silicon-on-insulator polarization splitter, *IEEE Photonics Technology Letters*, **17**(1), pp. 100–102.
- KNAP-W., DYAKONOV-M., COQUILLAT-D., TEPPE-F., DYAKONOVA-N., ŁUSAKOWSKI-J., KARPIERZ-K., SAKOWICZ-M., VALUSIS-G., AND SELIUTA-D. (2009). Field effect transistors for terahertz detection: Physics and first imaging applications, *Journal of Infrared, Millimeter, and Terahertz Waves*, **30**(12), pp. 1319–1337.
- KOENIG-S., LOPEZ-DIAZ-D., ANTES-J., BOES-F., HENNEBERGER-R., LEUTHER-A., TESSMANN-A., SCHMOGROW-R., HILLERKUSS-D., AND PALMER-R. (2013). Wireless sub-THz communication system with high data rate, *Nature Photonics*, **7**(12), pp. 977–981.
- KOJIMA-T., KIUCHI-H., UEMIZU-K., UZAWA-Y., KROUG-M., GONZALEZ-A., DIPPON-T., AND KAGEURA-T. (2020). Demonstration of a wideband submillimeter-wave

BIBLIOGRAPHY

- low-noise receiver with 4–21 GHz IF output digitized by a high-speed 32 GSps ADC, *Astronomy & Astrophysics*, **640**, art. no. L9.
- KOMATSU-M.-A., SAITOH-K., AND KOSHIBA-M. (2009). Design of miniaturized silicon wire and slot waveguide polarization splitter based on a resonant tunneling, *Optics Express*, **17**(21), pp. 19225–19234.
- KUDALIPPALLIYALIL-R., MURPHY-T. E., AND GRUTTER-K. E. (2020). Low-loss and ultra-broadband silicon nitride angled MMI polarization splitter/combiner, *Optics Express*, **28**(23), pp. 34111–34122.
- LEE-K. K., LIM-D. R., KIMERLING-L. C., SHIN-J., AND CERRINA-F. (2001). Fabrication of ultralow-loss Si/SiO₂ waveguides by roughness reduction, *Optics Letters*, **26**(23), pp. 1888–1890.
- LEES-H., GAO-W., AND WITHAYACHUMNANKUL-W. (2021a). All-silicon, low-cross-talk terahertz waveguide crossing based on effective medium, *Optics Letters*, **46**(21), pp. 5469–5472.
- LEES-H., GAO-W., AND WITHAYACHUMNANKUL-W. (2021b). Waveguide crossing based on air-silicon effective medium, *2021 46th International Conference on Infrared, Millimeter, and Terahertz Waves (IRMMW-THz)*, IEEE, pp. 1–2.
- LEE-W. S. L. (2018). *Terahertz Metasurfaces for Wideband Polarisation Control*, PhD thesis, The University of Adelaide.
- LIANG-J., GAO-W., LEES-H., AND WITHAYACHUMNANKUL-W. (2021). All-silicon terahertz planar horn antenna, *IEEE Antennas and Wireless Propagation Letters*, **20**(11), pp. 2181–2185.
- LIANG-T. K., AND TSANG-H. K. (2005). Integrated polarization beam splitter in high index contrast silicon-on-insulator waveguides, *IEEE Photonics Technology Letters*, **17**(2), pp. 393–395.
- LI-C., AND DAI-D. (2018). Compact polarization beam splitter based on a three-waveguide asymmetric coupler with a 340-nm-thick silicon core layer, *Journal of Lightwave Technology*, **36**(11), pp. 2129–2134.

- LI-C., ZHANG-M., BOWERS-J. E., AND DAI-D. (2020). Ultra-broadband polarization beam splitter with silicon subwavelength-grating waveguides, *Optics Letters*, **45**(8), pp. 2259–2262.
- LI-H., ATAKARAMIANS-S., YUAN-J., XIAO-H., WANG-W., LI-Y., WU-B., AND HAN-Z. (2018). Terahertz polarization-maintaining subwavelength filters, *Optics Express*, **26**(20), pp. 25617–25629.
- LIU-H., FENG-J., GE-J., ZHUANG-S., YUAN-S., CHEN-Y., LI-X., TAN-Q., YU-Q., AND ZENG-H. (2021). Tilted nano-grating based ultra-compact broadband polarizing beam splitter for silicon photonics, *Nanomaterials*, **11**(10), art. no. 2645.
- LIU-Y., CHANG-L., LI-Z., LIU-L., GUAN-H., AND LI-Z. (2019). Polarization beam splitter based on a silicon nitride–silica–silicon horizontal slot waveguide, *Optics Letters*, **44**(6), pp. 1335–1338.
- LOU-F., DAI-D., AND WOSINSKI-L. (2012). Ultracompact polarization beam splitter based on a dielectric–hybrid plasmonic–dielectric coupler, *Optics Letters*, **37**(16), pp. 3372–3374.
- LOUISELL-W. (1955). Analysis of the single tapered mode coupler, *The Bell System Technical Journal*, **34**(4), pp. 853–870.
- MACLEOD-H. A. (2017). *Thin-Film Optical Filters*, CRC Press.
- MA-J., SHRESTHA-R., MOELLER-L., AND MITTLEMAN-D. M. (2018). Invited article: Channel performance for indoor and outdoor terahertz wireless links, *APL Photonics*, **3**(5), art. no. 051601.
- MALEKABADI-A., CHARLEBOIS-S. A., DESLANDES-D., AND BOONE-F. (2014). High-resistivity silicon dielectric ribbon waveguide for single-mode low-loss propagation at F/G-bands, *IEEE Transactions on Terahertz Science and Technology*, **4**(4), pp. 447–453.
- MARCATILI-E. A. J. (1969). Dielectric rectangular waveguide and directional coupler for integrated optics, *Bell System Technical Journal*, **48**(7), pp. 2071–2102.

BIBLIOGRAPHY

- MA-T., MARKOV-A., WANG-L., AND SKOROBOGATIY-M. (2015). Graded index porous optical fibers—dispersion management in terahertz range, *Optics Express*, **23**(6), pp. 7856–7869.
- MCGOWAN-R., GALLOT-G., AND GRISCHKOWSKY-D. (1999a). Propagation of ultrawideband short pulses of terahertz radiation through submillimeter-diameter circular waveguides, *Optics Letters*, **24**(20), pp. 1431–1433.
- MCGOWAN-R., GALLOT-G., AND GRISCHKOWSKY-D. (1999b). Propagation of ultrawideband short pulses of terahertz radiation through submillimeter-diameter circular waveguides, *Optics Letters*, **24**(20), pp. 1431–1433.
- MEI-X., YOSHIDA-W., LANGE-M., LEE-J., ZHOU-J., LIU-P.-H., LEONG-K., ZAMORA-A., PADILLA-J., AND SARKOZY-S. (2015). First demonstration of amplification at 1 THz using 25-nm InP high electron mobility transistor process, *IEEE Electron Device Letters*, **36**(4), pp. 327–329.
- MELLONI-A., AND MARTINELLI-M. (2002). Synthesis of direct-coupled-resonators bandpass filters for WDM systems, *Journal of Lightwave Technology*, **20**(2), art. no. 296.
- MENDIS-R., AND GRISCHKOWSKY-D. (2001). Undistorted guided-wave propagation of subpicosecond terahertz pulses, *Optics Letters*, **26**(11), pp. 846–848.
- MILTON-A., AND BURNS-W. (1975). Tapered velocity couplers for integrated optics: Design, *Applied Optics*, **14**(5), pp. 1207–1212.
- MORIWAKI-A., OKANO-M., AND WATANABE-S. (2017). Internal triaxial strain imaging of visibly opaque black rubbers with terahertz polarization spectroscopy, *APL Photonics*, **2**(10), art. no. 106101.
- MOSALLAEI-H., AND RAHMAT-SAMII-Y. (2000a). Photonic band-gap (PBG) versus effective refractive index: a case study of dielectric nanocavities, *IEEE Antennas and Propagation Society International Symposium. Transmitting Waves of Progress to the Next Millennium. 2000 Digest. Held in conjunction with: USNC/URSI National Radio Science Meeting (C)*, Vol. 1, IEEE, pp. 338–341.

- MOSALLAEI-H., AND RAHMAT-SAMII-Y. (2000b). Photonic band-gap (PBG) versus effective refractive index: a case study of dielectric nanocavities, *IEEE Antennas and Propagation Society International Symposium.*, IEEE, pp. 338–341.
- MOSTAJERAN-A., CATHELIN-A., AND AFSHARI-E. (2017). A 170-GHz fully integrated single-chip FMCW imaging radar with 3-D imaging capability, *IEEE Journal of Solid-State Circuits*, **52**(10), pp. 2721–2734.
- MURANO-K., WATANABE-I., KASAMATSU-A., SUZUKI-S., ASADA-M., WITHAYACHUMNANKUL-W., TANAKA-T., AND MONNAI-Y. (2017). Low-profile terahertz radar based on broadband leaky-wave beam steering, *IEEE Transactions on Terahertz Science and Technology*, **7**(1), pp. 60–69.
- MURPHY-T. E. (2001). *Design, Fabrication and Measurement of Integrated Bragg Grating Optical Filters*, Massachusetts Institute of Technology.
- NAFTALY-M., AND MILES-R. E. (2007). Terahertz time-domain spectroscopy for material characterization, *Proceedings of the IEEE*, **95**(8), pp. 1658–1665.
- NAGATSUMA-T., DUCOURNAU-G., AND RENAUD-C. C. (2016). Advances in terahertz communications accelerated by photonics, *Nature Photonics*, **10**(6), pp. 371–379.
- NAGATSUMA-T., HORIGUCHI-S., MINAMIKATA-Y., YOSHIMIZU-Y., HISATAKE-S., KUWANO-S., YOSHIMOTO-N., TERADA-J., AND TAKAHASHI-H. (2013). Terahertz wireless communications based on photonics technologies, *Optics Express*, **21**(20), pp. 23736–23747.
- OKAMOTO-K. (2007). *Fundamentals of Optical Waveguides*, II edn, Academic.
- ONG-J. R., ANG-T. Y., SAHIN-E., PAWLINA-B., CHEN-G., TAN-D., LIM-S. T., AND PNG-C. E. (2017). Broadband silicon polarization beam splitter with a high extinction ratio using a triple-bent-waveguide directional coupler, *Optics Letters*, **42**(21), pp. 4450–4453.
- OTHONOS-A., KALLI-K., PUREUR-D., AND MUGNIER-A. (2006). Fibre Bragg gratings, *Wavelength Filters in Fibre Optics*, Springer, pp. 189–269.

BIBLIOGRAPHY

- OTTER-W., RIDLER-N., YASUKOCHI-H., SOEDA-K., KONISHI-K., YUMOTO-J., KUWATA-GONOKAMI-M., AND LUCYSZYN-S. (2017). 3D printed 1.1 THz waveguides, *Electronics Letters*, **53**(7), pp. 471–473.
- PARK-J.-D., KANG-S., THYAGARAJAN-S. V., ALON-E., AND NIKNEJAD-A. M. (2012). A 260 GHz fully integrated CMOS transceiver for wireless chip-to-chip communication, *2012 Symposium on VLSI Circuits (VLSIC)*, IEEE, pp. 48–49.
- PATROVSKY-A., AND WU-K. (2006). Substrate integrated image guide (SIIG)- A planar dielectric waveguide technology for millimeter-wave applications, *IEEE Transactions on Microwave Theory and Techniques*, **54**(6), pp. 2872–2879.
- PATROVSKY-A., WU-K., AND SYNTHESIZED-A. (2006). Substrate integrated image guide (SIIG)— a low-loss waveguide for millimetre-wave applications, *IEEE Transactions on Microwave Theory and Techniques*, **1**, pp. 1–4.
- PENADES-J. S., ORTEGA-MOÑUX-A., NEDELJKOVIC-M., WANGÜEMERT-PÉREZ-J., HALIR-R., KHOKHAR-A., ALONSO-RAMOS-C., QU-Z., MOLINA-FERNÁNDEZ-I., AND CHEBEN-P. (2016). Suspended silicon mid-infrared waveguide devices with subwavelength grating metamaterial cladding, *Optics Express*, **24**(20), pp. 22908–22916.
- PÉREZ-ESCUADERO-J. M., QUEMADA-C., GONZALO-R., AND EDERRA-I. (2020). Design of 300 GHz combined doubler/subharmonic mixer based on Schottky diodes with integrated MMIC based local oscillator, *Electronics*, **9**(12), art. no. 2112.
- PFAU-T., PEVELING-R., HAUDEN-J., GROSSARD-N., PORTE-H., ACHIAM-Y., HOFFMANN-S., IBRAHIM-S. K., ADAMCZYK-O., AND BHANDARE-S. (2007). Coherent digital polarization diversity receiver for real-time polarization-multiplexed QPSK transmission at 2.8 Gb/s, *IEEE Photonics Technology Letters*, **19**(24), pp. 1988–1990.
- PFEIFFER-U. R., JAIN-R., GRZYB-J., MALZ-S., HILLGER-P., AND RODRÍGUEZ-VÍZQUEZ-P. (2018). Current status of terahertz integrated circuits—from components to systems, *2018 IEEE BiCMOS and Compound Semiconductor Integrated Circuits and Technology Symposium (BCICTS)*, IEEE, pp. 1–7.

- POZAR-D. M. (2011). *Microwave Engineering*, John Wiley & Sons.
- RAHMAN-B., SOMASIRI-N., THEMISTOS-C., AND GRATTAN-K. (2001). Design of optical polarization splitters in a single-section deeply etched MMI waveguide, *Applied Physics B*, **73**(5), pp. 613–618.
- RANJKESH-N., BASHA-M., TAEB-A., AND SAFAVI-NAEINI-S. (2015). Silicon-on-glass dielectric waveguide—Part II: For THz applications, *IEEE Transactions on Terahertz Science and Technology*, **5**(2), pp. 280–287.
- RECK-T. J., AND CHATTOPADHYAY-G. (2013). A 600 GHz asymmetrical orthogonal mode transducer, *IEEE Microwave and Wireless Components Letters*, **23**(11), pp. 569–571.
- RIESEN-N., AND LOVE-J. D. (2013). Tapered velocity mode-selective couplers, *Journal of Lightwave Technology*, **31**(13), pp. 2163–2169.
- RODRÍGUEZ-VÁZQUEZ-P., GRZYB-J., SARMAH-N., HEINEMANN-B., AND PFEIFFER-U. R. (2018). Towards 100 Gbps: A fully electronic 90 Gbps one meter wireless link at 230 GHz, *2018 48th European Microwave Conference (EuMC)*, IEEE, pp. 1389–1392.
- SACHER-W. D., BARWICZ-T., TAYLOR-B. J., AND POON-J. K. (2014). Polarization rotator-splitters in standard active silicon photonics platforms, *Optics Express*, **22**(4), pp. 3777–3786.
- SAKAGUCHI-J., AWAJI-Y., WADA-N., KANNO-A., KAWANISHI-T., HAYASHI-T., TARU-T., KOBAYASHI-T., AND WATANABE-M. (2011). 109-Tb/s ($7 \times 97 \times 172$ -Gb/s SDM/WDM/PDM) QPSK transmission through 16.8-km homogeneous multi-core fiber, *2011 Optical Fiber Communication Conference and Exposition and the National Fiber Optic Engineers Conference*, IEEE, pp. 1–3.
- SCHNEIDER-T., WIATREK-A., PREUSSLER-S., GRIGAT-M., AND BRAUN-R.-P. (2012). Link budget analysis for terahertz fixed wireless links, *IEEE Transactions on Terahertz Science and Technology*, **2**(2), pp. 250–256.
- SELVARAJA-S. K., AND SETHI-P. (2018). *Emerging Waveguide Technology*, IntechOpen, chapter 6.

BIBLIOGRAPHY

- SENGUPTA-K. (2019). Integrated circuits for terahertz communication beyond 100 GHz: Are we there yet?, *2019 IEEE International Conference on Communications Workshops (ICC Workshops)*, IEEE, pp. 1–6.
- SENGUPTA-K., NAGATSUMA-T., AND MITTLEMAN-D. M. (2018). Terahertz integrated electronic and hybrid electronic–photonic systems, *Nature Electronics*, **1**(12), art. no. 622.
- SEOK-E., SHIM-D., MAO-C., HAN-R., SANKARAN-S., CAO-C., KNAP-W., AND O-K. K. (2010). Progress and challenges towards terahertz CMOS integrated circuits, *IEEE Journal of Solid-State Circuits*, **45**(8), pp. 1554–1564.
- SHEN-B., WANG-P., POLSON-R., AND MENON-R. (2015). An integrated-nanophotonics polarization beamsplitter with $2.4 \times 2.4 \mu\text{m}^2$ footprint, *Nature Photonics*, **9**(6), pp. 378–382.
- SHIODE-T., MUKAI-T., KAWAMURA-M., AND NAGATSUMA-T. (2011). Giga-bit wireless communication at 300 GHz using resonant tunneling diode detector, *Asia-Pacific Microwave Conference 2011*, IEEE, pp. 1122–1125.
- SHI-Y., DAI-D., AND HE-S. (2007). Proposal for an ultracompact polarization-beam splitter based on a photonic-crystal-assisted multimode interference coupler, *IEEE Photonics Technology Letters*, **19**(11), pp. 825–827.
- SOLDANO-L., DE VREEDE-A., SMIT-M., VERBEEK-B., METAAL-E., AND GREEN-F. (1994). Mach-Zehnder interferometer polarization splitter in InGaAsP/InP, *IEEE Photonics Technology Letters*, **6**(3), pp. 402–405.
- SONG-H.-J., AND NAGATSUMA-T. (2011). Present and future of terahertz communications, *IEEE Transactions on Terahertz Science and Technology*, **1**(1), pp. 256–263.
- SONG-J. H., KONGNYUY-T. D., DE HEYN-P., LARDENOIS-S., JANSEN-R., AND ROTTENBERG-X. (2020). Low-loss waveguide bends by advanced shape for photonic integrated circuits, *Journal of Lightwave Technology*, **38**(12), pp. 3273–3279.

- SONG-J. H., KONGNYUY-T. D., STASSEN-A., MUKUND-V., AND ROTTENBERG-X. (2016a). Adiabatically bent waveguides on silicon nitride photonics for compact and dense footprints, *IEEE Photonics Technology Letters*, **28**(20), pp. 2164–2167.
- SONG-J. H., KONGNYUY-T. D., STASSEN-A., MUKUND-V., AND ROTTENBERG-X. (2016b). Adiabatically bent waveguides on silicon nitride photonics for compact and dense footprints, *IEEE Photonics Technology Letters*, **28**(20), pp. 2164–2167.
- SUBASHIEV-A. V., AND LURYI-S. (2006). Modal control in semiconductor optical waveguides with uniaxially patterned layers, *Journal of Lightwave Technology*, **24**(3), pp. 1513–1522.
- SUN-X., AITCHISON-J. S., AND MOJAHEDI-M. (2017). Realization of an ultra-compact polarization beam splitter using asymmetric MMI based on silicon nitride/silicon-on-insulator platform, *Optics Express*, **25**(7), pp. 8296–8305.
- SUN-X., ALAM-M., AITCHISON-J., AND MOJAHEDI-M. (2016). Compact and broadband polarization beam splitter based on a silicon nitride augmented low-index guiding structure, *Optics Letters*, **41**(1), pp. 163–166.
- TAEB-A. (2015). *A New Silicon-Based Dielectric Waveguide Technology for Millimeter-Wave/Terahertz Devices and Integrated Systems*, PhD thesis, University of Waterloo.
- TAEB-A., CHEN-L., GIGOYAN-S., BASHA-M., RAFI-G., CHAUDHURI-S., AND SAFAVINAEBINI-S. (2016a). A silicon image guide (SIG) technology platform for high performance sub-millimeter-wave passive structures, *IEEE MTT-S International Microwave Symposium (IMS)*, IEEE, pp. 1–4.
- TAEB-A., CHEN-L., GIGOYAN-S., BASHA-M., RAFI-G., CHAUDHURI-S., AND SAFAVINAEBINI-S. (2016b). A silicon image guide (SIG) technology platform for high performance sub-millimeter-wave passive structures, *2016 IEEE MTT-S International Microwave Symposium (IMS)*, IEEE, pp. 1–4.
- TAN-D., IKEDA-K., AND FAINMAN-Y. (2009). Cladding-modulated Bragg gratings in silicon waveguides, *Optics Letters*, **34**(9), pp. 1357–1359.

BIBLIOGRAPHY

- TORRES-GARCÍA-A. E., PÉREZ-ESCUADERO-J. M., TENIENTE-J., GONZALO-R., AND EDERRA-I. (2020). Silicon integrated subharmonic mixer on a photonic-crystal platform, *IEEE Transactions on Terahertz Science and Technology*, **11**(1), pp. 79–89.
- TSURUDA-K., FUJITA-M., AND NAGATSUMA-T. (2015a). Extremely low-loss terahertz waveguide based on silicon photonic-crystal slab, *Optics Express*, **23**(25), pp. 31977–31990.
- TSURUDA-K., FUJITA-M., AND NAGATSUMA-T. (2015b). Extremely low-loss terahertz waveguide based on silicon photonic-crystal slab, *Optics Express*, **23**(25), pp. 31977–31990.
- UHER-J., BORNEMANN-J., AND ROSENBERG-U. (1993). *Waveguide components for antenna feed systems: Theory and CAD*, Artech House Antenna Library.
- UNG-B. S.-Y., LI-J., LIN-H., FISCHER-B. M., WITHAYACHUMNANKUL-W., AND ABBOTT-D. (2013). Dual-mode terahertz time-domain spectroscopy system, *IEEE Transactions on Terahertz Science and Technology*, **3**(2), pp. 216–220.
- VDI. (2010). *Virginia Diodes Inc. Waveguide Band Designations*, Virginia Diodes Inc.
- VINCETTI-L. (2009). Hollow core photonic band gap fiber for THz applications, *Microwave and Optical Technology Letters*, **51**(7), pp. 1711–1714.
- WANG-F., PAVLIDIS-V. F., AND YU-N. (2020). Miniaturized SIW bandpass filter based on TSV technology for THz applications, *IEEE Transactions on Terahertz Science and Technology*, **10**(4), pp. 423–426.
- WANG-X. (2013). *Silicon Photonic Waveguide Bragg Gratings*, University of British Columbia.
- WANG-X., GRIST-S., FLUECKIGER-J., JAEGER-N. A., AND CHROSTOWSKI-L. (2013). Silicon photonic slot waveguide Bragg gratings and resonators, *Optics Express*, **21**(16), pp. 19029–19039.

- WANG-X., SHI-W., VAFAEI-R., JAEGER-N. A., AND CHROSTOWSKI-L. (2010). Uniform and sampled Bragg gratings in SOI strip waveguides with sidewall corrugations, *IEEE Photonics Technology Letters*, **23**(5), pp. 290–292.
- WANG-X., SHI-W., YUN-H., GRIST-S., JAEGER-N. A., AND CHROSTOWSKI-L. (2012). Narrow-band waveguide Bragg gratings on SOI wafers with CMOS-compatible fabrication process, *Optics Express*, **20**(14), pp. 15547–15558.
- WANG-Y., MA-M., YUN-H., LU-Z., WANG-X., JAEGER-N. A., AND CHROSTOWSKI-L. (2016). Ultra-compact sub-wavelength grating polarization splitter-rotator for silicon-on-insulator platform, *IEEE Photonics Journal*, **8**(6), pp. 1–9.
- WITHAYACHUMNANKUL-W. (2010). *Engineering Aspects of Terahertz Time-Domain Spectroscopy*, PhD thesis, The University of Adelaide.
- WITHAYACHUMNANKUL-W., FISCHER-B. M., AND ABBOTT-D. (2008). Quarter-wavelength multilayer interference filter for terahertz waves, *Optics Communications*, **281**(9), pp. 2374–2379.
- WITHAYACHUMNANKUL-W., FUJITA-M., AND NAGATSUMA-T. (2018a). Integrated silicon photonic crystals toward terahertz communications, *Advanced Optical Materials*, **6**(16), pp. 1–7.
- WITHAYACHUMNANKUL-W., YAMADA-R., FUJITA-M., AND NAGATSUMA-T. (2018b). All-dielectric rod antenna array for terahertz communications, *APL Photonics*, **3**(5), pp. 051707–051718.
- WITHAYACHUMNANKUL-W., YAMADA-R., FUMEAUX-C., FUJITA-M., AND NAGATSUMA-T. (2017). All-dielectric integration of dielectric resonator antenna and photonic crystal waveguide, *Optics Express*, **25**(13), pp. 14706–14714.
- WOOTTEN-A., AND THOMPSON-A. R. (2009). The Atacama large millimeter/submillimeter array, *Proceedings of the IEEE*, **97**(8), pp. 1463–1471.
- WU-H., TAN-Y., AND DAI-D. (2017). Ultra-broadband high-performance polarizing beam splitter on silicon, *Optics Express*, **25**(6), pp. 6069–6075.

BIBLIOGRAPHY

- WU-K., BOZZI-M., AND FONSECA-N. J. (2021). Substrate integrated transmission lines: Review and applications, *IEEE Journal of Microwaves*, **1**(1), pp. 345–363.
- WU-K., DESLANDES-D., AND CASSIVI-Y. (2003). The substrate integrated circuits-a new concept for high-frequency electronics and optoelectronics, *6th International Conference on Telecommunications in Modern Satellite, Cable and Broadcasting Service, 2003. TELSIKS 2003.*, Vol. 1, IEEE, pp. P–III.
- WU-X., AND SENGUPTA-K. (2018). Single-chip source-free terahertz spectroscope across 0.04–0.99 THz: combining sub-wavelength near-field sensing and regression analysis, *Optics Express*, **26**(6), pp. 7163–7175.
- XING-HAI-Z., GUANG-CUN-S., YI-JIA-D., JING-FU-B., HAO-SHEN-Z., YING-BIN-Z., CHAN-HUNG-S., AND YONG-SHENG-C. (2012). G-band rectangular waveguide filter fabricated using deep reactive ion etching and bonding processes, *Micro & Nano Letters*, **7**(12), pp. 1237–1240.
- YANG-Y., YAMAGAMI-Y., YU-X., PITCHAPPA-P., WEBBER-J., ZHANG-B., FUJITA-M., NAGATSUMA-T., AND SINGH-R. (2020). Terahertz topological photonics for on-chip communication, *Nature Photonics*, **14**(7), pp. 446–451.
- YIN-Y., LI-Z., AND DAI-D. (2017). Ultra-broadband polarization splitter-rotator based on the mode evolution in a dual-core adiabatic taper, *Journal of Lightwave Technology*, **35**(11), pp. 2227–2233.
- YU-X. (2020). *Terahertz Integrated Circuits Based on Photonic-Crystal Waveguide Platform*, PhD thesis, Osaka University.
- YU-X., HOSODA-Y., MIYAMOTO-T., OBATA-K., KIM-J.-Y., FUJITA-M., AND NAGATSUMA-T. (2019a). Terahertz fibre transmission link using resonant tunnelling diodes integrated with photonic-crystal waveguides, *Electronics Letters*, **55**(7), pp. 398–400.
- YU-X., KIM-J.-Y., FUJITA-M., AND NAGATSUMA-T. (2019b). Efficient mode converter to deep-subwavelength region with photonic-crystal waveguide platform for terahertz applications, *Optics Express*, **27**(20), pp. 28707–28721.

- YU-X., KIM-J.-Y., FUJITA-M., AND NAGATSUMA-T. (2019c). Efficient mode converter to deep-subwavelength region with photonic-crystal waveguide platform for terahertz applications, *Optics Express*, **27**(20), pp. 28707–28721.
- YU-X., MIYAMOTO-T., OBATA-K., HOSODA-Y., KIM-J.-Y., FUJITA-M., AND NAGATSUMA-T. (2019d). Direct terahertz communications with wireless and fiber links, *2019 44th International Conference on Infrared, Millimeter, and Terahertz Waves (IRMMW-THz)*, IEEE, pp. 1–2.
- YU-X., OHIRA-T., KIM-J.-Y., FUJITA-M., AND NAGATSUMA-T. (2020). Waveguide-input resonant tunnelling diode mixer for THz communications, *Electronics Letters*, **56**(7), pp. 342–344.
- YU-X., SUGETA-M., YAMAGAMI-Y., FUJITA-M., AND NAGATSUMA-T. (2019e). Simultaneous low-loss and low-dispersion in a photonic-crystal waveguide for terahertz communications, *Applied Physics Express*, **12**(1), art. no. 012005.
- ZABELIN-V., DUNBAR-L. A., LE THOMAS-N., HOUDRÉ-R., KOTLYAR-M., O’FAOLAIN-L., AND KRAUSS-T. (2007). Self-collimating photonic crystal polarization beam splitter, *Optics Letters*, **32**(5), pp. 530–532.
- ZHANG-F., ZHENG-J., SONG-Y., LIU-W., XU-P., AND MAJUMDAR-A. (2020). Ultra-broadband and compact polarizing beam splitter in silicon photonics, *OSA Continuum*, **3**(3), pp. 560–567.
- ZHANG-J., AND HSIANG-T. Y. (2005). Dispersion characteristics of coplanar waveguides at subterahertz frequencies, *Journal of Electromagnetic Waves and Applications*, **20**(10), pp. 1411–1417.
- ZHANG-Y., LI-Z., AND LI-B. (2006). Multimode interference effect and self-imaging principle in two-dimensional silicon photonic crystal waveguides for terahertz waves, *Optics Express*, **14**(7), pp. 2679–2689.
- ZHU-H.-T., XUE-Q., LIAO-S.-W., PANG-S. W., CHIU-L., TANG-Q.-Y., AND ZHAO-X.-H. (2016a). Low-cost narrowed dielectric microstrip line—a three-layer dielectric

BIBLIOGRAPHY

waveguide using PCB technology for millimeter-wave applications, *IEEE Transactions on Microwave Theory and Techniques.*, **65**(1), pp. 119–127.

ZHU-H., XUE-Q., HUI-J., AND PANG-S. W. (2016b). Design, fabrication, and measurement of the low-loss SOI-based dielectric microstrip line and its components, *IEEE Transactions on Terahertz Science and Technology*, **6**(5), pp. 696–705.

ZOU-C.-L., SUN-F.-W., DONG-C.-H., REN-X.-F., CUI-J.-M., CHEN-X.-D., HAN-Z.-F., AND GUO-G.-C. (2011). Broadband integrated polarization beam splitter with surface plasmon, *Optics Letters*, **36**(18), pp. 3630–3632.

Biography



Weijie Gao was born in Inner Mongolia, China in 1989. He received his Bachelor of Engineering in the field of Mechanical Design, Manufacturing and Automation from the Hubei University of Technology, China in 2011. In 2016, he received his Master of Engineering Science in Telecommunications from the University of New South Wales, Sydney, Australia. After obtaining his master degree, in 2016 as a volunteer researcher, he joined the Adelaide Applied Electromagnetics Group, School of Electrical and Electronic Engineering at the

University of Adelaide in the area of microwave reconfigurable antennas under the supervisions of Prof. Christophe Fumeaux and A/Prof. Withawat Withayachumnankul. In 2018, he commenced his doctoral program with Terahertz Engineering Laboratory, School of Electrical and Electronic Engineering, The University of Adelaide in the area of terahertz integrated waveguides and platforms under the supervisions of A/Prof. Withawat Withayachumnankul and Prof. Christophe Fumeaux.

During his candidature, he received the Full-Fee Scholarship from the University of Adelaide, and ECMS Divisional Scholarship from the Faculty of Engineering, Computer and Mathematical Sciences. In 2018, he was fully funded by A/Prof. Withayachumnankul to visit Osaka University, Japan to conduct experiments on terahertz communications. From 2019-2021, he was granted various travel scholarships including Research Travel Scholarship and the ECMS Travelling Scholarships to attend various flagship international conferences in terahertz, photonic, and microwave regimes, e.g., International Conference on Infrared, Millimetre and Terahertz Waves (IRMMW-THz). During his Ph.D candidature, his research works were selected as Keynote talks in the IRMMW-THz conferences in 2019, 2020, and 2021, respectively. He was the recipient of the Student Prize in the Asia-Pacific Microwave Conference, 2021 (APMC 2021). He has been awarded a Postdoctoral Fellowship to undertake at Osaka University, Japan under the supervisions of Prof. Tadao Nagatsuma and A/Prof. Masayuki Fujita, which he will commence in 2022. His research interests include terahertz integrated waveguides, components, antennas, and microwave reconfigurable antennas.